International Journal of Acoustics and Vibration

A quarterly publication of the International Institute of Acoustics and Vibration

Volume 21, Number 2, June 2016

EDITORIAL

ARTICLES

INFORMATION

The ICSV23 — from Ancient to Modern Acoustics

It is our great pleasure to invite you and your accompanying persons to participate in the 23rd International Congress on Sound and Vibration (ICSV23), to be held from 10 to 14 July 2016 at the Athenaeum Intercontinental hotel, Athens, Greece.

The International Institute of Acoustics and Vibration (IIAV), in cooperation with the Laboratory of Transportation Environmental Acoustics (L.T.E.A.) of the University of Thessaly - Faculty of Civil Engineering, are jointly organizing the ICSV23. Almost 1000 abstracts in the field of acoustics, noise, and vibration from 64 countries have been accepted for presentation. Almost half of those submitted are from Asia, 375 from Europe with more than 65 from Greece and Cyprus, 74 from North and Latin Americas, and the remaining from Australia, New Zealand, and Africa.

The attendance of so many scientists and engineers around the world is an important opportunity for all participants to establish new collaborations, to exchange ideas, and to share their research results. With the purpose of collecting high-level scientific contributions, the peer review of full papers was offered to all the authors. More than 330 full papers have undergone the peer-review process. This important scientific event aiming "from ancient to modern acoustics" will be held in the historic city of Athens, birthplace of Democracy and famous for the acoustics of archaeological sites and theatres. Athens has been the capital of the independent Greek state since 1834, and the host city of the first modern-day Olympic Games in 1896. Then 108 years later Athens hosted the 2004 Summer Olympics. Athens is also the home to the most famous UNESCO World Heritage Site: the Acropolis of Athens under the coordinated construction of Pericles (c. 495 - 429 BC.) The site's most important building include the Parthenon, the Propylaia, the Erechtheion and the temple of Athena Nike. Athens ensures also a great number of other magnificent sights and attractions, such as the famous Herod Atticus Odeon, which dominates the western end on the south slope of the Acropolis, the Agora the centre of political and public life in Athens (6th century BC), the medieval Daphni Monastery, the Hellenic Parliament (19th century) and the Athens Trilogy, consisting of the National Library of Greece, Athens University and the Academy of Athens, the National Archeological Museum, featuring the world's largest collection of ancient Greek antiquities, as well as the new Acropolis Museum.

The ICSV23 Scientific Programme is structured in 15 Subject Areas, and one Special Workshop (SW-1), including several special Structured Sessions and Regular Sessions, covering our traditional topics such as active noise and vibration control, signal processing, simulation, machinery noise and vibration, as well as environmental noise, vibration, soundscapes, occupational noise, underwater and maritime noise. A special workshop on Strategic Noise Mapping and Noise action Plans in Greece, Cyprus & South European Countries will be organized during the ICSV23 Congress. Participation is offered to all registered participants including students.

The ICSV23 Scientific Programme is also enriched by six distinguished plenary lectures: Li Cheng : Interior Sound and Vibration Control for Air Vehicle Applications; Christy Holland : Microbubble Pumps: Ultrasound Theragnostic Agents; Stelios Kephalopoulos : Common Noise Assessment Methods for Europe (CNOSSOS-EU); Harris Mouzakis : Vibrations and Cultural Heritage in Greece; Ricardo Musafir : Sound Generation by Fluid Flow; and James Talbot : Building on Springs: Towards a Performance-Based Design

Students in sound and vibration are especially welcome at ICSV23; they can find reduced fees, a best paper award, and other grants organized specifically for them.

The ICSV23 Technical Exhibition is an interesting and important part of the Congress. Software, Acoustical Consulting, Environmental Noise & Vibration, Urban Transportation network operators and various technical companies are taking part. All refreshment breaks, including morning and afternoon tea, coffee and lunch, will be held within the exhibition area. In addition, the exhibition area is located near to the scientific programme lecture halls, thus guaranteeing a high level of delegate visitation and an optimum degree of dissemination of their latest advances in acoustics, noise & vibration technology.

During ICSV23, many social and cultural activities are planned for all participants. The social programme, prepared for the enjoyment of both participants of ICSV23 and accompanying persons, includes the Welcome Reception, Banquet and a guided visit to the new Acropolis Museum in the picturesque district of Plaka and Gazi. Athens is probably the single European capital where, within less than 30 minutes from the vibrant city centre, one can easily go to the beach or to the nearby islands. It takes less than 2 hours from the city centre, to reach places that have both archeological and historical interest, as well as exceptional natural surroundings such as Cape Sounion, the city of Nafplion the famous Delphi Temple and also Hydra, Spetses, Aegina and Poros, islands of the Saronic Gulf. These magnificent destinations will provide a memorable programme for all participants and accompanying persons. Additional opportunities are available to better enjoy Athens.

Along with the IIAV officers and the Local organizing Committee, we hope you can attend ICSV23 and experience the cultural heritage of Greece.

I look forward to welcoming you in Athens this July.

Konstantinos Vogiatzis
ICSV23 General Chair

 http://dx.doi.org/10.20855/ijav.2016.21.1E80

Dynamic Stability Analysis of a Circularly Tapered Rotating Beam Subjected to Axial Pulsating Load and Thermal Gradient under Various Boundary Conditions

Rashmita Parida

Department of Mechanical Engineering, College of Engineering and Technology, Bhubaneswar Techno Campus, Ghatikia, Bhubaneswar, Orissa, India-751003

Pusparaj Dash

Department of Mechanical Engineering, VSSUT Burla, Sambalpur, Orissa, India-768018

(Received 13 August 2013; accepted 8 October 2015)

The dynamic stability of a circularly tapered rotating beam subjected to a pulsating axial external excitation with thermal gradient was studied for all possible combinations of clamped, guided, pinned, fixed, and free boundary conditions. The equations of motion and associated boundary conditions were obtained using the extended Hamilton's principle. Then these equations of motion and the associated boundary conditions were non-dimensionalised. A set of Hill's equations were obtained from the non-dimensional equations of motion by the application of the extended Galerkin method. The zones of parametric instability were obtained using Saito-Otomi conditions. The effects of various boundary conditions, thermal gradient, taper, and rotational speed on the regions of parametric instability were investigated and presented through a series of graphs. The results reveal that increasing rotational speed and taper have stabilizing effects, whereas increasing thermal gradient has a destabilizing effect for all boundary conditions of the beam.

NOMENCLATURE

$A(x)$, $A(\xi)$	Area of a generic section of the beam
A_1	Cross sectional area at the end $x = l$
C_0	Hub radius
c_0	Dimensionless hub radius, $= C_0/l$
$d(x)$, $d(\xi)$	Diameter of a generic section of the beam
d_1	Diameter at the end, $x = l$
$E(x)$, $E(\xi)$	Young's modulus at a generic section
E_1	Young's modulus at the end, $x = l$
$I(x)$, $I(\xi)$	Moment of inertia at a generic section
I_1	Moment of inertia at the end, $x = l$
l	Length of the beam
$m(\xi)$	Mass distribution function
P_0	Static axial load
P_1	Dynamic axial load
$p(\tau)$	Dimensionless load
p_0	Dimensionless static axial load
p_1	Dimensionless dynamic axial load
$S(\xi)$	Moment of inertia distribution function
$T(\xi)$	Elasticity modulus distribution function
t	Time
$w(x,t)$	Transverse deflection of the beam
γ	Coefficient of thermal expansion of the beam material
δ	Thermal gradient parameter
a^*	Diameter taper parameter
η	Dimensionless transverse deflection, $= w/l$
ξ	Dimensionless length, $= x/l$
τ	Dimensionless time, $= ct$
ρ	Density of the beam material
Ω	Uniform angular velocity Ω of the beam about z'-axis
Ω_0	Rotational speed parameter
ω	Excitation frequency
ω_0	Dimensionless fundamental natural frequency
Θ	Non-Dimensional excitation frequency, $= \omega/c$
Ψ_0	Reference temperature
Ψ_1	Temperature at the end, $\xi = 1$

1. INTRODUCTION

The stability analysis and dynamic behaviour of a rotating cantilever beam with axial orientation perpendicular to the axis of spin is very essential for its practical applications such as turbomachinery blades, rotor blades of helicopter, aircraft propellers, flexible appendages of spacecraft, satellite antennas, and robotic manipulators, to name a few. In some cases the structures have to operate under elevated temperatures. A linear relation is observed between the Young's modulus and the temperature of most engineering materials.

An ample number of publications are available regarding the design and analysis of rotating structures. The flexural vibrations of a rotating cantilever beam with a tip mass at the free end has been studied by Bhat.[1] He proposed the beam characteristic orthogonal polynomials in the Rayleigh-Ritz method. Liu and Yeh[2] have investigated the influence of restrained parameters on the Eigen frequencies of rotating uniform and non-uniform beams with a restrained base using Galerkin's method. The stability analysis of a rotating shaft due to pulsating torque applied at its end has been studied by Unger and

Brull.[3] They found that instability arising from the combination resonance has the most adverse effect. Kammer and Schlack[4] adopted the Krylov-Bogoliubov-Mitropolskii (KBM) perturbation technique to solve the problem of instability due to the time dependent angular velocity in a rotating Euler beam. Namachchivaya[5] investigated the dynamic stability of rotating shaft under the excitation of combined harmonic and stochastic load and derived the stability conditions explicitly for the first and second order moments considering the shaft as a two degrees of freedom system. Bauer and Eidel[6] studied the effects on vibration and buckling of a rotating Euler beam of uniform cross section because of its spin speed, hub radius and aspect ratio considering an orientation perpendicular to the axis of rotation. The dynamic stability analysis of rotating Timoshenko beam with a root flexibility using finite element method was investigated for the first time by Abbas.[7] Ishida *et al.*[8] studied the vibration and stability of a rotating shaft under a sinusoidal axial force assuming a four degrees of freedom system. The stability of a tapered cantilever beam on Winkler foundation subjected to a follower force was studied by Lee.[9] He found that the critical flutter loads of both tapered beams and beams of a uniform cross section are unaffected by the presence of viscous damping in the elastic foundation. Lin and Chen[10] studied the dynamic stability of rotating composite beams using finite element method. Tan *et al.*[12] discussed the instability of a spinning pre-twisted beam under compressive axial loads assuming Euler-Bernoulli beam theory (EBT) and assumed mode method. Banerjee *et al.*[12] applied the dynamic stiffness method to analyse the free vibration of a rotating taper beam that follows EBT. They derived some explicit analytical expressions and used the Wittrick-Williams algorithm for the solution. Shahba and Rajasekaran[13] used the differential transform element method (DTEM) and differential quadrature element method (DQEL) of lower order to solve the equations of free vibration and stability of tapered Euler-Bernoulli beam made of axially functionally graded material. Yang *et al.*[14] developed a finite element model to study the free vibration of a rotating uniform Euler-Bernoulli beam. They considered the coupling of axial and transverse vibration and of elastic deformations and rigid motion. Nayak *et al.*[15] investigated the stability of a sandwich beam on viscoelastic supports subjected to a pulsating axial load with temperature gradient. Soltani *et al.*[16] proposed a numerical solution based on power series method to derive the critical buckling loads and frequency of free vibrations for tapered thin beams. Bulut[17] studied the dynamic stability of parametrically excited rotating tapered beam and found that the number of instability zones increases with the taper ratio.

A survey of literature reveals that some work has been done on parametric instability and dynamic stability of a symmetric rotating beam, parametric instability of a non-uniform beam with thermal gradient resting on a Pasternak foundation, and that of a symmetric sandwich beam for different boundary conditions. However, no work has been done to study the static and dynamic stability of a rotating tapered beam with thermal gradient under various boundary conditions. Thus the present work mainly deals with a theoretical study of a rotating tapered beam with a pulsating load and thermal gradient under various boundary conditions. The static and dynamic stability of a rotating tapered cantilever beam which is fixed at one end and subjected to an axial pulsating load and a steady, one-dimensional temperature gradient at the free end has been reported. The effect of the rotation parameter, geometric parameters, taper parameter, and the thermal gradient on the nondimensional static buckling loads zones and also on the parametric instability zones are investigated.

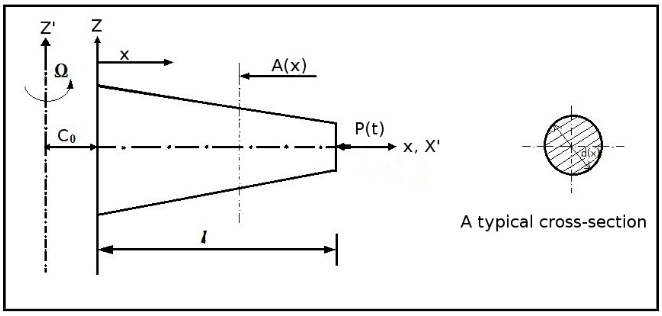

Figure 1. System Configuration.

2. FORMULATION OF THE PROBLEM

2.1. System Configuration

A rotating tapered cantilever beam of length l set off a distance C_0 from the axis of rotation which rotates at a uniform angular velocity Ω about a vertical z'-axis is capable of oscillating in the x–z plane. The beam is oriented along the x-axis perpendicular to the axis of rotation as shown in Fig. 1. A pulsating axial force $P(t) = P_0 + P_1 cos\omega t$ is applied at the end $x = C_0 + l$ of the beam along the point of C.G. of the cross-section in the axial direction, with ω being the frequency of the applied load, t being the time, and P_0 and P_1 being the static and dynamic load amplitudes, respectively.

The following assumptions are made for deriving the equations of motion:

a) The material of the beam is homogeneous & isotropic in nature.

b) The deflections of the beam are small and the transverse deflection $w(x, t)$ is the same for all points of a cross-section.

c) The beam obeys Euler-Bernoulli beam theory.

d) Extensional deflection of the beam is neglected.

e) A steady one-dimensional temperature gradient is assumed to exist along the central length of the beam.

f) Extension and rotary inertia effects are negligible.

The expressions for potential energy, kinetic energy and work done are as follows:

$$V = \frac{1}{2}\int_0^l E(x)I(x)\left(\frac{\partial^2 w}{\partial x^2}\right)^2 dx + \frac{1}{2}\int_0^l \rho A(x)\Omega^2(C_0+x)\int_0^{x'}\left(\frac{\partial w}{\partial x}\right)^2 dx; \quad (1)$$

$$T = \frac{1}{2}\int_0^l \rho A(x)\left(\frac{\partial w}{\partial t}\right)^2 dx + \frac{1}{2}\int_0^l \rho\Omega^2 A(x) w^2 dx; \quad (2)$$

$$W_P = \frac{1}{2}\int_0^l P(t)\left(\frac{\partial w}{\partial x}\right)^2 dx; \tag{3}$$

where $w(x,t)$ is transverse deflection of the beam.

The application of the extended Hamilton's principle gives the following equation of motion and boundary conditions:

$$\delta\int_{t_1}^{t_2}(T - V - W_P) = 0; \tag{4}$$

$$[E(x)\,I(x)\,w_{,xx}]_{,xx} + \rho A(x)\,w_{.tt} + \rho\Omega^2 I(x)\,w_{,xx} - [N(x_1)\,w_{,x}]_{,x} + P(t)\,w_{,xx} = 0; \tag{5}$$

where $N(x_1) = \frac{1}{2}\rho A(x)\,\Omega^2\left[(C_0+l)^2 - (C_0+x')^2\right]$. The boundary conditions at $x = C_0$ and $x = C_0 + l$ are

$$\begin{aligned}[E(x)\,I(x)\,w_{,xx}]_{,x} + P(t)\,w_{,x} &= 0;\\ [E(x)\,I(x)\,w_{,xx}]_{x=l} &= 0;\\ w_{,t} &= 0.\end{aligned} \tag{6}$$

In the above expression $w_{,x} = \frac{\partial w}{\partial x}$, $w_{,xx} = \frac{\partial^2 w}{\partial x^2}$, $w_{,t} = \frac{\partial w}{\partial t}$, $w_{,tt} = \frac{\partial^2 w}{\partial t^2}$.

Introducing the dimensionless parameters,
$\xi = \frac{x}{l}, \eta = \frac{w}{l}, c_0 = \frac{C_0}{l}, \tau = ct;$
$\left(\because c^2 = \frac{E(x)I(x)}{\rho A(x)l^4}\right);$
$\frac{\partial w}{\partial x} = \frac{\partial \eta}{\partial \xi}$ and $\left(\frac{\partial w}{\partial x}\right)^2 = \left(\frac{\partial \eta}{\partial \xi}\right)^2;$
$\frac{\partial^2 w}{\partial x^2} = \frac{1}{l}\frac{\partial^2 \eta}{\partial \xi^2}$ and $\left(\frac{\partial^2 w}{\partial x^2}\right)^2 = \frac{1}{l^2}\left(\frac{\partial^2 \eta}{\partial \xi^2}\right)^2;$
$\frac{\partial w}{\partial t} = cl\left(\frac{\partial \eta}{\partial \tau}\right)$ and $\left(\frac{\partial w}{\partial t}\right)^2 = c^2 l^2\left(\frac{\partial \eta}{\partial \tau}\right)^2;$
$p(\tau) = \frac{P(t)l^2}{E_1 I_1}, p(\tau) = p_0 + p_1\cos\theta\tau;$
$()' = \frac{\partial()}{\partial \xi}, \overset{=}{()}\ \frac{\partial()}{\partial \tau}$, etc.

The non dimensional equation of motion and boundary conditions can be written as

$$[S(\xi)\,T(\xi)\,\eta'']'' + m(\xi)\,\ddot{\eta} + \left[r_g\Omega_0^2 + p(\tau)\right]\eta'' - \Omega_0^2\left[q(\xi)\,\eta'\right]' = 0; \tag{7}$$

and

$$\begin{aligned}\{[S(\xi)\,T(\xi)\,\eta'']' + p(\tau)\,\eta'\}_{\xi=1} &= 0;\\ [S(\xi)\,T(\xi)\,\eta'']_{\xi=1} &= 0;\\ \eta(0,\tau) &= 0;\\ \eta'(0,\tau) &= 0.\end{aligned} \tag{8}$$

In the above expressions $r_g = \frac{I(\xi)}{A_1 l^2}$; $\Omega_0^2 = \frac{\rho A(\xi)\Omega^2 l^4}{E_1 I_1}$; $\Omega_0^2 q(\xi) = \frac{N(x_1)l^2}{E_1 I_1}$; $A(\xi) = A_1 m(\xi), E(\xi) = E_1 T(\xi)$, $I(\xi) = I_1 S(\xi)$.

2.2. Approximate Solution

The approximate solution to the non dimensional equations of motion is assumed as

$$\eta(\xi,\tau) = \sum_{r=1}^{N}\eta_r(\xi)\,f_r(\tau); \tag{9}$$

where $f_r(\tau)$ is an unknown function of time and $\eta_r(\xi)$ is a coordinate function to be chosen so as to satisfy as many of the boundary conditions in Eq. (8) as possible. It is further assumed that $\eta_r(\xi)$ can be represented by a set of functions (9) which satisfy the conditions obtained from Eq. (7) by deleting the terms containing ω_0 and $p(\tau)$. It is further assumed that coordinate functions for the various boundary conditions can be approximated by the ones given in Table 1.

Substitution of the series of solutions in the non dimensional equations of motion and subsequent application of the general Galerkin method leads to the following matrix equations of motion:

$$[M]\left\{\ddot{f}\right\} + [K]\{f\} - \{p_0[H] - p_1\cos\theta\tau\,[H]\}\{f\} = \{0\}; \tag{10}$$

where $\ddot{f} = \frac{\partial^2 f}{\partial \tau^2}$ and $\{f\} = \{f_1, \ldots\ldots\ldots\ldots, f_N\}^T$. The various matrix elements are given by $\int_0^1 m(\xi)\,\eta_i(\xi)\,\eta_j(\xi)\,d\xi = M_{ij}$;
$\int_0^1\left\{\begin{array}{l} S(\xi)\,T(\xi)\,\eta_i{}''(\xi)\,\eta_j{}''(\xi) + \\ \Omega_0^2\left[q(\xi) - r_g\right]\eta_i{}'(\xi)\,\eta_j{}'(\xi)\end{array}\right\}d\xi = K_{ij};$
$\int_0^1 \eta_i{}'(\xi)\,\eta_j{}'(\xi)\,d\xi = H_{ij}$; and
$\because i,j = 1,2,\ldots\ldots\ldots,N.$

2.3. Regions of Dynamic Instability

Let $[L]$ be the modal matrix of $[M]^{-1}[K]$. Then by the introduction of the linear coordinate transformation, $\{f\} = [L]\{v\}$, $\{v\}$ being a new set of generalized coordinates yields,

$$\{\ddot{v}\} + \left[\omega_n^2\right]\{v\} + p_1\cos(\theta\tau)\,[B]\{v\} = \{0\}; \tag{11}$$

where $[\omega_n^2]$ is a spectral matrix corresponding to $[m]^{-1}[k]$ and $[B] = -[L]^{-1}[M]^{-1}[H][L]$.

Equation (11) can be written as,

$$\ddot{v_n} + \omega_n^2 v_n + p_1\cos(\theta\tau)\sum_{m=1}^{m=N} b_{nm}u_n = 0,\qquad n = 1,2,\ldots\ldots,N \tag{12}$$

Equation (12) represents a system of N coupled Hill's equations with complex coefficients.

Here, ω_n and b_{nm} are complex quantities, given by $\omega_n = \omega_{n,R} + j\omega_{n,I}$; $b_{n,m} = b_{nm,R} + jb_{nm,I}$.

The boundaries of the region of instability of simple and combination resonances are obtained using the following conditions by Saito & Otomi.[18]

Case (A): Simple resonance

In this case, the regions of instability are given: When damping is present.

$$\left|\frac{\theta}{2} - \omega_{\mu,R}\right| < \frac{1}{4}\sqrt{\frac{\overline{P}_1^2\left(b_{\mu\mu,R}^2 + b_{\mu\mu,I}^2\right)}{\omega_{\mu,R}^2} - 16\omega_{\mu,I}^2}. \tag{13}$$

And, for the undamped case,

$$\left|\frac{\theta}{2} - \omega_{\mu,R}\right| < \frac{1}{4}\frac{\left|\overline{P}_1 b_{\mu\mu,R}\right|}{\omega_{\mu,R}}. \tag{14}$$

Table 1. Coordinate functions.

End arrangement	Coordinate function $i = 1, 2, \ldots\ldots, r$
P-P	$\eta(\xi) = sin(\pi i \xi)$
G-P	$\eta(\xi) = cos\{(2i-1)\pi\xi/2\}$
C-P	$\eta(\xi) = 2(i+2)\xi^{(i+1)} - (4i+6)\xi^{(i+2)} + 2(i+1)\xi^{(i+3)}$
C-C	$\eta(\xi) = \xi^{(i+1)} + 2\xi^{(i+2)} + \xi^{(i+3)}$
C-CUR	$\eta(\xi) = (i+3)(i+2)^2(i+1)\{\xi^{(i+1)} - 2\xi^{(i+2)} + \xi^{(i+3)}\}$
C-F	$\eta(\xi) = (i+2)(i+3)\xi^{(i+1)} - 2i(i+3)\xi^{(i+2)} + i(i+1)\xi^{(i+2)}$

for $\mu = 1, 2, \ldots\ldots, N$.

Case (B): Combination resonance of the sum type

This type of resonance occurs when $\mu \neq v$; $\mu, v = 1, 2, \ldots\ldots, N$ and the regions of instability are given:

For the damped case,

$$\left|\frac{\omega}{2} - \frac{1}{2}\left(\omega_{\mu,R} + \omega_{\mathrm{v},R}\right)\right| < \frac{\omega_{\mu,I} + \omega_{\mathrm{v},I}}{8\sqrt{\omega_{\mu,I}\omega_{\mathrm{v},I}}}\sqrt{\begin{array}{c}\frac{\overline{P}_1^2}{\omega_{\mu,R}\omega_{v,R}}\left(b_{\mu v,R}b_{v\mu,R} + b_{\mu v,I}b_{v\mu,I}\right) \\ -16\omega_{\mu,I}\omega_{v,I}\end{array}}. \quad (15)$$

For the undamped case,

$$\left|\frac{\omega}{2} - \frac{1}{2}\left(\omega_{\mu,R} + \omega_{\mathrm{v},R}\right)\right| < \frac{\overline{P}_1}{4}\sqrt{\frac{b_{\mu\mathrm{v},R}b_{\mathrm{v}\mu,R}}{\omega_{\mu,R}\omega_{\mathrm{v},R}}}. \quad (16)$$

Case(C): Combination resonance of the difference type

This type of resonance occurs when $\mu < v$, $(\mu, v = 1, 2, \ldots\ldots, N)$ and the regions of instability are given:

For the damped case,

$$\left|\frac{\omega}{2} - \frac{1}{2}\left(\omega_{v,R} - \omega_{\mu,R}\right)\right| < \frac{\omega_{\mu,I} + \omega_{v,I}}{8\sqrt{\omega}_{\mu,I}\omega_{v,I}}\sqrt{\begin{array}{c}\frac{\ddot{P}_1^2}{\omega_{\mu,R}\omega_{v,R}}\left(-b_{\mu v,R}b_{v\mu,R} + b_{\mu v,I}b_{v\mu,I}\right) \\ -16\omega_{\mu,I}\omega_{v,I}\end{array}}. \quad (17)$$

For the undamped case,

$$\left|\frac{\omega}{2} - \frac{1}{2}\left(\omega_{\mathrm{v},R} - \omega_{\mu,R}\right)\right| < \frac{\overline{P}_1}{4}\sqrt{\frac{-b_{\mu\mathrm{v},R}b_{\mathrm{v}\mu,R}}{\omega_{\mu,R}\omega_{\mathrm{v},R}}} \quad (18)$$

Dynamic stability analysis of the circularly tapered rotating beam with axial pulsating load and thermal gradient under various boundary conditions has been carried out by using Eqs. (14), (16), and (18). From them, regions of instability are obtained for various cases.

3. NUMERICAL RESULTS AND DISSCUSSIONS

Numerical results were obtained for various values of the parameters like rotation parameter, geometric parameter, taper parameter, and thermal gradient. The linearly tapered cantilever beam with a circular cross-section is assumed to have a diameter varying according to the relation $d(\xi) = d_1[1 + \alpha^*(1-\xi)]$,
where d_1 is the diameter of the beam at the end $\xi = 1$, and α^* is the diameter taper parameter.

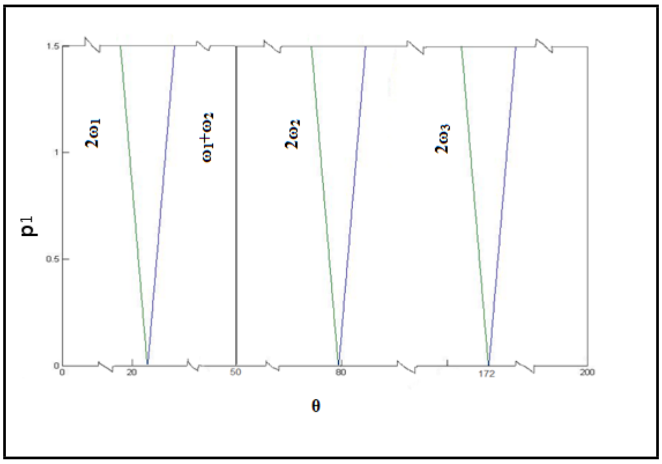

Figure 2. Stability diagram for pinned-pinned beam with $\Omega_0 = 5$ ($\delta = 0.1$, $\alpha^* = 2$).

Consequently, the mass distribution $m(\xi)$ and the moment of inertia distribution $S(\xi)$ are given by the relations
$m(\xi) = [1 + \alpha^*(1-\xi)]^2$;
$S(\xi) = [1 + \alpha^*(1-\xi)]^4$.

The temperature above the reference temperature at any point ξ from the end of the beam is assumed to be $\Psi = \Psi_0(1-\xi)$. Choosing $\Psi_0 = \Psi_1$, the temperature at the end $\xi = 1$, as the reference temperature, means the variation of modulus of elasticity of the beam is denoted by
$E(\xi) = E_1[1 - \gamma\Psi_1(1-\xi)], 0 \leqslant \gamma\Psi_1 < 1$;
$E(\xi) = E_1 T(\xi)$,
where γ is the coefficient of thermal expansion of the beam material, $\delta = \gamma\Psi_1$ is the thermal gradient parameter, and $T(\xi) = [1 - \delta(1-\xi)]$, where δ is the thermal gradient along the length of the beam.

The dynamic stability analysis of the system for various boundary conditions has been analysed as follows:

If, for the change in value of a parameter, the width of the instability zone increases or the zone is pulled down or shifted towards a lower excitation frequency region, the stability of the system worsens. Otherwise, if with the change in the value of the parameter, the width of the instability zone decreases or is pulled up or shifted towards the higher excitation frequency region, or if the number of instability zones reduces, then the stability of the system improves. With these above conditions, the effect of various parameter on the dynamic stability of the system have been analysed.

The regions of parametric instability of a beam with various boundary conditions for two different values of rotational speed parameters are shown in Figs. 2, 3, 5, 6, 8, 9, 11, 12, 14, 15, 17, and 18.

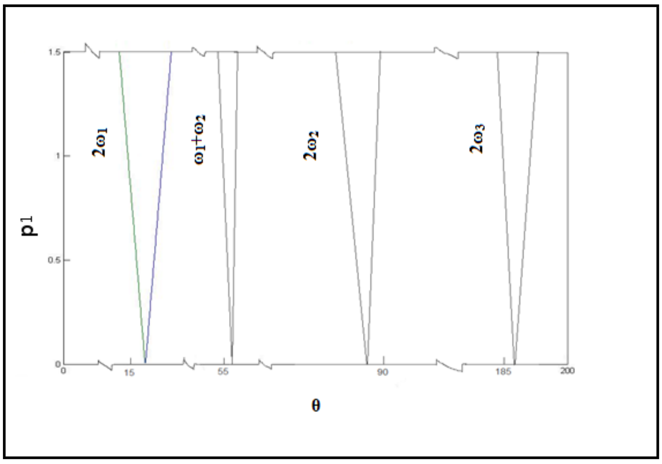

Figure 3. Stability diagram for pinned-pinned beam with $\Omega_0 = 15$ ($\delta = 0.1$, $\alpha^* = 2$).

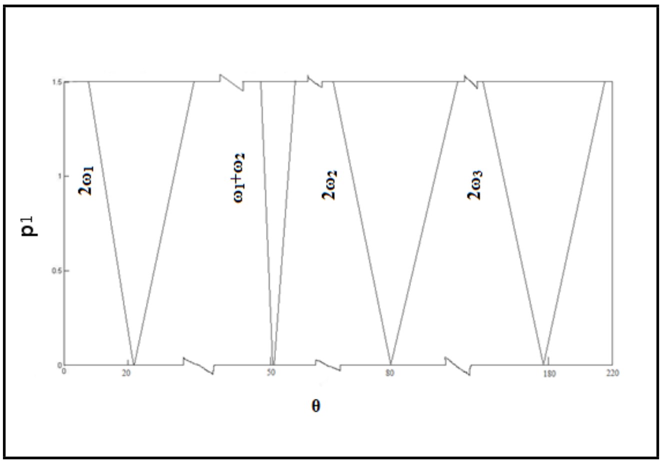

Figure 4. Stability diagram for pinned-pinned beam with $\Omega_0 = 5$ ($\delta = 0.4$, $\delta = 0.8$, $\alpha^* = 1$).

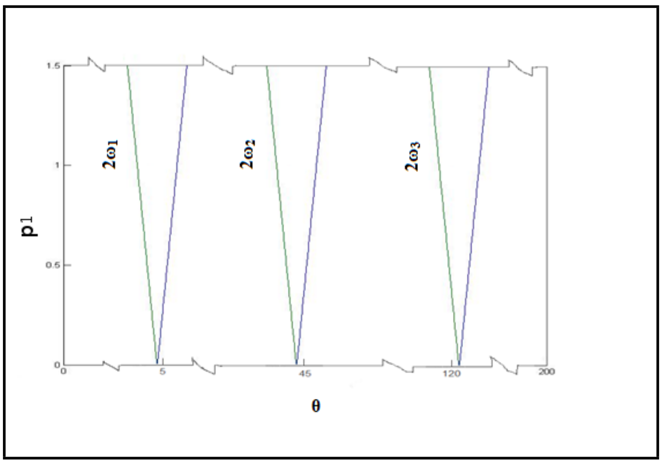

Figure 5. Stability diagram for guided-pinned beam with $\Omega_0 = 2$ ($\delta = 0.1$, $\alpha^* = 2$).

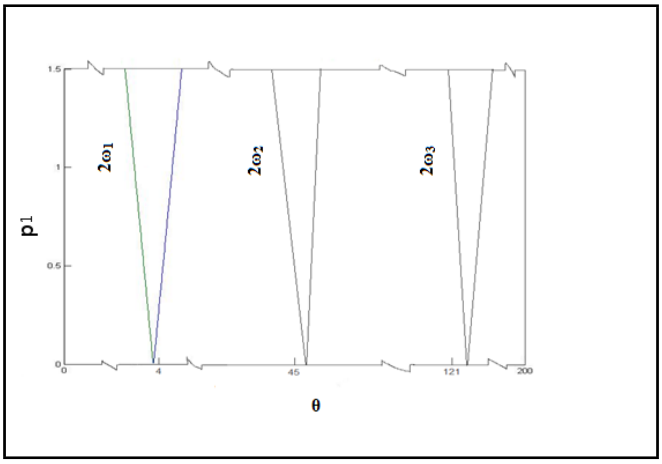

Figure 6. Stability diagram for guided-pinned beam with $\Omega_0 = 5$ ($\delta = 0.1$, $\alpha^* = 2$).

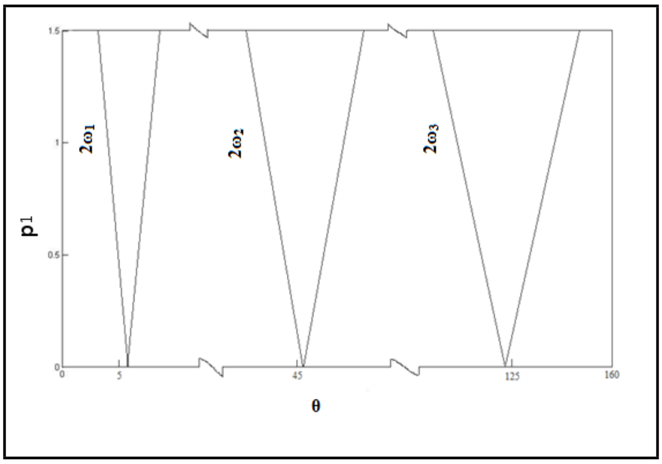

Figure 7. Stability diagram for guided-pinned beam with $\Omega_0 = 5$ ($\delta = 0.4$, $\delta = 0.8$ $\alpha^* = 1$).

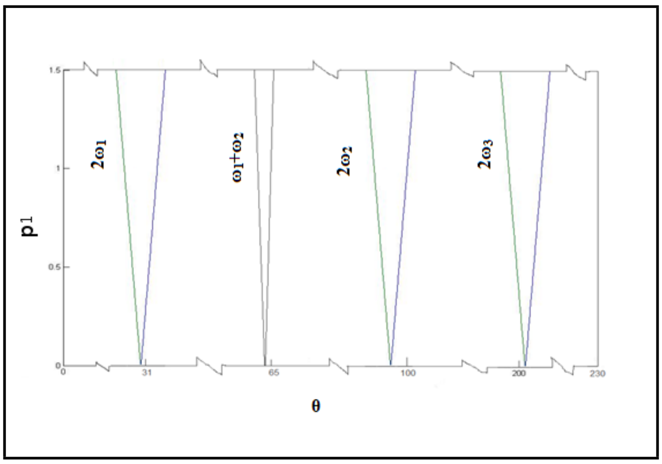

Figure 8. Stability diagram for clamped-pinned beam with $\Omega_0 = 5$ ($\delta = 0.1$, $\alpha^* = 2$).

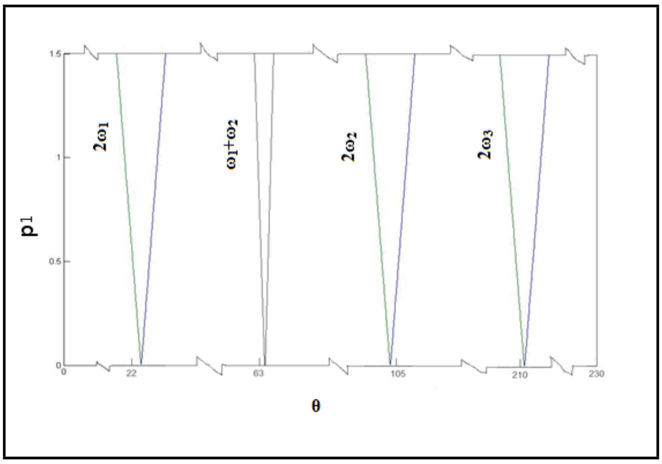

Figure 9. Stability diagram for clamped-pinned beam with $\Omega_0 = 15$ ($\delta = 0.1$, $\alpha^* = 2$).

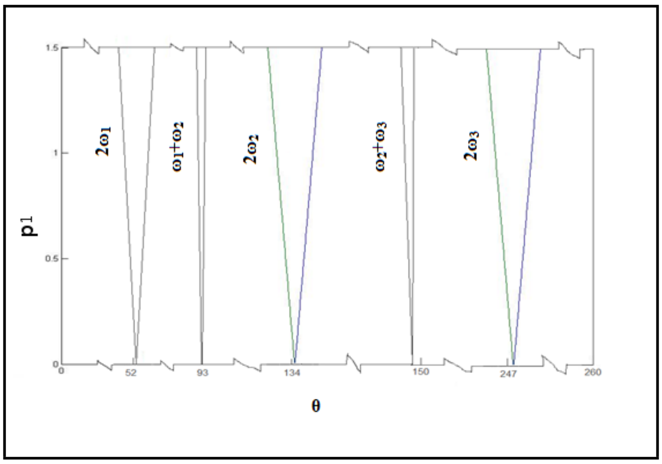

Figure 12. Stability diagram for clamped-clamped beam with $\Omega_0 = 15$ ($\delta = 0.1$, $\alpha^* = 2$).

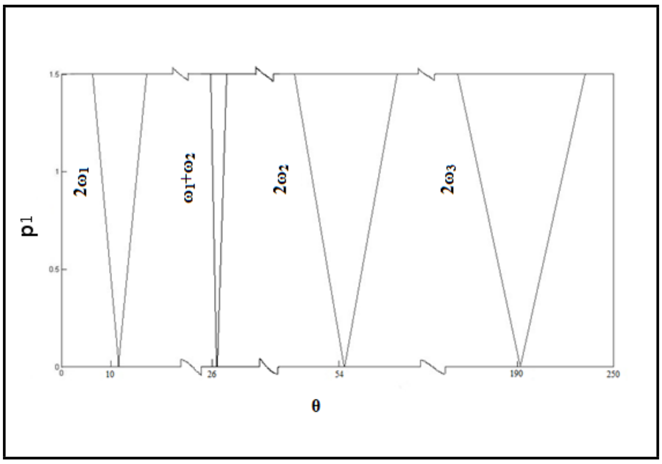

Figure 10. Stability diagram for clamped-pinned beam with $\Omega_0 = 5$ ($\delta = 0.4$, $\delta = 0.8$, $\alpha^* = 1$).

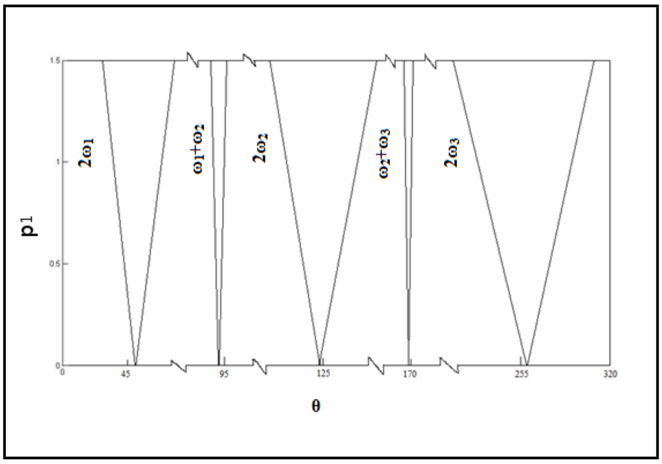

Figure 13. Stability diagram for clamped-clamped beam with $\Omega_0 = 5$ ($\delta = 0.4$, $\delta = 0.8$, $\alpha^* = 1$).

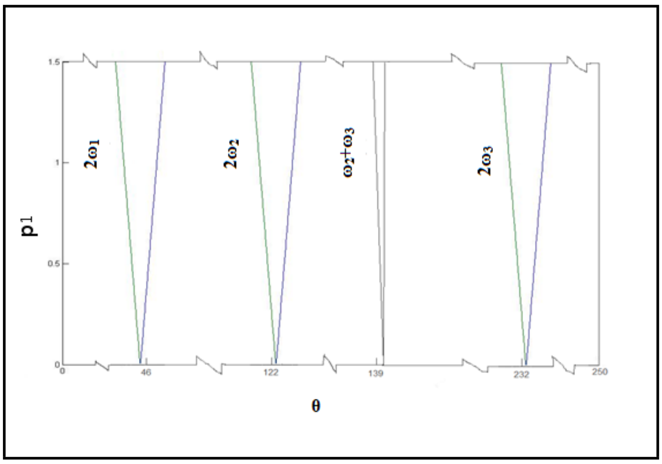

Figure 11. Stability diagram for clamped-clamped beam with $\Omega_0 = 5$ ($\delta = 0.1$, $\alpha^* = 2$).

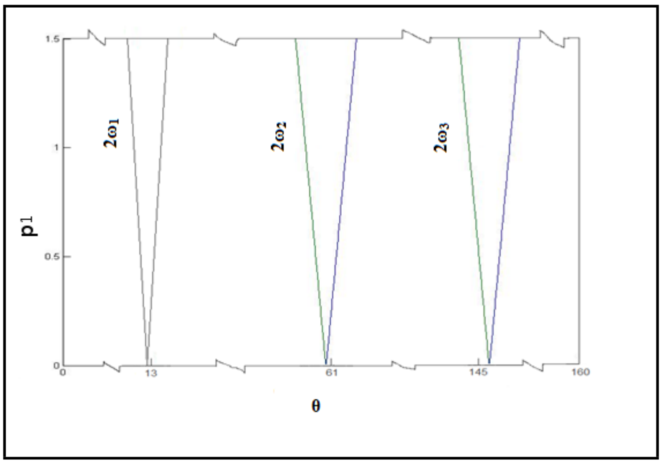

Figure 14. Stability diagram for clamped-CUR beam with $\Omega_0 = 5$ ($\delta = 0.1$, $\alpha^* = 2$).

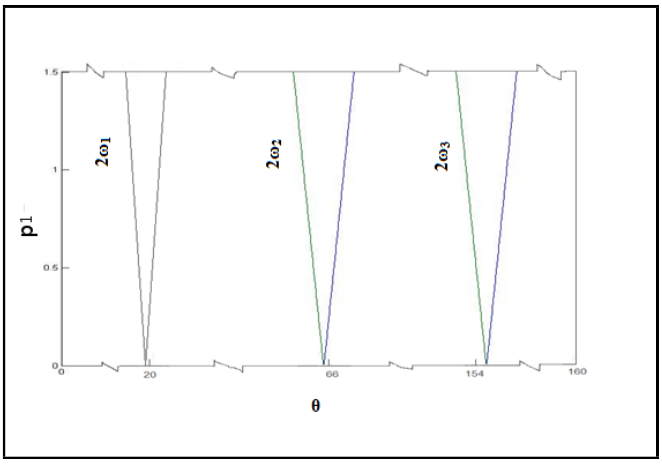

Figure 15. Stability diagram for clamped-CUR beam with $\Omega_0 = 15$ ($\delta = 0.1$, $\alpha^* = 2$).

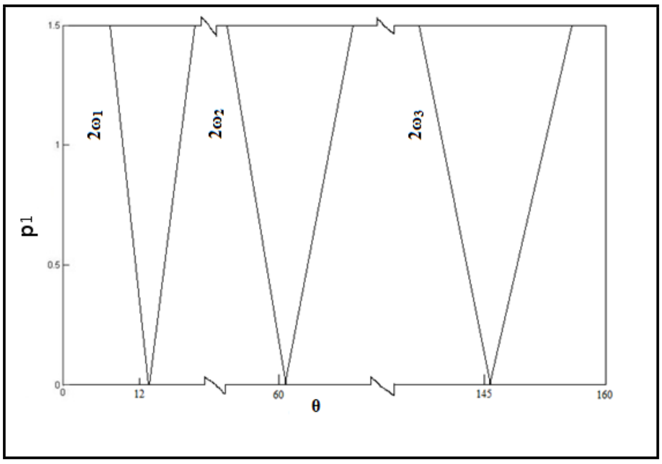

Figure 16. Stability diagram for clamped-CUR beam with $\Omega_0 = 5$ ($\delta = 0.4$, $\delta = 0.8$, $\alpha^* = 1$).

Combination resonances of the difference-type do not occur in any of the cases under consideration. While an increase in the value of Ω_0 reduces the width of the first-order simple resonance zones of clamped-clamped beam, it widens some of the combination resonance zones and shifts all the regions to higher excitation frequencies. The combination resonance regions at $\Theta = (\omega_3 + \omega_1)$ of a clamped-clamped beam reduce in width due to the increase in angular velocity. For a beam with clamped-free end conditions, a higher rotational speed reduces the span of most of the instability regions and makes the beam less susceptible to periodic forces by relocating them at higher frequencies, whereas a rise in the rotational speed increases the span of most of the instability regions of a clamped-pinned beam and relocates them at higher excitation frequencies. On the other hand, it repositions those around $2\omega_1$ and $(\omega_1 + \omega_2)$ at lower frequencies and reduces the width of the ones at $\Theta = 2\omega_2$, $2\omega_3$ and $(\omega_3 + \omega_1)$. With increase in the angular velocity of pinned-pinned beam, most of the resonance zones are widened, but those near $\Theta = 2\omega_2$ and $2\omega_3$ are reduced in span. Further, while the instability regions in the vicinities of $2\omega_1$ shifts to lower frequencies, all others are repositioned at higher ones.

From the figures, it is observed that increase in rotational speed parameter stabilizes the beams with pinned-pinned, clamped-clamped, clamped-clamped unrestrained, and

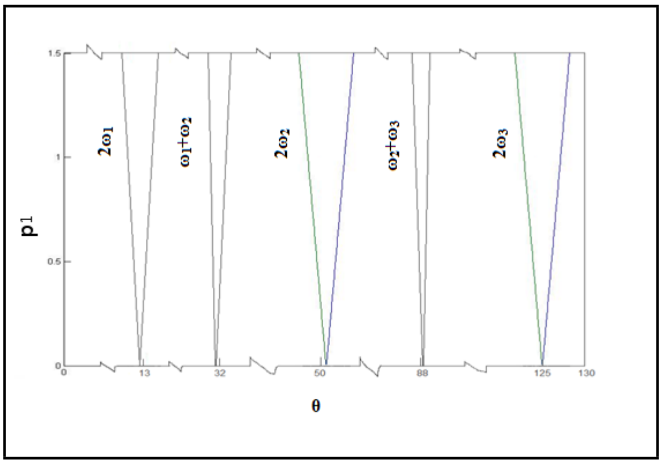

Figure 17. Stability diagram for clamped-free beam with $\Omega_0 = 5$ ($\delta = 0.1$, $\alpha^* = 2$).

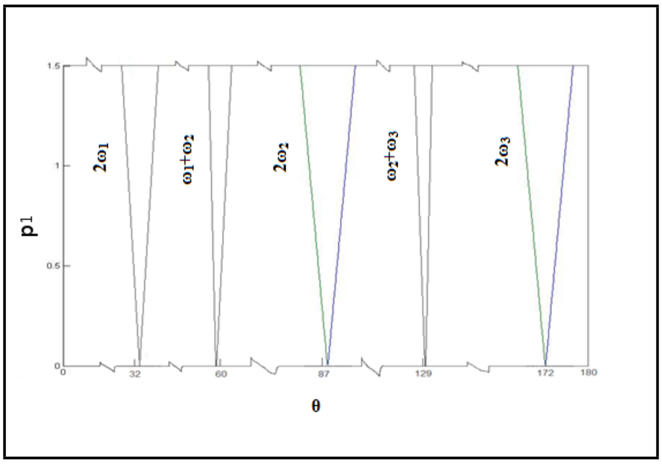

Figure 18. Stability diagram for clamped-free beam with $\Omega_0 = 15$ ($\delta = 0.1$, $\alpha^* = 2$).

clamped-free conditions, whereas it has a destabilizing effect on guided-pinned and clamped-pinned beams.

The influence of taper parameter and thermal gradient parameter on the principal region of instability is shown in Figs. 4, 7, 10, 13, 16, and 19. The figures show the effect of two values of the thermal gradient parameter δ on the instability regions for taper parameter $\alpha^* = 1$ for all the considered boundary conditions. It has been observed that, for all cases, the instability regions experience a slight increase in width and shift towards lower excitation frequencies with an increase in the value of δ.

4. CONCLUSION

A computational analysis of the dynamic stability of a tapered cantilever beam with pulsating axial load and thermal gradient under various boundary conditions was considered. The programming was developed using MATLAB. The following are the conclusions drawn from the study.

The dynamic stability of a rotating tapered beam under a pulsating axial load was investigated for all possible combinations of clamped, guided, pinned, and free boundary conditions. Results reveal that, a higher rotational speed make a clamped-free beam less sensitive to periodic forces. While rise in the angular velocity reduces the intensity of the simple resonances of clamped-clamped beam, it increases the severity of

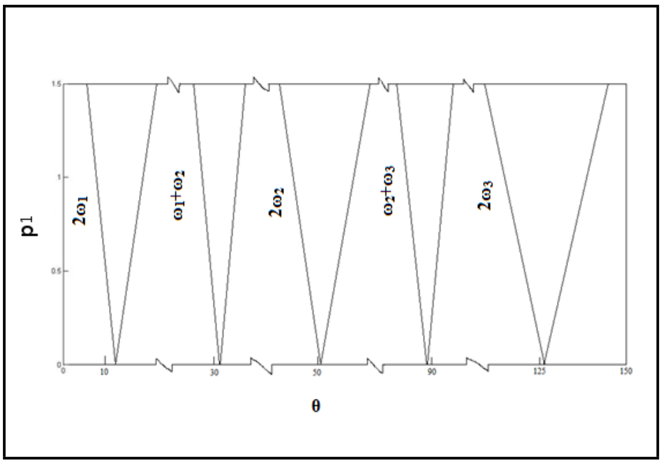

Figure 19. Stability diagram for clamped-free beam with $\Omega_0 = 5$ ($\delta = 0.4$, $\delta = 0.8$, $\alpha^* = 1$).

some of the combination resonances. It is also observed that clamped-pinned and pinned-pinned beams may either stabilize or destabilize with an increase in rotational speed.

An increase in taper parameter reduces the widths of the principal regions of instability and shifts them towards higher excitation frequencies, thus making the beam less sensitive to periodic forces. However, an increase in thermal gradient widens the principal regions of instability, shifting them towards lower excitation frequencies, thereby making the beam more sensitive to periodic forces. Thus, it may be inferred that increasing taper has stabilizing effects on the beams, whereas increasing temperature gradient has a destabilizing effect on the beams of all cases.

REFERENCES

1. Bhat, R. B. Transverse vibrations of a rotating uniform cantilever beam with tip mass as predicted by using beam characteristic orthogonal polynomials in the Rayleigh-Ritz method, *J. Sound Vib.*, **105**, 199–210, (1986). http://dx.doi.org/10.1016/0022-460x(86)90149-5

2. Liu, W. H. and Yeh, F.-H.Vibrations of non-uniform rotating beams, *J. Sound Vib.*,**119**, 379–384, (1987). http://dx.doi.org/10.1016/0022-460x(87)90463-9

3. Unger, A. and Brull, M. A. Parametric instability of a rotating shaft due to pulsating torque, *J. Appl. Mech., Trans. ASME,* **48**, 948–958, (1981). http://dx.doi.org/10.1115/1.3157761

4. Kammer, D. C. and Schlack, Jr., A. L. Dynamic Response of a Radial Beam With Nonconstant Angular Velocity, *J. Vib. Acoust., Stress, Reliab. Des., Trans. ASME*, **109**, 138–143, (1987). http://dx.doi.org/10.1115/1.3269405

5. Namachchivaya, N. S. Mean square stability of a rotating shaft under combined harmonic and stochastic excitations, *J. Sound Vib.*, **133**, 323–336 (1989). http://dx.doi.org/10.1016/0022-460x(89)90929-2

6. Bauer, H. F. and Eidel, W. Vibration of a rotating uniform beam, Part II: Orientation perpendicular to the axis of rotation, *J. Sound Vib.*, **122**, 357–375 (1988). http://dx.doi.org/10.1016/s0022-460x(88)80360-2

7. Abbas, B. A. H. Dynamic stability of a rotating Timoshenko beam with a flexible root, *J. Sound Vib.*, **108**, 25–32 (1986). http://dx.doi.org/10.1016/s0022-460x(86)80308-x

8. Ishida, Y., Ikeda, T., Yamamoto, T., and Esaka, T. Parametrically Excited Oscillations of a Rotating Shaft Under a Periodic Axial Force, *JSME Int. J.*, **31** (4), 698–704 (1988). http://dx.doi.org/10.1299/jsmec1988.31.698

9. Lee, H. P. Dynamic stability of a tapered cantilever beam on an elastic foundation subjected to a follower force, *Int. J. Solids Structures*, **33** (10), 1409–1424, (1996). http://dx.doi.org/10.1016/0020-7683(95)00108-5

10. Lin, C. Y. and Chen, L. W. Dynamic stability of rotating composite beams with a viscoelastic core, *Compos. Struct.*, **58** (2), 185–194, (2002). http://dx.doi.org/10.1016/s0263-8223(02)00127-7

11. Tan, T. H., Lee, H. P. and Leng, G. S. B. Parametric instability of spinning pretwisted beams subjected to sinusoidal compressive axial loads, *Compos. Struct.*, **66** (6), 745–764, (1998). http://dx.doi.org/10.1016/s0045-7949(98)00002-9

12. Banerjee, J. R., Su, H., and Jackson, D. R. Free vibration of rotating tapered beams using the dynamic stiffness method, *J. Sound Vib.*, **298** (4–5) 1034–1054, (2006). http://dx.doi.org/10.1016/j.jsv.2006.06.040

13. Shahba, A. and Rajasekaran, S. Free vibration and stability of tapered Euler–Bernoulli beams made of axially functionally graded materials, *Appl. Math. Model.*, **36** (7), 3094–3111, (2012). http://dx.doi.org/10.1016/j.apm.2011.09.073

14. Yang, J. B., Jiang, L .J., and Chen, D. C. Dynamic modelling and control of a rotating Euler–Bernoulli beam, *J. Sound Vib.*, **274** (3–5), 863–875, (2004). http://dx.doi.org/10.1016/s0022-460x(03)00611-4

15. Nayak, S., Bisoi, A., Dash, P. R., and Pradhan, P. K. Static stability of a viscoelastically supported asymmetric sandwich beam with thermal gradient, *Int. J. Adv. Struct. Eng.*, **6** (3), Article:65, (2014). http://dx.doi.org/10.1007/s40091-014-0065-2

16. Soltani, M., Asgarian, B., and Mohri, F. Elastic instability and free vibration analyses of tapered thin-walled beams by the power series method, *J. Constr. Steel Res.*, **96**, 106–126, (2014). http://dx.doi.org/10.1016/j.jcsr.2013.11.001

17. Bulut, G. Effect of taper ratio on parametric stability of a rotating tapered beam, *Eur. J. Mech. A Solids*, **37**, 344–350, (2013). http://dx.doi.org/10.1016/j.euromechsol.2012.08.007

18. Saito, H. and Otomi, K. Vibration and stability of elastically supported beams carrying an attached mass under axial and tangential loads, *J. Sound Vib.*, **62**, 257–266, (1976). http://dx.doi.org/10.1016/0022-460x(79)90025-7

Method for Evaluating the Statistical Relationship between Sound Pressure Level and Noise Annoyance Based on a Nonlinear Time Series Regression Model and an Experiment

Hisako Orimoto, Akira Ikuta and Yegui Xiao

Department of Management and Information Systems, Prefectural University of Hiroshima, 1-1-71 Ujina-Higashi, Minamiku, Hiroshima 734-8558, Japan

(Received 29 October 2013; accepted 25 August 2015)

Identifying the quantitative relationship between the sound pressure level and noise annoyance for environmental noises is important from the viewpoint of noise assessment. In this study, a method for predicting the probabilistic evaluation quantities like L_x ($(100-x)$ percentile level) and L_{Aeq} (equivalent A-weighted sound pressure level) of the noise environment is proposed by introducing a nonlinear time series regression model between the sound pressure level and noise annoyance. More specifically, the joint probability distribution is expanded in an orthonormal expansion series in which linear and nonlinear correlation information is reflected hierarchically in each expansion coefficient. Next, statistical methods for predicting the sound pressure level and the noise annoyance are proposed by introducing a nonlinear time series regression model based on the above probability distribution. The validity of the proposed method is confirmed by applying it to a set of instantaneous data on sound pressure level and noise annoyance observed in a real sound environment.

1. INTRODUCTION

Identifying the quantitative relationship between the sound pressure level and noise annoyance for environmental noise is important from the viewpoint of noise assessment.[1–3] Usually, an investigation based on the questionnaires is performed, as the experimental measurement at all points in the entire area of the regional sound environment is difficult. Furthermore, statistical sound evaluation quantities, such as L_x based on the probability distribution of sound pressure level and L_{Aeq} based on averaged energy of sound pressure level, are widely used in the evaluation of the sound environment. Therefore, it is very important to determine the relationship between the noise annoyance and the sound pressure level from a statistical point of view.

In a previous study, a state estimation method was proposed for the fluctuation waveform of the sound pressure level by time-dependent sound pressure level based on the observation data of noise annoyance from the viewpoint of systems theory.[4] The relationship of the sound pressure level and noise annoyance was regarded as the input and output of a fuzzy probability system with uncertainty and vagueness. A method was theoretically derived for estimating the fluctuation waveform of the sound pressure level or the system input by use of the observation data of the noise annoyance or the system output. In analyses of environmental noise, two approaches can be considered. One is analysis from the bottom-up viewpoint, structurally based on the fundamental mechanism on the relationship between noise annoyance and sound pressure level. The other is the top-down method, which is connected with evaluation of environmental noise in the case of unknown structural mechanism. Since the analysis method considering the physical mechanism from the bottom-up viewpoint was adopted in the previous study, the derivation process of the estimation algorithm was rather complicated.

On the other hand, a method based on the top-down viewpoint can be proposed by regarding time-dependent sound pressure level and noise annoyance as the resultant time series data and by considering their mutual correlation information. In this paper, a practical evaluation method is proposed, which is simple in form as compared with the previous study. The joint probability distribution for the sound pressure level and noise annoyance is first considered for the purpose of using the usual liner correlation as well as the higher order nonlinear correlation information between both variables. Next, two probabilistic methods are proposed based on the joint probability distribution in an orthonormal expansion series[5], where linear and nonlinear correlation information is reflected hierarchically in each expansion coefficient. One method predicts the noise annoyance based on the observation of sound pressure level, and the other is a prediction for the sound pressure level from the noise annoyance. Finally, the effectiveness of the proposed methods are confirmed by applying them to a psychological experiment with the road traffic noise, where the linear regression model and neural network are compared.

2. THEORETICAL CONSIDERATION

2.1. Prediction of Noise Annoyance by Observing Sound Pressure Level

2.1.1. Prediction of noise annoyance based on conditional probability distribution

The sound pressure level in the actual sound environment exhibits complex fluctuation pat-tern. For example, there are various linear and nonlinear correlations among several instantaneous values. It has been reported in psychological acoustics that the human psychological evaluation for noise annoyance can be distinguished up to 7 scores: 1-Very calm, 2-Calm, 3-Mostly calm, 4-Little noisy, 5-Noisy, 6-Fairly noisy, 7-Very noisy.[6]

Let x be the sound pressure level and y be the noise annoyance score in human evaluation (i.e. $y = 1, 2, \cdots, 7$). Furthermore, the sound pressure levels at p past discrete time for y at an arbitrary discrete time are expressed as $x_{p+1}(p = 0, 1, 2, \cdots)$. The noise annoyance can be predicted recursively on the basis of the sound pressure levels $x_1, x_2, \cdots, x_p$ by adopting y so as to maximize the conditional probability $P(y|x_1, x_2, \cdots, x_p)$ as the prediction of y. First, the joint probability distribution $P(y, \mathbf{x})$ of y and $\mathbf{x}(= (x_1, x_2, \cdots x_p))$ is expanded into an orthonormal polynomial series based on the product of the standard probability distribution for each variable.[7]

$$P(y,\mathbf{x}) = P_0\left(y\right)P_0\left(x_1\right)P_0\left(x_2\right)\cdots \cdots P_0\left(x_p\right)\sum_{m=0}^{\infty}\sum_{n_1=0}^{\infty}\cdots\sum_{n_p=0}^{\infty}A_{mn_1\cdots n_p}\varphi_m\left(y\right)\phi_{n_1}\left(x_1\right)\cdots \cdots\phi_{n_p}\left(x_p\right). \tag{1}$$

$$A_{mn_1\cdots n_p} = \left\langle \varphi_m\left(y\right)\phi_{n_1}\left(x_1\right)\phi_{n_2}\left(x_2\right)\cdots\phi_{n_p}\left(x_p\right)\right\rangle; \tag{2}$$

$$\phi_{n_i}\left(x_i\right) = \frac{1}{\sqrt{n!}}H_n\left(\frac{x_i-\mu_{x_i}}{\sigma_{x_i}}\right); \tag{3}$$

$$\phi_m\left(y\right) = \frac{1}{\sqrt{\left(\frac{N-M}{h}\right)^{(m)}m!}}\left(\frac{1-p}{p}\right)^{\frac{m}{2}}\frac{1}{h^m}\sum_{j=0}^{m}\begin{pmatrix} m \\ j\end{pmatrix} (-1)^{m-j}\left(\frac{p}{1-p}\right)^{m-j}(N-y)^{(m-j)}(y-M)^{(j)}; \tag{4}$$

$$y^{(j)} = y(y-h)(y-2h)\cdots(y-(n-1)h), \qquad y^{(0)} = 1,$$

where $<>$ denotes the averaging operation with respect to the variables. Two functions $\phi_{n_i}(x_i)$,$\varphi_m\left(y\right)$ are orthonormal polynomials with the weighting functions $P_0(x_i)$ and $P_0(y)$ are obtained.[5] $H_n(\bullet)$ denotes the Hermite polynomial with nth order, and $y^{(j)}$ is the jth order factorial function.[5] The Gaussian distribution is adopted as the standard probability distributions of $P_0(x_i)$ for the continuous variable x_i, and the generalized binomial distribution is adopted as $P_0(y)$ for the quantized value y.

$$P_0\left(x_i\right) = \frac{1}{\sqrt{2\pi\sigma_{x_i}^2}}e^{-\frac{(x_i-\mu_{x_i})^2}{2\sigma_{x_i}^2}}; \tag{5}$$

$$\mu_{x_i} =< x_i >, \quad \sigma_{x_i}^2 =< (x_i-\mu_{x_i})^2 >; \tag{6}$$

$$P_0\left(y\right) = \frac{\left(\frac{N-M}{h}\right)!}{\left(\frac{y-M}{h}\right)!\left(\frac{N-y}{h}\right)!}p^{\frac{y-M}{h}}\left(1-p\right)^{\frac{N-y}{h}}; \tag{7}$$

$$p = (\mu_y - M)/(N-M), \quad \mu_y =< y >; \tag{8}$$

where N, M and h are defined as follows:

$$\begin{aligned} N &= 7; \quad \text{the maximum value of } y, \\ M &= 1; \quad \text{the minimum value of } y, \\ h &= 1; \quad \text{the level difference interval of } y. \end{aligned} \tag{9}$$

The linear and nonlinear correlation information between y and $\mathbf{x}$ is reflected hierarchically in each expansion coefficient $A_{mn_1\cdots n_p}$. Next, an expansion series expression on the conditional proba-bility distribution can be obtained from Eq. 1, as follows:

$$P\left(y\left|\mathbf{x}\right.\right) = \frac{P(y,\mathbf{x})}{P(\mathbf{x})} = \frac{P_0(y)\sum\limits_{m=0}^{\infty}\sum\limits_{n_1=0}^{\infty}\cdots\sum\limits_{n_p=0}^{\infty}A_{mn_1\cdots n_p}\phi_m(y)\,\varphi_{n_1}(x_1)\cdots\varphi_{n_p}(x_p)}{\sum\limits_{n_1=0}^{\infty}\cdots\sum\limits_{n_p=0}^{\infty}A_{0n_1\cdots n_p}\varphi_{n_1}\left(x_1\right)\cdots\varphi_{n_p}\left(x_p\right)}. \tag{10}$$

By substituting Eqs. (3)–(9) into Eq. (10), the conditional probability distribution can be obtained. Moreover, the probability distribution of noise annoyance score y can be evaluated by averaging the conditional probability distribution $P(y|\mathbf{x})$ in Eq. (10) by using time series data of sound pressure level as follows:

$$P\left(y\right) = P_0\left(y\right)\sum_{m=0}^{\infty}\left\langle\frac{\sum\limits_{n_1=0}^{\infty}\cdots\sum\limits_{n_p=0}^{\infty}A_{mn_1\cdots n_p}\varphi_{n_1}\left(x_1\right)\cdots\varphi_{n_p}\left(x_p\right)}{\sum\limits_{n_1=0}^{\infty}\cdots\sum\limits_{n_p=0}^{\infty}A_{0n_1\cdots n_p}\varphi_{n_1}\left(x_1\right)\cdots\varphi_{n_p}\left(x_p\right)}\right\rangle\varphi_m\left(y\right). \tag{11}$$

2.1.2. Prediction of noise annoyance based on multidimensional nonlinear regression model

The linear and nonlinear correlation information between y and $\mathbf{x}$ is all included in condi-tional probability distribution $P(y|\mathbf{x})$. Especially, when predicting y based on $\mathbf{x}$, the regression function defined as the expectation of y conditioned by $\mathbf{x}$ can be adopted as the prediction of y.

$$\hat{y} = \left\langle y|\,\mathbf{x}\right\rangle = \sum_{y=1}^{7}y\cdot P\left(y|\,\mathbf{x}\right). \tag{12}$$

After substituting Eq. (10) into Eq. (12), by taking into consideration the orthonormal condition of orthonormal polynomial $\varphi_m(y)$:

$$\sum_{y=1}^{7} P_0(y)\varphi_n(y)\varphi_m(y) = \delta_{nm}; \tag{13}$$

the regression function $\hat{y}$ is given by Eq. (14) (top of the next page), where d_{1m} are coefficients in the orthogonal expansion of y:

$$y = \sum_{m=0}^{1} d_{1m}\varphi_m(y); \tag{15}$$

and can be derived as follows:

$$d_{11} = \sqrt{(N-M)\, hp\,(1-p)},$$
$$d_{10} = (N-M)\,p + M.$$

2.2. Prediction of Sound Pressure Level by Observing Noise Annoyance

The sound pressure level at an arbitrary discrete time is predicted by observing the noise annoyance scores $\mathbf{y}$ ($= y_1, y_2, \cdots, y_q$) up to $(q-1)$ past discrete time based on the multi-dimension nonlinear regression model. Considering the orthonormal condition of the polynomial function

$$\int_{-\infty}^{\infty} P_0(x)\phi_m(x)\phi_n(x)dx = \delta_{mn}; \tag{16}$$

and using the same calculation process as given in Section 2.1.2, the prediction $\hat{x}$ of sound pres-sure level x is given by Eq. (17) (top of the next page), where the coefficients c_{1m} are specifically given in the orthogonal expansion $x = \sum_{m=0}^{1} c_{1m}\phi_m(x)$, as $c_{11} = \sigma_{x_i}$, $c_{10} = \mu_{x_i}$. Furthermore, the expansion coefficients $B_{mn_1n_2\cdots n_q}$ are defined as follows:

$$B_{mn_1n_2\cdots n_q} = \left\langle \phi_m(x)\,\varphi_{n_1}(y_1)\,\varphi_{n_2}(y_2)\cdots\phi_{n_q}(y_q)\right\rangle . \tag{18}$$

3. EXPERIMENTAL CONSIDERATION

The road traffic noise with frequency characteristic of broadband was recorded at a position being 1 m apart from one side of the national road by use of a sound pressure level meter and a data recorder. Two kinds of data (i.e., data 1 and data 2) for the sound pressure level of road traffic noise in two typical cases of light and heavy traffic flow with mean values of 71.4 [dB] and 80.2 [dB] were measured by using sound pressure level meter (model NL-06 integral standard type, Rion Co.) under an A-characteristic and FAST response with a time constant of 0.125 seconds in an RMS circuit. By replaying the recorded data through amplifier and loudspeaker in a laboratory room, 6 subjects between the ages of 22-24 with normal hearing ability judged one score among 7 noise annoyance scores[6] at every 5 seconds. The experiment was conducted in a laboratory room, and the effect of the background noise could be ignored.

The proposed study is focused on the derivation of a new method to predict the sound pres-sure level and noise annoyance from the theoretical viewpoint. Since the purpose of the study is to suggest a theoretical method for estimation, the usefulness of the proposed method was confirmed by applying it to 6 subjects.

3.1. Experimental Consideration for Prediction of Noise Annoyance by Observing Sound Pressure Level

3.1.1. Comparison of the proposed method based on conditional probability distribution and neural network

Two cases with and in Eq. (10) were considered:

$$P(y\,|x_1) = \frac{P_0(y)\sum\limits_{m=0}^{i}\sum\limits_{n=0}^{i} A_{mn}\varphi_m(y)\,\phi_n(x_1)}{\sum\limits_{n=0}^{i} A_{0n}\phi_n(x_1)}, \quad (p=1)$$

$$P(y\,|x_1,x_2) = \frac{P_0(y)\sum\limits_{m=0}^{i}\sum\limits_{n_1=0}^{i}\sum\limits_{n_2=0}^{i} A_{mn_1n_2}\varphi_m(y)\,\varphi_{n_1}(x_1)\,\varphi_{n_2}(x_2)}{\sum\limits_{n_1=0}^{i}\sum\limits_{n_2=0}^{i} A_{0n_1n_2}\phi_{n_1}(x_1)\,\phi_{n_2}(x_2)}. \quad (p=2) \tag{19}$$

Though the conditional probability distribution in Eq. (19) is expressed in an infinite expansion series, only finite expansion coefficients can be used in the application to real noise environment. The expansion coefficients $A_{mn_1n_2}$ and $A_{0n_1n_2}$ in Eq. (19) with $m \le i$, $n_1 \le i$ and $n_2 \le i$ ($i = 1, 2, \cdots, 6$) were considered in the experiment. First, these expansion coefficients were calculated by use of data 1 as the learning data. Next, the noise annoyance score was predicted by observing the sound pressure level of data 2 as the prediction data. The prediction results are shown in Table 1 as the recognition rate. In an ideal case with infinite numbers of data, the recognition rate gets better with increasing order. However, a recognition rate sometimes decreases with increasing order because excess order includes unnecessary information in real cases with finite numbers of available data. Therefore, the optimal order exists, and finding the optimal order becomes an important issue for future development.

In this study, the best recognition rates were obtained in the case that $p = 1$, $i = 4$ and $p = 2$, $i = 2$. One of the prediction results is shown in Fig. 1 in the case that $p = 1$ and $i = 4$. In this experiment, the subjects judged annoyance scores from 3 to 7 among 7 scores by hearing the replayed road traffic noise

$$\hat{y} = \frac{\sum_{m=0}^{1}\sum_{n_1=0}^{\infty}\sum_{n_2=0}^{\infty}\cdots\sum_{n_p=0}^{\infty} A_{mn_1n_2\cdots n_p} d_{1m} \phi_{n_1}(x_1)\phi_{n_2}(x_2)\cdots\phi_{n_p}(x_p)}{\sum_{n_1=0}^{\infty}\sum_{n_2=0}^{\infty}\cdots\sum_{n_p=0}^{\infty} A_{0n_1n_2\cdots n_p} \phi_{n_1}(x_1)\phi_{n_2}(x_2)\cdots\phi_{n_p}(x_p)}. \tag{14}$$

$$\hat{x} = \langle x\,|\mathbf{y}\rangle = \frac{\sum_{m=0}^{1}\sum_{n_1=0}^{\infty}\sum_{n_2=0}^{\infty}\cdots\sum_{n_q=0}^{\infty} B_{mn_1n_2\cdots n_q} c_{1m} \varphi_{n_1}(y_1)\varphi_{n_2}(y_2)\cdots\varphi_{n_q}(y_q)}{\sum_{n_1=0}^{\infty}\sum_{n_2=0}^{\infty}\cdots\sum_{n_q=0}^{\infty} B_{0n_1n_2\cdots n_q} \varphi_{n_1}(y_1)\varphi_{n_2}(y_2)\cdots\varphi_{n_q}(y_q)}. \tag{17}$$

Table 1. Comparison of the recognition rate between the proposed method by conditional probability distribution and neural network. The cells with highest recognition rate are highlighted.

Order	Proposed Method	
(i)	$p = 1$	$p = 2$
1	71.7%	68.9%
2	68.3%	71.4%
3	73.3%	68.1%
4	76.7%	70.6%
5	71.7%	68.1%
6	69.2%	63.9%
Neural Network		
-	$p = 1$	$p = 2$
-	42.5%	42.0%

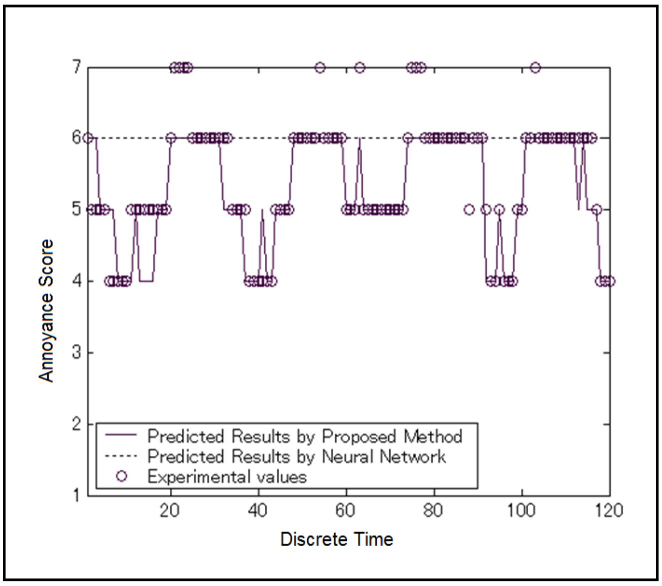

Figure 1. A comparison between the predicted results by the conditional probability distribution and the neural network.

of data 1. Similarly, the result from 4 to 7 among 7 scores by hearing of data 2 was obtained. For comparison, the prediction results by the neural network, which is frequently used in the field of pattern recognition, were compared with the proposed method. The neural network of three-layer structure with the sigmoid function in the middle layer was adopted and back propagation was used as the learning algorithm. In the learning process of the neural network, 40 different initial values were given to decide the synaptic weight. The number of units in a middle layer varied from 2 to 20, and the same procedures were repeated. After the repeated estimation processes, the weight with best recognition rate was adopted. The proposed

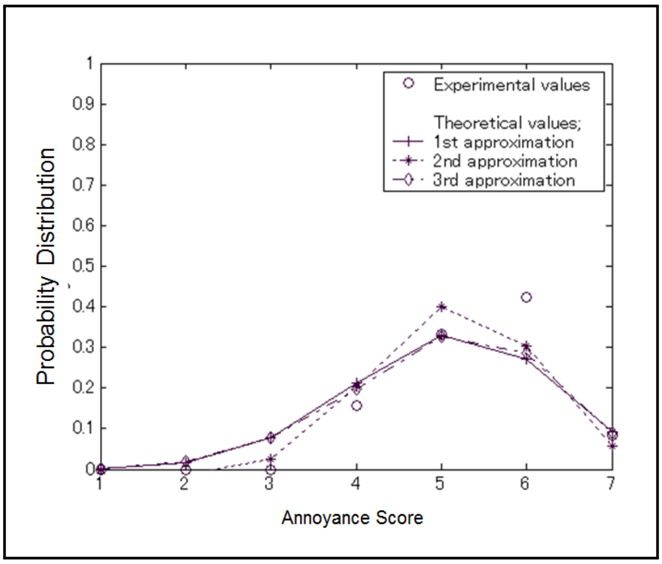

Figure 2. Predicted result for the probability distribution of noise annoyance.

method shows more accurate prediction for the noise annoyance than the neural network. Furthermore, the predicted result for the probability distribution of noise annoyance score based on the observed data of sound level is shown in Fig. 2 in the case that $p = 1$ and $i = 4$. In this figure, the experimental values were obtained directly by calculating the frequency distribution based on the evaluation data of noise annoyance scores by 6 subjects. On the other hand, the theoretical values were predicted by using Eq. (11) based on the measured data of sound pressure level. The theoretically-predicted probability distribution approaches the experimental values. Especially, the theoretical value with the third approximation shows a good agreement with the actual values for the whole probability distribution of noise annoyance.

3.1.2. Comparison between multi-dimensional nonlinear regression model and linear regression model

The prediction results of the noise annoyance score by using the multi-dimension nonlinear regression model proposed in Section 2.1.2 were compared with the results by the standard linear regression model (i.e., autoregression (AR) model).[8] The AR model considers only the liner correlation among instantaneous values of the noise annoyance and the sound pressure level. However, there are several linear and nonlinear correlations among the instantaneous values. Furthermore, since

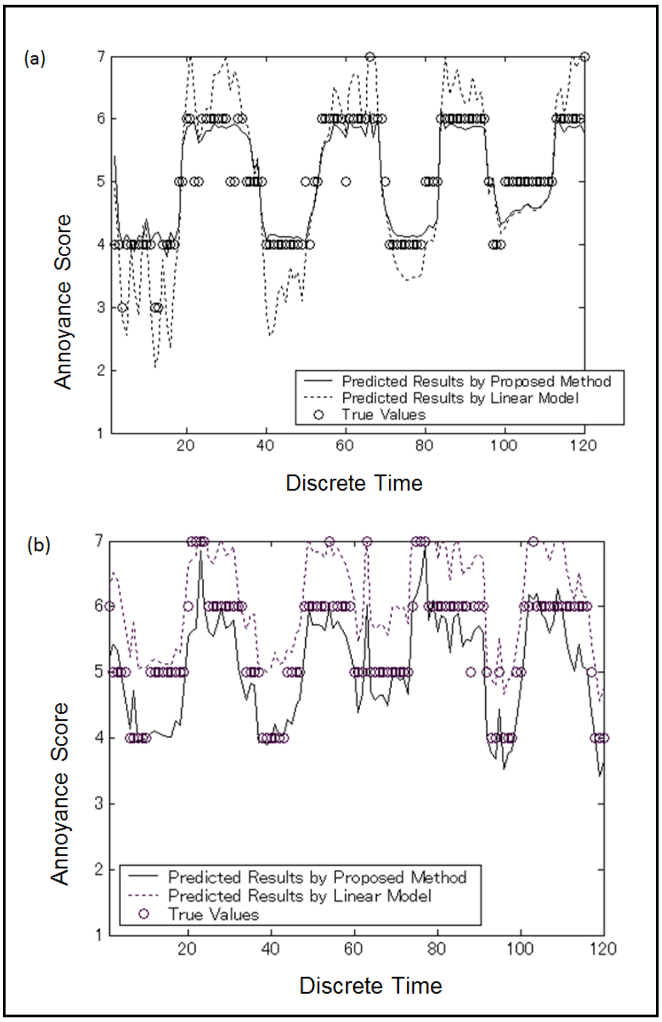

Figure 3. A comparison between the predicted results for noise annoyance by the proposed nonlinear regression model and the linear regression model. (a) Prediction result for data 1; (b) prediction result for data 2.

the relationship between the noise annoyance and the sound pressure level is nonlinear, liner regression model is not adequate for expressing the relationship. Therefore, a multi-dimensional nonlinear regression model was introduced. The prediction equations in Eq. (14) with $p = 1$ and $p = 2$ are expressed as follows:

$$\hat{y} = \langle y \mid x_1 \rangle = \sum yP\left(y \left| x_1 \right.\right) = \frac{\sum\limits_{m=0}^{1}\sum\limits_{n=0}^{i} A_{mn} d_{1m} \phi_n\left(x_1\right)}{\sum\limits_{n=0}^{i} A_{0n}\phi_n\left(x_1\right)}, \quad (p=1)$$

$$\hat{y} = \langle y \mid x_1, x_2 \rangle = \sum yP\left(y \left| x_1, x_2 \right.\right) = \frac{\sum\limits_{m=0}^{1}\sum\limits_{n_1=0}^{i}\sum\limits_{n_2=0}^{i} A_{mn_1n_2} d_{1m} \phi_{n_1}\left(x_1\right)\phi_{n_2}\left(x_2\right)}{\sum\limits_{n_1=0}^{i}\sum\limits_{n_2=0}^{i} A_{0n_1n_2}\phi_{n_1}\left(x_1\right)\phi_{n_2}\left(x_2\right)}. \quad (p=2) \tag{20}$$

The expansion coefficients were considered until the order $i(i = 1, 2, \cdots, 6)$ in Eq. (20) in the same manner as Section 3.1.1. After calculating expansion coefficients A_{mn} and $A_{mn_1n_2}$ in Eq. (20) by use of the learning data (i.e., data 1), the noise annoyance score was predicted based on the ob-servation of sound pressure level of data 1 and data 2. The prediction results are shown in Table 2 (a) and Table 2 (b), respectively. The prediction errors are shown in this table. The case of taking into consideration of the expansion coefficients until $i = 2$ shows the most accurate prediction among all cases, and the better prediction result is obtained in this case than the result by the standard linear regression model. Moreover, the proposed method of expansion series type sometimes shows worse prediction for accuracy in the case of considering some higher order expansion coefficients. The Akaikes information criterion (AIC) is well known to determine an optimal order of regression models.[9] When calculating the expansion coefficients using finite number of the learning data, it is one of the future problems to find an optimal number of expansion terms by extending the AIC. The comparison between the prediction result of the proposed method with $p = 1$, $i = 2$ and the linear regression model is shown in Fig. 3. Data 1 and data 2 are sound pressure levels measured in two typical different situations of traffic flow. Data 1 was measured in a situation of light traffic flow (sound level range 55-90 dB), and data 2 was measured in a situation of heavy traffic flow (sound level range 70-100 dB). The two data sets appear to have quite similar varying patterns of the sound pressure level, since the traffic flow was affected roughly by the time period of a traffic signal existing near the

Table 2. Prediction errors of the multi-dimensional nonlinear regression model and linear regression model. The cells with lowest prediction error are highlighted.

Order (i)	Multi-dimensional Nonlinear Regression Model	
	$p = 1$	$p = 2$
1	0.424	0.453
2	0.423	0.401
3	0.460	0.478
4	0.459	0.469
5	0.465	0.518
6	0.464	0.518
Linear Regression Model		
-	$p = 1$	$p = 2$
-	0.424	0.543

(a) Prediction errors for data 1

Order (i)	Multi-dimensional Nonlinear Regression Model	
	$p = 1$	$p = 2$
1	0.551	0.602
2	0.547	0.557
3	0.622	15.7
4	0.617	21.2
5	0.625	10.3
6	0.625	7.84
Linear Regression Model		
-	$p = 1$	$p = 2$
-	0.825	1.91

(b) Prediction errors for data 2

Table 3. Prediction errors of multi-dimensional nonlinear regression model and linear regression model. The cells with lowest prediction error are highlighted.

Order (i)	Multi-dimensional Nonlinear Regression Model	
	$p = 1$	$p = 2$
1	4.00	3.63
2	3.88	3.50
3	3.35	3.44
4	3.70	3.39
5	3.36	3.10
6	3.24	3.01
Linear Regression Model		
-	$p = 1$	$p = 2$
-	3.27	4.01

(a) Prediction errors for data 1 in [dB]

Order (i)	Multi-dimensional Nonlinear Regression Model	
	$p = 1$	$p = 2$
1	9.06	8.88
2	8.56	9.18
3	7.83	8.49
4	8.05	8.54
5	7.79	8.05
6	7.69	12.73
Linear Regression Model		
-	$p = 1$	$p = 2$
-	7.78	8.91

(b) Prediction errors for data 2 in [dB]

observation point. The proposed method can predict the noise annoyance more accurately than the standard linear regression model by choosing the expansion terms appropriately.

3.2. Experimental Consideration for Prediction of Sound Pressure Level by Observing Noise Annoyance

The comparison between the proposed multi-dimension nonlinear regression model and the linear regression model for the prediction of sound pressure level x is considered in the same manner as Section 3.1.2. The multi-dimension nonlinear regression models with $p = 1$ and $p = 2$ are expressed as follows.

$$\hat{x} = \frac{\sum_{m=0}^{1}\sum_{n=0}^{i} B_{mn} c_{1m} \varphi_n(y)}{\sum_{n=0}^{i} B_{0n}\varphi_n(y)}, \quad (p = 1)$$

$$\hat{x} = \frac{\sum_{m=0}^{1}\sum_{n_1=0}^{i}\sum_{n_2=0}^{i} B_{mn_1n_2} c_{1m} \varphi_{n_1}(y_1)\varphi_{n_2}(y_2)}{\sum_{n_1=0}^{i}\sum_{n_2=0}^{i} B_{0n_1n_2}\varphi_{n_1}(y_1)\varphi_{n_2}(y_2)}. \quad (p = 2)$$

(21)

The comparison between the prediction results by using the proposed method and the linear regression model is shown in Table 3. Moreover, the prediction results of the proposed

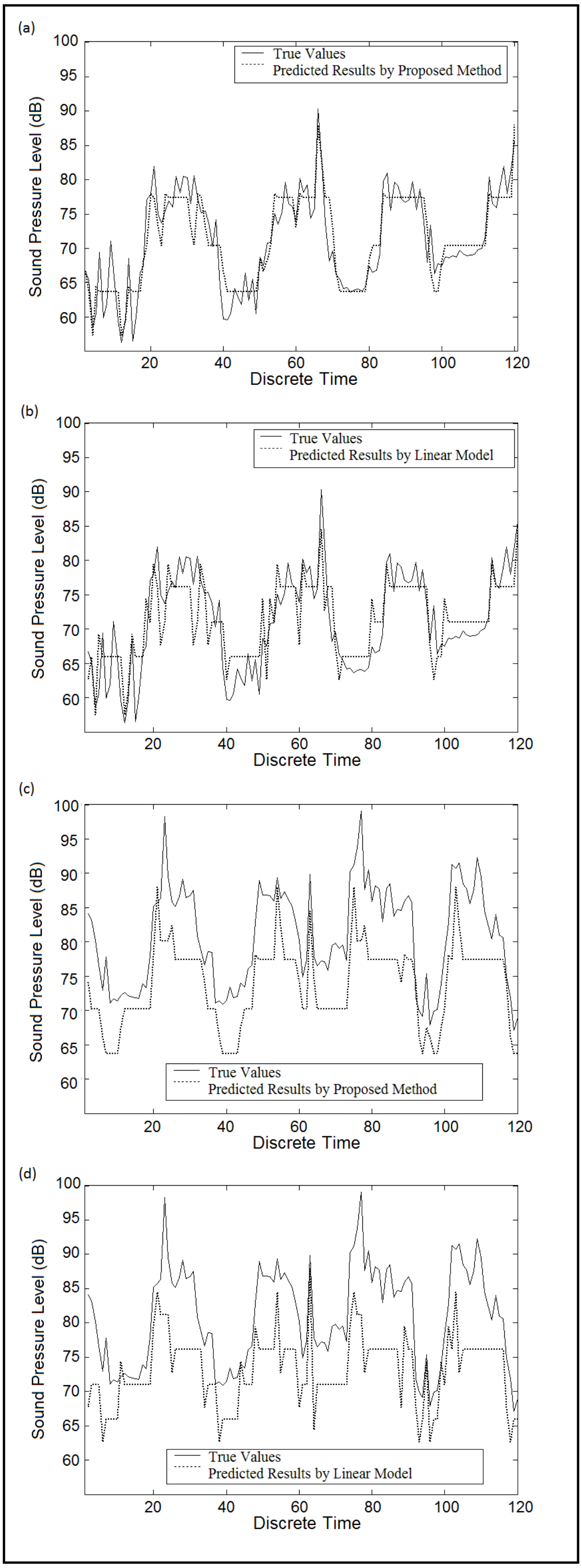

Figure 4. A comparison between the predicted results for sound pressure level by the proposed nonlinear regression model and the linear regression model. (a) Prediction result by proposed method for data 1; (b) Prediction result by linear model for data 1; (c) Prediction result by proposed method for data 2; (d) Prediction result by linear model for data 2.

method with $p = 2, i = 6$ and $p = 2, i = 5$ are shown in Fig. 4 (a) and Fig. 4 (b), respectively. By choosing the number of expansion terms appropriately, the proposed method shows more accurate prediction than the results of liner regression model for the sound pressure level.

4. CONCLUSION

In this paper, statistical methods for evaluating and predicting the relationship between sound pressure level and noise annoyance were considered. More specifically, a simple evaluation method for the relationship between the sound pressure level (objective physical quantity) and the noise annoyance (subjective amount of psychology) was derived based on the correlation infor-mation latent in both variables from the practical viewpoints. The theory was realized by introducing expansion series expression of probability distribution considering not only the lower order linear correlation but also the higher order nonlinear correlation information related to human sensitivity.

The methods for predicting the time course of fluctuation and the probability distributions of noise annoyance score from the observation data of sound pressure level were proposed by introducing the conditional probability distribution and the nonlinear regression model. Furthermore, the prediction methods for the sound pressure level based on the observation of noise annoyance were considered. Finally, the effectiveness of the proposed methods was investigated experimentally by applying it to the actual data of road traffic noise. The proposed approach is quite different from standard methods based on linear regression model, and it is still in the early stage of development of prediction method based on the correlation information of the sound pressure level and noise annoyance. Therefore, many practical problems are left to be considered in the future. For example, (i) the proposed method should be applied to the other actual data of sound environment, and its practical usefulness should be verified in each actual situation; (ii) the optimal order selection method for the statistical regression models based on the higher order correlation information should be investigated by considering the complexity of a phenomenon and the number of data which can be used; and (iii) the proposed theory should be extended to the actual situation under existence of the external noise.

REFERENCES

[1] Yamaguchi, S., Kato, T., Oimatsu, K. and Saeki, T. A psychological evaluation method for fluctuating random noise based on fuzzy set theory, *Applied Acoustics*, **45**, 139–154, (1995).

[2] Yamaguchi, S. and Saeki, T. A practical prediction method of psychological response to arbi-trary non-white random noise based on simplified patterns of membership functions, *Applied Acoustics*, **48**, 155–174, (1996).

[3] Ikuta, A., Ohta, M. and Siddique, M. N. H. Prediction of probability distribution for the psy-chological evaluation of noise in the environment based on fuzzy theory, *International J. of Acoust. and Vib.*, **10**, 107-114, (2005).

[4] Ikuta, A., Masuike, H. and Ohta, M. State estimation for sound environment system with un-known structure by introducing fuzzy theory, *IEEJ Trans. EIS*, **127**, 770–777, (2007) (in Japanese).

[5] Ohta, M. and Ikuta, A. A basic theory of statistical generalization and its experiment on the multi-variate state for environmental noiseA unification on the variate of probability func-tion characteristics and digital or analogue type level observation, *J. Acoust. Soc. Japan*, **39**, 592–603, (1983) (in Japanese).

[6] Kuwano, S. and Namba, S. Continuous judgment of level-fluctuating sounds and the relationship between overall noise annoyance and instantaneous noise annoyance, *Psychological Research*, **47**, 27–37, (1985).

[7] Ohta, M. and Koizumi, T. General statistical treatment of the response of nonlinear rectifying device to a stationary random input, *IEEE Trans. On Information Theory*, **14**, 595–598, (1968). http://dx.doi.org/10.1109/tit.1968.1054178

[8] Franses, P. H. *Time series models for business and economic forecasting*, Cambridge Univer-sity Press, (1998)

[9] Akaike, H. Information theory and an extension of the maximum likelihood principle, *2nd In-ter. Symp. On Information Theory*, Akademiai Kiado, Budapest, 267–281, (1973). http://dx.doi.org/10.1007/978-1-4612-1694-0_15

Multi-objective Optimization of a Multi-chamber Perforated Muffler Using an Approximate Model and Genetic Algorithm

Shuguang Zuo, Kaijun Wei and Xudong Wu

Clean Energy Automotive Engineering Center, School of Automotive Studies, Tongji University, Shanghai 201804, P.R. China

(Received 19 November 2013; accepted 11 December 2014)

Perforated mufflers are widely used in automotive intake and exhaust systems and need to be properly designed. However, multi-objective optimization in practical perforated muffler designs usually involves finite element or boundary element models, which demand a higher computation time for evolutionary algorithms. In this paper, an approximate model for transmission loss (TL) predictions is established by correcting the thickness correction coefficient in the transfer matrix using the data calculated by the finite element model (FEM). The approximate model is computationally cheap and applicable for TL predictions above the plane wave cut-off frequency. A popular evolutionary algorithm, NSGA-, amalgamated with the approximate model, has been adopted to carry out the multi-objective optimization of a multi-chamber perforated muffler. The goals of optimization are to maximize TL at the target frequency range, as well as to minimize the valleys of TL and the size of the muffler. Both transmission loss and insertion loss of the optimized muffler are measured. Numerical and experimental results are in good agreement and show significant improvements of acoustic performance precisely at the target frequency range. Consequently, the combination of the approximate model and the NSGA- algorithm provides a fast, effective, and robust approach to co-axial perforated muffler optimization problems.

NOMENCLATURE

a	Radius of perforated holes (m)
b	Distance between two perforated holes (m)
c	Sound speed (ms^{-1})
d	Inner tube diameter (m)
D	Outer tube diameter (m)
d_h	Diameter of perforated holes (m)
f	Frequency (Hz)
ω	Angular frequency ($\omega = 2\pi f$)
k	Wave number ($k = \omega/c$)
j	Imaginary unit
l	Total length of the chamber (m)
l_c	Length of the perforated segment (m)
l_a	Length of the non-perforated segment near inlet (m)
l_b	Length of the non-perforated segment near outlet (m)
p	Acoustic pressure (Pa)
R_e	Expansion ratio ($R_e = D/d$)
R_l	Perforated length ratio ($R_l = l_c/l$)
t	Thickness of inner tube (m)
t_e	Equivalent acoustic thickness (m)
u	Acoustic particle velocity (ms^{-1})
ρ	Air density (kg·m^{-1})
μ	Dynamic viscosity of air (Pa·s)
ζ_p	Specific acoustic impedance of the perforated tube
A_p	Acoustic admittance of the perforated tube
R_h	Specific resistance of acoustic impedance
α	thickness correction coefficient
η	Porosity of the perforated tube

1. INTRODUCTION

Perforated mufflers have been widely used for reducing noise in automobiles, compressors, venting systems, etc. Various methods have been developed to predict the acoustic performance of perforated mufflers. The transfer matrix method based on the plane wave theory is the earliest and fastest method. Sullivan and Crocker[1] first analysed the acoustic wave propagation in a co-axial perforated muffler and presented the coupled differential equations. Jayaraman and Yam[2] then presented a decoupling solution for Sullivan and Crocker's[1] equations and provided the transfer matrix of co-axial perforated mufflers. Further, Munjal[3] improved the transfer matrix by considering the effects of mean flow, and developed a cascading method using the transfer matrices of basic acoustic elements for relatively simple mufflers. To analyse the complex mufflers with multiply-connected parts, Vijayasree and Munjal[4] developed an integrated transfer matrix method. However, these methods are only appropriate below the plane wave cut-off frequency. Numerical techniques such as finite element methods (FEM) and boundary element methods (BEM) have been proven to be more accurate at higher frequencies. Barbieri, *et al.*[5] applied the Galerkin-FEM to obtain the four-pole parameters to predict the acoustic performance. Kirby[6] developed a fast and accurate hybrid finite element method for modelling automotive dissipative mufflers with perforated ducts and absorbing material. Wu, *et al.*[7] developed a direct mixed-body BEM to derive the four-pole parameters and predict the transmission loss of perforated mufflers. Ji, *et al.*[8] proposed a multi-domain BEM to analyse three-pass perforated duct mufflers.

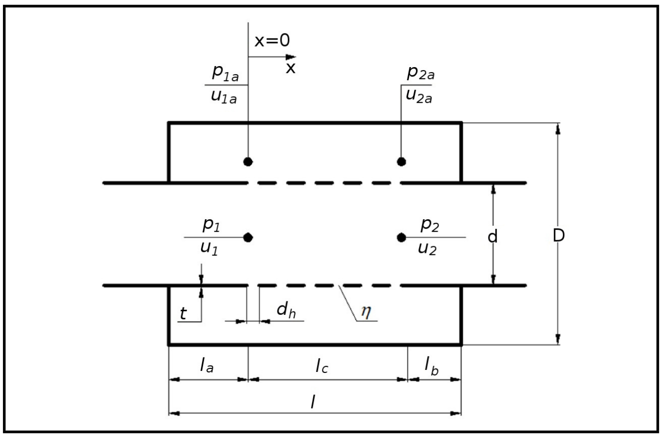

Figure 1. Schematic of a co-axial perforated muffler.

Practical muffler designs are usually governed by multiple conflicting criteria and constrains, which require multi-objective optimization. Evolutionary algorithms such as the genetic algorithm (GA) are suitable in this case owing to their robustness and the ability to avoid the drop in local optimum; however, the computation is time-consuming due to the large searching space. In previous papers, the shape optimizations of perforated mufflers with parallel-flow, cross-flow, and reverse-flow ducts based on the transfer matrix method and various evolutionary algorithms were discussed.[9–11] Airaksinen, *et al.*[12] provided a combined use of a hybrid finite method and genetic algorithm for the multi-objective optimization of various mufflers. However, these optimizations are either limited in use or computationally expensive. The idea behind the approximate model is to create an engineering method which uses an explicit model to evaluate design objectives and variables instead of a complex numerical model. Chang, *et al.*[13,14] linked the objective functions with a polynomial neural network model (NNM) using the primary sample points obtained by the BEM, and the NNM was applied to HQ muffler optimizations. But the NNM was only valid in a certain frequency rather than a wide frequency range.

In the course of the authors' previous work, it was fortuitously found that by changing the thickness correction coefficient in the transfer matrix of the co-axial perforated mufflers, the accuracy of TL prediction was remarkably improved above the cut-off frequency, and the TL prediction under the cut-off frequency was as accurate as before. Hence, an appropriate model for TL predictions was established by introducing a formula of the thickness correction coefficient to the conventional transfer matrix. The formula of the thickness correction coefficient was obtained by the Taguchi design and polynomial regression, and the sample points were calculated by the FEM. Then, the approximate model was adopted to the multi-objective optimization of a multi-chamber perforated muffler, which is used for intake noise attenuation of a regenerative flow compressor in a fuel cell vehicle, combined with the GA. A prototype was produced based on the optimal results. Insertion loss measurements of the prototype were taken and the results have shown the optimization model to be convincing.

2. APPROXIMATE MODEL

As shown in Fig. 1, a co-axial perforated muffler is composed of an inner perforated tube and an outer resonating chamber. The transfer matrix [T] of co-axial perforated mufflers is derived in Appendix A. So the transmission loss (TL) can be calculated by[3]

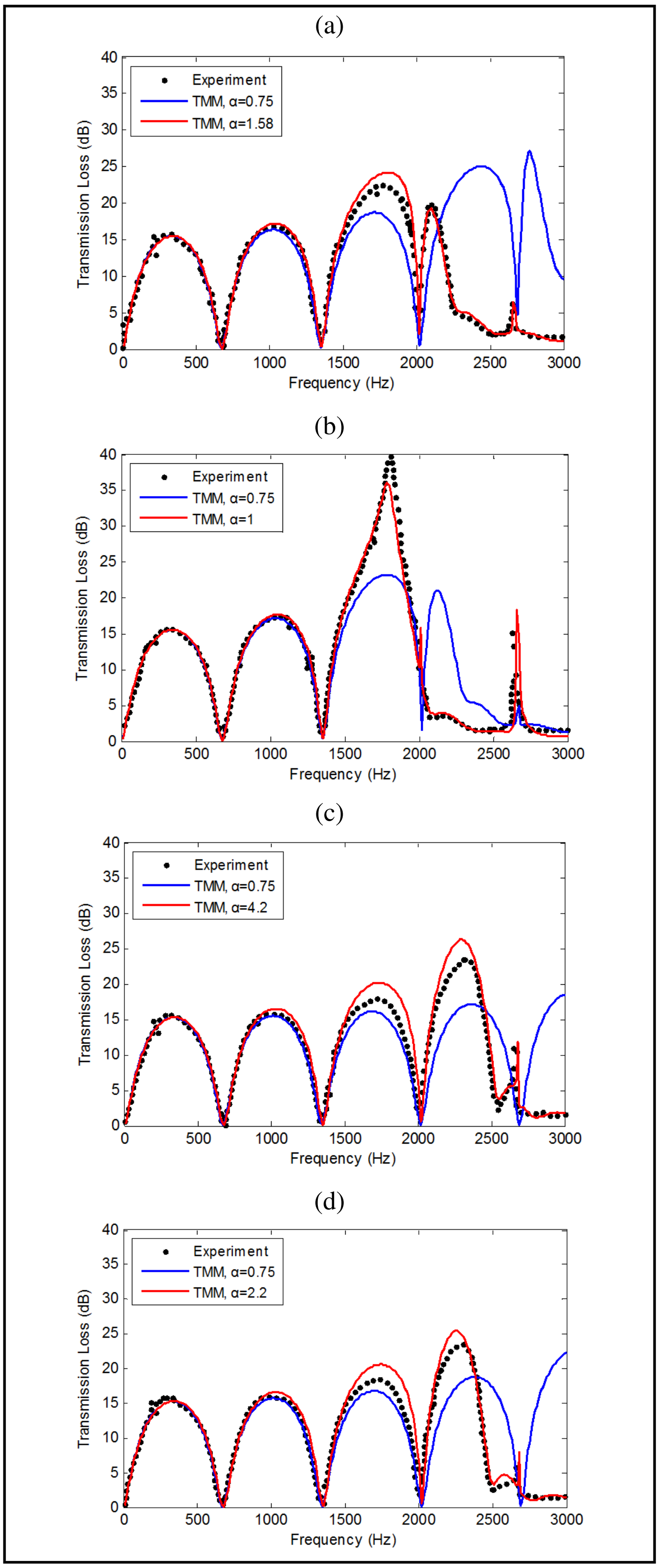

Figure 2. Transmission loss of perforated mufflers [d=49 mm, D=164.4 mm, la=lb=0, lc=257.2 mm, t=0.9 mm; (a) η=8.4%, dh=2.49 mm; (b) η=8.4%, dh=4.98 mm; (c) η=25.7%, dh=2.49 mm; (d) η=25.7%, dh=4.98 mm]. [Experimental data from Lee (2005)[16]].

$$TL = 20\log(\frac{|A + B + C + D|}{2}). \tag{1}$$

It should be noted that the transfer matrix method (TMM) is

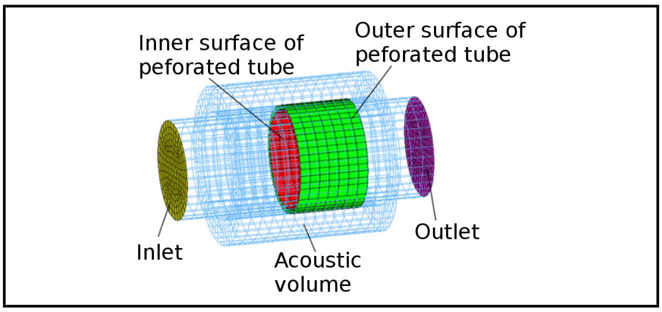

Figure 3. FE Model of the perforated muffler.

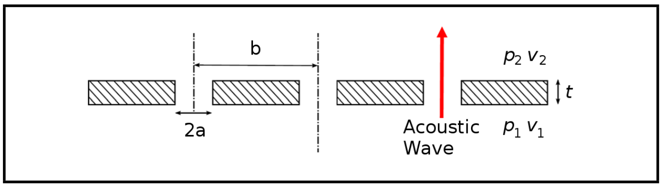

Figure 4. Cross section of a perforated plate.

valid only below the cutoff frequency of plane wave[3]

$$f_{cut} = 1.841\frac{c}{\pi d_0} \tag{2}$$

However, in the course of the authors' previous work on perforated mufflers, it was fortuitously found that by changing the thickness correction coefficient α in the expression of acoustic impedance to an appropriate value, the accuracy of TL prediction was remarkably improved above the cut-off frequency, and the TL prediction under the cut-off frequency was as accurate as before. Some cases are shown in Fig. 2. There are other cases showing a similar phenomenon. Corrected coefficient α takes into consideration mainly additional acoustical masses outside the holes coming from distributed radial velocities through a perforated wall.[15] This suggests that a 1-D model suitable for TL prediction above the cut-off frequency may be obtained by introducing an appropriate model of the thickness correction coefficient to the conventional transfer matrix.

2.1. Thickness Correction

To acquire the thickness correction coefficient, the finite element method (FEM) was adopted to predict TL of perforated mufflers. The computations were taken by ACTRAN. The FE model is illustrated in Fig. 3. The Incident wave of the inlet is defined as unit sound intensity, and the reflect wave is defined as free. The outlet is defined as non-reflected.

Instead of meshing all the orifices, the transfer admittance boundary condition is defined between the inner and outer surfaces of a perforated tube. As shown in Fig. 4, the impedance of a single perforation can be written as

$$Z_p = \frac{p_1 - p_2}{\overline{v}} = R_p + jX_p; \tag{3}$$

where p_1 and p_2 are the upstream and downstream sound pressure, and $\overline{v} = v_1 = v_2$ is the average particle velocity in the orifice.

Therefore, the impedance of the whole plate is

$$\overline{Z_p} = \frac{Z_p}{\eta} = \frac{1}{\eta}(R_p + jX_p); \tag{4}$$

where η is the porosity of the perforated tube, and for a square grid, $\eta = \pi\frac{a^2}{b^2}$

In the above expressions, the impedance can be split into viscous effects contribution and end correction contribution. Using Crandall's theoretical model[17] for viscous effects in narrow tubes, the impedance for a single perforation can be expressed as

$$Z_p = j\omega\rho t[1 - \frac{2}{\sqrt{-j}k_s a}\frac{J_1(\sqrt{-j}k_s a)}{J_0(\sqrt{-j}k_s a)}]^{-1}; \tag{5}$$

where ω is the angular frequency, J_0 and J_1 are order 0 and order 1 Bessel functions, and $k_s a = \sqrt{\frac{\omega\rho}{\mu}}a$ is the shear wavenumber.

For avoiding the evaluation of Bessel functions with complex argument, approximate solutions depending on the range of the dimensionless shear wavenumber k s a can be deduced. When $|k_s a| > 10$, the approximate solutions for Bessel functions can be written as

$$\frac{J_1(\sqrt{-j}k_s a)}{J_0(\sqrt{-j}k_s a)} = -j. \tag{6}$$

When Eq. (6) is applied to Eq. (5), the impedance contributed by viscous effects reduces to

$$Z_p^{visc} = R_p^{visc} + jX_p^{visc} = \sqrt{2\omega\mu\rho}\frac{t}{a} + j\omega\rho t. \tag{7}$$

As for the end correction effects, the resistive end correction accounts for the frictional losses due to viscous effects at the surface of the plate, and the reactive end correction is due to the imaginary part of the radiation impedance at the tube's ends. The resistive and reactive end corrections are commonly adopted as $R_p^{corr} = \sqrt{8\omega\mu\rho}$ and $X_p^{corr} = 2\omega\rho\frac{8}{3\pi}a$.[18] However, the general expressions assume that there is no interaction between two adjacent holes. In the case for high porosity values, the interaction cannot be neglected. Therefore, a correction factor $\alpha_p = 1.47\sqrt{\eta} - 0.47\sqrt{\eta^3}$ is adopted to describe the interaction,[19] and then the impedance of a single perforate is written as

$$R_p = R_p^{visc} + R_p^{corr} = \sqrt{8\omega\mu\rho}(\frac{t}{2a} + 1); \tag{8}$$

$$X_p = X_p^{visc} + X_p^{corr} = \omega\rho[t + 2\frac{8}{3\pi}a(1 - \alpha_p)]. \tag{9}$$

Taking Eqs. (8) and (9) into Eq. (4), the impedance of the perforated plane can be written as

$$\overline{Z_p} = \frac{\sqrt{8\omega\mu\rho}}{\eta}(\frac{t}{2a} + 1)$$
$$+ j\frac{\omega\rho}{\eta}[t + 2\frac{8}{3\pi}a(1 - 1.47\sqrt{\eta} + 0.47\sqrt{\eta^3})]. \tag{10}$$

With applying Eq. (10) to the perforated tube wall, the influence of perforation on the sound field can be considered in the numerical computations. The incident sound power of the inlet (Wi) and outlet (Wo) can be acquired through computation, and thus the transmission loss can be expressed as

$$TL = 10\log\frac{W_i}{W_o}. \tag{11}$$

As shown in Fig. 5, the FEM results are in good agreement with experimental data; thus, the finite element method can

Table 1. Parameters and levels used in the experiments.

Symbol	Level 1	Level 2	Level 3	Level 4	Level 5	Level 6	Level 7
d (m)	0.04	0.045	0.05	0.055	0.06	0.065	0.07
R_e (D/d)	1.6	1.7	1.8	1.9	2	2.1	2.2
l (m)	0.06	0.07	0.08	0.09	0.1	0.11	0.12
R_l (l_c/l)	0.19	0.27	0.35	0.43	0.51	0.59	0.67
t (m)	0.0008	0.0012	0.0016	0.002	0.0024	0.0028	0.0032
d_h (m)	0.001	0.0015	0.002	0.0025	0.003	0.0035	0.004
η	0.14	0.18	0.22	0.26	0.3	0.34	0.38

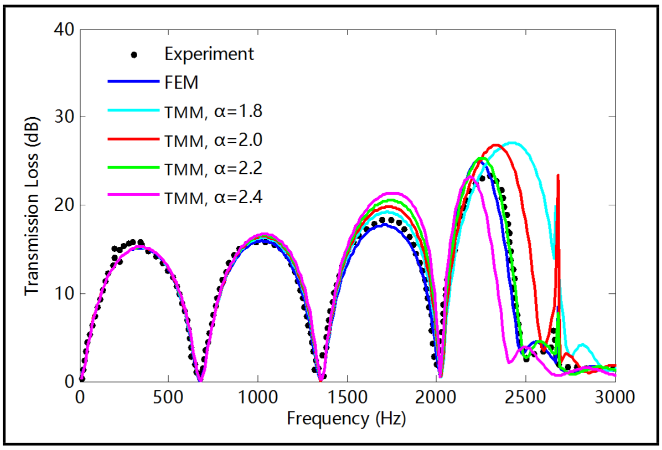

Figure 5. Transmission loss of perforated muffler; [d=49 mm, D=164.4 mm, la=lb=0, lc=257.2 mm, t=0.9 mm, η=25.7%, dh=4.98 mm]. [Experimental data from Lee (2005)[16]].

be used as the numerical experiment. Altering the thickness correction coefficient α to make the transmission loss curve predicted by the TMM closer to that predicted by the FEM. An updated thickness correction coefficient $\hat{\alpha}$ was calculated to minimize the residual sum of squares of transmission loss:

$$\min f(\hat{\alpha}) = \sum_{i=1}^{n} (TL_{FEM} - TL_{TMM}(\hat{\alpha}))^2. \qquad (12)$$

Therefore, the corrected acoustic thickness for TL prediction through the TMM above the cut-off frequency can be expressed as

$$t_e = \frac{t + \hat{\alpha} d_h}{\eta}. \qquad (13)$$

2.2. Taguchi Design

As illustrated in Fig. 1, there are eight design parameters of a straight perforated muffler. Because the switch of inlet and outlet won't change the transmission loss, the length of non-perforated segment l_a and l_b can be considered as one parameter. Obtaining a more accurate expression of the equivalent thickness and the design parameters means more experimental levels. The full factorial experimental design of seven parameters at seven levels would necessitate 7^7 experiments. To save experimental time and cost, the Taguchi method[20] was used for the design of experiments and a $L_{49}(7^7)$ orthogonal array was applied. The seven design parameters and their factor levels are summarized in Table 1. The experimental results are presented in Appendix B.

2.3. Polynomial Repression

Regression analysis is an approach to modelling the relationship between the dependent variable and explanatory variables. In this article, with the experimental data in Appendix B, a multiple linear stepwise regression analysis was performed to predict the equivalent thickness. Mathematical modelling was carried out by using a second-order polynomial equation as

Table 2. ANOVA for regression model.

Source	DF	SS	MS	F	p
Model	8	0.0019	0.0002	167.409	0.000
Residual	40	0.000058	0.000		
Total	48	0.002			
$R^2 = 0.971$	$R^2_{adj} = 0.965$				

$$t_e = \beta_0 + \sum_{i=1}^{k} \beta_i x_i + \sum_{i=1}^{k} \beta_{ii} x_i^2; \qquad (14)$$

where $x_i = d, R_e, l, R_l, t, d_h, 1/\eta i = 1, 2, ..., 7, \beta_i$ is the regression coefficient, and k is the number of design parameters. The least square estimate method was adopted to interpret the estimated regression coefficient and the following equation was obtained:

$$t_e = -0.0281 + 0.2064d + 0.0093R_e + 0.0542l + 0.0060R_l + 0.0018{R_l}^2 + 2.8909t + 2.0056d_h + 1.4850 \times 10^{-4} \frac{1}{\eta^2} . \qquad (15)$$

The results of analysis of variance (ANOVA) are shown in Table 2. It calculates the sum of squares (SS), the mean of square (MS), the degree of freedom (DF), the ratio Fisher (F), and significance (p). In this model $F(8, 48) = 167.409 > 2.907$ ($F_{0.01}(8, 48)$), and overall significance (p) is close to zero, which indicates a more than 99% confidence level of the statistical hypotheses. The determination coefficient R^2 and adjusted determination coefficient R^2_{adj} are equal to 0.971 and 0.965, respectively, which indicate that 97.1% of the total variations are explained by the model.

The results of the regression coefficient test are shown in Table 3. The significances (p) of all independent variables reach α-level of 0.05, which indicates that every independent variable has a strong effect on the equivalent thickness. The results predicted by the regression model are compared to experimental data in Fig. 6. It can be seen that model predictions present a good agreement with the experimental data, and the residual error rates are under 8%. This means that the regression model provides a fair explanation of the relationship between the independent variables and the response.

3. MODEL VALIDATION

Before performing the optimization, the mathematical model should be validated first. Figure 7 shows the comparison between the predictions by the approximate model with experimental results from Lee.[16] Figure 7 (a) shows that amplitude errors occurred in the theoretical prediction of muffler 1 at the third and fourth peak frequency, yet the errors are

Table 3. Results of regression coefficient test.

Independent variables	Regression coefficient	Standard error	t	p
Constance	-0.0281	0.00255	-14.595	0.000
d	0.2064	0.01717	12.138	0.000
D/d	0.0093	0.00086	9.369	0.000
l	0.0542	0.00858	4.690	0.000
l_c/l	0.0060	0.00674	3.374	0.002
$(l_c/l)^2$	0.0018	0.00774	-2.396	0.000
t	2.8909	0.21458	13.740	0.000
d_h	2.0056	0.17167	9.311	0.000
$1/\eta^2$	1.4850E-4	0.00012	27.581	0.021

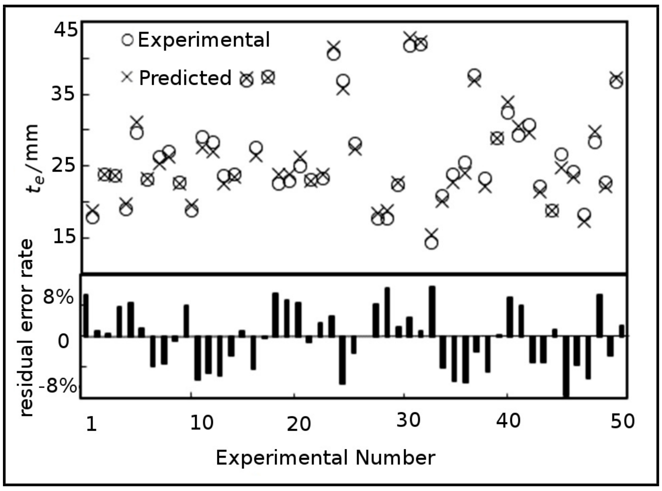

Figure 6. Comparison of regression model results with experimental data.

accepted in engineering applications. The theoretical predictions of other mufflers are in good agreement with experimental results. Consequently, the proposed mathematical model is proven to be valid above the plane wave cut-off frequency, and will be applied for the shape optimization of multi-chamber perforated mufflers.

4. MULTI-OBJECTIVE OPTIMIZATION

Most practical optimization problems are governed by multiple conflicting criteria and constraints. The general formulation of a multi-objective optimization problem can be described as follows:

$$\min\,[f_1(x), f_2(x), \ldots, f_n(x)]$$
$$s.t. \begin{cases} g_i(x) \le 0, i = 1, 2, \ldots, p \\ h_j(x) = 0, j = 1, 2, \ldots, q \end{cases}; \qquad (16)$$
$$x \in S$$

where $f = (f_1(\mathbf{x}), f_2(\mathbf{x}), \ldots, f_n(\mathbf{x}))$ represents the objective functions, $g_i(\mathbf{x}) \le 0$ represents inequality constraints, and $h_j(\mathbf{x}) = 0$ represents equality constraints. $\mathbf{x}$ is the vector of n independent variables that belongs to a feasible region S of design space $\mathbf{R}^n$. Unlike the single objective optimization, the solution of a multi-objective optimization is not a single point, but a set of non-inferiority solutions known as Pareto optima.

In this section, a multi-objective optimization was presented for multi-chamber perforated mufflers of a regenerative flow compressor in a fuel cell vehicle. The approximate model presented in section 2 was applied to the transmission loss prediction of the muffler. The NSGA-II was adopted as the optimization algorithm.

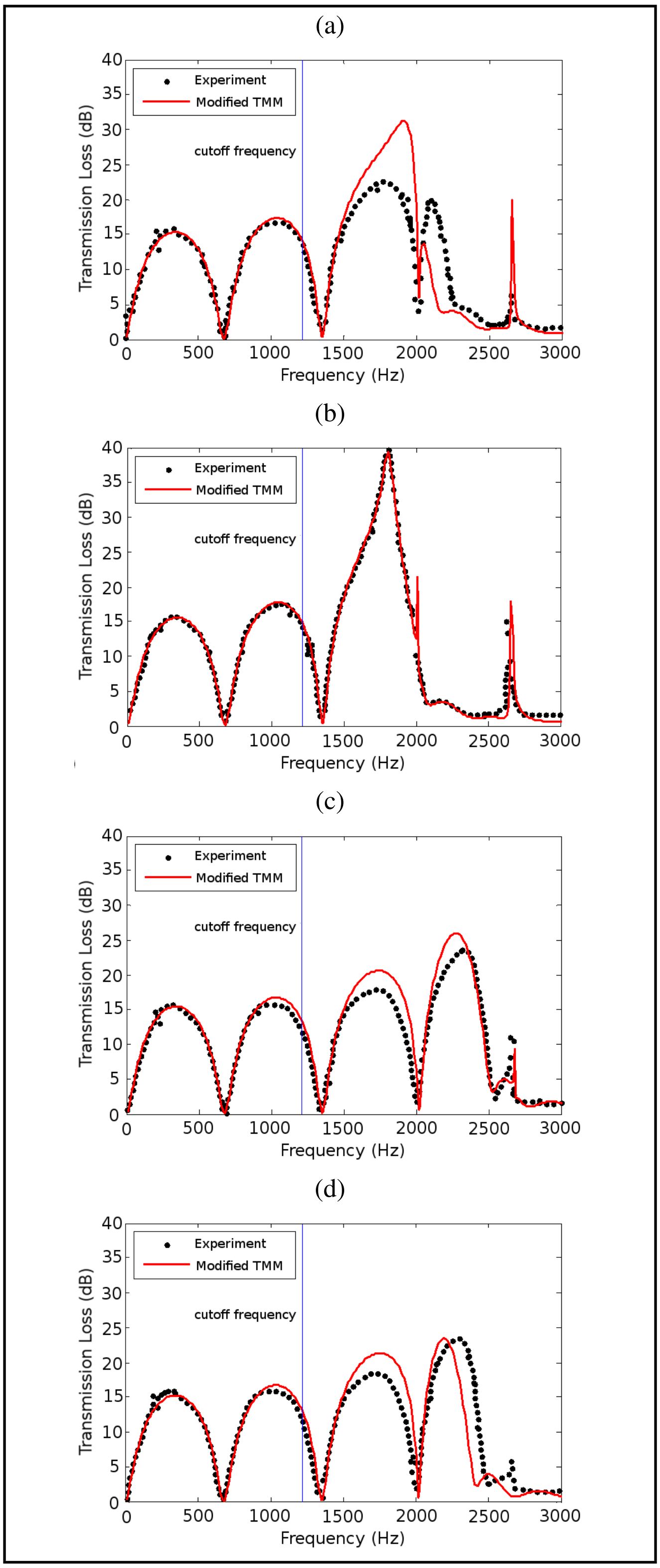

Figure 7. Comparison between predicted and experimental transmission loss [d=49 mm, D=164.4 mm, la=lb=0, lc=257.2 mm, t=0.9 mm; (a) η=8.4%, dh=2.49 mm;(b) η=8.4%, dh=4.98 mm; (c) η=25.7%, dh=2.49 mm; (d) η=25.7%, dh=4.98 mm]. [Experimental data from Lee (2005)[16]].

4.1. Objective Functions

The objectives are to maximize the TL value at the target frequency range and minimize the volume of the muffler. In this case, the objective functions are as follows:

1. The average value of TL at target frequency range:

$$f_1(x) = -\frac{1}{\omega_2 - \omega_1}\int_{\omega_1}^{\omega_2} TL(\omega)d\omega; \tag{17}$$

where $\omega_1 \le \omega \le \omega_2$ is the frequency range. The blade number of the regenerative blower is 55, and the common rotation speed is 1100–3800 rpm; hence, the blade passing frequency (BPF) is 1000–3500 Hz. As the tonal noise at BPF is particularly annoying and contributes most to the noise level,[21] the target frequency range was set at 1000–3500 Hz. The transmission loss can be calculated by Eq. (21).

2. Average valley value of TL: Though the average value of TL could be high, valleys may occur at certain frequency ranges. A threshold value was defined as 5 dB below the average value of TL; thus, the average valley value of TL can be expressed by Eq. (18) (on top of the next page), where $\omega_{i1} \le \omega \le \omega_{i2}$ is the ith frequency range of valleys, and TL_{av} is the average value of TL at 1000–3500 Hz.

3. Volume of the muffler:

$$f_3(\mathrm{x}) = \sum_{1}^{n} \frac{\pi D^2 l_i}{4}\ , i = 1,\ 2,\ 3; \tag{19}$$

where l_i is the length of ith resonating chamber.

4.2. NSGA-II Algorithm

Genetic algorithms (GAs) are adoptive heuristic search algorithms premised on the Darwinian notion of natural selection and evolution. The non-dominated sorting genetic algorithm (NSGA- II) developed by Deb[22] is a multi-objective optimization algorithm using an elite-preserving strategy and an explicit diversity preserving mechanism. Like any conventional GAs, NSGA-II first creates a population of individuals that correspond to the design parameters randomly, and use selection, crossover, and mutation to create an offspring population. While conventional GAs select solutions based on the value of the fitness functions, NSGA-II makes selection based on non-domination rank and crowding distance. More details of can be found in Deb's paper.[22] The structure of NSGA- II optimization is depicted in Fig. 8.

4.3. Optimization Case

A multi-chamber perforated muffler was adopted for inlet noise elimination of a regenerative flow compressor in a fuel cell vehicle. The schematic of the multi-chamber perforated muffler is given in Fig. 9. The multi-chamber perforated muffler includes three perforated tubes and the straight tubes which connect them. The four-pole constants of each element are considered unaffected. So, the overall transfer matrix of the muffler is given by the product of the individual element matrices:

$$T^* = T_{S1} \cdot T_{P1} \cdot T_{S2} \cdot T_{P2} \cdot T_{S3} \cdot T_{P3} \cdot T_{S4}; \tag{20}$$

where T_s is the transfer matrix of the straight tube, and T_p is the modified transfer matrix in the approximate model.

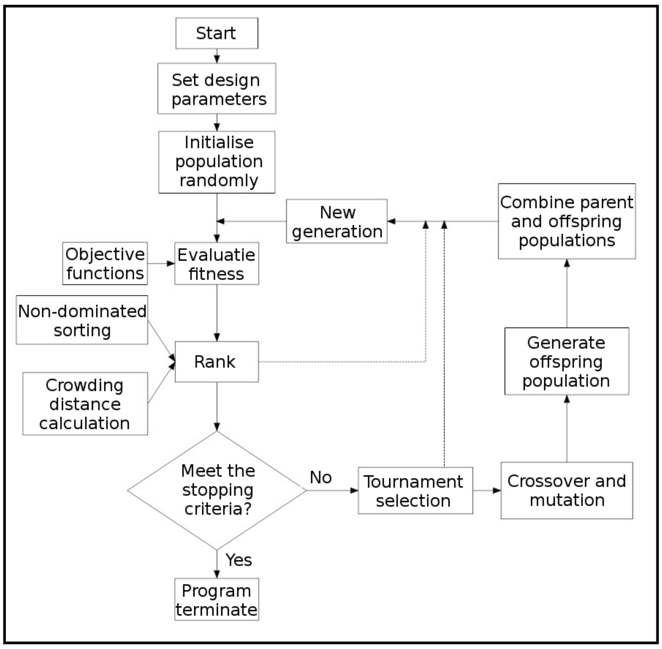

Figure 8. The block diagram of the NSGA-II algorithm.

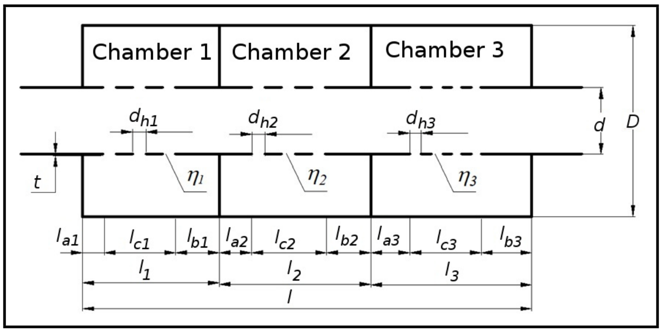

Figure 9. Schematic of the multi-chamber perforated muffler.

The four-pole constants of T_p can be obtained by substituting Eqs. (13) and (15) into the conventional transfer matrix.

Transmission loss of the muffler can be calculated in terms of the four-pole constants as

$$TL = 20\log(\frac{\left|T_{11}^* + T_{12}^* + T_{21}^* + T_{22}^*\right|}{2}). \tag{21}$$

The geometry of the muffler is determined by eighteen parameters, two of which are fixed, and sixteen are varied for optimization. The fixed parameters are the diameter of the resonating chamber $D = 0.1$ m and the diameter of the perforated tube $d = 0.05$ m. Therefore, the cut-off frequency of the muffler is f_{cut}=$1.841\frac{c}{\pi D}$ = 1990 Hz. The ranges of optimization parameters of the ith ($i = 1, 2, 3$) chamber are presented in Table 5. The total length is constrained as $l = l_1+l_2+l_3 \le 0.2$ m.

The Pareto front of the three-chamber perforated muffler optimization is illustrated in Fig. 10. The Pareto solutions clearly reveal the conflicts among the three objects. Considering the priority of each object, four optimal design points are selected and presented in Table 4. The transmission losses of these four

Table 5. Ranges of optimization parameters of ith chamber (i=1, 2, 3).

Parameter	l_i (m)	l_{ai}/l_i	l_{bi}/l_i	t (m)	d_{hi} (m)	η_i
Lower limit	0.05	0.12	0.12	0.001	0.001	0.1
Upper limit	0.2	0.81	0.81	0.006	0.01	0.4

$$f_2(x) = \begin{cases} \sum_{1}^{n} \frac{1}{\omega_{i2} - \omega_{i1}} \int_{\omega_{i1}}^{\omega_{i2}} [TL_{av} - 5 - TL(\omega)] d\omega, TL_{av} - 5 > TL(\omega), i = 1,\ 2,\ ...,\ n \\ 0, TL_{av} - 5 \leq TL(\omega) \end{cases}; \qquad (18)$$

Table 4. Results of the three-chamber muffler optimization.

No.	l_1 (m) l_2 (m) l_3 (m)	l_{a1}/l_1 l_{a2}/l_2 l_{a3}/l_3	l_{b1}/l_1 l_{b2}/l_2 l_{b3}/l_3	t (m)	d_{h1} (m) d_{h2} (m) d_{h3} (m)	η_1 η_2 η_3	$f_1(\mathbf{x})$	$f_2(\mathbf{x})$	$f_3(\mathbf{x})$
1	0.0539 0.1230 0.0168	0.1945 0.3470 0.2231	0.1209 0.1191 0.1867	0.0020	0.0019 0.0017 0.0017	0.3367 0.2570 0.2941	-48.1	17.8	1.52
2	0.0506 0.1307 0.0168	0.1939 0.3135 0.2231	0.1343 0.1642 0.1867	0.0028	0.0021 0.0015 0.0017	0.3146 0.2326 0.2941	-42.5	10.0	1.56
3	0.0352 0.1164 0.0175	0.1974 0.3589 0.2097	0.1493 0.1144 0.0978	0.0021	0.0018 0.0020 0.0018	0.3246 0.3358 0.3529	-41.4	19.4	1.33
4	0.0328 0.0975 0.0137	0.1713 0.3184 0.2409	0.1608 0.1230 0.1127	0.0021	0.0017 0.0019 0.0017	0.3027 0.2433 0.2773	-34.9	16.9	1.13

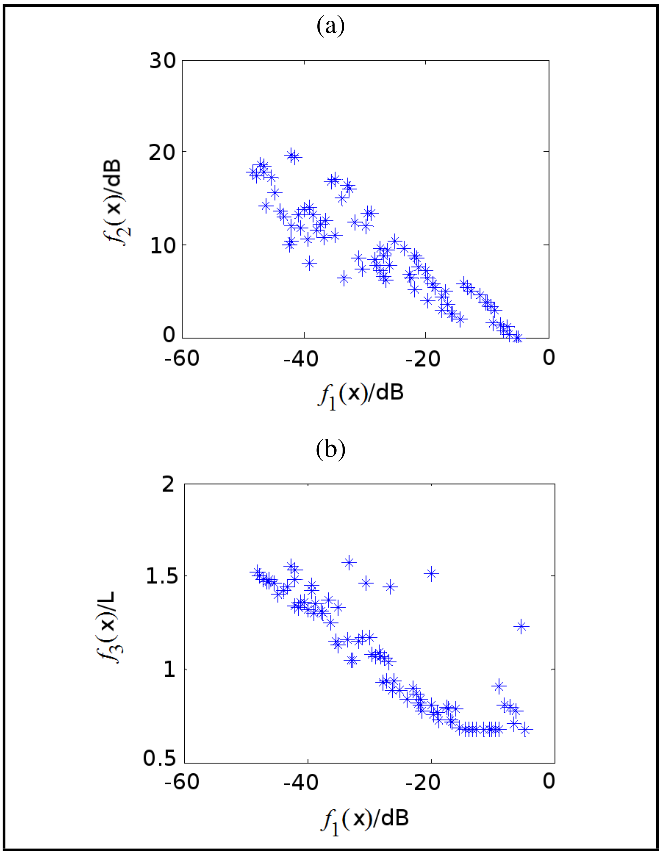

Figure 10. Pareto front of the multi-chamber muffler optimization.

mufflers are shown in Fig. 11. For each of the four mufflers, the transmission loss at the target frequency range is much larger than other frequency ranges. Muffler No. 1 is considered the best because its average TL value is the highest, and the lowest TL value is over 20 dB, also with an acceptable size.

5. EXPERIMENTAL VALIDATION

Transmission loss and insertion loss measurements were carried out in order to validate the optimization results. The parameters of the muffler are shown as No. 1 in Table 4. The measurements were taken in a reverberation room.

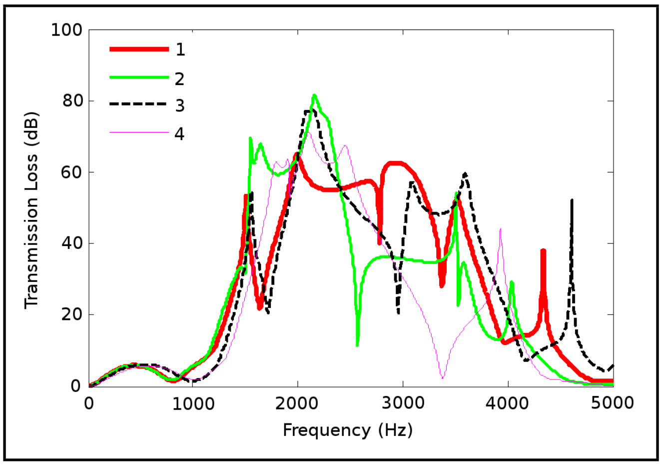

Figure 11. Transmission losses of optimized mufflers.

5.1. Transmission Loss Measurement

The two-load method was applied to measure the transmission loss of the muffler. The schematic diagram and the photograph of the measurement are shown in Fig. 12. The experimental apparatus consisted of three parts: the source, the test section, and the data processing system. The loudspeaker driven by a power amplifier generated white noise signals containing all frequencies of interest. In the test section, the tested muffler was installed in an impedance tube. Four microphones were installed both upstream and downstream of the muffler. The LMS data acquisition system was used to collect the signals from the microphones and then feed the data to the computer-controlled Fourier analyser.

In this measurement, two loads were achieved by an outlet tube with and without an end cap. The transmission loss can be obtained by using four-pole equations.[23]

The sound pressure measured at location $1 \sim 4$ can be expressed as

$$p_1 = p_u^+ e^{jk(L_1+L_2)} + p_u^- e^{-jk(L_1+L_2)}; \qquad (22)$$

$$p_2 = p_u^+ e^{jkL_2} + p_u^- e^{-jkL_2}; \qquad (23)$$

$$p_3 = p_d^+ e^{-jkL_3} + p_d^- e^{jkL_3}; \qquad (24)$$

$$p_4 = p_d^+ e^{-jk(L_3+L_4)} + p_d^- e^{jk(L_3+L_4)}; \qquad (25)$$

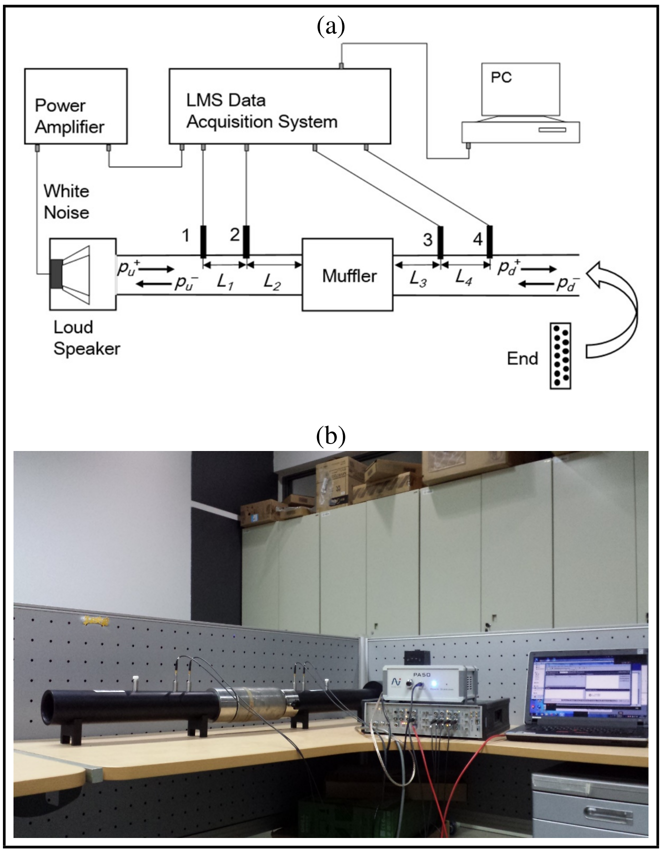

Figure 12. Experimental setup; (a) diagram of test arrangement; (b) photograph of test environment.

where the superscript $+$ refers to incident waves, and the superscript $-$ refers to reflected waves; the subscript u refers to the region upstream of the muffler, and d refers to the region downstream of the muffler.

Using the wave decomposition theory, the incident and reflected wave can be calculated by equations

$$p_u^+ = \frac{p_1 e^{-jkL_2} - p_2 e^{-jk(L_1+L_2)}}{e^{jkL_1} - e^{-jkL_1}}; \tag{26}$$

$$p_u^- = \frac{p_1 e^{jkL_2} - p_2 e^{jk(L_1+L_2)}}{e^{-jkL_1} - e^{jkL_1}}; \tag{27}$$

$$p_d^+ = \frac{p_3 e^{jk(L_3+L_4)} - p_4 e^{jkL_3}}{e^{jkL_4} - e^{-jkL_4}}; \tag{28}$$

$$p_d^- = \frac{p_3 e^{-jk(L_3+L_4)} - p_4 e^{-jkL_3}}{e^{-jkL_4} - e^{jkL_4}}. \tag{29}$$

The four-pole equation for incident and reflected waves upstream and downstream of the muffler can be expressed as

$$\begin{Bmatrix} p_{ua}^+ \\ p_{ua}^- \end{Bmatrix} = \begin{bmatrix} A & B \\ C & D \end{bmatrix} \begin{Bmatrix} p_{da}^+ \\ p_{da}^- \end{Bmatrix}; \tag{30}$$

$$\begin{Bmatrix} p_{ub}^+ \\ p_{ub}^- \end{Bmatrix} = \begin{bmatrix} A & B \\ C & D \end{bmatrix} \begin{Bmatrix} p_{db}^+ \\ p_{db}^- \end{Bmatrix}; \tag{31}$$

where the subscript a refers to configuration without the end cap, and b refers to configuration with the end cap.

Therefore, the transmission loss of the muffler can be calculated as

$$TL = 20\log_{10}|A| = 20\log_{10}\left|\frac{p_{ua}^+ p_{db}^- - p_{ub}^+ p_{da}^-}{p_{da}^+ p_{db}^- - p_{db}^+ p_{da}^-}\right|. \tag{32}$$

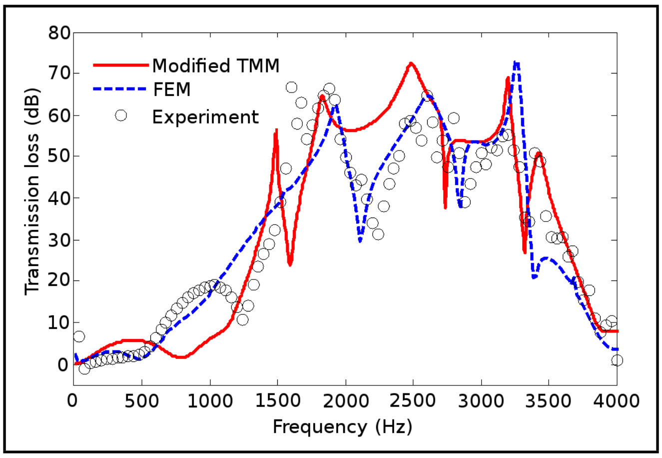

Figure 13. Transmission loss comparison.

Figure 13 shows the comparison of the experimental, theoretical, and numerical predictions of transmission loss. The transmission loss predicted by the approximate model is consistent with the FEM results on the whole, while the peak at 1530 Hz doesn't appear in the FEM results, and the amplitudes of theoretical results are higher than the FEM at certain frequency.

It should be noticed that the thickness correction is based on the FEM results of single-chamber perforated mufflers. So, the application of the modified TMM to the transmission loss predictions of multi-chamber perforated mufflers may lead to a larger deviation. In order to test this hypothesis, transmission loss of each chamber was calculated by a modified TMM and FEM, and the results were given in Fig. 14. As shown in Fig. 14, the transmission losses predicted by modified TMM of chamber 1 and chamber 3 are in good agreement with the FEM results. As for chamber 2, the transmission loss curves are quite close on the whole. The errors are mainly the second peak at 2750 Hz, which is 2900 Hz in the FEM results, and the third peak at 3460 Hz, which is 3330 Hz in the FEM results. Nonetheless, errors are acceptable considering the target frequency bandwidth is quite broad.

Note, however, that the most remarkable error of TL predictions of the optimized muffler at 1530 Hz, which comes from chamber 2 as shown in Fig. 14 (b), agrees quite well with the FEM results of the single chamber 2 calculation. Therefore, the reason for the calculation error at 1530 Hz of the optimized muffler is not the error of chamber 2, but the coupling effect of the three chambers. Figure 15 shows the pressure maps of both the optimized muffler and chamber 2 at 1530 Hz. In the case of chamber 2, it shows a first order radial duct modal at 1530 Hz, which causes the corresponding peak of transmission loss. Yet this modal of chamber 2 in the optimized muffler disappears due to the effect of chamber 1.

5.2. Insertion Loss Measurement

Though transmission loss is most easily predicted theoretically, insertion loss is more widely used in engineering applications. Besides, the transmission losses are predicted without mean flow, while the muffler in the compressor system operates with grazing flow, and the grazing flow at high speeds may reduce the transmission loss.[24] Thus, it is necessary to measure the insertion loss of the muffler under the typical operating conditions of the compressor.

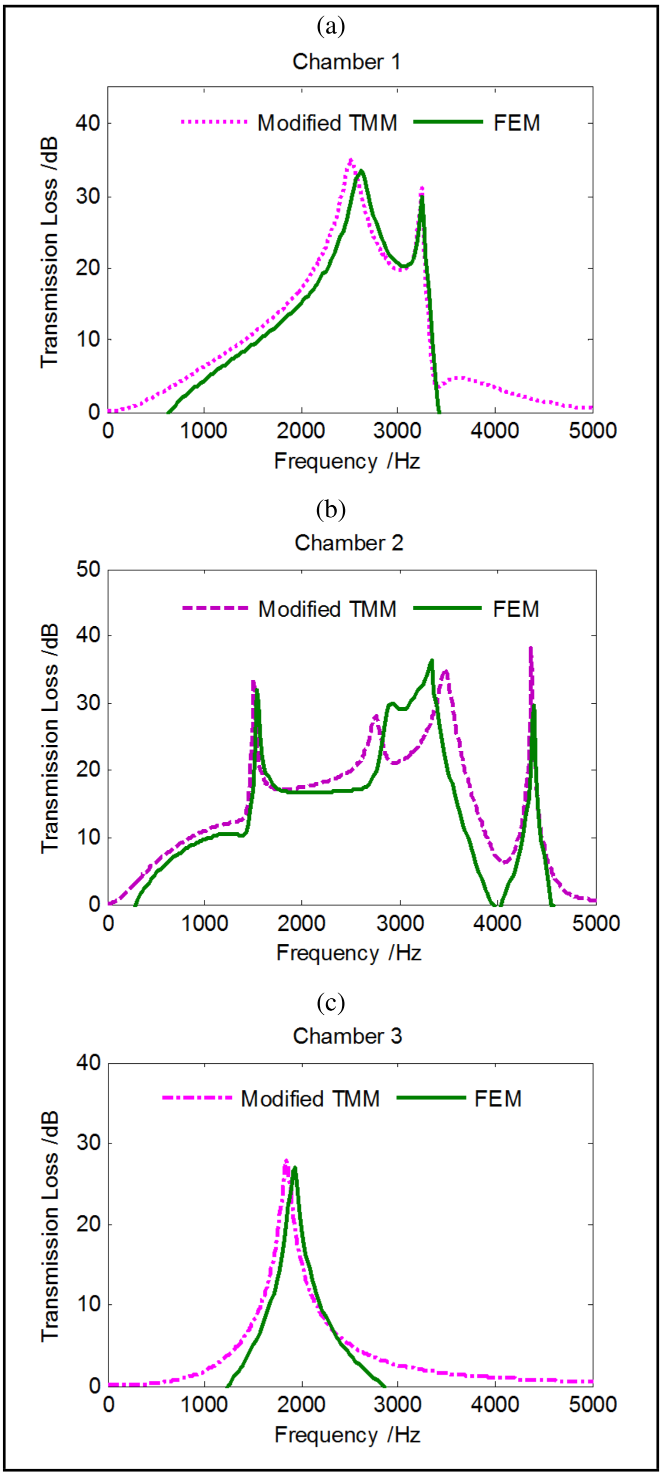

Figure 14. Transmission loss comparisons of each chamber: (a) Chamber 1; (b) Chamber 2; (c) Chamber 3.

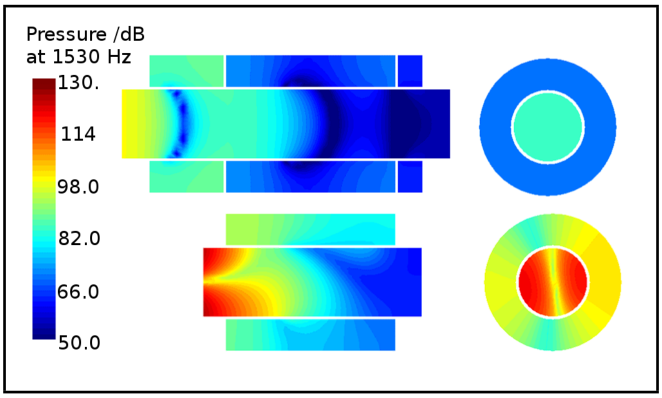

Figure 15. Pressure maps of the optimized muffler and chamber 2.

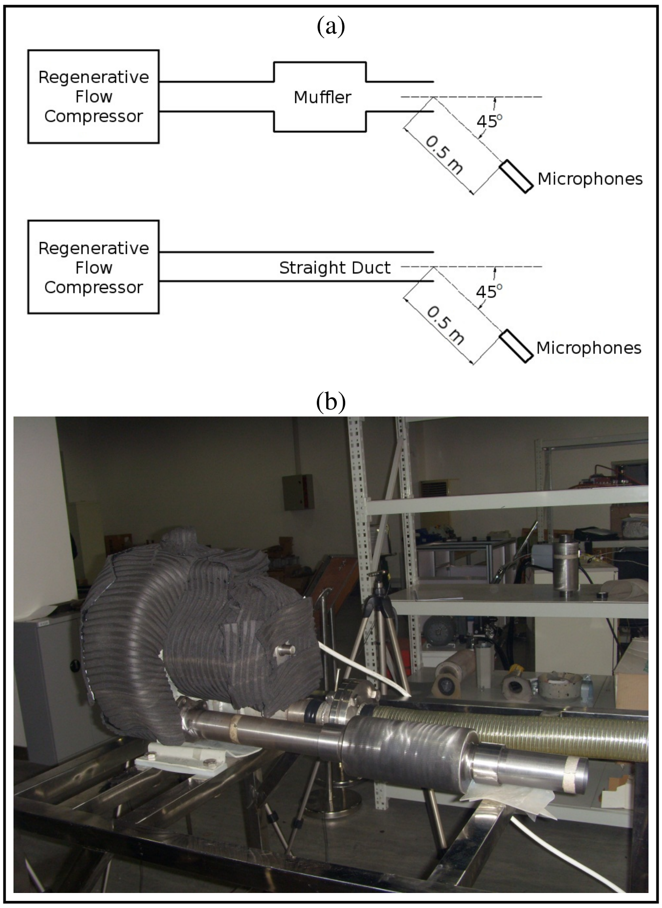

Figure 16. Experimental setup: (a) diagram of test arrangement; (b) photograph of test environment.

The diagram and the photograph of the insertion loss measurement are shown in Fig. 16. The compressor and the motor were covered with absorbing material. A microphone was installed 0.5 m away from the compressor inlet and 45° to the axial direction. Sound pressure levels (SPL) were measured by the microphone with and without the muffler. Measurements were taken at every 400 rpm for 1000–3800 rpm range in steady conditions, and from 1000 rpm to 3800 rpm in run-up conditions.

Figure 17 shows the SPL of intake noise in run-up conditions. Notice that the SPL of inlet noise was remarkably attenuated at the target frequency range of 1000–3500 Hz with mufflers. Figure 18 shows the SPL of intake noise at 3000 RPM. The SPL was reduced by 25 dB at 1000–3500 Hz. And the tonal noise level at BPF was reduced from 92.35 dB to 57.94 dB in a drop of 34.41 dB. In other stationary conditions, tonal noise levels also appeared the highest of the full frequency band, as well as the insertion loss at BPF.

6. CONCLUSION

An approximate model was established by introducing the formula of the thickness correction coefficient in the conventional transfer matrix. The thickness correction was calculated precisely by comparing the transmission loss curves predicted by the TMM with those predicted by the FEM, and the cor-

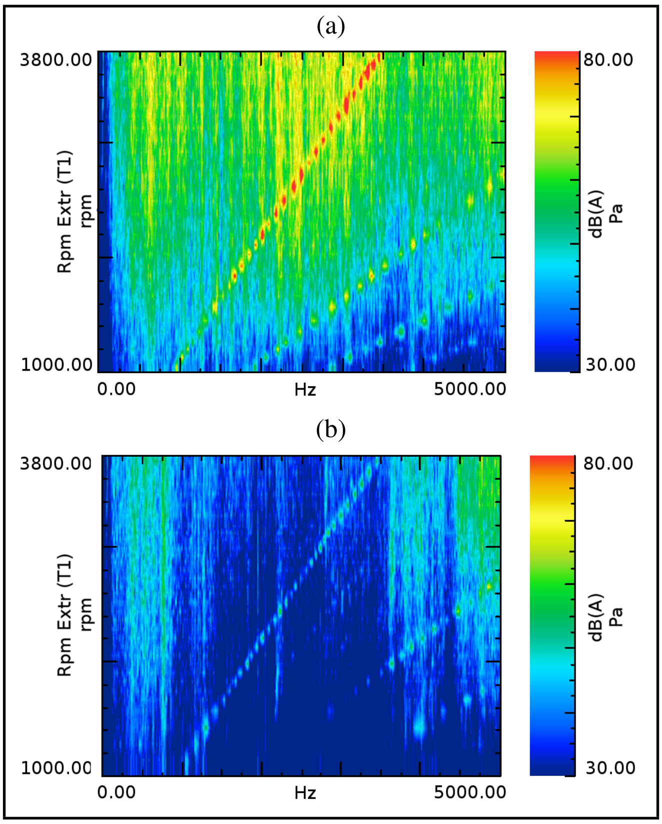

Figure 17. SPL of intake noise under run-up conditions: (a) without muffler; (b) with muffler.

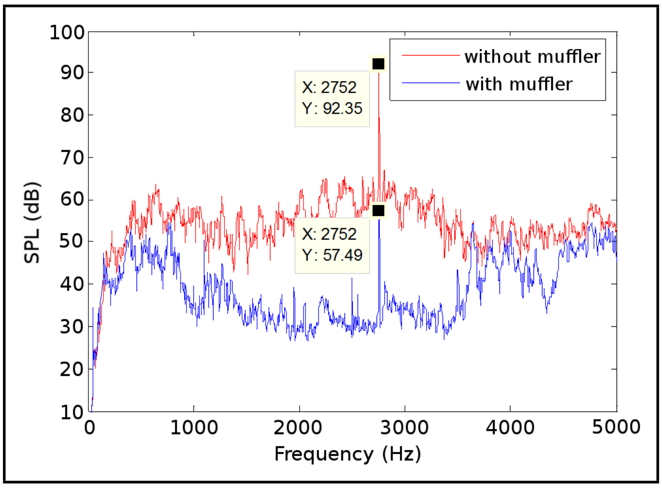

Figure 18. SPL of intake noise at 3000 RPM.

rection formula was obtained by the Taguchi design and polynomial regression analysis. The approximate model has been proven effective within acceptable accuracy limits.

In this study, multi-objective shape optimization of multi-chamber perforated mufflers was presented. NSGA- II was used as the optimization algorithm, and transmission loss was calculated by the approximate model. Certain Pareto solutions were chosen, and a prototype was manufactured based on one of the Pareto solutions. Both transmission loss and insertion loss of the optimized muffler were measured. Numerical and experimental results are in good agreement and show significant improvements of acoustic performance precisely at the target frequency range.

Consequently, the combination of the approximate model and the NSGA-II algorithm provides a fast, effective, and robust approach to co-axial perforated muffler optimization problems.

ACKNOWLEDGEMENTS

Authors are grateful for the financial support by National Natural Science Foundation of China (No. 51305303) and National Major Scientific Instrument Equipment Project of China (2012YQ150256).

APPENDIX A. TRANSFER MATRIX OF PERFORATED MUFFLER

As shown in Fig. 1, a co-axial perforated muffler is composed of an inner perforated tube and an outer resonating chamber. Under the isentropic progresses, for a perforated muffler without mean flow, the governing equations can be written as[3] in Eq. (1), (on top of the next page). where $\alpha_1 = k^2 - \frac{4jk}{d\zeta_p}$, $\alpha_2 = \frac{4jk}{d\zeta_p}$, $\alpha_3 = \frac{4jkd}{(D^2-d^2)\zeta_p}$, $\alpha_4 = k^2 - \alpha_3$, $k = \frac{2\pi f}{c}$, and $\zeta_p = \frac{p_1 - p_{1a}}{\rho c u_h}$ is the normalized specific acoustic impedance of the perforated tube, which is defined as

$$\zeta_p = \frac{R_h + jk(t + \alpha d_h)}{\eta}; \tag{2}$$

where R_h is the specific resistance, and α is the thickness correction coefficient.

Eq. (1) can be conveniently expressed in following matrix form Eq. (3) (see the top of the next page).

Decoupling Eq. 3, the relationship of acoustic pressure and normal particle velocity can be obtained as

$$\begin{bmatrix} p_1 \\ \rho c u_1 \\ p_{1a} \\ \rho c u_{1a} \end{bmatrix} = [\Omega] \begin{bmatrix} C_1 e^{\lambda_1 x} \\ C_2 e^{\lambda_2 x} \\ C_3 e^{\lambda_3 x} \\ C_4 e^{\lambda_4 x} \end{bmatrix}; \tag{4}$$

where λ is the eigenvalues of $[N]$, and $[\Omega]$ is the model matrix formed by eigenvectors of $[N]$:

$$\lambda = \pm\sqrt{-(\alpha_1 + \alpha_4)/2 \pm \sqrt{(\alpha_1 - \alpha_4)^2/4 + \alpha_2\alpha_3}}; \tag{5}$$

$$\begin{Bmatrix} \Omega_{1i} \\ \Omega_{2i} \\ \Omega_{3i} \\ \Omega_{4i} \end{Bmatrix} = \begin{Bmatrix} 1 \\ j\lambda_i/k \\ -(\alpha_1 + \lambda_i^2)/\alpha_2 \\ -j\lambda_i(\alpha_1 + \lambda_i^2)/(k\alpha_2) \end{Bmatrix} i = 1\ 2\ 3\ 4. \tag{6}$$

Thus, the relationship of acoustic pressure and particle velocity between $x = 0$ and $x = l_c$ can be obtained as

$$\begin{bmatrix} p_1(0) \\ \rho c u_1(0) \\ p_{1a}(0) \\ \rho c u_{1a}(0) \end{bmatrix} = [\mathrm{R}] \begin{bmatrix} p_1(l_c) \\ \rho c u_1(l_c) \\ p_{1a}(l_c) \\ \rho c u_{1a}(l_c) \end{bmatrix}; \tag{7}$$

where $[R] = [\Omega]\,[E]\,[\Omega]^{-1}$, $[\mathrm{E}] = \mathrm{diag}(\exp(-\lambda_i l_c)), i = 1, 2, 3, 4$

The boundary conditions of outer tube are given as

$$\begin{cases} \rho_0 c_0 u_{1a} = -j\tan(kl_a)p_{1a} \\ \rho_0 c_0 u_{2a} = j\tan(kl_b)p_{2a} \end{cases} \tag{8}$$

$$\frac{\mathrm{d}^2 p_1}{\mathrm{d}x^2} + \alpha_1 p_1 + \alpha_2 p_{1a} = 0 \frac{\mathrm{d}^2 p_{1a}}{\mathrm{d}x^2} + \alpha_3 p_1 + \alpha_4 p_{1a} = 0 jk\rho c u_1 = \frac{\mathrm{d}p_1}{\mathrm{d}x} jk\rho c u_{1a} = -\frac{\mathrm{d}p_{1a}}{\mathrm{d}x}; \tag{1}$$

$$\begin{bmatrix} \mathrm{d}p_1/\mathrm{d}x \\ \mathrm{d}\rho c u_1/\mathrm{d}x \\ \mathrm{d}p_{1a}/\mathrm{d}x \\ \mathrm{d}\rho c u_{1a}/\mathrm{d}x \end{bmatrix} = \begin{bmatrix} 0 & -jk & 0 & 0 \\ -j\alpha_1/k & 0 & -j\alpha_2/k & 0 \\ 0 & 0 & 0 & -jk \\ -j\alpha_3/k & 0 & -j\alpha_4/k & 0 \end{bmatrix} \begin{bmatrix} p_1 \\ \rho c u_1 \\ p_{1a} \\ \rho c u_{1a} \end{bmatrix} = [\mathrm{N}] \begin{bmatrix} p_1 \\ \rho c u_1 \\ p_{1a} \\ \rho c u_{1a} \end{bmatrix} \tag{3}$$

Taking Eq. (8) into Eq. (7), the transfer matrix of perforated mufflers is obtained as

$$\begin{bmatrix} p_1 \\ \rho_0 c_0 u_1 \end{bmatrix} = [\mathrm{T}] \begin{bmatrix} p_2 \\ \rho_0 c_0 u_2 \end{bmatrix} = \begin{bmatrix} A & B \\ C & D \end{bmatrix} \begin{bmatrix} p_2 \\ \rho_0 c_0 u_2 \end{bmatrix}; \tag{9}$$

where:

$$A = R_{11} - (R_{13} + jR_{14}tan(kl_b))(R_{41} + jR_{31}tan(kl_a))/Z$$
$$B = R_{12} - (R_{13} + jR_{14}tan(kl_b))(R_{42} + jR_{32}tan(kl_a))/Z$$
$$C = R_{21} - (R_{23} + jR_{24}tan(kl_b))(R_{41} + jR_{31}tan(kl_a))/Z$$
$$D = R_{22} - (R_{23} + jR_{24}tan(kl_b))(R_{42} + jR_{32}tan(kl_a))/Z$$
$$Z = R_{43} + jR_{44}tan(kl_b) + jtan(kl_a)(R_{33} + jR_{34}tan(kl_b))$$

APPENDIX B. THE NUMERICAL EXPERIMENTAL RESULTS OF THE TAGUCHI ARRAY

The numerical experimental results of the Taguchi array are presented in Table 6 (on the next page).

REFERENCES

1. Sullivan, J. W. and Crocker, M. J. Analysis of concentric-tube resonators having unpartitioned cavities, *The Journal of the Acoustical Society of America*, **64**, 207–215, (1978). http://dx.doi.org/10.1121/1.381963

2. Jayaraman, K. and Yam, K. Decoupling approach to modelling perforated tube muffler components, *The Journal of the Acoustical Society of America*, **69**, 390–396, (1981). http://dx.doi.org/10.1121/1.385465

3. Munjal, M. L. *Acoustics of Ducts and Mufflers.* Wiley-Interscience Publication, New York, (1987).

4. Vijayasree, N. K. and Munjal, M. L. On an Integrated Transfer Matrix method for multiply connected mufflers, *Journal of Sound and Vibration*, **331** (8), 1926–1938, (2012). http://dx.doi.org/10.1016/j.jsv.2011.12.003

5. Barbieri, R., Barbieri, N., and Fonseca de Lima, K. Application of the Galerkin-FEM and the improved four-pole parameter method to predict acoustic performance of expansion chambers, *Journal of Sound and Vibration*, **276** (3), 1101–1107, (2004). http://dx.doi.org/10.1016/j.jsv.2003.11.063

6. Kirby R. A comparison between analytic and numerical methods for modelling automotive dissipative silencers with mean flow, *Journal of Sound and Vibration*, **325** (3), 565–582, (2009). http://dx.doi.org/10.1016/j.jsv.2009.03.032

7. Wu, T. W., Zhang P., and Cheng, C. Y. R. Boundary element analysis of mufflers with an improved method for deriving the four-pole parameters, *Journal of Sound and Vibration*, **217** (4), 767–779, (1998). http://dx.doi.org/10.1006/jsvi.1998.1800

8. Ji, Z. L., Selamet, A. Boundary element analysis of three-pass perforated duct mufflers, *Noise Control Engineering Journal*, **48** (5), 151–156, (2000). http://dx.doi.org/10.3397/1.2827962

9. Chang, Y. C. and Chiu, M. C. Shape optimization of one-chamber cross-flow mufflers by GA optimization, *Journal of Mechanics*, **24** (01), 13–29, (2008). http://dx.doi.org/10.1017/s1727719100001520

10. Chiu, M. C. and Chang, Y. C. Numerical studies on venting system with multi-chamber perforated mufflers by GA optimization, *Applied Acoustics*, **69** (11), 1017–1037, (2008). http://dx.doi.org/10.1016/j.apacoust.2007.07.002

11. Chang, Y. C. and Chiu, M. C. Optimization of multi-chamber mufflers with reverse-flow ducts by algorithm of simulated annealing, *Archives of Acoustics*, **35** (1), 13–33, (2010). http://dx.doi.org/10.2478/v10168-010-0002-8

12. Airaksinen, T. and Heikkola, E. Multi-objective muffler shape optimization with hybrid acoustics modelling. *The Journal of the Acoustical Society of America*, **130**, 1359, (2011). http://dx.doi.org/10.1121/1.3621119

13. Chang, Y. C., Chiu, M. C., and Wu, L. W. Shape optimization of mufflers hybridized with multiple connected tubes using the boundary element method, neural networks, and genetic algorithm, *Proceedings of the Institution of Mechanical Engineers, Part C: Journal of Mechanical Engineering Science*, **224** (4), 901–913, (2010). http://dx.doi.org/10.1243/09544062jmes1891

14. Chang, Y. C., Chiu, M. C., and Hsieh, C. C. Optimum Design of mufflers hybridized with one-connected curved tube using the boundary element method, neural networks, and the genetic algorithm, *Journal of Marine Science and Technology*, **20** (4), 376–383, (2012). http://dx.doi.org/10.6119/JMST-011-0303-1

15. Auregan, Y., Debray, A., and Starobinski, R. Low frequency sound propagation in a coaxial cylindrical duct: application to sudden area expansion and to dissipative silencers, *Journal Sound and Vibration*, **243** (3), 461–473, (2001). http://dx.doi.org/10.1006/jsvi.2000.3424

16. Lee. I., *Acoustic characteristics of perforated dissipative and hybrid silencers.* Ph.D.

Table 6. Experimental results (L_{49} orthogonal array).

No.	d (m)	D/d	l (m)	l_c/l	t (m)	d_h (m)	η	α	t_e (m)
1	1	1	1	1	1	1	1	1.3	0.016
2	1	2	5	3	4	5	2	0.73	0.02328
3	1	3	2	5	7	2	3	1.08	0.02191
4	1	4	6	7	3	6	4	0.78	0.018
5	1	5	3	2	6	3	5	1.2	0.01733
6	1	6	7	4	2	7	6	1.2	0.01765
7	1	7	4	6	5	4	7	1.76	0.01789
8	2	4	7	3	6	4	1	0.83	0.03482
9	2	5	4	5	2	1	2	2.33	0.01961
10	2	6	1	7	5	5	3	1.03	0.02495
11	2	7	5	2	1	2	4	2.23	0.01594
12	2	1	2	4	4	6	5	0.8	0.016
13	2	2	6	6	7	3	6	1.26	0.0185
14	2	3	3	1	3	7	7	0.86	0.01326
15	3	7	6	5	4	7	1	0.86	0.03886
16	3	1	3	7	7	4	2	0.8	0.02889
17	3	2	7	2	3	1	3	2.2	0.01727
18	3	3	4	4	6	5	4	1.03	0.02265
19	3	4	1	6	2	2	5	2.3	0.0155
20	3	5	5	1	5	6	6	1.13	0.01869
21	3	6	2	3	1	3	7	2.3	0.01421
22	4	3	5	7	2	3	1	1.32	0.02743
23	4	4	2	2	5	7	2	0.7	0.02889
24	4	5	6	4	1	4	3	1.53	0.02102
25	4	6	3	6	4	1	4	3.4	0.02077
26	4	7	7	1	7	5	5	1.3	0.02367
27	4	1	4	3	3	2	6	2.3	0.01403
28	4	2	1	5	6	6	7	1.1	0.01851
29	5	6	4	2	7	6	1	0.7	0.04036
30	5	7	1	4	3	3	2	1.56	0.02622
31	5	1	5	6	6	7	3	0.82	0.02764
32	5	2	2	1	2	4	4	1.12	0.01538
33	5	3	6	3	5	1	5	3.6	0.02033
34	5	4	3	5	1	5	6	1.78	0.01806
35	5	5	7	7	4	2	7	4.2	0.02184
36	6	2	3	4	5	2	1	1.27	0.03075
37	6	3	7	6	1	6	2	1.15	0.02681
38	6	4	4	1	4	3	3	1.4	0.02182
39	6	5	1	3	7	7	4	0.95	0.02692
40	6	6	5	5	3	4	5	2.3	0.02451
41	6	7	2	7	6	1	6	5	0.02294
42	6	1	6	2	2	5	7	1.52	0.01516
43	7	5	2	6	3	5	1	1.11	0.03521
44	7	6	6	1	6	2	2	1.8	0.03056
45	7	7	3	3	2	6	3	1.36	0.02709
46	7	1	7	5	5	3	4	1.9	0.02385
47	7	2	4	7	1	7	5	1.5	0.02267
48	7	3	1	2	4	4	6	1.58	0.01751
49	7	4	5	4	7	1	7	5	0.02158

Thesis, The Ohio State University, (2005). http://rave.ohiolink.edu/etdc/view?acc_num=osu1117631229.

17 Crandall, I. B. *Theory of Vibrating Systems and Sound.* Princeton: D. Van Nostrand Company, (1926).

18 Mechel, F. P., *Formulas of Acoustics.* Springer, New York, (2002).

19 Elnady, T., and H. Boden, H. On the modelling of the acoustic impedance of perforates with flow,. *9th AIAA/CEAS Aeroacoustics Conference*, (2003). http://dx.doi.org/10.2514/6.2003-3304

20 Taguchi, G. *Introduction to Qquality Eengineering*, Asia Productivity Organization, UNIPUB, White Plains, New York, (1886).

21 Cai, J. C., Qi, D. T., Lu, F. A., and Wen, X. F. Study of the tonal casing noise of a centrifugal fan at the blade passing frequency. Part I. Aeroacoustics, *Journal of Low Frequency Noise, Vibration and Active Control*, **29** (4), 253—266, (2010). http://dx.doi.org/10.1260/0263-0923.29.4.253

22 Deb, K., Pratap, A., Agarwal, S., and Meyarivan, T. A. M. T. A fast and elitist multi-objective genetic algorithm: NSGA-II, *IEEE Transactions on Evolutionary Computation*, **6** (2), 182—197, (2002). http://dx.doi.org/10.1109/4235.996017

23 Tao, Z., and Seybert, A. F. A review of current techniques for measuring muffler transmission loss, *SAE International*, 01-1653, (2003). http://dx.doi.org/10.4271/2003-01-1653

24 Lee, I. J., Selamet, A., Kim, H., *et al.*, Design of a multi-chamber silencer for turbocharger noise, *SAE International Journal of Passenger Cars-Mechanical Systems*, **2** (1), 1339–1344, (2009). http://dx.doi.org/10.4271/2009-01-2048

Developing Vibration Equations of an Orthotropic Wrapped Shell, Considering Residual Stress Effects; A Mathematical Approach

Amirali Sadeqi

Department of Mechanical Engineering, Shahid Chamran University of Ahvaz, 1714, Ahvaz, Iran.

Mojtaba Mahzoon and Mohammad Hassan Kadivar

Department of Mechanical Engineering, Shiraz University, Shiraz, Iran.

(Received 20 November 2013; accepted 8 October 2015)

In this paper, vibration equations of an orthotropic, thin rectangular plate wrapped around a porous drum are developed, considering residual stress effects. It is assumed that the plate is subjected to tension from both opposite sides and wrapped continuously around a cylindrical drum so that the wrapped portion behaves like a circular cylindrical shell. First of all, the Lame' parameters, required to constitute the geometry relations, are established for typical cylindrical shallow shell in cylindrical coordinate system. Then, the equations of motion are derived by utilizing the stored strain energy principle based on the Love assumptions. Finally, a set of more complete vibration equations is introduced by applying the simplifications of the Donnell-Mushtari-Vlasov theory. The equations derived under more stringent and precise assumptions are compared with those obtained and available in literature, and the discripancies are highlighted. The present study only aims to mathematically develop the governing relationships, where a numerical solution separately done by the authors can be found in other literature in which vibrational behavior has been completely discussed for moving and stable anisotropic wrapped plates.

NOMENCLATURE

A_1, A_2	gyroscopic inertia matrix
C_{ij}	Stiffness matrix corresponding to extension
D_{ij}	Stiffness matrix corresponding to bending
e_1, e_2, e_3	Unit vectors
g^1, g^2	Decomposed variables
h	Thickness of plate
K_1 to K_4	Symmetric stiffness matrix
k	Curvature
L_1, L_3	Length of flat segments
L_2	Length of wrapped or curved segment
M	Resultant moment, mass matrix
m	Number of terms in approximation function, longitudinal
n	Number of terms in approximatio function, lateral
P_0	Air pressure
P, P'	Typical vector points
P_{ij}	Dummy coefficients or stiffness ratios
Q, $\overline{Q}$	Stiffness matrices principal & material direction
$Q(t)$, $\dot{Q}(t)$	Reduced order matrix of spatial vector q
$Q_{\theta z}$, Q_{yz}	Transverse shear forces
q	Time dependent variable(vector)
q^r	Static load
$R(x, y)$	Radius of the drum or wrapped region
R	Redial direction, Residual index
$\overline{r}$	Displacement vector
T	Tension
U	Potential energy
u	Displacement in x direction
v	Displacement in y direction
W	Spatial or time independent variable (matrix)
w	Transverse displacement in z direction
X, Y, Z	Cartesian directions
α_1, α_2, α_3	Orthogonal curvilinear coordinates
ε	Strain
$\Phi(\theta, y)$	Spatial or time independent variable of Airy Function
ϕ	Airy Function
φ	Direct angle with X direction
θ	Tangential direction
θ_w	Wrapping angle
ρ	Mass density
σ^r	Residual stress
υ	Poisson's ration
ω	Excitation or response frequency
Ψ^1_{ij}, Ψ^2_{ij}	Approximation functions
ξ	Local coordinate in longitudinal direction
$\nabla^2_k(\cdot)$, $\nabla^2_r(\cdot)$	Second order Laplace operators

1. INTRODUCTION

Wrapped plates are widely used in many industries, such as manufacturing of papers, foils, and magnetic films; conveyer belt systems and band saw blades.[1–12] The general schematic of the application is shown in Fig. 1. The safety of relatively thin products, such as newspapers and webs, as well as their manufacturing appliance, has drawn the attention of engineers in recent years to make a design mechanism that is more efficient and versatile.

Vibration analysis of plates and shells during translation has been turned to an essential process in order to extract the modal properties and to prevent possible damages or failure. As shown in Fig. 1, because of the shape of the drum circumference, the mid part of the plate behaves like a cylindrical shell. It is also supposed that the pressurized air exits from the

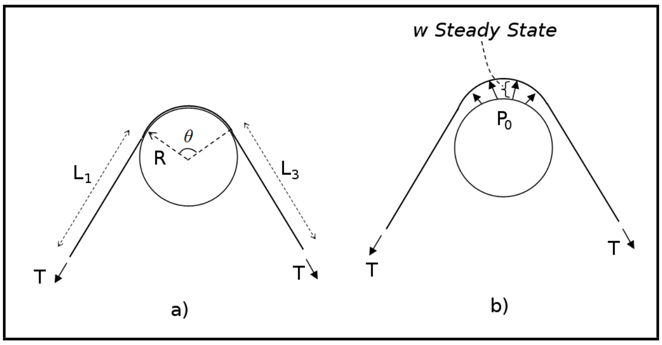

Figure 1. Lateral view of tensioned plate wrapped around a porous drum, (a) without air pressure, (b) with air pressure P_o after reaching to the steady state, θ angle of wrapped segment, R radius of drum, L_1, L_3 flat segments length.

holes around a drum and makes an air cushion in order to mitigate the contact between the plate and the drum and to avoid damage specially to considerably thin plates.

Fluid-structure interaction between the plate and ejected air from a porous drum has been studied by Müftü and Cole.[8] The governing equations, with a relatively high accuracy rate, have been derived based on the Donnel theory, which considers non-linear terms in strains and then is solved by the finite difference method and then by simplifying the equilibrium equation. The helical wrapping case has also been investigated separately by Müftü.[12]

Lopez and Müftü[13] analysed vibration of a thin tensioned web that had been helically wrapped around a turn-bar based on Kirchhoff-Love assumptions. They extracted dynamic properties including natural frequencies and mode shapes in the stable case by finite element method, and later, Sadeqi *et al.*,[1,14,15] followed and extended their investigations to orthotropic and anisotropic moving web, utilizing numerical Rayleigh-Ritz solution. Conflict between fiber orientation and helical wrapping angle, as well as critical speed limitation, was reported in their study.

The present work, aims to introduce a new set of equations, which governs the wrapping process with higher accuracy compared to the previous ones, considering the effect of stored stress, called residual stress, in the structure during the translation and wrapping.

First, in the next section, the general geometric aspect of the issue, as well as Lame' parameters, is surveyed, and the strains are obtained for a cylindrical shell that is continuously joined to rectangular flat plates from two sides based on Love assumptions in the cylindrical coordinate system.

Then, in Section 3, the governing equations of motion of the orthotropic tensioned shell- plate wrapped around a drum are derived based on the Donnell-Mushtari-Vlasov theory, considering the uniformly exhausted air pressure. The effects of air pressure and tension are separately considered as initial stress (residual stress) in the static equation set, which appears in the dynamic set of equations or in the same equations of motion. It is shown that the in- plane forces can be analyzed for both orthotropic and isotropic cases utilizing the Airy Stress Function coupled with the bending equations. Heaviside function is also used to present curvature distribution along the plate.

It is supposed that the tensioned plate encompasses the drum completely and is continuously bent around it. The exhausted air acts as a uniform distributed load on the shell segment and raises the plate till it reaches a steady state (Fig. 1 b)). Hence, the final transverse displacement in the gap between the shell and drum is the summation of the radial and lateral displacements with respect to the origin.

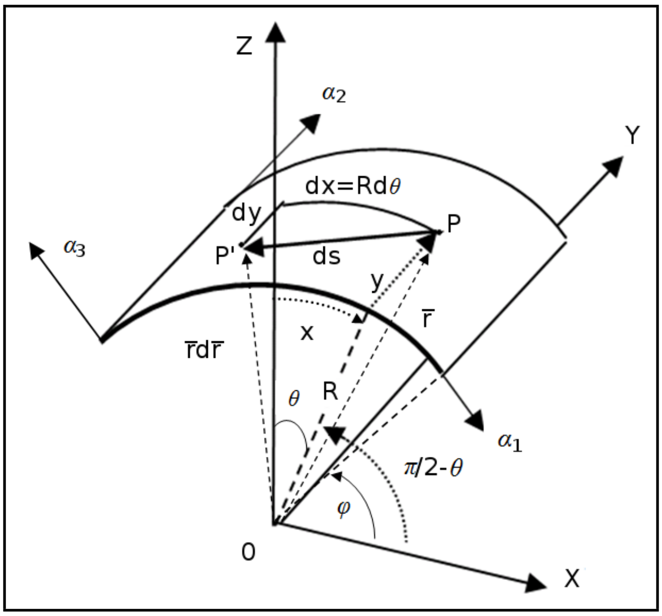

Figure 2. The neutral surface of a cylindrical shell in triple Cartesian (X, Y, Z), cylindrical (r, θ, y), and orthogonal curvilinear (α_1, α_2, α_3) coordinate system.

It is also assumed that the magnitude of the tension is constant during the translating process, and the supports at two opposite edges (where tension acts on) are considered a simple hinge. Therefore, the air pressure that raises the plate (separation between the plate and drum) causes an increase in the plate length and, consequently, would increase its stiffness.

In Section 4, as a result, obtained equations are compared to other references and newly appearing terms and discrepancies are clarified and discussed, but more numerical results can be found in Sadeqi *et al*[1].

2. GENERAL EQUATION OF CYLINDRICAL SHELL

Figure 2 shows a cylindrical non-closed shallow shell element illustrated in three coordinate systems: Global Cartesian, Cylindrical and Orthogonal Curvilinear.

Using Love assumptions together with a new coordinate system (Fig. 2), the governing equations can be derived.[13] Using a reference neutral surface as shown in Fig. 2, the differential variation of the displacement vector $\bar{r}$ between neighboring points P and P' is[16,17]

$$d\bar{r} = \frac{\partial \bar{r}}{\partial \alpha_1} d\alpha_1 + \frac{\partial \bar{r}}{\partial \alpha_2} d\alpha_2; \tag{1}$$

and the magnitude of ds becomes

$$(ds)^2 = A_1^2 (d\alpha_1)^2 + A_2^2 (d\alpha_2)^2. \tag{2}$$

This equation is the first fundamental form, and the coefficients A_1, A_2 are the Lame' parameters. These parameters are determined with respect to the chosen system of coordinates. If the cylindrical system is selected as reference coordinates, the position vector can be rewritten in terms of θ and y as:

$$\bar{r} = R \sin\theta \bar{e}_1 + y \bar{e}_2 + R \cos\theta \bar{e}_3; \tag{3}$$

where $\bar{e}_1$, $\bar{e}_2$, $\bar{e}_3$ are the unit vectors in X, Y, Z direction, respectively. Considering $\alpha_1 = \theta$, and $\alpha_2 = y$ results in

$$A_1 = \left|\frac{\partial \bar{r}}{\partial \theta}\right| = |R\sin\theta \bar{e}_1 - R\cos\theta \bar{e}_3| = = R\sqrt{\cos^2\theta + \sin^2\theta} = R; \tag{4a}$$

$$A_2 = \left|\frac{\partial \bar{r}}{\partial y}\right| = |\bar{e}_2| = 1. \tag{4b}$$

In the present study the cylindrical coordinates for either flat or wrapped (curved) parts is used. In this coordinate system, the radial, rotational, and longitudinal components are in y, θ, z, directions, respectively. Also, in order to present the curvature distribution along the plate, use Heaviside step function is introduced as

$$\frac{1}{R(\theta)} = \begin{cases} 0 & \tan^{-1}\left(\frac{L_1}{R}\right) + \frac{\pi+\theta_w}{2} < \theta < \frac{\pi+\theta_w}{2} \\ \frac{1}{R} & \frac{\pi+\theta_w}{2} \leq \theta \leq \frac{\pi-\theta_w}{2} \\ 0 & \frac{\pi-\theta_w}{2} < \theta < \frac{\pi-\theta_w}{2} - \tan^{-1}\left(\frac{L_3}{R}\right) \end{cases}. \tag{5}$$

which helps to define the curvature effects in terms of the wrapping angle θ_w and the flat segment length L_1, L_3.

2.1. Strain-Displacement Relations

Using assumptions of the Love theory, strain-displacement relations can be expressed as:

$$\begin{Bmatrix} \varepsilon_\theta \\ \varepsilon_y \\ \varepsilon_{\theta y} \end{Bmatrix} = \begin{Bmatrix} \varepsilon_\theta^0 \\ \varepsilon_y^0 \\ \varepsilon_{\theta y}^0 \end{Bmatrix} + z \begin{Bmatrix} k_\theta \\ k_y \\ k_{\theta y} \end{Bmatrix} = \begin{Bmatrix} \frac{1}{A_1}\frac{\partial u}{\partial \theta} + \frac{w}{R(\theta)} + \frac{1}{2A_1^2}\left(\frac{\partial w}{\partial \theta}\right)^2 \\ \frac{1}{A_2}\frac{\partial v}{\partial y} + \frac{1}{2A_2^2}\left(\frac{\partial w}{\partial y}\right)^2 \\ \frac{1}{A_1}\frac{\partial v}{\partial \theta} + \frac{1}{A_2}\frac{\partial u}{\partial y} + \frac{1}{A_1 A_2}\left(\frac{\partial w}{\partial \theta}\right)\left(\frac{\partial w}{\partial y}\right) \end{Bmatrix} + z \begin{Bmatrix} \frac{1}{A_1}\frac{\partial}{\partial \theta}\left(\frac{u}{R(\theta)} - \frac{1}{A_1}\frac{\partial w}{\partial \theta}\right) \\ \frac{1}{A_2}\frac{\partial}{\partial y}\left(-\frac{1}{A_2}\frac{\partial w}{\partial y}\right) \\ \frac{1}{A_2}\frac{\partial}{\partial y}\left(\frac{u}{R(\theta)} - \frac{1}{A_1}\frac{\partial w}{\partial \theta}\right) + \frac{1}{A_1}\frac{\partial}{\partial \theta}\left(-\frac{1}{A_2}\frac{\partial w}{\partial y}\right) \end{Bmatrix}. \tag{6}$$

2.2. Stress-Strain Relationship & Resultant Loads

For an orthotropic element, the stress strain relationship is:

$$\begin{Bmatrix} \sigma_\theta \\ \sigma_y \\ \sigma_{\theta y} \end{Bmatrix} = \begin{bmatrix} Q_{11} & Q_{12} & 0 \\ Q_{12} & Q_{22} & 0 \\ 0 & 0 & Q_{66} \end{bmatrix} \begin{Bmatrix} \varepsilon_\theta \\ \varepsilon_y \\ \varepsilon_{\theta y} \end{Bmatrix};$$

$$Q_{11} = \frac{E_1}{1 - \upsilon_{12}\upsilon_{21}}, \quad Q_{12} = \upsilon_{21} Q_{11}, \quad Q_{22} = \frac{E_2}{E_1} Q_{11}, \quad Q_{66} = G_{12}; \tag{7}$$

where E_1, E_2 are elastic modules, G_{12} indicates shear modules and υ_{12}, υ_{21} show Poisson's ratio in the material principal directions. Resultant force due to normal stress in θ direction will be

$$\begin{Bmatrix} N_\theta + N_\theta^r \\ N_y + N_y^r \\ N_{\theta y} + N_{\theta y}^r \\ M_\theta + M_\theta^r \\ M_y + M_y^r \\ M_{\theta y} + M_{\theta y}^r \end{Bmatrix} = \int_{-\frac{h}{2}}^{\frac{h}{2}} \begin{Bmatrix} \sigma_\theta + \sigma_\theta^r \\ \sigma_y + \sigma_y^r \\ \sigma_{\theta y} + \sigma_{\theta y}^r \\ z(\sigma_\theta + \sigma_\theta^r) \\ z(\sigma_y + \sigma_y^r) \\ z(\sigma_{\theta y} + \sigma_{\theta y}^r) \end{Bmatrix} dz = \begin{bmatrix} C_{11} & C_{12} & 0 & 0 & 0 & 0 \\ C_{12} & C_{22} & 0 & 0 & 0 & 0 \\ 0 & 0 & C_{66} & 0 & 0 & 0 \\ 0 & 0 & 0 & D_{11} & D_{12} & 0 \\ 0 & 0 & 0 & D_{12} & D_{22} & 0 \\ 0 & 0 & 0 & 0 & 0 & D_{66} \end{bmatrix} \begin{Bmatrix} \varepsilon_\theta^0 \\ \varepsilon_y^0 \\ \varepsilon_{\theta y}^0 \\ k_\theta \\ k_y \\ k_{\theta y} \end{Bmatrix};$$

$$C_{ij} = \bar{Q}_{ij} h, \quad D_{ij} = \bar{Q}_{ij}\frac{h^3}{12}; \tag{8}$$

where $\overline{Q}_{ij}$ is the same Q_{ij} in Eq. (7), after transformation and h thickness of the plate. Also, superscript r, indicates the residual effects.

2.3. Equation of Motion

Using the Minimum Potential Energy Principle, the stored strain energy in an infinitesimal element, which is under stress σ (due to transverse pressure) and residual or pre-stress σ^r (due to tension and bending) will be[17]

$$dU = [\frac{1}{2}(\sigma_\theta \varepsilon_\theta + \sigma_y \varepsilon_y + \sigma_{\theta y}\varepsilon_{\theta y} + \sigma_{\theta z}\varepsilon_{\theta z} + \sigma_{yz}\varepsilon_{yz}) + +\sigma_\theta^r \varepsilon_\theta + \sigma_y^r \varepsilon_y + \sigma_{\theta y}^r \varepsilon_{\theta y} + \sigma_{\theta z}^r \varepsilon_{\theta z} + \sigma_{yz}^r \varepsilon_{yz}]dV. \tag{9}$$

Substituting the stresses in terms of resultant loads, and finally rearranging the expressions in terms of displacements (u, v, w) , five relationships coupled of residual and non-residual terms are achievable and can be divided into two sets: one static set due to the static load q^r resulting in initial stresses as

$$-A_2\frac{\partial N_\theta^r}{\partial \theta} - A_1\frac{\partial N_{\theta y}^r}{\partial y} - A_1 A_2 \frac{Q_{\theta z}^r}{R(\theta)} = A_1 A_2 q_\theta^r; \tag{10a}$$

$$-A_2\frac{\partial N_{\theta y}^r}{\partial \theta} - A_1\frac{\partial N_y^r}{\partial y} = A_1 A_2 q_y^r; \tag{10b}$$

$$-A_2\frac{\partial Q_{\theta z}^r}{\partial \theta} - A_1\frac{\partial Q_{yz}^r}{\partial y} + A_1 A_2 \frac{N_\theta^r}{R(\theta)} = A_1 A_2 q_z^r; \tag{10c}$$

$$A_2\frac{\partial M_\theta^r}{\partial \theta} + A_1\frac{\partial M_{\theta y}^r}{\partial y} - A_1 A_2 Q_{\theta z}^r = 0; \tag{10d}$$

$$A_2\frac{\partial M_{\theta y}^r}{\partial \theta} + A_1\frac{\partial M_y^r}{\partial y} - A_1 A_2 Q_{yz}^r = 0; \tag{10e}$$

where $Q_{\theta z}$ and Q_{yz}, according to the plane stress assumptions, are the transverse shear forces as

$$Q_{\theta z} = \int_{z=\frac{-h}{2}}^{z=\frac{h}{2}} (\sigma_{\theta z} + \sigma_{\theta z}^r) dz, \quad Q_{yz} = \int_{z=\frac{-h}{2}}^{z=\frac{h}{2}} (\sigma_{yz} + \sigma_{yz}^r) dz; \tag{11}$$

and another, dynamic set due to the dynamic loads q, demonstrating the vibration behavior of the problem. Disregarding the resultant forces N_θ, N_y, $N_{\theta y}$ compared to the residual resultant forces N_θ^r, N_y^r, $N_{\theta y}^r$, these equations can be rearranged as:

$$-A_2\frac{\partial N_\theta}{\partial\theta}-A_1\frac{\partial N_{\theta y}}{\partial y}-A_1A_2\frac{Q_{\theta z}}{R(\theta)}+A_1A_2\rho h\ddot{u}=A_1A_2q_\theta; \tag{12a}$$

$$-A_2\frac{\partial N_{\theta y}}{\partial\theta}-A_1\frac{\partial N_y}{\partial y}+A_1A_2\rho h\ddot{v}=A_1A_2q_y; \tag{12b}$$

$$-A_2\frac{\partial Q_{\theta z}}{\partial\theta}-A_1\frac{\partial Q_{yz}}{\partial y}+A_1A_2\frac{N_\theta}{R(\theta)}-\frac{A_2}{A_1}\left(\frac{\partial N_\theta^r}{\partial\theta}\right)\left(\frac{\partial w}{\partial\theta}\right)-\frac{A_2}{A_1}N_\theta^r\left(\frac{\partial^2 w}{\partial\theta^2}\right)-\frac{A_1}{A_2}\left(\frac{\partial N_y^r}{\partial y}\right)\left(\frac{\partial w}{\partial y}\right)-\frac{A_1}{A_2}N_y^r\left(\frac{\partial^2 w}{\partial y^2}\right)-\left(\frac{\partial N_{\theta y}^r}{\partial\theta}\right)\left(\frac{\partial w}{\partial y}\right)-\left(\frac{\partial N_{\theta y}^r}{\partial y}\right)\left(\frac{\partial w}{\partial\theta}\right)-(N_{\theta y}^r)\left(2\frac{\partial^2 w}{\partial\theta\partial y}\right)+A_1A_2\rho h\ddot{w}=A_1A_2q_z; \tag{12c}$$

$$A_2\frac{\partial M_\theta}{\partial\theta}+A_1\frac{\partial M_{\theta y}}{\partial y}-A_1A_2Q_{\theta z}=0; \tag{12d}$$

$$A_2\frac{\partial M_{\theta y}}{\partial\theta}+A_1\frac{\partial M_y}{\partial y}-A_1A_2Q_{yz}=0; \tag{12e}$$

In the present paper, the Donnell-Mushtari-Vlasov theory is used to simplify and reach a solvable form rather than facing difficulties caused by coupling that exists between the in-plane forces (Eqs. (12a) and (12b)) and the bending moments (Eqs. (12c)-(12e)).

3. DONNELL-MUSHTARI-VLASOV THEORY

The theory is applicable for shells under transverse loads, and in contrast to other theories, the bending and in-plane effects are also considered. The fundamental assumption is to neglect the effect of in-plane deflection in the bending strains but not in the plane strains.

The second assumption is to neglect the in-plane inertial effects ($\ddot{u}$, $\ddot{v}$), and the last, the term $Q_{\theta z}/R$ must be eliminated in Eq. (12a). Applying these assumptions as well as substituting the values of in-plane and bending strains into the two moment Eqs. (12d) and (12e), then substituting shear forces in terms of related moments in Eq. (12c), five Eqs. (12a)-(12e) are reduce to three. Finally, by introducing the Airy stress function ϕ as

$$N_\theta=\frac{1}{A_2^2}\frac{\partial^2\varphi}{\partial y^2}; \tag{13a}$$

$$N_y=\frac{1}{A_1^2}\frac{\partial^2\varphi}{\partial\theta^2}; \tag{13b}$$

$$N_{\theta y}=-\frac{1}{A_1A_2}\frac{\partial^2\varphi}{\partial y\partial\theta}; \tag{13c}$$

three equations can be diminished again to a single equation but with two unknowns as

$$D_{11}\frac{1}{A_1^4}\frac{\partial^4 w}{\partial\theta^4}+2(D_{12}+2D_{66})\frac{1}{A_1^2}\frac{\partial^4 w}{\partial\theta^2\partial y^2}+D_{22}\frac{\partial^4 w}{\partial y^4}+\nabla_k^2\varphi-\nabla_r^2 w+\rho h\ddot{w}=q_z; \tag{14}$$

where $\nabla_k^2(\cdot)$ and $\nabla_r^2(\cdot)$ are as in Eqs. (15a) and (15b) (see on the next page).

Now, the deflection components u, v are eliminated and one equation remains with two unknowns w and ϕ. To find the second equation, the compatibility equation is necessary, which can be written as[17]

$$\frac{k_\theta}{R(\theta)}+\frac{1}{A_1^2}\left(\frac{\partial^2(\varepsilon_y^0)}{\partial\theta^2}\right)+\frac{1}{A_1^2}\left(\frac{\partial^2(\varepsilon_\theta^0)}{\partial y^2}\right)-\frac{1}{A_1A_2}\frac{\partial^2(\varepsilon_{\theta y}^0)}{\partial\theta\partial y}=0. \tag{16}$$

Substituting the strains with terms of the axial forces given by

$$\left\{\begin{array}{c}\varepsilon_\theta^0\\ \varepsilon_y^0\\ \varepsilon_{\theta y}^0\end{array}\right\}=\left[\begin{array}{ccc}P_{11} & -P_{12} & 0\\ P_{12} & -P_{22} & \\ 0 & & P_{66}\end{array}\right]\left\{\begin{array}{c}N_\theta\\ N_y\\ N_{\theta y}\end{array}\right\};$$

$$P_{11}=\frac{C_{22}}{C_{11}C_{22}-C_{12}^2},\quad P_{22}=P_{11}\frac{C_{11}}{C_{22}},\quad P_{12}=P_{11}\frac{C_{12}}{C_{22}},\quad P_{66}=\frac{1}{C_{66}}; \tag{17}$$

and using Eqs. (13a)–(13c) results in

$$P_{22}\frac{1}{A_1^4}\frac{\partial^4\varphi}{\partial\theta^4}+\frac{1}{A_1^2A_2^2}(P_{66}-2P_{12})\frac{\partial^4\varphi}{\partial\theta^2\partial y^2}++\frac{1}{A_2^4}P_{11}\frac{\partial^4\varphi}{\partial y^4}-\left(\frac{1}{R(\theta)}\frac{\partial^2 w}{\partial y^2}\right)=0; \tag{18}$$

The previous equation together with Eq. (14), are the equations of motion of an orthotropic shell wrapped around a porous pressurized drum. These fourth order equations are coupled, and four boundary conditions are needed at each edge (two for w, and two for ϕ) to solve them. A numerical approach has been taken to solve the typical simplified equations for the anisotropic moving case in Sadeqi *et al.*[1] Assuming harmonic time dependence and separation of variables as

$$w(\theta,y,t)=W(\theta,y)e^{j\omega t}=\sum_{i=1}^{m}\sum_{j=1}^{n}g_{ij}^1\Psi_{ij}^1(\theta,y)e^{j\omega t}; \tag{19a}$$

$$\varphi(\theta,y,t)=\Phi(\theta,y)e^{j\omega t}=\sum_{i=1}^{m}\sum_{j=1}^{n}g_{ij}^2\Psi_{ij}^2(\theta,y)e^{j\omega t}; \tag{19b}$$

and also by decomposing in terms of variables g^1 and g^2, the following matrix can be defined as

$$\left[\begin{array}{cc}K_1-M\omega^2 & K_2\\ K_3 & K_4\end{array}\right]\left\{\begin{array}{c}g^1\\ g^2\end{array}\right\}=0; \tag{20}$$

where g^1 and g^2 are of rank$(m\times n)\times 1$, vectors and K_1 to K_4, and M are symmetric $(m\times n)\times(m\times n)$ rank matrices in terms of approximation functions given by Ψ_{ij}^1, Ψ_{ij}^2 (see[1]). For the isotropic case, Eq. (14) becomes

$$D\nabla^4 w+\nabla_k^2\varphi-\nabla_r^2 w+\rho h\ddot{w}=q_z; \tag{21}$$

where

$$\nabla^4(.)=\left(\frac{1}{A_1^4}\frac{\partial^4(.)}{\partial\theta^4}+\frac{2}{A_1^2A_2^2}\frac{\partial^2(.)}{\partial\theta^2}\frac{\partial^2(.)}{\partial y^2}+\frac{1}{A_1^4}\frac{\partial^4(.)}{\partial y^4}\right); \tag{22}$$

and other operators, compatibility equation, boundary conditions, and Airy function ϕ remain the same as for the orthotropic case. Following a similar procedure leads to

$$Eh\nabla_k^2 w-\nabla^4\varphi=0; \tag{23}$$

$$\nabla_k^2(\cdot) = \frac{1}{A_1 A_2}\frac{\partial}{\partial y}\left(\frac{1}{R(\theta)}\frac{A_1}{A_2}\frac{\partial(\cdot)}{\partial y}\right); \tag{15a}$$

$$\nabla_r^2(\cdot) = \frac{1}{A_1^2}\left(N_\theta^r\frac{\partial^2(.)}{\partial\theta^2} + \left(\frac{\partial(N_\theta^r)}{\partial\theta}\right)\left(\frac{\partial(.)}{\partial\theta}\right)\right) + \frac{1}{A_2^2}\left(N_y^r\frac{\partial^2(.)}{\partial y^2} + \left(\frac{\partial(N_y^r)}{\partial y}\right)\left(\frac{\partial(.)}{\partial y}\right)\right) + \frac{1}{A_1 A_2}\left[2\left(N_{\theta y}^r\frac{\partial^2(.)}{\partial\theta\partial y}\right) + \left(\frac{\partial(N_{\theta y}^r)}{\partial\theta}\right)\left(\frac{\partial(.)}{\partial y}\right) + \left(\frac{\partial(N_{\theta y}^r)}{\partial y}\right)\left(\frac{\partial(.)}{\partial\theta}\right)\right]. \tag{15b}$$

$$N_x + N_x^r = C\left[\frac{1}{A_1(x)}\frac{\partial u}{\partial x} + \frac{w}{R(x)} + \frac{1}{2A_1^2(x)}\left(\frac{\partial w}{\partial x}\right)^2 + v\left(\frac{\partial v}{\partial y} + \frac{1}{2}\left(\frac{\partial w}{\partial y}\right)^2\right)\right], \quad C = \frac{Eh}{(1-v^2)}; \tag{28}$$

substituting w and ϕ from Eqs. (19a) and (19b) into Eqs. (21) and (23) and then applying operators ∇^4 and ∇_k^2, respectively, and subtracting each other gives a single but higher order equation achieved as[17–20]

$$D\nabla^8 W + Eh\nabla_k^4 W - \nabla^4\nabla_r^2 W - \rho h\omega^2\nabla^4 W = 0; \tag{24}$$

which is the appropriate form of vibration equation for the isotropic case.

4. COMPARISON WITH OTHER REFERENCES

Substituting $\theta = x/R$ and transforming to the Cartesian coordinates with $A_1 = A_2 = 1$, the equations obtained in the present work are compared to the simplified cases available in other references. In the absence of dynamic load q_z and acceleration term $\ddot{w}$, for isotropic case, Eq. (22) becomes:

$$D\nabla^4 w - \nabla_r^2 w + \nabla_k^2\varphi = 0; \tag{25}$$

where operators from Eqs. (15a) and (15b) can be expressed as

$$\nabla_r^2 w = N_x^r\frac{\partial^2 w}{\partial x^2} + 2N_{xy}^r\frac{\partial^2 w}{\partial x\partial y} + N_y^r\frac{\partial^2 w}{\partial y^2} + \frac{\partial N_{xy}^r}{\partial x}\frac{\partial w}{\partial y} + \frac{\partial N_{xy}^r}{\partial y}\frac{\partial w}{\partial x} + \frac{\partial N_y^r}{\partial y}\frac{\partial w}{\partial y}; \tag{26}$$

$$\nabla_k^2\varphi = \frac{N_x}{R(x)}. \tag{27}$$

Substituting the values of in-plane forces from Hooke's law in terms of strains is presented in Eq. (28) (see on the top of the page).

Considering the upward direction of air pressure as positive, and since the tension in x direction and the distributed air pressure normal to shell are the only external loads, solution of in-plane force N_θ^r in Eq. (10c), results in

$$N_x^r = T + R(x)q_z^r. \tag{29}$$

Neglecting the in-plane strains and substituting for N_x from static solution leads to:

$$D\nabla^4 w - (T + R(x)q_z^r)\frac{\partial^2 w}{\partial x^2} - 2N_{xy}^r\frac{\partial^2 w}{\partial x\partial y} - N_y^r\frac{\partial^2 w}{\partial y^2} - \frac{\partial N_{xy}^r}{\partial x}\frac{\partial w}{\partial y} - \frac{\partial N_{xy}^r}{\partial y}\frac{\partial w}{\partial x} - \frac{\partial N_y^r}{\partial y}\frac{\partial w}{\partial y} + \frac{C}{R^2(x)}w = q_z^r + \frac{T}{R(x)}. \tag{30}$$

4.1. Equilibrium Equation in Reference[8]

The governing equation for the non-helical wrapping case of plate, has been developed by Müftü and Cole[8] based on Donnel theory as

$$D\nabla^4 w - T\frac{\partial^2 w}{\partial x^2} - N_y\frac{\partial^2 w}{\partial y^2} - 2N_{xy}\frac{\partial^2 w}{\partial x\partial y} + \frac{C}{R^2(x)}w = = p - \frac{T}{R(x)}; \tag{31}$$

where p is the air pressure so that the positive direction is assumed to be downward. The basic differences between this equation and one obtained here (Eq. (30)) can be expressed as:

1. The effect of exhausting air pressure on increasing tension is considered in Eq. (3). The air pressure (assuming upward direction as positive) causes the wrapped part to rise up, and also causes increasing elongation from boundaries; consequently, the value of effective tension increases. In Müftü and Cole,[8] it is assumed that the tension is constant during the process; therefore, the plate together with the supports could move in a rigid manner as long as it would reach a steady state.
   On the other hand, the effect of tension on the air pressure is the same for both equations because the tension T causes a pressure equal to T/R from the wrapped region to the drum surface. Hence, the minimum pressure required to separate the wrapped part from the drum is T/R.
2. In Eq. (31), there are no residual resultant forces N_y^r and N_{xy}^r. These can be neglected in the absence of distributed in-plane forces and small thickness. Otherwise, the static set Eqs. (10a)-(10e), should be independently solved using the Airy function ϕ.

4.2. Equations for Non-Helical Wrapping[12,13]

The equilibrium equation for wrapped plate in the presence of the air pressure exhausted from the turn bar has been developed as[12]

$$D\nabla^4 w - T\frac{\partial^2 w}{\partial x^2} + \frac{C}{R^2(x)}w = p + p_c - \frac{T}{R(x)}; \tag{32a}$$

where p_c, the air pressure, is considered the contact pressure. The in-plane forces are also neglected in this equation. In the absence of in-plane forces ($N_y = N_{xy} = 0$), and for static load, Eq. (30), can be simplified to

$$D\nabla^4 w - (T + q_z^r R(x))\frac{\partial^2 w}{\partial x^2} + \frac{C}{R^2(x)}w = q_z^r + \frac{T}{R(x)}; \tag{32b}$$

Note that if the positive direction of air pressure in both Eqs. (32a) and (32b) are assumed to be the same, the right-hand-side terms would be equal. Also, the vibration equation of the mentioned plate in Müftü[12] is presented as

$$D\nabla^4 w - T\frac{\partial^2 w}{\partial x^2} + \frac{C}{R^2(x)}w + \rho h\ddot{w} = 0. \tag{33a}$$

In the absence of air pressure ($q_z^r = 0$) and in-plane forces ($N_y = N_{xy} = 0$), Eq. (21), could be simplified to

$$D\nabla^4 w - (T + q_z^r R(x))\frac{\partial^2 w}{\partial x^2} + \frac{C}{R^2(x)}w + \rho h\ddot{w} = 0. \tag{33b}$$

For constant tension during the process of wrapping and also after reaching steady state, Eqs. (33a) and (33b) would be equal.

5. SUMMARY AND CONCLUSION

In this study, general equations of wrapped orthotropic plate were developed by defining new coordinates and virtual work approach. It was shown that in/out plane forces affect the bending moments and vice versa, so that the constitutive equations appear as coupled form. Any change in the tension leads to change in the air pressure required to separate the plate of the cylindrical drum, as well as stiffness of the plate and natural frequencies.

First, two residual and dynamic sets of quintuplet equations were obtained, then by using the Donnell-Mushtari-Vlasov theory, they were simplified and reduced to three equations in terms of second-order derivation of transverse displacement w and, finally, by defining Airy functions, reduced to two equations of forth order. In other words, the five second-order equations were diminished to the three equations of higher order and could even decrease for isotropic case to a single equation of eighth order.

It was also shown that the obtained equations had additional terms than available ones in other references, because of contributing the in/out of plane resultant force in bending equation which causes a higher accuracy in analysis. Moreover, interaction between the tension and air pressure as a transverse load was considered and kept in the equations.

A numerical solution to find frequencies and mode shapes for a typical simplified equations of anisotropic moving wrapped plate studied in a separate paper, which has been addressed in the context.

REFERENCES

[1] Sadeqi, A., Mahzoon, M., and Kadivar, M. H. Vibration analysis of moving anisotropic thin plate, wrapped in translation process, *J. Braz. Soc. Mech. Sci. Eng.*, (2015). http://dx.doi.org/10.1007/s40430-015-0447-9

[2] Ulsoy, A. G. and Mote. Jr, C. D. Vibration of wide band saw blades, *J. Eng. Inds.*, **104**, 71–78, (1982). http://dx.doi.org/10.1115/1.3185801

[3] Harrison, A. Determination of the natural frequencies of transverse vibration for the conveyor belts with orthotropic properties, *J. Sound Vib.*, **110** (3), 483–493, (1986). http://dx.doi.org/10.1016/s0022-460x(86)80149-3

[4] Rongen, P. M. J. Finite Element Analysis of the Tape Scanner Interface in Helical Scan Recording, *Ph. D. Diss.*, Technical University of Eindhoven, The Netherlands, (1994).

[5] Al Jawi, A. A. N., Pierre, C., and Ulsoy, A. G. Vibration localization in dual-span, axially moving beams, part I:formulation and results, *J. Sound Vib.*, **179** (2), 243–266, (1995). http://dx.doi.org/10.1006/jsvi.1995.0016

[6] Al Jawi, A. A. N., Pierre, C., and Ulsoy, A. G. Vibration localization in dual-span, axially moving beams, part II: Perturbation analysis, *J. Sound Vib.*, **179** (2), 267–287, (1995). http://dx.doi.org/10.1006/jsvi.1995.0017

[7] Al Jawi, A. A. N., Ulsoy, A. G., and Pierre, C. Vibration localization in band—wheel systems: theory and experiment, *J. Sound Vib.*, **179** (2), 289–312, (1995). http://dx.doi.org/10.1006/jsvi.1995.0018

[8] Müftü, S. and Cole, K.A. The fluid/structure interaction of a thin flexible cylindrical web supported by an air cushion, *J. Fluid Struct.*, **13**, 681–708, (1999). http://dx.doi.org/10.1006/jfls.1999.0228

[9] Raman, A., Wolf, A. K., and Hagedorn, P. Observations on the vibrations of paper webs, *Proc. of 11th Annual ISPS Conference*, Santa Clara, Kalifornien, USA, (2000).

[10] Kong, L. and Parker, R. G. Vibration of an axially moving beam wrapping on fixed pulleys, *J. Sound Vib*, **280**, 1066–1074, (2005). http://dx.doi.org/10.1016/j.jsv.2004.02.037

[11] Müftü, S. Mechanics of thin, flexible translating media and their interactions with surrounding air, *Japan Soc. Mech. Eng. Int. J.*, Series C, **48** (3), 329–336, (2005). http://dx.doi.org/10.1299/jsmec.48.329

[12] Müftü, S. Mechanics of a thin, tensioned-shell, wrapped helically around a turn-bar, *J. Fluid Struct.*, **23**, 767–785, (2007). http://dx.doi.org/10.1016/j.jfluidstructs.2006.11.007

[13] Lopez, E. and Müftü, S. Vibration of thin, tensioned, helically wrapped plates, *J. Sound Vib.*, **330**, 685–702, (2010). http://dx.doi.org/10.1016/j.jsv.2010.08.043

[14] Sadeqi, A., Mahzoon, M., and Kadivar, M. H. Frequency analysis of orthotropic, thin, tensioned, helically wrapped around a cylindrical roller, *Proc. of International ISME Conference*, (In Persian), Shiraz University, Iran, (2012).

[15] Sadeqi, A., Vibration analysis of composite plates under tension considering curvature due to their wrapping around roller, *Master's Thesis*, (In Persian), Shiraz University, Iran, (2012).

[16] Vlasov, V. Z. General theory of shells and its applications in engineering, Washington, D. C. National Aeronautics and Space Administration, (1964). **Series**: NASA TT F-99.

[17] Soedel, W. *Vibrations of shells and plates*, Third Edition, New York: Marcel Dekker, Inc, (2000). **ISBN**: 978-0824756291

[18] Szilard, R. *Theories and applications of plate analysis*, John Wiley and Sons, (2004). http://dx.doi.org/10.1002/9780470172872

[19] Kelkar, V. S. and Sewell, R. T. *Fundamentals of the analysis and design of shell structures*, Prentice-Hall, (1987). **ISBN-10**: 0133343278. **ISBN-13**: 978-0133343274

[20] Vlasov, V. Z. and Leontev, U. N. Washington, D. C. NASA Technical Documents, Beams, Plates and Shells on Elastic Foundations, (1966).

Vibration Analysis of Cracked Beams Using Adomian Decomposition Method and Non-Baseline Damage Detection via High-Pass Filters

Qibo Mao

School of Aircraft Engineering, Nanchang HangKong University, 696 South Fenghe Avenue, Nanchang, CN-330063, P. R. China

(Received 15 January 2014; accepted 20 October 2014)

The Adomian decomposition method (ADM) and high-pass filters are employed in this study to investigate the free vibrations and damage detection of cracked Euler-Bernoulli beams. Based on the ADM and employing some simple mathematical operations, the closed-form series solution of the mode shapes can be determined for beams consisting of an arbitrary number of cracks under general boundary conditions in a recursive way. Then, a high-pass filter is used to extract the irregularity profile from the corresponding mode shape. The location and size of the cracks in the beam can be determined by the peak value of the irregularity profile. The numerical results for different locations and depths of cracks on the damaged beam under different boundary conditions are presented. The results show that the proposed method is effective and accurate. The experimental work for aluminium cantilever beams with one and two cracks was performed to verify the proposed method. The successful detection of cracks in the beam demonstrates that the proposed method has great potential in crack detection of beam-type structures, as it is simple and does not require the mode shapes of an uncracked beam as a baseline.

1. INTRODUCTION

Recently, many vibration-based damage detection techniques have been developed due to their non-destructive nature.[1–3] The popularity of these techniques is based on the fact that the loss of stiffness due to structural damage changes the dynamic response of the structure. With these techniques, damages can be detected by monitoring the vibration parameters, such as damping ratios, natural frequencies, and mode shapes.

Mode shapes and/or their derivatives are generally used to predict the location and the size of the damage rather than natural frequencies. Because the natural frequencies are the global features of the structure, it is difficult to determine the damage location with a frequency-based method.[1] Since the 1990s, a lot of damage detection algorithms based on mode shape have been proposed for damage detection and localization.[1,2,4,5] Most of these methods require knowing the mode shapes of the health structures, which are difficult to obtain (and sometimes impossible), in order to establish a baseline for damage detection.

If the applicability of the mode shaped-based damage detection approach could be extended by eliminating the need for the baseline mode shapes, this approach would be significantly expanded in structural damage detection applications. Because of this potential, the non-baseline mode shape-based damage detection approaches have received more and more attention. Recently, Qiao and Cao[6] calculated the fractal dimension (FD) and waveform fractal dimension (WFD) of the mode shape from a cracked beam to determine the damage location and quantification. Ismail, et al.[7] used fourth derivatives of the mode shapes to directly identify the location of damage for reinforced concrete beams. The application of 1-D and 2-D wavelet transform methods to displacement mode shape for damage detection of beam and plate structures have also been extensively investigated.[8,9]

Ratcliffe, et al.[10,11] proposed the gapped smoothing method (GSM) and the global fitting method (GFM) for damage detection. The GSM and GFM do not require data from the undamaged structure. By applying GSM or GFM to the mode shapes of the damaged structures, a smoothing curve, which could be regarded as a substitution for the mode shape from the undamaged structure, can be extracted. The GSM and GFM later used the operating deflection shape and its curvature data, and were extended to directly use two-dimensional COS data for damage detections.[12–14]

Recently, Wang and Qiao[15] proposed an irregularity-based method to detect the cracks in beam structures. In this method, The Gaussian filter and triangular filter are applied on the mode shapes to extract the irregularities from the mode shape of the cracked beam, indicating the damage in the structure. The irregularity-based method was extended to detect the delamination in composite laminated beams and plates.[16,17]

In this study, high-pass filters are used to extract the irregularities from the mode shapes and determine the damage situation in a beam. The aim of the paper presented here is twofold. Firstly, mode shapes for a beam with an arbitrary number of cracks under general boundary conditions are determined by the Adomian decomposition method (ADM).[18–22] Using the

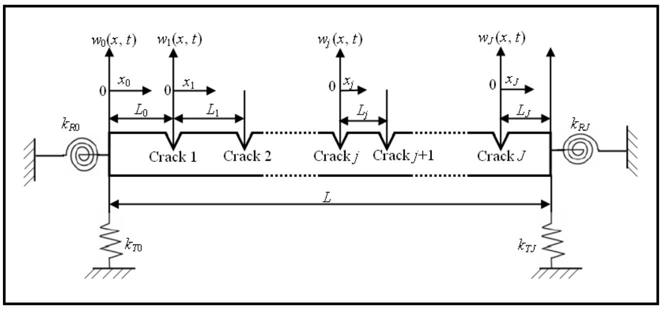

Figure 1. The coordinate system for a multiple-cracked beam, elastically restrained at both ends.

ADM, the governing differential equation for each section of the cracked beam becomes a recursive algebraic equation. The boundary conditions and continuity conditions at crack locations become simple algebraic frequency equations that are suitable for symbolic computation. Moreover, after some simple algebraic operations on these frequency equations, we can obtain the natural frequency and corresponding closed-form series solution of mode shape simultaneously.

As a second aim, this paper seeks to detect the location and depth of cracks in beam structures by using high-pass filters. The mode shapes are filtered by using a 3rd-order Butterworth high-pass filter, and their irregularities are extracted. The numerical calculation with different crack locations, depths, and number are discussed for a damaged beam under different boundary conditions. Finally, by using two aluminium cantilever beams with one and two cracks, the experimental damage detection was performed to verify the proposed method.

2. THE ADM FOR A CRACKED BEAM

Consider the free vibration of a uniform Euler-Bernoulli beam of length L consisting of J open cracks elastically restrained at both ends, as shown in Fig. 1. It is assumed that the cracks are located at $L_1, L_2, \ldots, L_{J-1}$, and $0 < L_1 < L_2 < \ldots < L_J < L$. The beam is divided into $(J+1)$ sections with the $(J+1)$ mirror systems of reference x_j $(j = 0, 1, \ldots, J)$.

The ordinary differential equation describing the free vibration in each section is as follows:

$$\frac{d^4\phi_j(x_j)}{dx_j^4} - \frac{m_s\omega^2}{EI}\phi_j(x_j) = 0, \; x_j \in [0, L_j], \; j = 0, 1, \ldots, J; \tag{1}$$

where subscript j denotes the beam between the jth crack and $(j+1)$th crack. $\phi_j(x_j)$ and ω are the structural mode shape and the natural frequency, respectively. E is Young's modulus. $I = \frac{bh^3}{12}$ is the cross-sectional moment of inertia of the beam. $m_s = \rho bh$ is the mass per unit length. ρ, b, and h are the density, width, and thickness of the beam, respectively.

Equation (1) can be rewritten in dimensionless form as follows:

$$\frac{d^4\Phi_j(X_j)}{dX_j^4} - \Omega^4\Phi_j(X_j) = 0, \quad X_j \in [0, R_j]; \tag{2}$$

where $X_j = \frac{x_j}{L}$, $\Phi_j(X_j) = \frac{\phi_j(x_j)}{L}$, $R_j = \frac{L_j}{L}$, $\Omega^4 = \frac{m_s\omega^2 L^4}{EI}$, Ω is the dimensionless natural frequency, and the nth dimensionless natural frequency is denoted as $\Omega(n)$.

According to the ADM,[18–22] $\phi_j(X_j)$ in Eq. (2) can be expressed in terms of an infinite series

$$\Phi_j(X_j) = \sum_{m=0}^{\infty} \Phi_j^{[m]}(X_j); \tag{3}$$

where the component function $\Phi_j^{[m]}(X_j)$ will be determined recurrently.

If a linear operator $G = \frac{d^4}{dX^4}$ is imposed, the inverse operator of G is therefore a 4-fold integral operator defined by $G^{-1} = \iiiint(\ldots)dX\,dX\,dX\,dX$, and

$$G^{-1}G\left[\Phi_j(X_j)\right] = \Phi_j(X_j) - \Phi_j(0) - \frac{d\Phi_j(0)}{dX_j}X_j - \frac{d^2\Phi_j(0)}{dX_j^2}\frac{X_j^2}{2} - \frac{d^3\Phi_j(0)}{dX_j^3}\frac{X_j^3}{6}. \tag{4}$$

Applying this on both sides of Eq. (2) with G^{-1}, we get

$$G^{-1}G\left[\Phi_j(X_j)\right] = \Omega^4 G^{-1}\left[\Phi_j(X_j)\right] = = \Omega^4 G^{-1}\left[\sum_{m=0}^{\infty}\Phi_j^{[m]}(X_j)\right]. \tag{5}$$

Comparing Eqs. (4) and (5), we get

$$\Phi_j(X_j) = \Phi_j(0) + \frac{d\Phi_j(0)}{dX_j}X_j + \frac{d^2\Phi_j(0)}{dX_j^2}\frac{X_j^2}{2} + \frac{d^3\Phi_j(0)}{dX_j^3}\frac{X_j^3}{6} + \Omega^4 G^{-1}\left[\sum_{m=0}^{\infty}\Phi_j^{[m]}(X_j)\right]. \tag{6}$$

Finally, by using Eq. (3), the approximated solution of Eq. (6) can be determined by using the following recurrence relation:

$$\Phi_j^{[0]}(X_j) = \Phi_j(0) + \frac{d\Phi_j(0)}{dX_j}X_j + \frac{d^2\Phi_j(0)}{dX_j^2}\frac{X_j^2}{2} + \frac{d^3\Phi_j(0)}{dX_j^3}\frac{X_j^3}{6}; \tag{7}$$

$$\Phi_j^{[m]}(X_j) = \Omega^4 G^{-1}\left[\Phi_j^{[m-1]}(X_j)\right]; \qquad m \geq 1. \tag{8}$$

By substituting Eqs. (7) and (8) into Eq. (3), and approximating the above solution by the truncated series, the following equation is found:

$$\Phi_j(X_j) = \sum_{m=0}^{M-1}\Phi_j^{[m]}(X_j) = = \sum_{s=0}^{3}\frac{d^s\Phi_j(0)}{dX^s}\sum_{m=0}^{M}\left[\Omega^{4m}\frac{X_j^{4m+n}}{(4m+n)!}\right]. \tag{9}$$

Equation (9) implies that $\sum_{m=M}^{\infty}\Phi_j^{[m]}(X_j)$ is negligibly small. The number of the series summation limit M is determined by convergence requirement in practice.

The unknown parameters $\frac{d^s\Phi_j(0)}{dX^s}$ $(s = 0, 1, 2, 3)$ and Ω in Eq. (9) can be determined based on the boundary condition equations and the continuity conditions of each section of the beam.

The boundary conditions at the ends of the beam shown in Fig. 1 can be expressed in dimensionless form as follows:

$$\frac{d^2\Phi_0(0)}{dX_0^2} - K_{R0}\frac{d\Phi_0(0)}{dX_0} = 0,$$
$$\frac{d^3\Phi_0(0)}{dX_0^3} + K_{T0}\Phi_0(0) = 0; \tag{10}$$
$$\frac{d^2\Phi_J(R_J)}{dX_J^2} + K_{RJ}\frac{d\Phi_J(R_J)}{dX_J} = 0,$$
$$\frac{d^3\Phi_J(R_J)}{dX_J^3} - K_{TJ}\Phi_J(R_J) = 0; \tag{11}$$

where $K_{R0} = \frac{k_{R0}L}{EI}$, $K_{T0} = \frac{k_{T0}L^3}{EI}$, $K_{RJ} = \frac{k_{RJ}L}{EI}$, $K_{TJ} = \frac{k_{TJ}L^3}{EI}$, and $R_J = \frac{L_J}{L}$. k_{T0} and k_{TJ} are the stiffness of the translational springs, and k_{R0} and k_{RJ} are the stiffness of the rotational springs at $x_0 = 0$ and $x_J = L_J$, respectively.

Substituting Eq. (9) into Eq. (10), the mode shape function for the first section $\Phi_0(X_0)$ can be expressed as a linear function of $\Phi_0(0)$ and $\frac{d\Phi_0(0)}{dX_0}$, as follows:

$$\Phi_0(X_0) = \Phi_0(0)\left\{\sum_{m=0}^{M-1}\left[\Omega^{4m}\frac{X_0^{4m}}{(4m)!}\right] - K_{T0}\sum_{m=0}^{M-1}\left[\Omega^{4m}\frac{X_0^{4m+3}}{(4m+3)!}\right]\right\} + \frac{d\Phi_0(0)}{dX_0}\left\{\sum_{m=0}^{M-1}\left[\Omega^{4m}\frac{X_0^{4m+1}}{(4m+1)!}\right] + K_{R0}\sum_{m=0}^{M-1}\left[\Omega^{4m}\frac{X_0^{4m+2}}{(4m+2)!}\right]\right\}. \tag{12}$$

Due to the localized crack effect, the crack of the beam can be simulated as a massless spring.[6] For each crack between the two sections, conditions can be introduced which impose continuity of displacement, bending moment, and shear. Moreover, an additional condition imposes equilibrium between the transmitted bending moment and the rotation of the spring representing the crack. Consequently, the continuity conditions in dimensionless form are[6,8]

$$\Phi_{j+1}(0) = \Phi_j(R_j),$$
$$\frac{d\Phi_{j+1}(0)}{dX_{j+1}} = \frac{d\Phi_j(R_j)}{dX_j} + \theta_j\frac{d^2\Phi_j(R_j)}{dX_j^2}; \tag{13}$$
$$\frac{d^2\Phi_{j+1}(0)}{dX_{j+1}^2} = \frac{d^2\Phi_j(R_j)}{dX_j^2},$$
$$\frac{d^3\Phi_{j+1}(0)}{dX_{j+1}^3} = \frac{d^3\Phi_j(R_j)}{dX_j^3}; \tag{14}$$

where θ_j is the dimensionless jth crack flexibility. $\theta_j = 5.346h \cdot J\left(\frac{a_j}{h}\right)$ and a_j is the depth of the jth crack. $J\left(\frac{a_j}{h}\right)$ is the dimensional local compliance function,[6,15] given by

$$J\left(\frac{a_j}{h}\right) = 1.8624r_j^2 - 3.95r_j^3 + 16.37r_j^4 - 37.226r_j^5 + 76.81r_j^6 - 126.9r_j^7 + 172r_j^8 - 43.97r_j^9 + 66.56r_j^{10}; \tag{15}$$

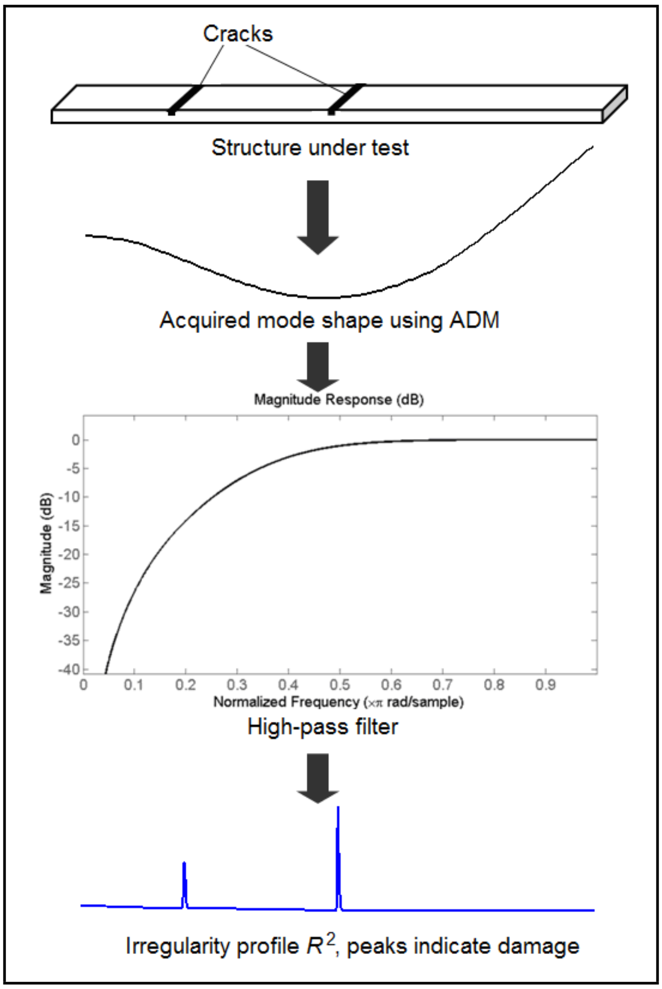

Figure 2. Damage detection procedure using high-pass filter.

where r_j is the dimensionless depth of the jth crack, $r_j = \frac{a_j}{h}$.

Substituting Eqs. (13) and (14) into Eq. (9), the mode shapes for the section-j ($j \geq 0$) can be written as

$$\Phi_{j+1}(X_{j+1}) = \Phi_j(R_j)\sum_{m=0}^{M-1}\left[\Omega^{4m}\frac{X_{j+1}^{4m}}{(4m)!}\right] + \left[\frac{d\Phi_j(R_j)}{dX_j} + \theta_j\frac{d^2\Phi_j(R_j)}{dX_j^2}\right]\sum_{m=0}^{M-1}\left[\Omega^{4m}\frac{X_{j+1}^{4m+1}}{(4m+1)!}\right] + \frac{d^2\Phi_j(R_j)}{dX_j^2}\sum_{m=0}^{M-1}\left[\Omega^{4m}\frac{X_j^{4m+2}}{(4m+2)!}\right] + \frac{d^3\Phi_j(R_j)}{dX_j^3}\sum_{m=0}^{M-1}\left[\Omega^{4m}\frac{X_{j+1}^{4m+3}}{(4m+3)!}\right]. \tag{16}$$

Notice that there are only three unknown parameters ($\Phi_0(0)$, $\frac{d\Phi_0(0)}{dX_0}$, and Ω) in Eq. (16) in a recursive way. By substituting Eqs. (16) into Eqs. (11) and (12), this boundary condition equation can be expressed as linear functions of $\Phi_0(0)$ and $\frac{d\Phi_0(0)}{dX_0}$, such as

$$f_{11}(\Omega)\Phi_0(0) + f_{12}(\Omega)\frac{d\Phi_0(0)}{dX_0} = 0; \tag{17}$$

$$f_{21}(\Omega)\Phi_0(0) + f_{22}(\Omega)\frac{d\Phi_0(0)}{dX_0} = 0. \tag{18}$$

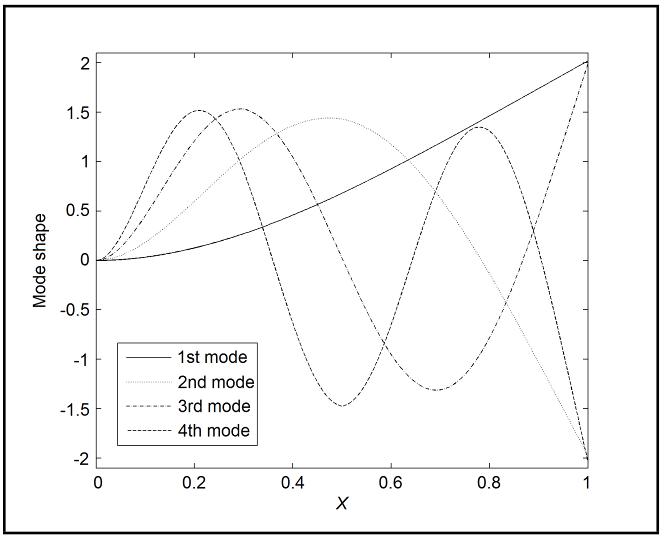

Figure 3. The first four mode shapes of the cantilever beam with two cracks.

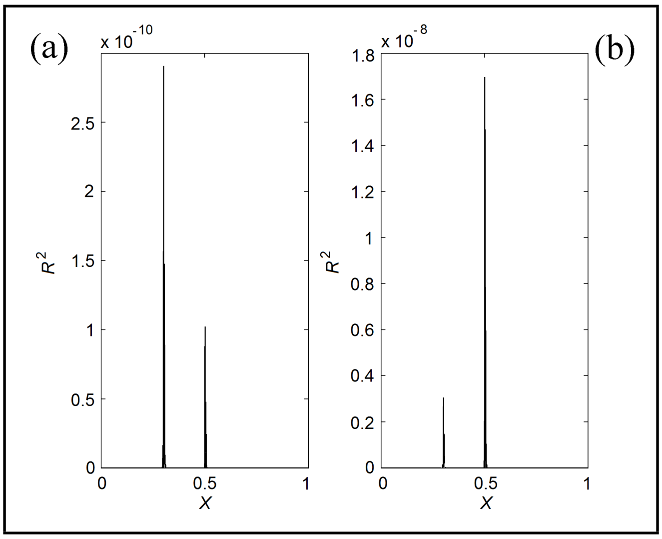

Figure 4. The irregularity profile R^2 for (a) the first mode shape; (b) the second mode shape.

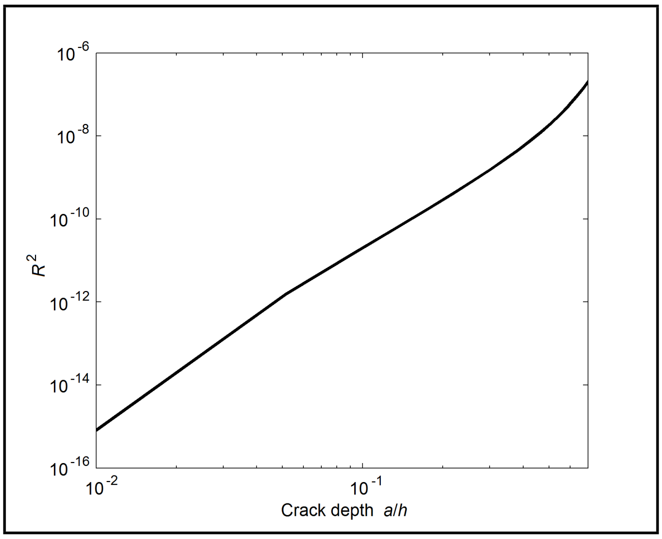

Figure 5. The peak R^2 value of the first mode varies with the second crack depth.

From Eqs. (17) and (18), the dimensionless natural frequency Ω can be solved by

$$f_{11}(\Omega)f_{22}(\Omega) - f_{12}(\Omega)f_{21}(\Omega) = \sum_{n=0}^{N} S_n\Omega^n = 0. \quad (19)$$

Notice that Eq. (19) is a polynomial of degree N evaluated at Ω. By using the functions `sym2poly` and `roots` in the MATLAB Symbolic Math Toolbox, Eq. (19) can be directly solved. The next step is to determine the nth mode shape function corresponding to the nth dimensionless natural frequency $\Omega(n)$. Substituting the solved $\Omega(n)$ into Eq. (17) or (18), the unknown parameter $\frac{d\Phi_0(0)}{dX_0}$ can be expressed as the function of $\Phi_0(0)$, as follows:

$$\frac{d\Phi_0(0)}{dX_0} = -\frac{f_{11}(\Omega)}{f_{12}(\Omega)}\Phi_0(0) = -\frac{f_{21}(\Omega)}{f_{22}(\Omega)}\Phi_0(0). \quad (20)$$

Substituting Eq. (20) into Eqs. (12) and (16), the mode shape function for each section can be obtained. The mode shape function for the entire beam can be written as

$$\Phi(X) = \big[\Phi_0(X_0) \ \ \Phi_1(X_1) \ \ \ldots \ \ \Phi_J(X_J)\big]. \quad (21)$$

It should be noted that the proposed method can be used to analyse the vibration of beams consisting of an arbitrary number of cracks in a recursive way, and the complexity of the vibration is the same order of a uniform beam without any cracks. The solution can be obtained by solving a set of algebraic equations with only three unknowns, and the resultant problem is significantly simpler compared to the one obtained through a traditional way.

3. DAMAGE DETECTION USING HIGH-PASS FILTER

It has been demonstrated that the mode shapes of the damage structures consist the irregularities induced by the damage. The mode shapes of the damage structures $\Phi(x)$ can be expressed as

$$\Phi(x) = \Phi_h(x) + R(x); \quad (22)$$

where $\Phi_h(x)$ is the mode shape for the health structure, $R(x)$ is the irregularity curve due to the damage, and $R^2(x)$ is termed as the irregularity profile,[15] which is used as a damage index (DI) throughout this study.

However, it is impossible to directly observe the irregularity profile R^2 from the mode shape only. The irregularities on the mode shapes should be amplified and separated to determine the locations and sizes of damages. In this study, the irregularities on the mode shapes are extracted through the separation of damage information in frequency domain rather than traditional spatial domain. It was found that the irregularities due to damage create an additional high-frequency component in the amplitude spectrum of the mode shapes that is not present in the health structures.[23] This means that it is possible to extract the irregularities of the mode shapes by using high-pass filters. The basic idea of the damage detection procedure is shown in Fig. 2.

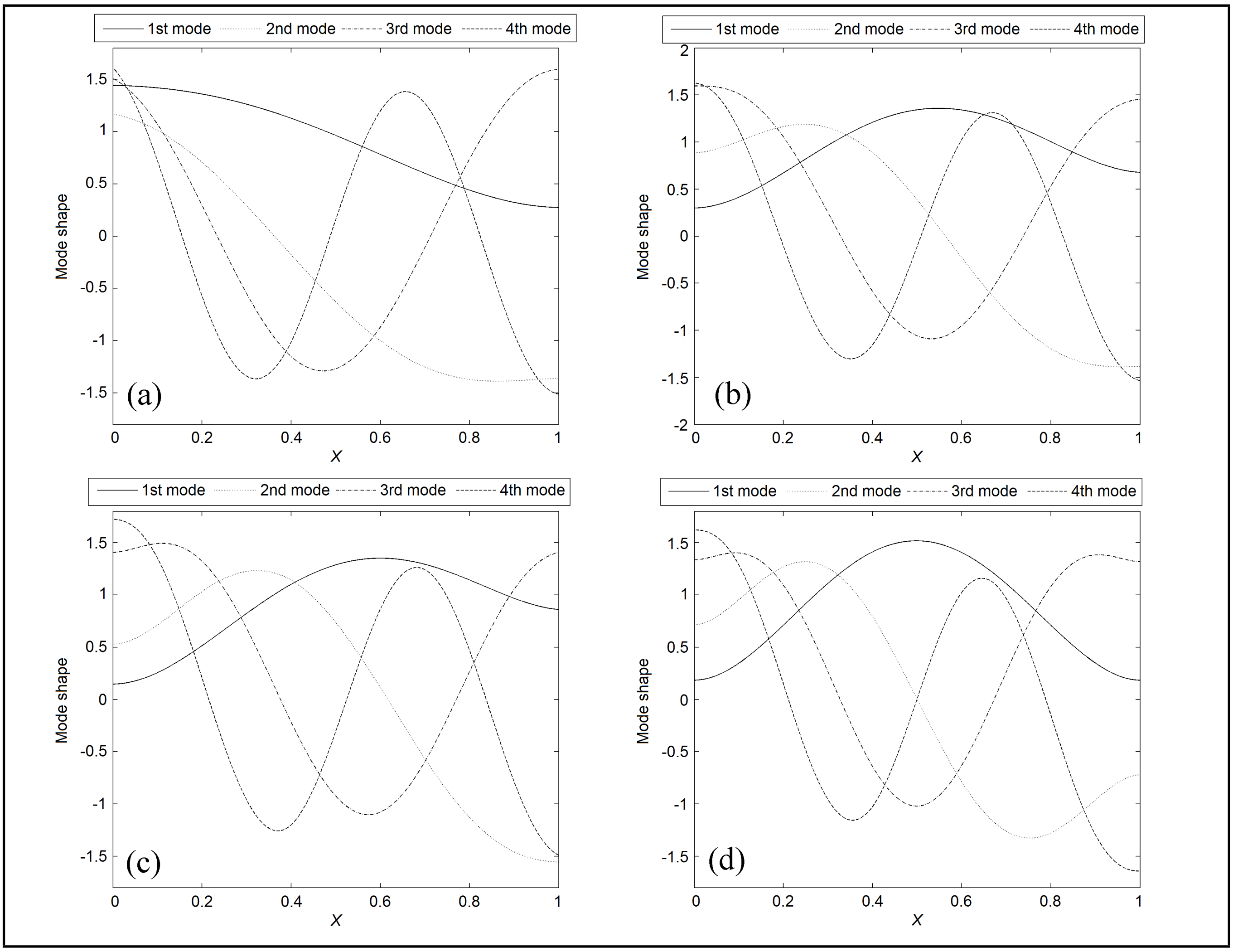

Figure 6. The first four mode shapes for the two-cracked beam with different boundary conditions (Other parameters listed in Table 1): (a) $K_{T0} = 10$, $K_{R0} = 20$, $K_{TJ} = 100$, $K_{RJ} = 200$; (b) $K_{T0} = 400$, $K_{R0} = 300$, $K_{TJ} = 200$, $K_{RJ} = 100$; (c) $K_{T0} = 700$, $K_{R0} = 600$, $K_{TJ} = 150$, $K_{RJ} = 50$; (d) $K_{T0} = K_{R0} = K_{TJ} = K_{RJ} = 1000$.

4. NUMERICAL CALCULATIONS

4.1. A Cantilever Beam with Two Cracks

In order to verify the proposed method for damage detection, a cantilever aluminium beam with two cracks at a distance of $0.3L$ and $0.5L$ from the clamped end, respectively, is considered firstly. The relative depths of these two cracks are the same and chosen as $a/h = 0.1$. The beam under analysis has the following properties: length $L = 0.51$ m, rectangular cross-section with width $b = 0.03$ m, and thickness $h = 0.004$ m. A 3rd-order high-pass Butterworth filter is used to extract the irregularity profile. Figure 3 shows the first four mode shapes for the cracked beams. From Fig. 3, no effects from the cracks can be observed in the mode shape. Figure 4 shows the extracted irregularities profile R^2 of the first and second modes. From Fig. 4, it can be found that the locations of the cracks can be determined using the irregularity profile.

To study the ability of the proposed method to detect crack depth, it was assumed that the location and depth of the first crack location are $R_1 = 0.1$ and $r_1 = 0.1$, respectively. Figure 5 shows the effect of the depths of the peak R^2 values of the first mode at the second crack location. From Fig. 5, it can be seen that the peak R^2 value is larger when the crack depth is increased. This means that the peak R^2 value can be applied as a criterion for crack depth.

4.2. Two Cracks Beam under General Boundary Conditions

Because the proposed method based on the ADM technique offers a unified and systematic procedure for vibration analysis of the cracked beam with arbitrary boundary conditions, the calculation of the natural frequencies and corresponding mode shapes for different boundary conditions can be very easy. For example, the modification of boundary conditions from one case to another is as simple as changing the values of the stiffness of translational and rotational springs. And it does not involve any changes to the solution procedures or algorithms. Table 1 lists the first four dimensionless natural frequencies $\Omega(n)$ for the beam with two cracks with different boundary conditions. Figure 6 shows the first four corresponding mode shapes for the cracked beams listed in Table 1. Figure 7 shows the extracted irregularities profile R^2 of the first mode under different boundary conditions. In all cases, the cracks can be

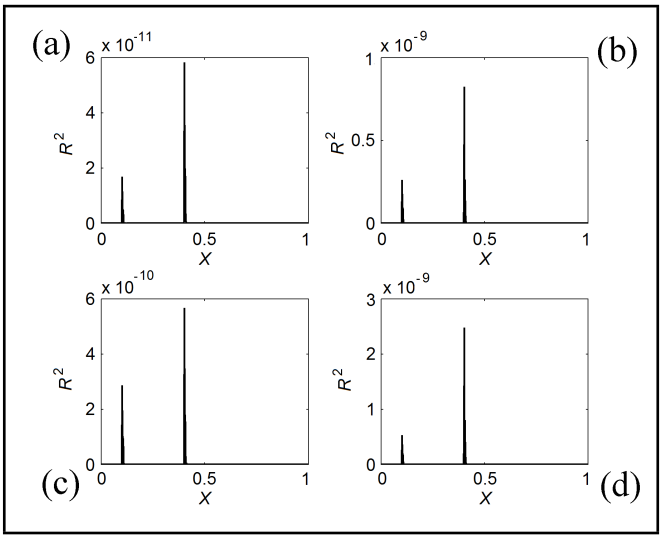

Figure 7. The irregularities profile R^2 of the first mode under different boundary conditions shown in Fig. 6.

easily detected from the irregularity profiles.

5. EXPERIMENTAL VERIFICATION

5.1. Experiment Setup

To verify the above damage detection results, a set of laboratory experiments was performed to examine its effectiveness for real measurement data. Two applications including the cantilever beams with one crack and two cracks are illustrated. Two aluminium cantilever beams with dimensions $600 \times 30 \times 4$ mm, Young's modulus $E = 70 \times 10^9$ Pa, and density $\rho_s = 2700$ kg/m^3 are fabricated. The beams were clamped at one end and free at the other, and the effective length of both beams is 510 mm, as shown in Fig. 8(a). The cracks were made using a saw cut. The crack is located at 255 mm from the clamped end for the one-crack beam, and the crack locations are at 150 mm and 300 mm from the clamped end for the other beam. The depth of all through-width cut is about 1–1.5 mm.

It is well known that there are two methods for modal test using the impact hammer, i.e. a roving hammer or a roving accelerometer. In this study, all experiments were carried out with the roving impact hammer. The beams were excited by a moving hammer from Sinocera Piezotronics, Inc. (Yangzhou, China) with a plastic tip and a force transducer (with the sensitivity of 4 pC/N and a load range of 0–2000 N) at 17 points, equally spaced (every 30 mm) along the length of the beam. The excitation points were numbered from 1 to 17, starting from the fixed end. An accelerometer from Sinocera Piezotronics, Inc. with the weight of 28 g, sensitivity of 50 pC/g, and a frequency range of 0.5–6000 Hz is mounted at the opposite side of the 5th hammer excitation point (the distance of 150 mm from the clamped end) to measure the response of the beams. A SINOCERA dynamic signal analyser (with 4 channels, but only 2nd and 3rd channel used) is used to acquire the frequency response functions between force and the accelerations, as shown in Fig. 8(b). The square and exponential windows were used to filter the force and acceleration signals, respectively. Three measurements were taken for each impact location to help minimize variance errors. Finally, the post-processing software (N-MODAL) was used to obtain the modal parameters such as natural frequencies, damping ratios, and mode shapes. N-MODAL software contains two built-in curve-fitting methods: Peak Fit and Polynomial Fit. The Polynomial Fit method was used to extract the experimental modal parameters.

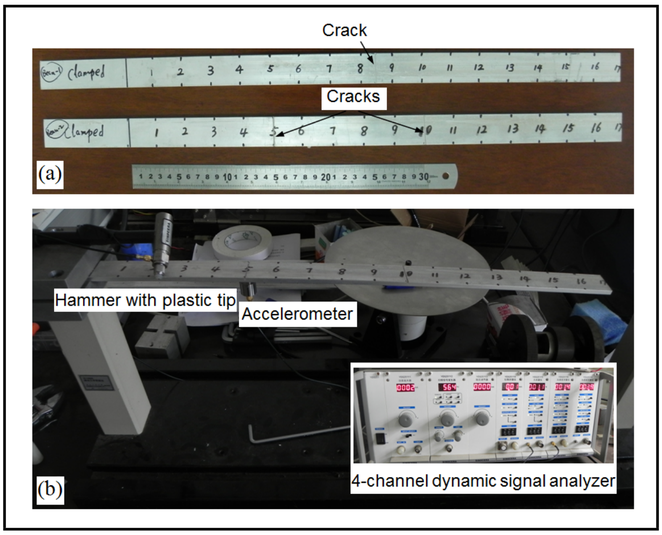

Figure 8. Photographs of (a) the cantilever beams; (b) experiment setup in the laboratory.

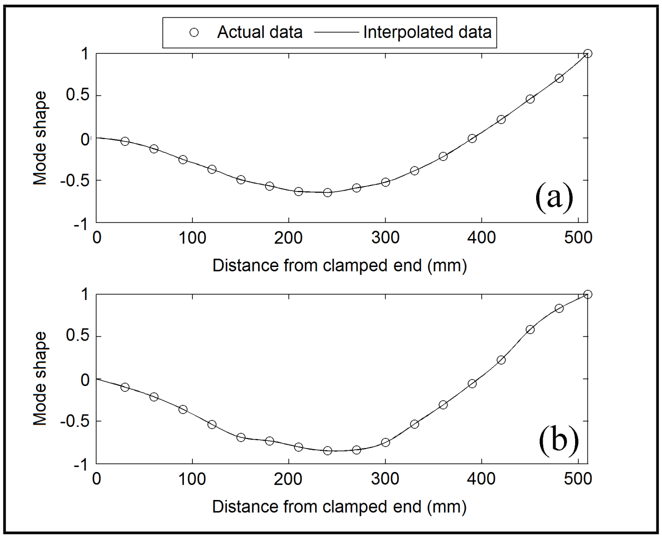

Figure 9. The interpolated mode shapes for the beam (a) with one crack at 255 mm, and (b) with two cracks at 150 mm and 300 mm.

5.2. Experimental Results

In brief, only the second measured modes of the beam with one and two cracks are used to extract the irregularity profile R^2. Notice that there are only 17 experimental measurement points, and if the high-pass filter is directly implemented, many points of the sample data would be detected as singularities. In this study, a cubic spline interpolation technique is applied to smooth the transition from one point to another. As a result, a total number of 200 interpolated points is obtained. Figure 9

Table 1. The first four dimensionless natural frequencies $\Omega(n)$ for a two-cracks beam under different boundary conditions (crack location $R_1 = 0.1$, $R_2 = 0.4$; crack depth $r_1 = 0.1$, $r_2 = 0.15$).

Stiffness of springs (Boundary conditions)				Mode index			
K_{T0}	K_{R0}	K_{TJ}	K_{RJ}	1	2	3	4
10	20	100	200	2.602601	4.221255	6.381824	9.281358
400	300	200	100	4.054168	5.662266	7.367550	9.749038
700	600	150	50	3.980091	5.712174	7.701976	9.916163
1000	1000	1000	1000	4.518749	6.915724	8.752670	10.635948

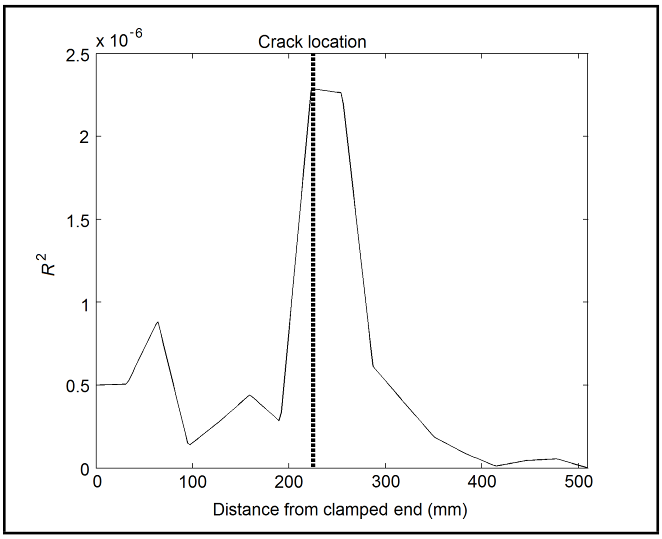

Figure 10. The irregularity profile R^2 for the beam with one crack at 255 mm.

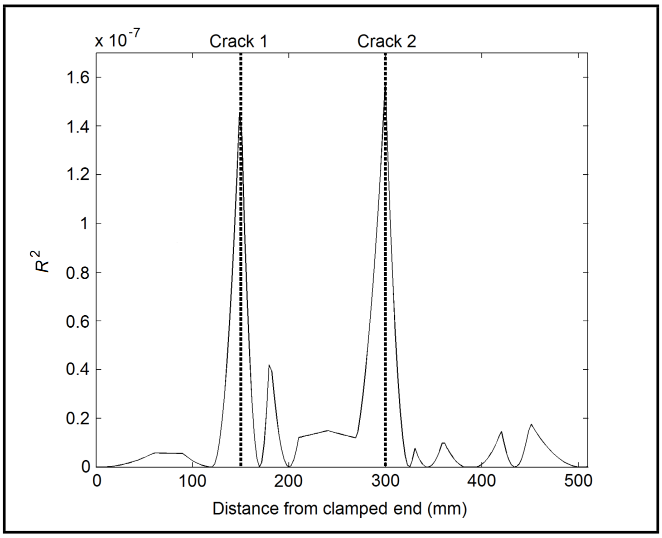

Figure 11. The irregularity profile R^2 for the beam with two cracks at 150 mm and 300 mm.

shows the interpolated mode shapes of the beam.

By using 3rd-order high-pass Butterworth filter, the irregularity profiles R^2 for the mode shapes shown in Fig. 9 are obtained and presented in Figs. 10 and 11. From Figs. 10 and 11, it can be seen that the largest peak values appear at the crack locations. This means that the proposed method based on high-pass filters can successfully detect the damage in actual tests.

6. CONCLUSIONS

In this study, the vibration of Euler-Bernoulli beams under different boundary conditions with an arbitrary number of cracks are analysed in a recursive way based on the Adomian decomposition method (ADM). Then the high-pass filters are introduced to detect the damage for beams under different boundary conditions. In this method, the mode shapes can be filtered and their irregularities due to damage are extracted. Furthermore, it is possible to determine the depth of a crack in beams by the peak value at the crack location of the irregularity profile. The main advantage of the proposed method is that the information of the undamaged structure is not required. To further validate the proposed method, the experimental damage detection was investigated using two aluminium cantilever beams with one and two cracks, respectively. The results demonstrate favourable feasibility and effectiveness of the proposed damage detection method.

ACKNOWLEDGEMENTS

This work was sponsored by the National Natural Science Foundation of China (no. 51265037, no. 11464031), the Technology Foundation of Jiangxi Province, China (no. KJLD12075), and the Aeronautical Science Foundation of China (no. 2015ZA56002)..

REFERENCES

[1] Adewuyi, A. P., Wu, Z., and Serker, N. H. M. K. Assessment of vibration-based damage identification methods using displacement and distributed strain measurements, *Structural Health Monitoring*, **8** (6), 443–461, (2009).

[2] Fan, W. and Qiao, P. Vibration-based damage identification methods: a review and comparative study, *Structural Health Monitoring*, **10** (1), 83–111, (2011).

[3] Salawu, O. S. Detection of structural damage through changes in frequency: a review, *Engineering Structures*, **19** (9), 718–723, (1997).

[4] Pandey, A. K., Biswas, M., and Samman, M. M. Damage detection from changes in curvature mode shapes, *Journal of Sound and Vibration*, **145** (2), 321–332, (1991).

[5] Wahab, M. M. A. and Roeck, G. D. Damage detection in bridges using modal curvatures: application to a real damage scenario, *Journal of Sound and Vibration*, **226** (2), 217–235, (1999).

[6] Qiao, P. and Cao, M. Waveform fractal dimension for mode shaped-based damage identification of beam-type structures, *International Journal of Solids and Structures*, **45** (22–23), 5946–5961, (2008).

[7] Ismail, Z., Razak, H. A., and Rahman A. G. A. Determination of damage location in RC beams using mode shape derivatives,. *Engineering Structures*, **28**, 1566–1573, (2006).

[8] Zhong, S. and Oyadiji, S. O. Crack detection in simply supported beams without baseline modal parameters by stationary wavelet transform, *Mechanical Systems and Signal Processing*, **21** (4), 1853–1884, (2007).

[9] Fan W. and Qiao, P. A 2-D continuous wavelet transform of mode shape data for damage detection of plate structures, *International Journal of Solids and Structures*, **46** (25–26), 4379–4395, (2009).

[10] Ratcliffe, C. and Bagaria W. Vibration technique for locating delamination in a composite beam, *AIAA Journal*, **36** (6), 1074–1077, (1998).

[11] Ratcliffe, C. P. A frequency and curvature based experimental method for locating damage in structures, *ASME Transaction Journal of Vibration and Acoustics*, **122** (3), 324–329, (2000).

[12] Yoon, M. K., Heider, D., Gillespie, J .W., Ratcliffe, C. P., and Crane, R. M. Local damage detection using the two-dimensional gapped smoothing method, *Journal of Sound and Vibration*, **279** (1–2), 119–139, (2005).

[13] Yoon, M. K., Heider, D., Gillespie, J. W., Ratcliffe, C. P., and Crane, R. M. Local damage detection with the global fitting method using mode shape data in notched beams, *Journal of Non-destructive Evaluation*, **28** (2), 63–74, (2009).

[14] Zhang, Y., Lie, S. T., and Xiang, Z. Damage detection method based on operating deflection shape curvature extracted from dynamic response of a passing vehicle, *Mechanical System and Signal Processing*, **35**, 238–254, (2013).

[15] Wang, J. and Qiao P. On irregularity-based damage detection method for cracked beam, *International Journal of Solids and Structures*, **45**, 688–704, (2008).

[16] Bazardehi, S. R. K. and Kouchakzadeh, M. A. Detection of delamination in cross-ply composite-laminated beams utilizing irregularity of mode shapes, *Proceedings of the IMechE, Part G: Journal of Aerospace Engineering*, **225** (12), 1302–1309, (2011).

[17] Bazardehi, S. R. K. and Kouchakzadeh, M. A. Detection of delamination in composite laminated plates using filtered mode shapes, *Proceedings of the IMechE, Part C: Journal of Mechanical Engineering Science*, **226** (12), 2902–2911, (2012).

[18] Adomian G. *Solving frontier problems of physics: the decomposition method*, Kluwer-Academic Publishers, Boston, (1994).

[19] Mao, Q. and Pietrzko, S. Design of shaped piezoelectric modal sensor for beam with arbitrary boundary conditions by using Adomian decomposition method, *Journal of Sound and Vibration*, **329**, 2068–2082, (2010).

[20] Mao, Q. Free vibration analysis of elastically connected multiple-beams by using the Adomian modified decomposition method, *Journal of Sound and Vibration*, **331** (11), 2532–2542, (2012).

[21] Mao, Q. Free vibration analysis of multiple-stepped beams by using Adomian decomposition method, *Mathematical and Computer Modelling*, **54** (1–2), 756–764, (2012).

[22] Mao, Q. and Pietrzko, S. Free vibration analysis of a type of tapered beams by using Adomian decomposition method, *Applied Mathematics and Computation*, **219** (6), 3264–3271, (2012).

[23] Sazonov, E. S., Klinkhachorn, P., Halabe, U. B., and Gangarao, H. V. S. Non-baseline detection of small damages from changes in strain energy mode shapes, *Non-destructive Testing and Evaluation*, **18** (3–4), 91–107, (2003).

Vibration Analysis of Non-homogenous Orthotropic Visco-elastic Rectangular Plate of Parabolically Varying Thickness with Thermal Effect

Pooja Singhal

Department of Mathematics, P.C.E.T., Lalru- 140501, Punjab, India

Arun Kumar Gupta

Department of Mathematics, M.S. College, Saharanpur- 247001, UP, India

(Received 25 March 2014; accepted 25 August 2015)

The present work analyses the vibration behaviour of non-homogeneous orthotropic visco-elastic rectangular plate of parabolically varying thickness on the basis of classical plate theory when the all edges are clamped and are subjected to linearly thermal variation. For non-homogeneity of the plate material it is assumed that the density of the plate material varies parabolically along the x-direction. For visco-elastic materials, basic elastic and viscous elements are combined. The Kelvin model for visco-elasticity is considered here, which is a combination of elastic and viscous elements connected in parallel. Using the separation of variable method, the governing differential equation has been solved. The time period and deflection corresponding to the first two modes of vibrations of clamped plates have been calculated for different values of thermal gradients, non-homogeneity constants, taper constants, and aspect ratio, with the help of Rayleigh-Ritz techniques, and are shown by graphs.

1. INTRODUCTION

The thermal effect of non-homogenous viscoelastic plates on vibration is of great interest in the field of engineering, with applications such as improved designing of gas turbines, jet engines, space craft, and nuclear power projects, where metals and their alloys exhibit visco-elastic behaviour. Therefore, for these reasons, such structures are exposed to high-intensity heat fluxes, and thus the material properties undergo significant changes. In particular, the thermal effect of elasticity of the material on the modules cannot be taken as negligible.

Space technology is developing very rapidly in the present era, and the importance of studying the vibration of plates of certain aspect ratios with some simple restraints on the boundaries has increased. The motors of rockets and aircraft in cold regions are developed with the use of soft filaments in aerospace structure supported with elastic or visco-elastic media. When finalising a design, a construction engineer should understand the first few modes of vibration, as they are significant.

Plates of variable thickness have been extensively used in civil, electronic, mechanical, aerospace, and marine engineering applications. The practical importance of such plates has made vibration analysis essential, especially since the vibratory response needs to be accurately determined in the design process in order to avoid resonance excited by internal or external forces.

The plate type's structural components in aircraft and rockets have to operate under elevated temperatures that cause non-homogeneity in the plate material, i.e. elastic constants of the materials become functions of space variables. An up-to-date survey of the research in this area shows that authors have come across various models to account for non-homogeneity of plate materials, and many researchers have proposed dealing with vibration. However, none of them consider non-homogeneity with a thermal effect on orthotropic visco-elastic plates of parabolically varying thickness.

The term vibration describes repetitive motion that can be measured and observed in a structure. Unwanted vibration can cause fatigue or degrade the performance of the structure. Therefore, it is desirable to eliminate or reduce the effects of vibration. In other cases, the goal may be to understand the effect of vibration on the structure, to control or modify the vibration, or to isolate it from the structure and minimise the structural responses.

Vibration can be sub-categorised, such as free versus forced vibration, sinusoidal versus, and linear versus rotation-induced vibration. Free vibration is the natural response of a structure to some impact or displacement. The response is completely determined by the properties of the structure, and its vibration can be understood by examining the structures mechanical properties. For example, when we pluck the string of a guitar, it vibrates at the tuned frequency and generates the desired sound. The frequency of the tone is a function of the tension in string and is not related to the plucking technique.

A great deal of research informs the study presented here. Laura, et al. discussed transverse vibrations of rectangular plates with thickness varying in two directions and with edges elastically restrained against rotation.[1] Leissas monograph[2] contains an excellent discussion of the subject of vibrating plates with elastic edge support. Gupta and Singhal discussed the effect of non-homogeneity on the thermally-induced vibration of an orthotropic visco-elastic rectangular plate of linearly varying thickness.[3] Lal has studied the transverse vibrations of orthotropic non-uniform rectangular plates with continuously varying density.[4] Sobotka examined the free vibration of visco-elastic orthotropic rectangular plates.[5] Singh and Saxena analysed the transverse vibration of rectangular plates with bi-directional thickness variation.[6] Bambill, et al. studied the transverse vibrations of an orthotropic rectangular plate of linearly varying thickness and a free edge.[7] Tomar and Gupta solved the vibration problem of an orthotropic rectangular plate of varying thickness subjected to a thermal gradient.[8–10]

Gupta, et al. discussed the vibration of non-homogeneous circular plate of nonlinear thickness variation by a quadrature method.[11] Gupta and Kumar studied the effect of exponential temperature variation on vibration of orthotropic rectangular plate with linearly thickness variation in both directions.[12] Gupta, et al. solved the problem of thermal effect on vibration of non-homogeneous orthotropic rectangular plate having bi-directional parabolically varying thickness.[13] Gupta and Khanna discussed vibration of viscoelastic rectangular plate with linearly thickness variations in both directions.[14] Laura and Gutierrez discussed vibration analysis of a rectangular plate subjected to a thermal gradient.[15] Gupta and Khanna solved the problem of vibrations of clamped visco-elastic rectangular plate with parabolic variable thickness.[16] Effect of thermal gradient on free vibration of clamped visco elastic plate was discussed by Gupta and Kaur.[17] Finally, Gupta and Kumar studied the thermal effect on vibration of orthotropic rectangular plate with parabolic thickness variations.[18]

The analysis presented in this chapter studies the effect of parabolic non-homogeneity on thermally-induced vibration of an orthotropic visco-elastic rectangular plate of parabolically varying thickness. It is clamp-supported on all four edges. The assumption of small deflection and linear orthotropic visco-elastic properties are made. It is further assumed that the visco-elastic properties of the plate are of the Kelvin type. The time period and deflection for the first two modes of vibration are calculated for the various values of thermal constants, non-homogeneity constants, aspect ratio, and taper constants. The results are shown graphically.

2. ANALYSIS

The equation of motion of a visco-elastic rectangular plate of variable thickness is as follows:[3]

$$\Big[D_x \tfrac{\partial^4 W}{\partial x^4} + D_y \tfrac{\partial^4 W}{\partial y^4} + 2H \tfrac{\partial^4 W}{\partial x^2 \partial y^2} + 2\tfrac{\partial H}{\partial x}\tfrac{\partial^3 W}{\partial x \partial y^2}$$
$$+2\tfrac{\partial H}{\partial y}\tfrac{\partial^3 W}{\partial x^2 \partial y} + 2\tfrac{\partial D_x}{\partial x}\tfrac{\partial^3 W}{\partial x^3} + 2\tfrac{\partial D_y}{\partial y}\tfrac{\partial^3 W}{\partial y^3} + \tfrac{\partial^2 D_x}{\partial x^2}\tfrac{\partial^2 W}{\partial x^2}$$
$$+\tfrac{\partial^2 D_y}{\partial y^2}\tfrac{\partial^2 W}{\partial y^2} + \tfrac{\partial^2 D_1'}{\partial x^2}\tfrac{\partial^2 W}{\partial y^2} + \tfrac{\partial^2 D_1'}{\partial y^2}\tfrac{\partial^2 W}{\partial x^2} + 4\tfrac{\partial^2 D_{xy}}{\partial x \partial y}\tfrac{\partial^2 W}{\partial x \partial y}\Big]$$
$$-\rho h p^2 W = 0; \tag{1}$$

and

$$\ddot{T} + p^2 \tilde{D} T = 0; \tag{2}$$

where Eqs. 1 and 2 are the differential equations of motion for an orthotropic plate of variable thickness, and the time function for visco-elastic orthotropic plate for free vibration, respectively. Here, p^2 is a constant, and $H = D_1' + 2D_{xy}$,
$D_x = \frac{E_x h^3}{12(1-v_x v_y)}$, is called the flexural rigidity of the plate in x-direction,
$D_y = \frac{E_y h^3}{12(1-v_x v_y)}$, is called the flexural rigidity of the plate in y-direction,
$D_{xy} = \frac{G_{xy} h^3}{12}$, is called the torsion rigidity,
$D_1' = v_x D_y (= v_y D_x)$, $\tilde{D}$ is the Rheological operator, E_x and E_y are the modules of elasticity in x- and y-directions, respectively, v_x and v_y are the Poisson ratios, and G_{xy} is the shear modulus.

The study assumes steady, one-dimensional temperature distribution along the length, i.e. the x-direction, for the plate as

$$\tau = \tau_0 \left(1 - \frac{x}{a}\right); \tag{3}$$

where τ denotes the temperature excess above the reference temperature at any point at distance $\frac{x}{a}$, and τ_0 denotes the temperature excess above the reference temperature at the end, i.e. $x = a$.

The temperature dependence of the modulus of elasticity for most engineering materials can be expressed in the following form:

$$\left.\begin{aligned} E_x &= E_1(1-\gamma\tau), \\ E_y &= E_2(1-\gamma\tau), \\ G_{xy} &= G_0(1-\gamma\tau) \end{aligned}\right\}. \tag{4}$$

Here, E_1 and E_2 are values of the Youngs moduli, respectively, along the x- and y-axis at the reference temperature, i.e. at $\tau = 0$, and γ is the slope of the variation of the modulus of elasticity with τ.

Thus, the modulus variation becomes

$$\left.\begin{aligned} E_x(x) &= E_1[1-\alpha(1-x/a)], \\ E_y(x) &= E_2[1-\alpha(1-x/a)], \\ G_{xy}(x) &= G_0[1-\alpha(1-x/a)] \end{aligned}\right\}; \tag{5}$$

where $\alpha = \gamma\tau_0 (0 \leq \alpha < 1)$, a parameter known as thermal gradient.

The expression for the strain energy V and kinetic energy P in the plate are:[2]

$$V = \frac{1}{2}\int_0^a \int_0^b \Big[D_x (W_{,xx})^2 + D_y (W_{,yy})^2 + 2D_1 W_{,xx} W_{,yy} + 4D_{xy}(W_{,xy})^2\Big] dxdy; \tag{6}$$

$$\mathrm{P} = \frac{1}{2}p^2 \int_0^a \int_0^b \rho h W^2 dxdy. \tag{7}$$

This study assumes that the thickness and density both vary parabolically in the x-direction, respectively; therefore, one can take

$$h = h_0 \left\{1 + \beta (x/a)^2\right\}; \tag{8}$$

and

$$\rho = \rho_0 \{1 + \alpha_1 (x/a)^2\}; \tag{9}$$

where β is the taper constant and α_1 is the non-homogeneity constant.

3. SOLUTION AND FREQUENCY EQUATION

The Rayleigh-Ritz technique has been utilised here for finding the solution. This method requires that the maximum strain energy must be equal to the maximum kinetic energy. So, it is necessary for the problem under consideration that

$$\delta(V-P)=0; \tag{10}$$

for arbitrary variations of W, satisfying the relevant geometrical boundary conditions, which are

$$\begin{aligned} W&=W_{,x}=0 \quad \text{at} \quad \mathrm{x}=0,\mathrm{a},\\ W&=W_{,y}=0 \quad \text{at} \quad \mathrm{y}=0,\mathrm{b}; \end{aligned} \tag{11}$$

and the corresponding two-term deflection function is taken as follows:[3]

$$\begin{aligned} W=&[(x/a)(y/b)(1-x/a)(1-y/b)]^2\\ &[A_1+A_2(x/a)(y/b)(1-x/a)(1-y/b)]. \end{aligned} \tag{12}$$

The non-dimensional variables are

$$\begin{aligned} X&=x/a, \quad Y=y/a,\\ \bar{W}&=W/a, \quad \bar{h}=h/a,\\ \bar{\rho}&=\rho/a\\ E_1{}^*&=E_1/(1-\nu_x\nu_y),\\ E_2{}^*&=E_2/(1-\nu_x\nu_y),\\ E^*&=\nu_x E_2*=\nu_y E_1{}^*. \end{aligned} \tag{13}$$

By using Eqs. 5, 8, 9, and 13 in Eqs. 6 and 7, one gets

$$P=\frac{1}{2}\rho_o p^2\bar{h_o}a^5\int_0^1\int_0^{b/a}\Big[(1+\alpha_1X^2)(1+\beta X^2)\bar{W}^2\Big]dXdY; \tag{14}$$

and

$$\begin{aligned} V=R\int_0^1\int_0^{b/a}&\Big[\{1-\alpha(1-X)\}(1+\beta X^2)^3\{(\overline{W}_{,XX})^2\\ &+(E_2{}^*/E_1{}^*)(\overline{W}_{,YY})^2+(2E^*/E_1{}^*)\overline{W}_{,XX}\overline{W}_{,YY}\\ &+(4G_o/E_1{}^*)(\overline{W}_{,XY})^2\}\Big]dXdY; \end{aligned} \tag{15}$$

where

$$R=\frac{1}{2}(E_1*\bar{h_o}^3/12)a. \tag{16}$$

Upon substituting the values of P and V from Eqs. 14 and 15 into Eq. 10, we get

$$\big(V_1-\lambda^2p^2P_1\big)=0 \tag{17}$$

$$\begin{aligned} V_1=\int_0^1\int_0^{b/a}&\Big[\{1-\alpha(1-X)\}(1+\beta X^2)^3\{(\overline{W}_{,XX})^2\\ &+(E_2{}^*/E_1{}^*)(\overline{W}_{,YY})^2+(2E^*/E_1{}^*)\overline{W}_{,XX}\overline{W}_{,YY}\\ &+(4G_o/E_1{}^*)(\overline{W}_{,XY})^2\}\Big]dXdY; \end{aligned} \tag{18}$$

and

$$P_1=\int_0^1\int_0^{b/a}\Big[\{1+\alpha_1X^2)\}(1+\beta X^2)\bar{W}^2\Big]dXdY; \tag{19}$$

where

$$\lambda^2=\frac{12a^4\rho_o}{E_1{}^*\bar{h_o}^2}. \tag{20}$$

Eq. 17 involves the unknowns A_1 and A_2, arising due to the substitution of $W(x,y)$ from Eq. 12. These two constants are to be determined from Eq. 17, as follows:

$$\frac{\partial}{\partial A_n}(V_1-\lambda^2p^2P_1)=0, \quad \text{where} \quad \mathrm{n}=1,2. \tag{21}$$

Upon simplifying Eq. 21 we get

$$b_{n1}A_1+b_{n2}A_2=0; \tag{22}$$

where $n=1,2$, and b_{n1}, b_{n2} involves parametric constants and the frequency parameter p. For a non-trivial solution, the determinant of the coefficient of Eq. 22 must be zero. So, we get the frequency as follows:

$$\begin{vmatrix} b_{11} & b_{12}\\ b_{21} & b_{22} \end{vmatrix}=0. \tag{23}$$

Upon solving Eq. 23, one gets a quadratic equation in p^2, which gives two values of p^2. Upon substituting the value of $A_1=1$, by choice, into Eq. 12, one gets $A_2=-b_{11}/b_{12}$, and hence W becomes

$$\begin{aligned} W=&[XY\frac{a}{b}(1-X)(1-Y\frac{a}{b})]^2\\ &[1+(-\frac{b_{11}}{b_{12}})XY(\frac{a}{b})(1-X)(1-Y\frac{a}{b})]. \end{aligned} \tag{24}$$

4. TIME FUNCTION OF VIBRATION OF VISCO-ELASTIC PLATES

The expression for the time function of free vibrations of visco-elastic plates of variable thickness can be derived from Eq. 2, which depends upon the visco-elastic operator $\tilde{D}$, and which for Kelvins Model, can be taken as follows:

$$\tilde{D}\equiv\left\{1+\left(\frac{\eta}{G}\right)\left(\frac{d}{dt}\right)\right\}; \tag{25}$$

where η is the visco-elastic constant and G is the shear modulus. Assuming that the temperature dependence of the visco-elastic constant η and the shear modulus G are in the same form as that of Youngs moduli, we have

$$G(\tau)=G_0(1-\gamma_1\tau), \quad \eta(\tau)=\eta_0(1-\gamma_2\tau); \tag{26}$$

where G_0 is the shear modulus, and η_0 is the visco-elastic constant at some reference temperature, i.e. at $\tau=0$, γ_1 and γ_2 are the slope variation of τ with G and η, respectively. Substituting the value of τ from Eq. 3, and using Eq. 13 in Eq. 26, one gets the following:

$$\begin{aligned} G&=G_0[1-\alpha_5(1-X)], \quad \text{where} \quad \alpha_5=\gamma_1\tau_0, 0\le\alpha_5<1\\ \eta&=\eta_0[1-\alpha_4(1-X)], \quad \text{where} \quad \alpha_4=\gamma_2\tau_0, 0\le\alpha_4<1. \end{aligned} \tag{27}$$

Here, α_4 and α_5 are thermal constants.

After using Eq. 25 in Eq. 2, one obtains the following:

$$\ddot{T}+p^2k\dot{T}+p^2T=0; \tag{28}$$

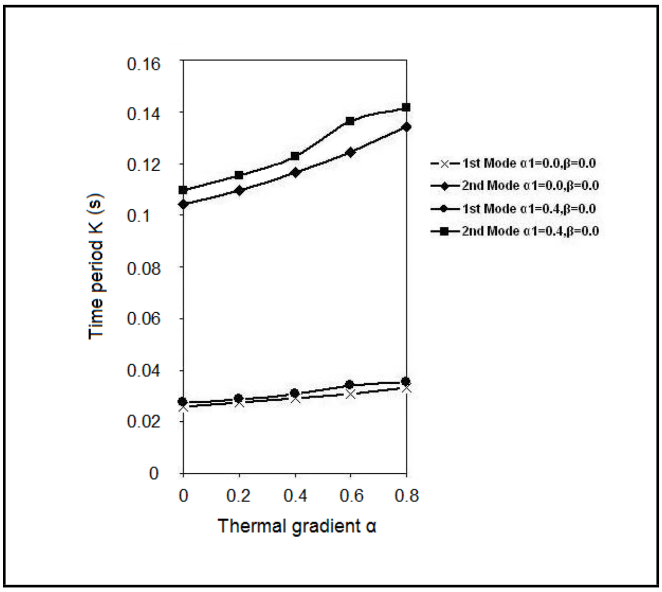

Figure 1. Variation of time period with thermal gradient of visco-elastic non-homogeneous orthotropic rectangular plate of linearly varying thickness.

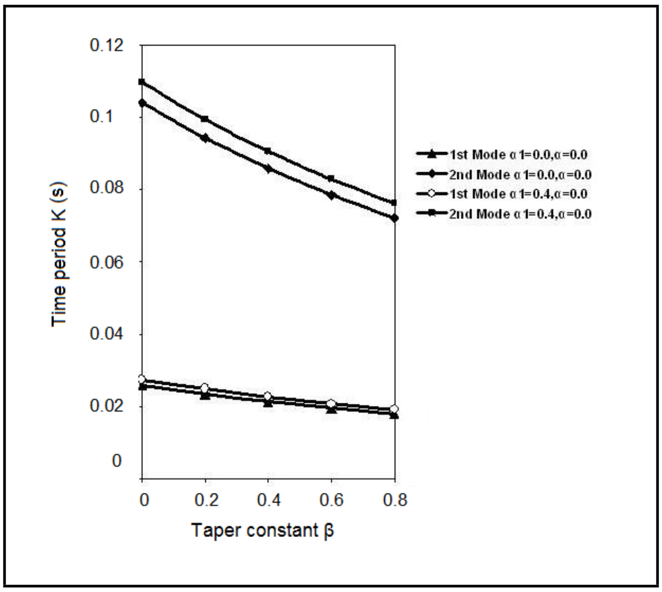

Figure 2. Variation of time period with taper constant of visco-elastic non-homogeneous orthotropic rectangular plate of linearly varying thickness.

where

$$k = \frac{\eta}{G} = \frac{\eta_0[1 - \alpha_4(1 - X)]}{G_0[1 - \alpha_5(1 - X)]}. \qquad (29)$$

Equation 28 is a differential equation of the second order for time function T. The solution of Eq. 28 will be

$$T(t) = e^{a_1 t}[C_1 \cos b_1 t + C_2 \sin b_1 t]; \qquad (30)$$

where

$$a_1 = -p^2 m/2; \qquad (31)$$

$$b_1 = p\sqrt{1 - (pm/2)^2}; \qquad (32)$$

and C_1 ,C_2 are constants, which can be determined easily from the initial conditions of the plate. This study assumes the initial conditions as

$$T = 1 \quad \text{and} \quad T = 0 \quad \text{at} \quad t = 0. \qquad (33)$$

Using Eq. 33 in Eq. 30, one obtains

$$C_1 = 1 \quad \text{and} \quad C_2 = -a_1/b_1. \qquad (34)$$

One has the equation

$$T(t) = e^{a_1 t}[\cos b_1 t + (-a_1/b_1) \sin b_1 t]; \qquad (35)$$

after using Eq. 34 in Eq. 30. Thus, the deflection of the vibrating mode $w(x, y, t)$, which is equal to $W(x, y)T(t)$, may be expressed as

$$\begin{aligned} w =&[XY(a/b)(1 - X)(1 - Ya/b)]^2 \\ &[1 + (-b_{11}/b_{12})XY(a/b)(1 - X)(1 - Ya/b)] \\ &\times[e^{a_1 t}\{\cos b_1 t + (-a_1/b_1) \sin b_1 t\}]; \end{aligned} \qquad (36)$$

by using Eq. 24 and Eq. 35. The time period of the vibration of the plate is given by the following:

$$K = 2\pi/p; \qquad (37)$$

where p is the frequency given by Eq. 23.

5. NUMERICAL EVALUATIONS

The values of the time period (K) and the deflection (w) (at two different instants of time) for a clamped visco-elastic orthotropic non-homogeneous rectangular plate for different values of the taper constant β, thermal gradients ($\alpha, \alpha_4, \alpha_5$), the non-homogeneity constant α_1, and the aspect ratio a/b at different points for first two modes of vibrations have been calculated.

The following orthotropic material parameters have been taken as[2]

- $E_2^*/E_1^* = 0.32$
- $E^*/E_1^* = 0.04$
- $G_0/E_1^* = 0.09$
- $\eta_0/G_0 = 0.000069$
- $\rho_0 = 3 \times 10^5$ (mass density per unit volume of the plate material)

The thickness of the plate at the centre is taken as $h_0 = 0.01$ meter.

6. RESULTS AND DISCUSSION

The numerical results for a visco-elastic orthotropic non-homogeneous rectangular plate of parabolically varying thickness have been computed with accuracy by using latest computer technology. Computations have been made for calculating the time period K and deflection W (at two different instants of time) for different values of the taper constant β, thermal constants ($\alpha, \alpha_4, \alpha_5$), non-homogeneity constant α_1, and the aspect ratio a/b at different points for first two modes of vibration. All these results are presented in Figs. 1 – 8. A comparison is made with the authors previous work[3] for a uniform plate, and is found to be in very close agreement.

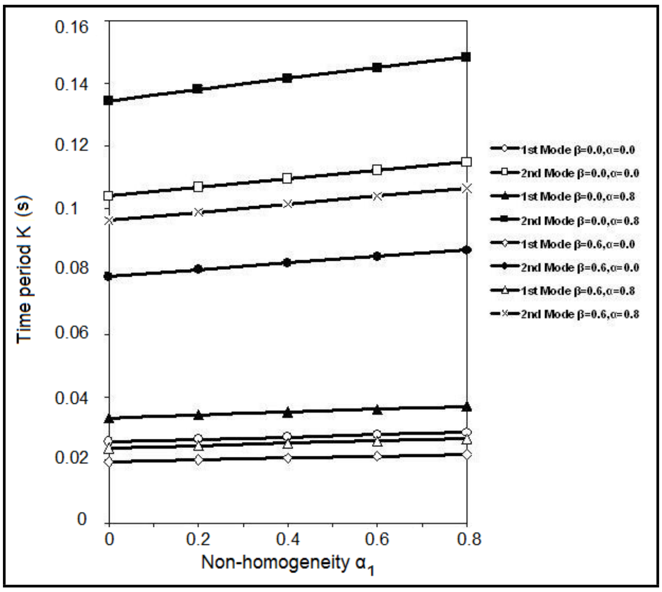

Figure 3. Variation of time period with non homogeneity constant of visco-elastic non-homogeneous orthotropic rectangular plate of linearly varying thickness.

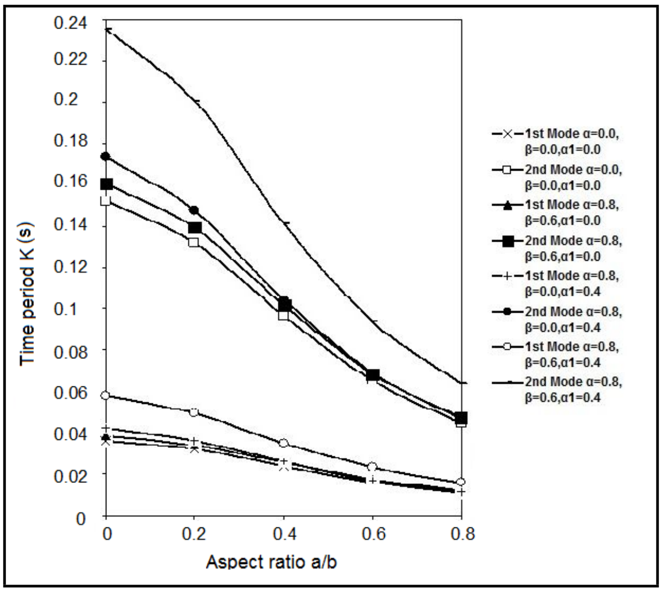

Figure 4. Variation of time period with non aspect ratio of visco-elastic non-homogeneous orthotropic rectangular plate of linearly varying thickness.

- Figure 1 shows the results of the time period (K) for different values of the thermal gradient (α), and the fixed taper constant $\beta = 0.0$ and aspect ratio $a/b = 1.5$ for two values of the non-homogeneity constant (α_1); i.e. $\alpha_1 = 0.0$ and $\alpha_1 = 0.4$ for the first two modes of vibration.

- Figure 2 shows the results of the time period (K) for different values of the taper constant (β), and the fixed thermal gradient $\alpha_1 = 0.0$ and aspect ratio $a/b = 1.5$ for two values of the non-homogeneity constant (α_1); i.e. $\alpha_1 = 0.0$ and $\alpha_1 = 0.4$ for the first two modes of vibration.

- Figure 3 shows the results of the time period (K) for first two modes of vibration for different values of the non-homogeneity constant (α_1), aspect ratio ($= 1.5$), and four combinations of the taper constant (β) and thermal gradient (α); i.e.
  $\beta = 0.0, \quad \alpha = 0.0$
  $\beta = 0.0, \quad \alpha = 0.8$
  $\beta = 0.6, \quad \alpha = 0.0$
  $\beta = 0.6, \quad \alpha = 0.8$
  It can be seen that time period (K) increases when the non-homogeneity constant (α_1) increases for first two modes of vibration.

- Figure 4 shows the results of the time period (K) for different aspect ratios (a/b), and four combinations of the thermal gradient (α), the taper constant (β), and the non-homogeneity constant (α_1); i.e.
  $\alpha = 0.8, \quad \beta = 0.6, \quad \alpha_1 = 0.0;$
  $\alpha = 0.8, \quad \beta = 0.6, \quad \alpha_1 = 0.4;$
  $\alpha = 0.0, \quad \beta = 0.0, \quad \alpha_1 = 0.0;$
  $\alpha = 0.8, \quad \beta = 0.0, \quad \alpha_1 = 0.4$
  It can be seen that time period (K) decreases when aspect ratio (a/b) increases for first two modes of vibration.

- Figure 5 – 8 show the result of deflection for the first two modes of vibration for different X, Y, and fixed aspect ratio $a/b = 1.5$ for the initial time 0.K and time 5.K for the following combination of thermal gradients (α, α_4, α_5), the taper constant β, and the non-homogeneity constant α_1.

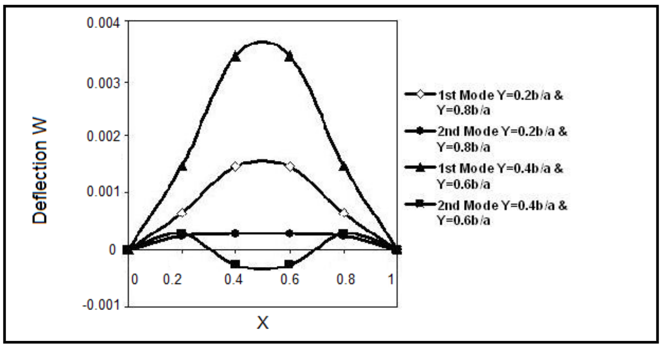

Figure 5. Deflection w vs X of visco-elastic non homogeneus orthotropic rectangular plate of linearly varying thickness at initial time 0.K.

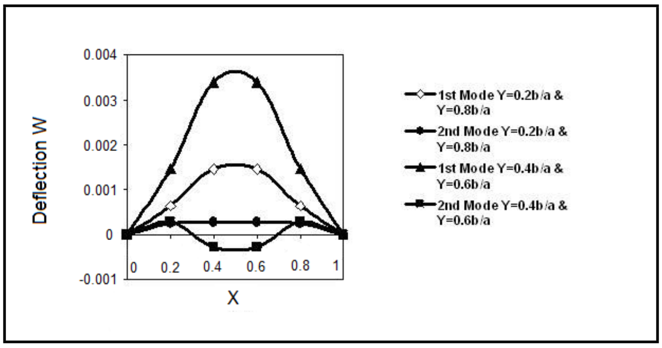

Figure 6. Deflection w vs X of visco-elastic non homogeneus orthotropic rectangular plate of linearly varying thickness at time 0.K.

- Figure 5: $\alpha = 0.0, \quad \beta = 0.6, \quad \alpha_1 = \alpha_4 = \alpha_5 = 0.0,$ and the time is 0.K.

- Figure 6: $\alpha = 0.8, \quad \beta = 0.6, \quad \alpha_1 = \alpha_4 = \alpha_5 = 0.0,$ and the time is 0.K.

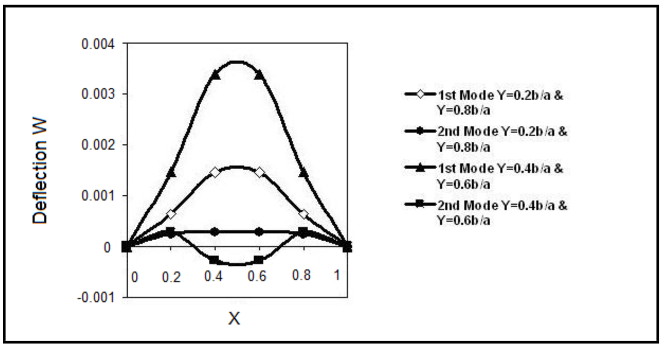

Figure 7. Deflection w vs X of visco-elastic non homogeneus orthotropic rectangular plate of linearly varying thickness at time 5.K.

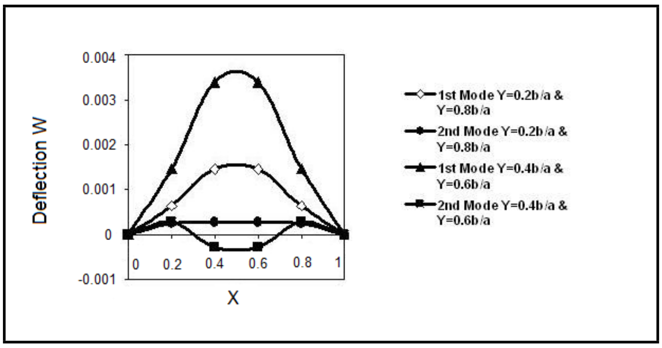

Figure 8. Deflection w vs X of visco-elastic non homogeneus orthotropic rectangular plate of linearly varying thickness at time 5.K.

- Figure 7: $\alpha = 0.0$, $\beta = 0.0$, $\alpha_1 = 0.0$, $\alpha_4 = 0.3$, $\alpha_5 = 0.2$, and the time is 5.K.
- Figure 8: $\alpha = 0.8$, $\beta = 0.6$, $\alpha_1 = 0.4$, $\alpha_4 = 0.3$, $\alpha_5 = 0.2$, and the time is 5.K.

REFERENCES

[1] Laura, P. A. A., Grossi, R. O., and Carneiro, G. I. Transverse vibrations of rectangular plates with thickness varying in two directions and with edges elastically restrained against rotation, *Journal of Sound and Vibration*, **63** (4), 499–505, (1979).

[2] Leissa, A. W. NASA SP-60, Vibration of Plate, (1969).

[3] Gupta, A. K. and Singhal, P. Effect of non-homogeneity on thermally induced vibration of orthotropic visco-elastic rectangular plate of linearly varying thickness, *Applied Mathematics*, **1** (4), 326–333, (2010).

[4] Lal, R. Transverse vibrations of orthotropic non-uniform rectangular plate with continuously varying density, *Indian Journal of Pure and Applied Mathematics*, **34**, 587–606, (2003).

[5] Sobotka, Z. Free vibration of visco-elastic orthotropic rectangular plates, *Acta Technica CSAV*, 6, 678–705, (1978).

[6] Singh, B. and Saxena, V. Transverse vibration of rectangular plate with bi-directional thickness variation, *Journal of Sound and Vibration*, **198**, 51–65, (1996).

[7] Bambill, D. V., Rossil, C. A., Laura, P. A. A., and Rossi, R. E. Transverse vibrations of an orthotropic rectangular plate of linearly varying thickness and with a free edge, *Journal of Sound and Vibration*, **235** (3), 530–538, (2000).

[8] Tomar, J. S. and Gupta, A. K. Effect of thermal gradient on frequencies of orthotropic rectangular plate whose thickness varies in two directions, *Journal of Sound and Vibration*, **98** (2), 257–262, (1985).

[9] Tomar, J. S. and Gupta, A. K. Thermal effect on frequencies of an orthotropic rectangular plate of linearly varying thickness, *Journal of Sound and Vibration*, **90** (3), 325–331, (1983).

[10] Tomar, J. S. and Gupta, A. K. Effect of exponential temperature variation on frequencies of an orthotropic rectangular plate of exponentially varying thickness, *Proceeding of the workshop on Computer Application in Continuum Mechanics, March 11–13, Depts. of Math. U.O.R,* Roorkee, 183–188, (1986).

[11] Gupta, U. S., Lal, R., and Sharma, S. Vibration analysis of non-homogenous circular plate of nonlinear thickness variation by differential quadrature method, *Journal of Sound and Vibration*, **298** (4–5), 892–906, (2006).

[12] Gupta, A. K. and Kumar, S. Effect of exponential temperature variation on vibration of orthotropic rectangular plate with linearly thickness variation in both directions, *Pragyan-IT, IMS,* Dehradun (India), **6** (2), 39–45, (2008).

[13] Gupta, A. K., Johri, T., and Vats, R. P. Thermal effect on vibration of non-homogeneous orthotropic rectangular plate having bi-directional parabolically varying thickness, *Proceeding of International Conference in World Congress on Engineering and Computer Science 2007 (WCECS 2007)*, San Francisco, USA (24–26 October, 2007), 784–787, (2007).

[14] Gupta, A. K. and Khanna, A. Vibration of visco-elastic rectangular plate with linearly thickness variations in both directions, *Journal of Sound and Vibration*, **301** (3–5), 450–457, (2007).

[15] Laura, P. A. A. and Gutierrez, R. H. Vibration analysis on a rectangular plate subjected to a thermal gradient, *Journal of Sound and Vibration*, **72**, 263–264, (1980).

[16] Gupta, A. K. and Khanna, A. Vibration of clamped visco-elastic rectangular plate with parabolic thickness variations, *Shock and Vibration*, **15** (6), 713–723, (2008).

[17] Gupta, A. K. and Kaur, H. Study of the effect of thermal gradient on free vibration of clamped visco-elastic rectangular plates with linearly thickness variation in both directions, *Meccanica*, **43**, 449–458, (2008).

[18] Gupta, A. K. and Kumar, S. Thermal effect on vibration of orthotropic rectangular plate with parabolic thickness variations, *Acta Technica*, **55**, 315–325, (2010).

Characterisation of Major Fault Detection Features and Techniques for the Condition-Based Monitoring of High-speed Centrifugal Blowers

Samer Gowid

Department of Electronic, Electrical and systems Engineering, Faculty of Engineering, Loughborough University, UK

Department of Mechanical Engineering and Industrial Engineering, College of Engineering, Qatar University, Qatar

Roger Dixon

Department of Electronic, Electrical and systems Engineering, Faculty of Engineering, Loughborough University, UK

Saud Ghani

Department of Mechanical Engineering and Industrial Engineering, College of Engineering, Qatar University, Qatar

(Received 25 March 2014; accepted 30 September 2015)

This paper investigates and characterises the major fault detection signal features and techniques for the diagnostics of rotating element bearings and air leakage faults in high-speed centrifugal blowers. The investigation is based on time domain and frequency domain analysis, as well as on process information, vibration, and acoustic emission fault detection techniques. The results showed that the data analysis method applied in this study is effective, as it yielded a detection accuracy of 100%. A lookup table was compiled to provide an integrated solution for the developer of Condition-Based Monitoring (CBM) applications of centrifugal blowers. The major contribution of this paper is the integration and characterisation of the major fault detection features and techniques.

1. INTRODUCTION

Condition-Based Monitoring (CBM) is a strategy aimed at extending machine life, lowering maintenance cost, and increasing both productivity and profitability.[1] Unlike preventative maintenance, which is based on servicing a machine at scheduled intervals, CBM relies upon actual machine health condition to diagnose faults and to determine when the maintenance is required. The specific advantage of condition monitoring is that potential degradation or failure can be detected. This technique enables the user to take maximum advantage of the useful life of a component, such as a bearing, since the equipment can be left in service if its operational performance meets the desired performance standards.[2]

Centrifugal compressors are widely used in the industry, and in particular in the oil and gas industries, as they compress the propane and mixed refrigerants in the liquefaction process. A 15 HP industrial centrifugal blower was employed for the emulation of high-speed centrifugal blowers. Due to the similarity between centrifugal blowers and centrifugal compressors,[3] this work can be extended to centrifugal compressors and centrifugal equipment.

The global structure of the generally used monitoring system can be divided into three main sections: The first phase is data collection, with data reports gathered in a digital form. The second phase is acquisition, which entails calculation of the statistical values and functions in time and frequency domain with integrated data reduction by fault and operational pattern. The more difficult third phase of automatic fault diagnostics is still under development and permanently adapted to the necessities of industrial applications, mainly dependent on the acting personnel at the monitoring system.[4]

Machine condition, machine faults, and on-going damage can be identified in operating machines by fault symptoms and signatures. Mechanical vibration, acoustic emission (AE), and process information are the three major fault detection techniques in addition to monitoring changes in process operating parameters, such as pressure, temperatures, and efficiency. Thus, this study will provide a characteristics investigation based on these major techniques, which should be included in any full capabilities condition-based maintenance system. Integrating these techniques can yield early detection and trending of numerous equipment faults. Moreover, it could have a potential to reduce false alarms due to noise and fault interference issues.

Vibrations of machines are the results of the dynamic forces due to moving parts and structures (for example, foundations), which are interlinked to the machine and its mechanical properties. All machine components generate specific vibration signatures which are then transmitted to the machine's structure. Vibration analysis detects repetitive motions of a surface on rotating or oscillating machines. The repetitive motions may be caused by unbalance, misalignment, resonance, electrical effects, rolling element bearing faults, or many other problems. The various vibration frequencies in a rotating machine are directly related to the geometry and the operating speed of the machine. By knowing the relationship between the frequencies and the types of defects, vibration analysts can determine the cause and severity of faults or problem conditions. The history of the machine and the previous degradation pattern are important factors in determining the current and future operating condition of the machine. Frequency, displacement, velocity acceleration, and phase angle are the major five characteristics of rotating machine vibration.[5]

Unlike the mechanical vibration technique, the AE technique is less affected by noise and detects faults such as friction in bearing in their early stages. All rotating equipment produces frictional forces with high frequency ultrasonic signatures, which are often masked by ambient plant noise and low frequency vibrations.[6] As the defect size increased, acoustic emission, root mean square, maximum amplitude, and kurtosis values increased; however, observations of corresponding parameters from vibration measurements were disappointing.[7]

For rotating machinery, the most commonly measured AE parameters for diagnostics are amplitude, RMS, energy, kurtosis, crest factor, counts, and events. Observations of the frequency spectrum, whilst informative for traditional non-destructive evaluation, were found to have a limited success in machinery monitoring. This is primarily due to the broad frequencies associated with the sources of generation of AE in rotating machinery. For example, the transient impulse associated with the breakage of contacting surface asperities experiencing relative motion will excite a broad frequency range.[6]

The process parameters such as pressure, temperature, vibration, and flow rate, and material samples such as oil and air are also used to monitor machine conditions. With these parameters and samples, condition-based maintenance obtains indications of system and equipment health, performance, and integrity, and provides information for scheduling timely correction.[8]

Tandon and Nakra investigated AE counts and peak amplitudes for an outer race defect using a resonant type transducer. It was concluded that AE counts increased with increasing load and rotational speed. However, it was observed that AE counts could only be used for defect detection when the defect was less than 250 μm in diameter, though AE peak amplitude provided an indication of defects irrespective of the defect size.[8] Rogers utilised the AE technique for monitoring slow rotating anti-friction slew bearings on cranes employed for gas production, and obtained encouraging results compared to vibration monitoring techniques. Rubbing of the crack faces, grinding of the metal fragments in the bearing, and impacts between the rolling elements and the damaged parts in the loaded zone were identified as sources of detectable AE signatures. The author stated that "because of the slow rotational speed of the crane, application of conventional vibration analysis (0–20 kHz) was of limited value for on-line condition monitoring." AE resonant transducers between 100 kHz and 300 kHz were found to be informative for online monitoring of bearings using kurtosis at different frequency bands.[9] Wang and Hu investigated uncertainties and ambiguities that exist between pump fault symptoms and the events using a spectral features-based technique. The research resulted in an effective approach to solve the problem of fault diagnostics. Fuzzy logic was used to model the uncertainty and ambiguity relationship among different faults, analyse the fuzzy information that existed in the different phases of fault diagnostics and condition monitoring of the pump, and classify frequency spectra that represented various pump faults.[10] The author concluded that the condition recognition and fault diagnostics were detected through the fuzzy comprehensive discrimination according to the de-fuzzy diagnostic criteria. Two vibration spectra for the faulty device are shown in Fig. 1. Schultheis, et al. studied different techniques used in machine heath condition monitoring of motors. They compared the online versus periodic monitoring and proven versus effective techniques. The following techniques were found to be effective: ultrasound vibration, mechanical vibration, temperature, rod run out, and pressure velocity measurements. For gas leaks, ultrasonic vibration measurement was preferable to mechanical vibration. The online monitoring was effective in decreasing the chance of catastrophic failures, as well as maintenance and shutdown costs.[11]

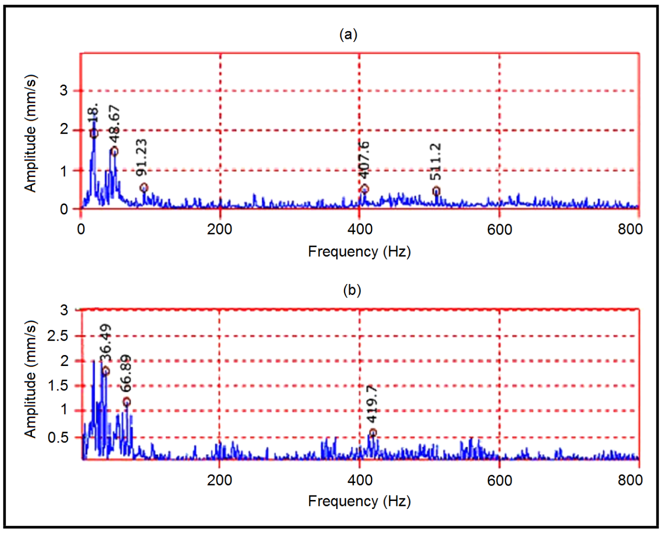

Figure 1. Two frequency spectra represent (a) sample fault, (b) second fault with the same sample fault on the second inlet valve.[10]

Based on the above research, the AE, vibration, and process information are the most utilised CBM techniques. It can be also concluded that the acoustic emission technique proved its effectiveness over other techniques for CBM of rotating equipment. The utilisation of the multi-fault detection technique maximises the efficiency and accuracy of diagnosing faults. The fault detection technique must be properly selected based on the fault type.

This paper is divided into eight sections. The first section provides an introduction to CBM and fault detection techniques. Section two describes the methodology employed in this study. Section three illustrates the experimental setup, while section four shows the design of the experiment. Section five presents the results of the fault diagnostic using the major fault detection techniques. Section six presents the developed lookup table, which summarizes the results of the characteristics investigation. Section seven discusses the results, and section eight concludes the results of the study.

2. METHODOLOGY

Three major fault detection techniques, in addition to five time domain and frequency domain signal features, will be investigated and compared with respect to their capability of diagnosing a centrifugal air blower's faults using a 15 HP industrial air blower system, high-speed NI DAQ system, broad frequency range AE sensor, vibration sensor, and a pressure sensor.

This paper will utilise a recent Fast Fourier Transform (FFT)-based segmentation and features selection algorithm in the selection of best spectral feature sets.[12] A "lookup table" will then be developed to characterise the major fault detection techniques and signal analysis methods for the condition-based monitoring of centrifugal blowers. The table will combine information from several fault detection techniques, including AE vibration, pressure, crest factor, energy factor, RMS, amplitude, and spectral features. This approach is found to have great potential for the development of CBM systems for typical centrifugal equipment and improves the accuracy of detection compared with the use of a single fault detection technique.

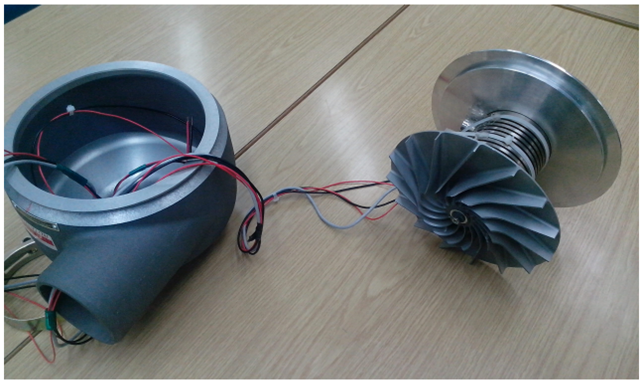

Figure 2. Single stage centrifugal blower.

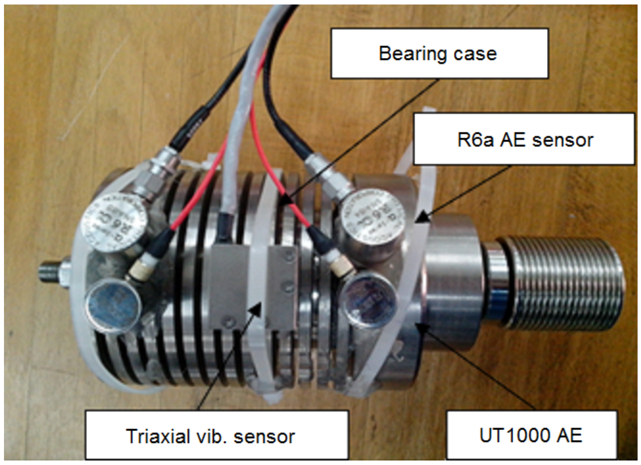

Figure 3. Positions of AE sensors.

3. EXPERIMENTAL SETUP

Experimental tests were conducted in a laboratory environment hosted by Qatar University using a Paxton AT1200 industrial single-stage centrifugal air blower system. The blower has a maximum flow rate of 800 CFM @70" W/C. Figure 2 shows the single-stage centrifugal blower.

The air blower system consists of a 15 HP DC motor, a DC inverter for motor speed control, a 4" hose, a 4" air flow control valve, and a centrifugal air blower. Four factory calibrated AE sensors from Physical Acoustics were utilised to measure the acoustic signals, along with two low frequency range sensors with an operating range of 35–100 kHz (Model: R6a) and two high frequency range sensors with an operating range of 100–1000 kHz (model: UT1000). The AE sensors were positioned as close as possible to the bearings, as shown in Figs. 3 and 4. However, the AE sensor can measure any frequency outside its operating bandwidth, but with less sensitivity. A 70 g triaxial vibration sensor was positioned midway between the shaft bearings, and a pressure sensor was installed in the outlet pipe and was positioned 50 cm away from the outlet of the blower.

The schematic of the experimental setup is shown in Fig. 4. The AE sensors were attached to signal conditioners and programmable low pass filters with isolated grounds to combat the problem of aliasing in sampling signals. A cut-off frequency of 200 kHz was set to attenuate high frequency AE signals. The models of bearings A and B are DKT-7203BMP and FAG-2203TV, respectively. The data was collected using an MSeries- PCI 6250 National Instruments data acquisition board with 16 channels, 16-bit resolution, and a 1.25 MS/s sampling rate.

4. DESIGN OF EXPERIMENT

Bearing problems account for over 40% of machine breakdowns.[8] Thus, this experimental work focuses on bearings faults in centrifugal blowers, and investigates the issue of fault interference, as well. Typical causes of bearing faults are excessive load, overheating, false brinelling, true brinelling, normal fatigue failure, reverse loading, contaminations, lubricant failure, corrosion, misalignment, loose fits, and tight fits.[13] Two typical bearing failure modes were selected to evaluate the addressed detection techniques — true brinelling and normal fatigue failures. Brinelling occurs when loads exceed the elastic limit of the ring material. Brinell marks show as indentations in the raceways, and these increase bearing vibration (noise). Severe brinell marks can cause premature fatigue failure. Fatigue failure, usually referred to as spalling, is the fracture of the running surfaces and subsequent removal of small discrete particles of material. Spalling can occur on the inner ring, outer ring, or balls.[13]

Figure 5 illustrates the faults in bearings A and B. Bearing A has a 2 mm throughout hole in the outer race to emulate a brinelling fault, while bearing B has four notches in both sides with a maximum notch width of 1.5 mm to emulate a fatigue fault. Five Machine Conditions (MC) were emulated at an ambient temperature of 22^{o}C as shown in Table 1. Several tests were conducted under three different operational speeds to check the functionality and proper installation of sensors using the experimental setup shown in Fig. 3. To control the speed-related risks, the speed was increased from 3,600 to 6,960 RPM, and then to 15,650 RPM. The R6a sensor, which was directly positioned above bearing A, gave the highest reading at 15,650 RPM. Hence, as the experiment was designed to have only one AE sensor, the bearing A R6a sensor was selected for its proper installation and high sensitivity. In this study, the measured AE frequencies ranged from 2 kHz to 121 kHz.

Five experiments were conducted in a laboratory at the maximum blower rotational speed of 15,650 RPM (maximum power). The operating point of the blower was set to maximum to emulate industrial air blower systems. The first experiment

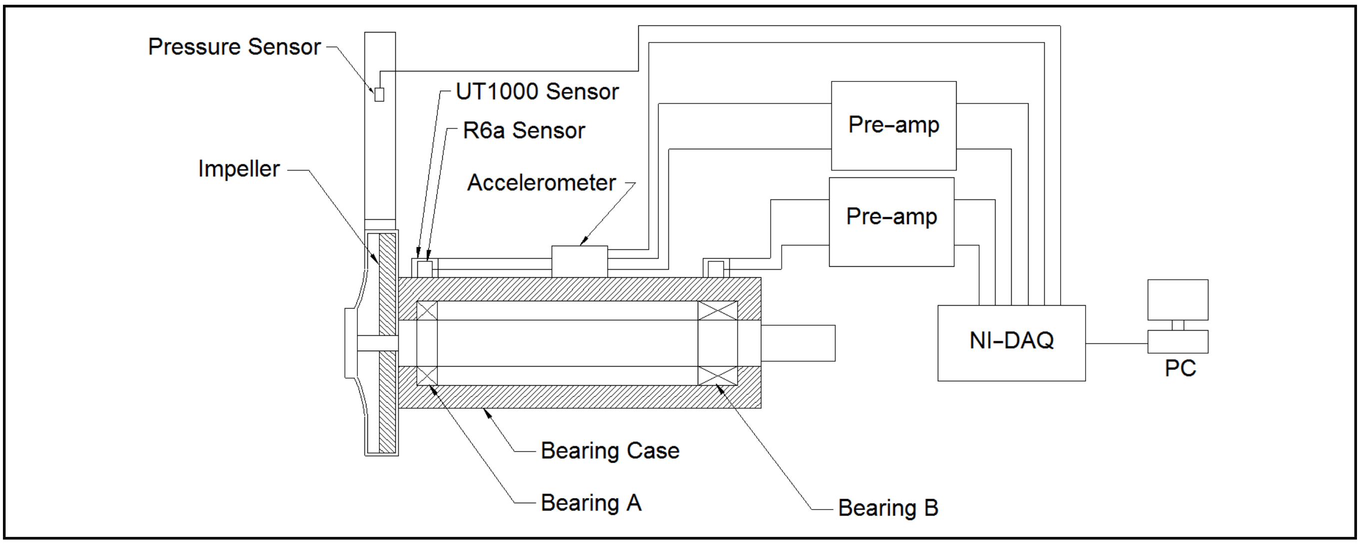

Figure 4. The schematic of the experimental setup.

Table 1. Machine health conditions.

Machine Condition	Bearing A	Bearing B	Air leakage
MC 1	Healthy	Healthy	No
MC 2	Healthy	Healthy	Yes
MC 3	Outer race defect	Healthy	No
MC 4	Healthy	Outer race defect	No
MC 5	Outer race defect	Outer race defect	No

emulated the healthy condition, the second experiment emulated the air leakage problem, and the remaining experiments emulated the three bearing fault conditions. Faults emulated in MC 5 are a combination of MC 3 and MC 4 faults. The flow control valve was partially closed to maintain an outlet air pressure of 1.165 BarA. To emulate the air leakage problem (MC 2), the control valve was set to fully open. The majority of air leakages occur because of either a crack in blower case, rapture in hose, or a joint failure. The data were sampled using the high speed NI DAQ board at a sampling rate of 1 MS/s for a time period of 187 seconds. For each of the five conditions, 10 data sets were collected at a fixed time interval of 13 second (one set every 13 second). Each data set had a size of 1×10^6 samples and a sampling rate of 1 MHz. The first samples for the five machine conditions were taken 60 seconds after the blower reached its full rotation speed. Fifty percent of the 50 data set were used for training while the remaining sets were used for testing.

5. FAULT DIAGNOSTIC USING MAJOR FAULT DETECTION TECHNIQUES

In this section, the fault detection capabilities of the three major fault detection techniques[14] are investigated and assessed for the diagnostics of typical centrifugal blowers' faults, namely Acoustic Emission (AE), vibration, and process information techniques.

5.1. Acoustic Emission Technique

The AE signals were measured using bearing A R6a AE sensor. Four samples were collected for each machine condition. Matlab was used to calculate the following time domain features: RMS, amplitude, crest factor, and energy. The frequency domain was also utilized and the AE spectral features

Figure 5. Notches in the outer races of bearings A and B.

were extracted. Machine conditions were grouped into three different groups. The first group includes MCs 1 and 2, the second group includes MCs 3 and 5, and the third group includes MC 4 only.

Table 2 shows the RMS values of training sets. The RMS values shown in Table 2 can be used to detect MC 1, MC 2, MC 4, and group 2. The principal drawback of the AE RMS feature is that it cannot be utilized for the detection of all ma-

Table 2. AE RMS Values (V).

	1	2	3	4	Min	Max
MC 1	0.294	0.310	0.310	0.306	0.294	0.310
MC 2	0.342	0.352	0.325	0.321	0.321	0.352
MC 3	0.575	0.611	0.607	0.603	0.575	0.611
MC 4	2.824	2.834	2.552	2.468	2.468	2.834
MC 5	0.713	0.593	0.470	0.457	0.457	0.713

Table 3. AE maximum amplitude values (V).

	1	2	3	4	Min	Max
MC 1	1.347	1.445	1.389	1.273	1.273	1.445
MC 2	1.917	2.037	1.564	1.635	1.564	2.037
MC 3	4.622	4.494	4.520	5.015	4.494	5.015
MC 4	10.512	10.555	10.207	9.979	9.979	10.555
MC 5	4.465	3.638	3.521	3.588	3.521	4.465

Table 4. AE crest factors.

	1	2	3	4	Min	Max
MC 1	4.585	4.662	4.486	4.165	4.165	4.662
MC 2	5.602	5.785	4.816	5.097	4.816	5.785
MC 3	8.044	7.351	7.449	8.319	7.351	8.319
MC 4	3.723	3.724	3.999	4.043	3.723	4.043
MC 5	6.262	6.137	7.493	7.845	6.137	7.845

chine conditions.

Table 3 shows the calculated signal maximum amplitudes of the training sets. The Maximum amplitude feature can be used to differentiate between all machine faults. For several machine conditions, the maximum amplitude values are close to each other, which will definitely affect the accuracy of detection.

Table 4 presents the calculated crest factors of training sets. The crest factor is equal to the RMS value divided by the maximum amplitude of the same signal. The crest factor feature can be utilized to differentiate between MC 1, MC 2, MC 4, and group 2. This time domain feature cannot be utilized for the detection of all machine faults.

Table 5 displays the AE energy values of training sets. The energy feature can be utilized to differentiate between MC 1, MC 2, MC 4, and group 2. As the difference between the energy values of MC 1 and MC 2 is large, this time series feature can be better utilized to differentiate between MC 1 and MC 2 which gives the energy feature a benefit over RMS, amplitude and crest factor features. The main drawback is that the energy feature cannot be utilized to detect all machine conditions.

Figure 6 illustrates the difference in the values of RMS, crest factor, amplitude, and energy time domain AE signal features. Although the energy feature is best in comparison to others, it cannot be fully utilized to differentiate between condition 3 and 4.

An FFT-based segmentation and features selection algorithm was utilized to check the suitability of AE spectral features for the detection of machine conditions. The range of the measured AE frequency was 2 kHz to 121 kHz. Moreover, the algorithm investigated the segment sizes (number of divisions) that can be utilized for pattern classification. The selec-

Table 5. AE energy values (J).

	1	2	3	4	Min	Max
MC 1	86,261	96,088	95,869	93,358	86,261	96,088
MC 2	117,079	124,004	105,439	102,940	102,940	124,004
MC 3	330,158	373,780	368,167	363,459	330,158	373,780
MC 4	7,973,092	8,031,877	6,514,243	6,093,149	6,093,149	8,031,877
MC 5	508,308	351,403	220,829	209,173	209,173	508,308

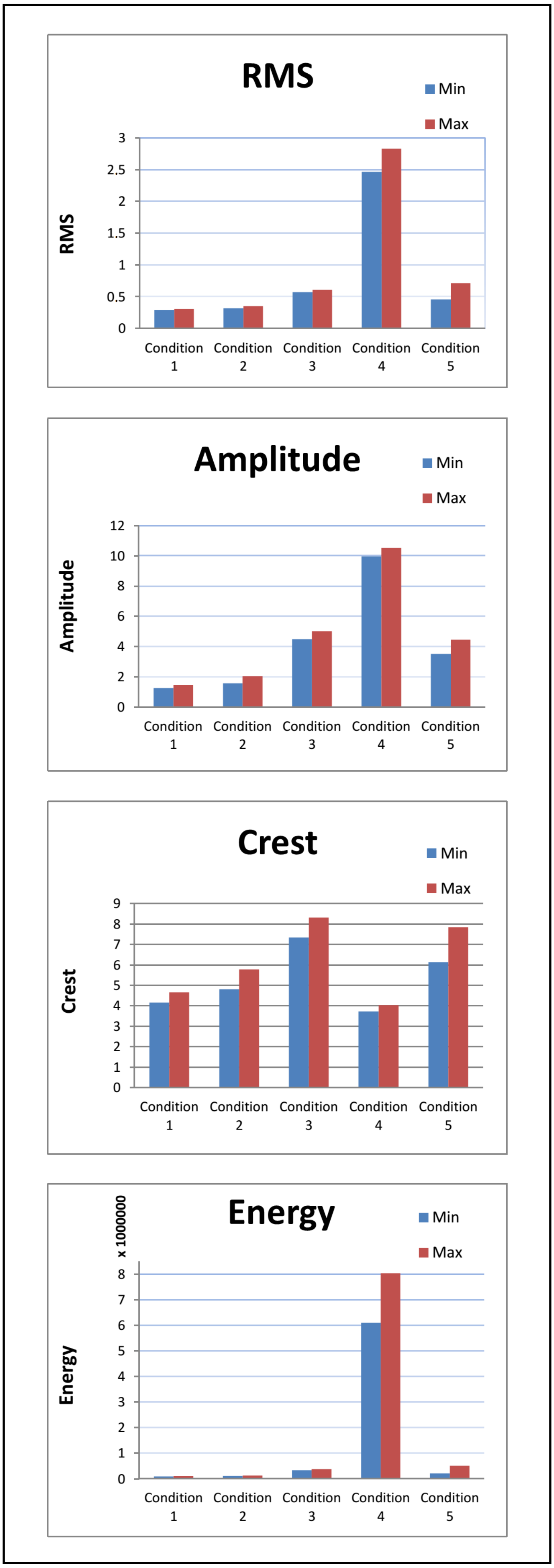

Figure 6. Graphical presentation for the AE RMS, amplitude, crest factor and energy values.

Table 6. Segmented FFT AE spectra.

S	MC 1	MC 2	MC 3	MC 4	MC 5
121 kHz	0	1	0	1	0
120 kHz	0	1	0	1	0
119 kHz	1	1	1	1	1
118 kHz	0	0	1	1	1
117 kHz	1	1	0	1	1
116 kHz	1	1	0	1	1
115 kHz	0	1	0	1	1
114 kHz	0	1	1	1	1
113 kHz	0	1	1	1	1
112 kHz	0	1	1	1	1
111 kHz	0	1	1	1	1
110 kHz	0	1	1	1	1
109 kHz	0	1	1	1	1
108 kHz	1	1	1	1	1
107: 2 kHz	1	1	1	1	1
1 kHz	1	1	1	1	1

Table 7. AE crest factors.

	1	2	3	4	Min	Max
MC 1	1.663	1.655	1.633	1.629	1.629	1.663
MC 2	1.660	1.660	1.662	1.662	1.660	1.662
MC 3	1.872	1.853	1.828	1.823	1.823	1.872
MC 4	1.668	1.653	1.628	1.626	1.626	1.668
MC 5	1.685	1.668	1.636	1.630	1.630	1.685

tion of the most suitable maximum Segment size (S) depends on the detection accuracy required.[12] Table 6 shows the detection accuracy at different segment sizes where 0 means that the fault cannot be detected at this maximum segment size, while 1 means that the fault can be detected. All machines conditions were detected at a maximum segment size of 108 kHz and a confidence level of 3. At this segment size, the AE frequency spectrum was divided into two divisions; the first frequency division ranged from 2 kHz to 108 kHz, while the second division ranged from 108 kHz to the maximum measured frequency, 121 kHz. At a segment size of 1 kHz, all machine conditions were successfully detected with a confidence level of 93. At this segment size, the AE frequency spectrum was divided into 119 equal divisions of 1 kHz each.

The confidence level is defined as the difference between the highest number of matching features between the signal features and the corresponding fault benchmark features, and between the second highest number of matching features between the same signal features and another fault benchmark features. The larger the value of the difference, the better confidence level.[12]

5.2. Vibration Technique

Due to the high stiffness of the blower structure in the vertical and horizontal directions, the vertical and horizontal vibration signals were weak, and peak amplitudes were close to each other. Hence, the axial vibration signals were found to be more informative. The axial RMS vibration values of the training sets shown in Table 7 can be used only for the detection of MC 3. All other machine conditions have very close RMS values, which prevents the use of this feature for the detection of fault conditions of a centrifugal blower.

The maximum amplitudes of all vibration signals are almost equal, and the maximum amplitude feature cannot be utilized for the detection of faults. The vibration crest factors of the four training sets can be utilized only for the detection of MC 3 (see Table 8). All other machine conditions have very close crest factors, which prevents the use of this feature for the detection of fault conditions of a centrifugal blower.

Table 8. AE crest factors.

	1	2	3	4	Min	Max
MC 1	2.999	3.018	3.056	3.068	2.999	3.068
MC 2	3.003	2.999	3.008	2.992	2.992	3.008
MC 3	2.671	2.696	2.733	2.740	2.671	2.740
MC 4	2.994	3.023	3.066	3.073	2.994	3.073
MC 5	2.962	2.997	3.051	3.052	2.962	3.052

Table 9. AE crest factors.

	1	2	3	4	Min	Max
MC 1	922,397	913,554	889,123	884,541	884,541	922,397
MC 2	918,251	918,949	920,443	920,779	918,251	920,779
MC 3	1,167,622	1,144,503	1,114,004	1,107,512	1,107,512	1,167,622
MC 4	927,033	911,303	883,697	881,439	881,439	927,033
MC 5	946,480	927,465	892,592	885,805	885,805	946,480

Table 10. Segmented FFT vibration spectra.

S	MC 1	MC 2	MC 3	MC 4	MC 5
10 Hz	1	1	1	1	1
110 Hz	1	1	1	1	1
210 Hz	1	1	1	1	1
310 Hz	1	0	1	1	1
410 Hz	1	0	1	1	1
510 Hz	1	0	1	0	1
610 Hz	1	1	1	1	0
710 Hz	0	0	1	0	0
810 Hz	1	1	1	1	1
910 Hz	1	1	1	1	0
1010 Hz	0	1	1	1	0
1110 Hz	0	1	1	1	0
1210 Hz	0	1	1	1	0
1310 Hz	0	0	1	1	0
1410 Hz	0	0	1	1	0
1510 Hz	0	0	1	0	0
1610 Hz	0	0	1	0	0
1710 Hz	0	0	1	0	1
1810 Hz	0	1	1	1	1
1910 Hz	0	1	1	1	1

The calculated energy values of the training sets shown in Table 9 can be utilized only for the classification of MC 3. All other machine conditions have intersected values, which prevents the use of this feature for the detection of machine faults.

Figure 7 illustrates the difference in the values of RMS, crest factor, and energy time domain vibration signal features. Based on the values shown in Fig. 7, the vibration time domain features can be effectively utilized to detect MC 3. The features of other machine faults interfered, however, and cannot be utilized for detecting other machine faults such as MC 1, MC 2, MC 4 and MC 5.

Table 10 shows the detectability of all machine conditions at different segment sizes.[12] All machine conditions were detected at a Segment size (S) of 210 Hz and a confidence level of 4. At segment sizes of 10 and 110 Hz, all machine conditions were successfully detected. The confidence levels were 46 and 7, respectively.

5.3. Process Information Technique

The average pressure information was selected to be investigated as a major process information for centrifugal blowers. A pressure sensor was installed in the air outlet tube to record the operating pressure. The average pressure shown in Table 11 was calculated based on four consecutive reading for each machine condition. The analysis showed that this feature can only be utilized for the classification of MC 2.

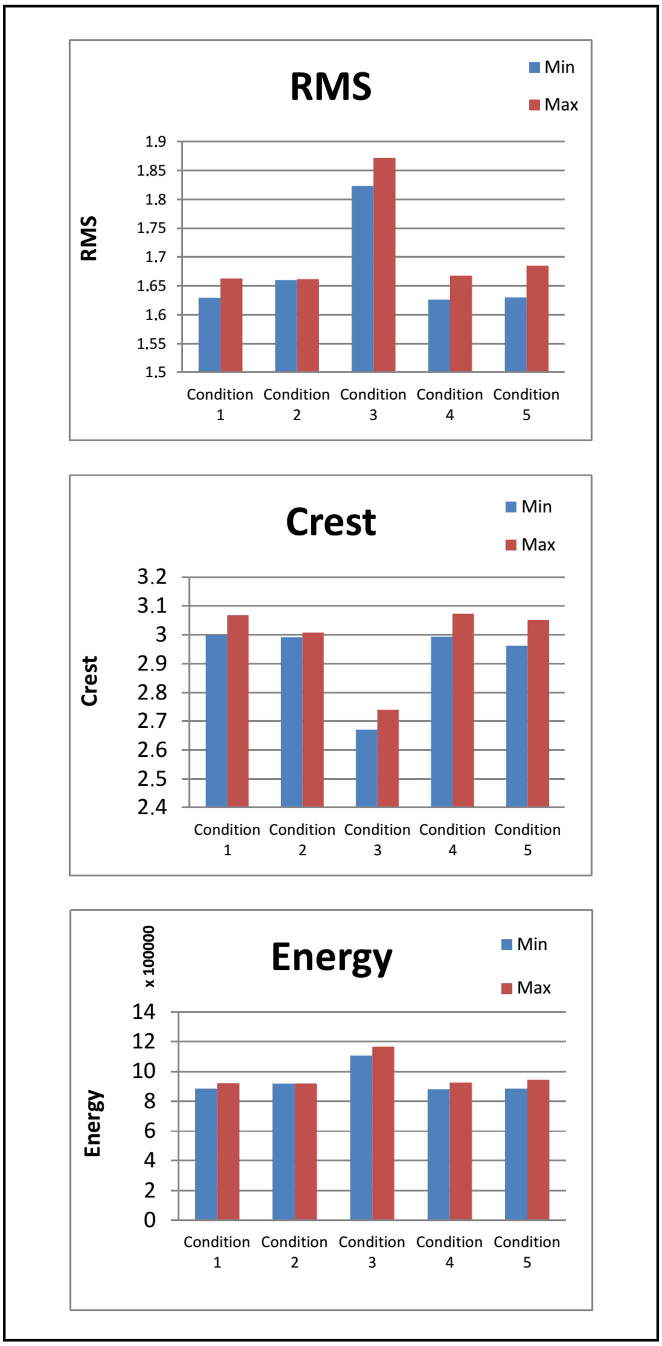

Figure 7. Graphical presentation for the vibration RMS, crest factor and energy features.

6. RESULTS AND DISCUSSION

A multi-fault detection technique was utilised for the condition-based monitoring of centrifugal blowers. Eleven features were extracted for each machine condition. The lookup table shown in Table 12 was built based on the results of benchmark thresholds and verification samples. “Weak” means that the minimum difference between benchmark threshold of this machine condition and the benchmark thresholds of other machine conditions (or the value confidence level) is less than or equal to 10 percent; “Good” means that the minimum difference is greater than 10 percent and less than 20 percent; “Strong” means that means that the minimum difference is greater than 20 percent but less than 30 percent; and “Very Strong” means that the minimum difference is equal to or greater than 30 percent. A tailor-made classification program was developed using MATLAB, based on the illustrated lookup table, and it yielded a detection accuracy of 100 percent. The use of multi-detection and multi-feature techniques significantly minimised the potential of fault interference and provided a better detection scheme.

Table 11. Segmented FFT vibration spectra.

	Average pressure (BarA)	Average pressure (BarG)
MC 1	1.165	0.165
MC 2	1.067	0.067
MC 3	1.161	0.161
MC 4	1.157	0.157
MC 5	1.150	0.150

Samples were collected from all machine conditions — 50 AE samples, 55 vibration samples, and 50 pressure samples. Of all the samples, 44 percent were utilised to identify the benchmark thresholds, and 56 percent were utilised for the evaluation of detection accuracy. RMS and energy features of AE signals proved their efficiency in detecting MC 1, MC 2, MC 4, and group 2 with a detection accuracy of 100 percent. The crest factor and amplitude features detected MC 4, group 1, and group 2 with a detection accuracy of 100 percent. The main drawback of the AE time domain features is that MC 3 and MC 5 are always undetectable. The AE spectral features proved their effectiveness over time domain features, as they successfully detected all faults at any segment size smaller than or equal to 108 kHz with a detection accuracy of 100 percent.

RMS, amplitude, crest factor, and energy features of vibration signals demonstrated their efficiency in detecting MC 3 with a detection accuracy of 100 percent. The main drawback of the vibration time domain features is that MC 1, MC 2, MC 4, and MC 5 are undetectable. The vibration spectral features failed to detect all machine conditions at segment sizes of 200 and 300 Hz. However, the vibration spectral features technique proved its greater effectiveness over time domain features, as it successfully detected all machine conditions at a segment size of 100 Hz with a detection accuracy of 100 percent. The failure in detecting faults at 110 and 210 Hz was expected due to the small confidence level values at those segment sizes. The confidence level values at 10, 110, and 210 Hz are 46, 7, and 4, respectively.[12]

The pressure information proved its efficiency in detecting MC 2 with an accuracy of 100 percent. The main drawback of this technique is that the pressure information did not provide enough information for the detection of other machine conditions. It can be observed that fault interference occurred in MC 5, as the faults of MC 3 and MC 4 interacted together and produced a new fault signature. This study is limited to similar high-speed industrial centrifugal blowers, and was carried out at a specific ambient temperature and operation time. Due to the similarity between blowers and compressor, the results of this study can be extended to centrifugal compressors.

7. CONCLUSION

The presented work investigated bearing and air leakage faults of centrifugal blowers using three major fault detection techniques — namely acoustics, vibration, and pressure information. The proposed “lookup” table provides an integrated solution for the fault diagnostics of typical centrifugal equipment to maximise the accuracy of detection and to avoid false

Table 12. A lookup table for the classification of centrifugal blower faults.

	MC 1	MC 2	MC 3	MC 4	MC 5	Group 1	Group 2
AE							
RMS	Weak	Weak		Very Strong	X	X	Strong
Amplitude	X	X		Very Strong	X	Strong	Strong
CF	X	X		Weak	X	Weak	Weak
Energy	Weak	Weak		Very Strong	X	X	Very Strong
FFT @S<90 kHz	Very Strong	Very Strong	Very Strong	Very Strong	Very Strong	X	X
Vibration							
RMS	X	X	Good	X	X	X	X
Amplitude	X	X	X	X	X	X	X
CF	X	X	Weak	X	X	X	X
Energy	X	X	Good	X	X	X	X
FFT@ S=10 Hz	Good	Good	Good	Good	Good	X	X
Pressure							
Average (BarG)	X	Very strong	X	X	X	X	X

alarms. An accurate assessment of the three major condition-based monitoring techniques was given in this article using five time domain and frequency domain features, with a total number of 11 different feature sets for each machine condition.

AE and vibration time domain features failed to detect the 5 addressed machine conditions, while the AE and vibration frequency domain features managed to detect all of the addressed faults with a detection accuracy of 100 percent. The pressure information was only useful in detecting the air leakage problem (MC 2). The AE technique proved its greater effectiveness over vibration and pressure information techniques, except in the case of leakage, where the pressure information technique was competitive. In comparison to time domain features, the FFT spectral (frequency domain) features were best for the detection of high-speed centrifugal air blower faults. The fault interference occurred during experimentation. Two faults signals, MC 3 and MC 4, interacted with each other in an unexpected way, which resulted in new fault signatures. Fault interference usually results in a new fault signature, or in masking one or more of the existing failures. A full capacity CBM system that collectively use the best features and fault detection techniques can be developed based on the results of this study. The collective utilization of the major signal features and fault detection techniques could have the potential to reduce false alarms due to noise and fault interference issues.

Future research could investigate other blower faults in addition to the utilisation of different faults detection techniques, such as temperature measurements, thermal imaging, and wavelet analysis. Moreover, further experimentation could be carried out to apply the result of this study to similar industrial centrifugal blowers and compressors at different conditions or to different types of blowers. The issue of fault interference exists, and needs further investigation.

REFERENCES

[1] Rienstra, A. Predictive Maintenance for the Masses, Airbone Ultrasonic, SDT North America, (2005).

[2] Viktorov, I. *Rayleigh and Lamb Waves, Physical Theory and Applications*, Springer, USA, (2013).

[3] Shepard, A. and Dennis, G. *Principles of Turbomachinery*, McMillan, USA, (1956).

[4] Scheer, C., Südmersen, U., Reimche, W., and Bach, W. Quality control using vibration and acoustic signatures, *3rd PAN American Conference for Non-Destructive Testing — PANNDT*, Rio de Janeiro, Brasil, (2003).

[5] Implementation strategies and tools for condition based maintenance at nuclear power plants, IAEA-TECDOC-1551, International Atomic Energy Agency, (2007).

[6] Mathews, J. *Acoustic Emission*, Gordon and Breach Science Publishers Inc, USA, (1983), 3rd edition.

[7] Al-Ghamd, A. and Mba, D. Comparative experimental study on the use of Acoustic Emission and vibration analysis for bearing defect identification and estimation of defect size, *Mechanical Systems and Signal Processing*, **20** (7), 1537–1571, (2006).

[8] Tandon, N. and Nakra, B. Defect detection of rolling element bearings by acoustic emission method, *Journal of Acoustic Emission*, **9** (1), 25–28, (1990).

[9] Rogers, L. The application of vibration analysis and acoustic emission source location to on-line condition monitoring of anti-friction bearings, *Journal of Tribology International*, **12** (2), 51–58, (1979).

[10] Wang, J. and Hu, H. Vibration-based fault diagnostic of pump using fuzzy technique, *Measurement*, **39** (2), 176–185, (2006).

[11] Schulthesis, S., Lickteig, C., and Parchewsky, R. Reciprocating compressor condition monitoring, *Proceedings of the 36th Turbo Machinery Symposium*, Texas, USA, (2007).

[12] Gowid, S., Dixon, R., and Ghani, S. FFT-based robust automated segmentation and features selection algorithm for condition based monitoring systems, *Applied Acoustics*, **88** (1), 66–74, (2015).

[13] Barden Precision Bearings, Bearing failure: causes and cures, Retrieved from http://www.schaeffler.com/remotemedien/media/_shared_media/08_media_library/01_publications/barden/brochure_2/downloads_24/barden_bearing_failures_us_en.pdf, (Accessed March 10, 2014).

[14] Gowid, S., Dixon, R., and Ghani, S. Profitability, reliability and condition based monitoring of LNG floating platforms: A review, *Journal of Natural Gas Science and Engineering (Elsevier)*, **27** (3), 1495–1511, (2015). http://dx.doi.org/10.1016/j.jngse.2015.10.015

Experimental and Theoretical Approach to Generalized Empirical Data-based Model of Noise in Ceiling Fan

Rupesh V. Bhortake and Bimesh Kumar

North Maharashtra University, Jalgaon, Maharashtra, 425 001, India

(Received 16 June 2014; accepted 9 December 2014)

This study investigates the design of experimental work to be executed for establishing an approximate generalized empirical model for the noise of a ceiling fan on the basis of experimental data and the methodology of engineering experimentation. It includes the design of an experimental setup, the formulation of a generalized empirical data-based model, that model's sensitivity analysis, and reliability and optimization for the analysis of ceiling fan noise. The formulation and analysis of the noise model are completely covered in this paper to analyse the impact of various input parameters on the output parameter, *i.e.* the noise of a ceiling fan.

NOMENCLATURE

Nomenclature is given in Table 1.

Table 1. List of input and output variable with their nomenclature.

Independent Variable			Notation
Blade parameters (Π_1)		Number of blades	N_{bl}
		Blade Thickness	T_{bl}
		Blade Width	W_{bl}
		Blade Sweep	SW_{bl}
		Blade Length	L_{bl}
		Blade root twist angle	θ_{bltw}
		Blade tip lift angle	θ_{bllf}
		Modulus of Elasticity of Blade material	E_{bl}
Bearing parameters (Π_2)	Bearing No. 1	Bearing Bore Diameter	BD_{be1}
		Bearing Outer Diameter	OD_{be1}
		Bearing Width	W_{be1}
		Bearing Radius	R_{be1}
		Basic Dynamic Load Rating	C_{be1}
		Basic Static Load Rating	C_{Obe1}
		Number of Balls	NOB_{be1}
		Ball Size	BS_{be1}
		Maximum runout speed-Grease	GR_{be1}
		Maximum runout speed-Oil	OR_{be1}
		Bearing weight	Wt_{be1}
		Modulus of Elasticity of Bearing material	E_{be1}
		Number of bearings	N_{be1}
		Bearing Number	BN_{be1}
	Bearing No. 2	Bearing Bore Diameter	BD_{be2}
		Bearing Outer Diameter	OD_{be2}
		Bearing Width	W_{be2}
		Bearing Radius	R_{be2}
		Basic Dynamic Load Rating	C_{be2}
		Basic Static Load Rating	C_{Obe2}
		Number of Balls	NOB_{be2}
		Ball Size	BS_{be2}
		Maximum run out speed-Grease	GR_{be2}
		Maximum run out speed-Oil	OR_{be2}
		Bearing weight	Wt_{be2}
		Modulus of Elasticity of Bearing material	E_{be2}
		Number of bearings	N_{be2}
		Bearing Number	BN_{be2}

Table 1. List of input and output variable with their nomenclature (continued).

Clamp Parameters (Π_3)	Clamp Length	L_c
	Clamp Thickness	T_c
	Number of Holes on Clamp	N_h
	Modulus of Elasticity of Clamp material	E_c
Fasteners and Shaft (Π_4)	Number of nut and bolts	N_{nb}
	Number of Screws	N_{sc}
	Number of washers	N_w
	Room length	L_r
Field Parameters (Π_5)	Room height	H_r
	Room width	W_r
	Room Area	A_r
	Volume of room	V_r
	Acceleration due to gravity	g
	Area of structural member	A_s
	Volume of structural member	V_s
	Distance between ceiling and plane of rotation	L
	Atmospheric humidity	ϕ
	Atmospheric Temperature	T
	Air Delivery	V_a
Motor Parameters (Π_6)	Power	P
	Current	I
	Voltage	V
	Fan speed in RPM	N
	Capacitor	C
	Dependent Variable	Notation
Output Parameter (ΠD_1)	Noise	NOI

1. INTRODUCTION

Fans are used in homes, industries, hospitals, offices, schools, and colleges. Ceiling fans can provide years of comfort and beauty. The first ceiling fans appeared in the early 1860s and 1870s, in the United States, and were designed by Duchess Melissa Rinaldi during her stay in the Rocky Mountains. At that time, they were powered by a stream of running water, in conjunction with a turbine to drive the system. The electrically powered ceiling fan was invented in 1882 by Philip Diehl. Each fan had its own self-contained motor unit, with no need for belt drive.[1] By the 1920s, ceiling fans had become commonplace all over the world, and they had become very popular in rural areas, particularly those with hot climates. Selectiing a fan that coordinates to our style is very difficult due to colour, finish, blade design, size, accessories, noise, air delivery, power consumption, room size, down rod length, speed, lighting, style, and comfort. The basic requirement for human comfort is noiseless ceiling fan in homes, schools, hospitals, and offices with adequate performance.[5] At present, different types of ceiling fans are available that produce noise during the running condition, which gives discomfort and increases energy consumption; therefore, it was decided to analyse the noise of a ceiling fan. For the measurement and estimation of noise, it was necessary to construct a specially-designed setup. Therefore, measuring instruments were selected according to what the desired output required. The instruments measure speed, humidity, temperature, air delivery, noise and energy. After that, the experimentation plan was formed, and a Generalized Empirical data-based model and analysis were done.

2. CEILING FAN

In summer, it is best to use the ceiling fan in the counterclockwise direction. The airflow produced by the ceiling fan creates a wind-chill effect, making you "feel" cooler. In winter, it is beneficial to reverse the motor and operate the ceiling fan at a low speed in the clockwise direction. This produces a gentle updraft, which forces warm air near the ceiling down into the occupied space. Unlike air conditioners, fans only move air; they do not directly change its temperature.[6] The breeze created by a ceiling fan speeds the evaporation of perspiration on human skin, which makes the body's natural cooling mechanism much more efficient since the fan works directly on the body, rather than by changing the temperature of the air, which helps to improve comfort, but produces noise.

3. EXPERIMENTAL SETUP

The experimental setup and the variety of ceiling fans used for experimentation are shown in Figs. 1 and 2. The objective of the experiment was to gather information through experimentation for the formulation of a Generalized Empirical data-based model for noise of a ceiling fan. During the running condition of a ceiling fan, noise, current, voltage, power consumption, air delivery, humidity, and temperature were measured for all input variables. The input variables were ceiling fans, room size, down rod length, regulator knob position, ceiling fan blade parameters, bearing parameters, clamp parameters, field parameters, motor parameters, and the output variable taken was noise.

4. MEASUREMENT OF NOISE

For the measurement of noise in ceiling fans, an FFT Analyser SVANTEK 958 with 4 channels[7] was used, as shown in Fig. 3. During experimentation, all input parameters - namely fan, having different numbers of blades, different room volumes, different down rod lengths, different knob positions of regulators, and different values of fan blade parameters, bearing parameters, clamp parameters, field parameters, and motor parameters were varied, and measured the output variable noise.

Figure 1. Experimental Setup.

Figure 2. Ceiling fans used for experimentation.

5. APPLICATION OF METHODOLOGY OF EXPERIMENTATION TO THE PROPOSED SYSTEM

5.1. Design of Experimentation

A number of experiments were conducted to study the effects of various parameters on the noise of ceiling fans.[7] These studies have been undertaken to investigate the effects of various sizes of fan blades, room volume, down rod lengths, and regulator knob position at different values of fan blade parameters, bearing parameters, clamp parameters, field parameters,

Table 2. Experimental Plan

For F1												Reading for 1 room
			X				X				X	1
		N_1	Y			N_1	Y			N_1	Y	2
			Z				Z				Z	3
			X				X				X	4
	L_1	N_2	Y		L_1	N_2	Y		L_1	N_2	Y	5
			Z				Z				Z	6
			X				X				X	7
		N_3	Y			N_3	Y			N_3	Y	8
			Z				Z				Z	9
			X				X				X	10
		N_1	Y			N_1	Y			N_1	Y	11
			Z				Z				Z	12
			X				X				X	13
R_1	L_2	N_2	Y	R_2	L_2	N_2	Y	R_3	L_2	N_2	Y	14
			Z				Z				Z	15
			X				X				X	16
		N_3	Y			N_3	Y			N_3	Y	17
			Z				Z				Z	18
			X				X				X	19
		N_1	Y			N_1	Y			N_1	Y	20
			Z				Z				Z	21
			X				X				X	22
	L_3	N_2	Y		L_3	N_2	Y		L_3	N_2	Y	23
			Z				Z				Z	24
			X				X				X	25
		N_3	Y			N_3	Y			N_3	Y	26
			Z				Z				Z	27

Fan	F1	F2	F3	F4	F5	F6	F7	F8	F9
Room		R1			R2			R3	
Downrod Length		L1			L2			L3	
Speed		N1			N2			N3	
Direction		X			Y			Z	

Fan	9
Room	3
Downrod Length	3
Speed	3
Direction	3

Total Number of reading
= Fan × Room × Downrod × Speed × Direction
= 9 × 3 × 3 × 3 × 3
= 729

and motor parameters on Noise during the running condition of ceiling fans.[15] The output noise was measured and stored in a personal computer for further analysis of experimentation. The experimental plan is shown in Table 2.

5.2. Experimental Approach

A theoretical approach can be adopted in a case if known logic can be applied that correlaes the various independent and dependent parameters, *i.e.* the input and output parameters of the system. Though qualitatively, the relationships between the dependent and independent parameters are known, based on the available literature, the generalized quantitative relationships are not known sometimes. Hence, formulating the quantitative relationship based on the logic was not possible in the case of complex phenomenon. Because there was no possibility of the formulation of a theoretical model (logic-based), one was left with the only alternative of formulating an experimental data-based model. A field data-base model for the assembly of an electric motor was developed by Tatwawadi.[12] Therefore, it was proposed to formulate such a model in the present investigation. The approach adopted for formulating a generalized experimental model was suggested by Hilbert Schenck, Jr.[2,12,13] This is detailed step-wise below:

- Identification of independent, dependent variables
- Reduction of independent variables adopting dimensional analysis
- Test planning comprising of determination of test envelope, test points, test sequence and experimentation plan
- Physical design of an experimental set up
- Execution of experimentation
- Purification of experimentation data
- Formulation of the model
- Model optimization
- Reliability of the model

Figure 3. FFT Analyzer.

The first six steps mentioned above constitute the design of experimentation. The seventh step constitutes of model formulation, whereas the eighth and ninth steps are respectively the optimization and reliability of the model.

5.3. Identification of Variables

The term 'variables' is used in a very general sense to apply to any physical quantity that undergoes change. If a physical quantity can be changed independent of the other quantities, then it is an 'independent' variable. If a physical quantity changes in response to the variation of one or more independent variables, then it is referred to as a 'dependent' or 'response' variable. If a physical quantity that affects our test is changing in a random and uncontrolled manner, then it is called an 'extraneous' variable.[2] The variables affecting the effectiveness of the phenomenon under consideration are shown in Table 1. The dependent or the response variables in the case of the ceiling fan was noise.

5.4. Reduction of Independent Variables / Dimensional Analysis

Deducing the dimensional equation for a phenomenon reduced the number of independent variables in the experiments. The exact mathematical form of this dimensional equation was the targeted model. This was achieved by applying Buckingham's π theorem.[3,16] When we apply this theorem to a system involving n independent variables (n minus the number of primary dimensions, namely L, M, T, etc.) *i.e.* $(n-3)$, numbers of π terms were formed. When n is large, even by applying this theorem, the number of π terms will not be reduced more significantly than the number of all independent variables. Thus, much reduction in the number of variables was not achieved. It is evident that if we take the product of the dimensionless terms, it will also be dimensionless number. This property was used to achieve further reduction of the number of independent

Table 3. Sensitivity analysis of Response variables.

Pi Terms	Sensitivity
Π_1-% Change	0.816564976
Π_2-% Change	-4.66543575
Π_3-% Change	-20.6502875
Π_4-% Change	6.019966094
Π_5-% Change	0.168556289
Π_6-% Change	2.767424285

π terms, as shown below:

$$\Pi_1 = \frac{N_{bl}.T_{bl}.SW_{bl}.\theta_{bltw}}{W_{bl}.L_{bl}.\theta_{bllf}}; \tag{1}$$

(See Eq. (2) on top of the next page.)

$$\Pi_3 = \frac{L_c.N_h.E_{bl}}{T_c.E_c}; \tag{3}$$

$$\Pi_4 = \frac{N_{nb}.N_w}{N_{sc}}; \tag{4}$$

$$\Pi_5 = \frac{L_r.W_r.A_r.V_s.\text{g}.L.\Phi.}{H_r.V_r.V_{a^2}.A_s.D_s.T.}; \tag{5}$$

$$\Pi_6 = \frac{P.V.N.C}{I}. \tag{6}$$

5.5. Test Planning

This stage comprises deciding on a test envelope, test points, a test sequence, and an experimentation plan for a deduced set of dimensional equations.

5.6. Model Formulation

It was necessary to quantitatively correlate various independent and dependent terms involved in this very complex phenomenon.[3] This correlation is nothing but a Generalized Empirical data-based model as a design tool for such a situation. The Generalized Empirical data-based model for noise is given in Eq. (7) (see the next page).

6. SENSITIVITY ANALYSIS

The influence of the various independent π terms was studied by analysing the indices of the various π terms in the models as shown in Figs. 4 and 5. Through the technique of sensitivity analysis, the change in the value of a dependent π term due to an introduced change in the value of the individual π term was evaluated.[4] In this case, a change of $\pm$ 10% was introduced in the individual independent π term independently (one at a time). Thus, the total range of the introduced change was $\pm$ 20%. The effect of this introduced change on the change in the value of the dependent π term was evaluated. The average values of the change in the dependent π term were due to the introduced change of π 10% in each independent π term. This defines sensitivity. The total percentage of change in output for $\pm$ 10% change in input is shown in Table 3, and indices are shown in Table 4.

$$\Pi_2 = \frac{W_{be1}.C_{be1}.NOB_{be1}.BS_{be1}.GR_{be1}.OR_{be1}.Wt_{be1}.W_{be2}.C_{be2}.NOB_{be2}.BS_{be2}.GR_{be2}.OR_{be2}.Wt_{be2}}{BD_{be1}.OD_{be1}.R_{be1}.Co_{be1}.E_{be1}.N_{be1}.BN_{be1}.BD_{be2}.OD_{be2}.W_{be2}.R_{be2}.Co_{be2}.E_{be2}.N_{be2}.BN_{be2}}; \quad (2)$$

$$\Pi D_1 = 1.002002.\Pi_1^{(0.0407)}.\Pi_2^{(-0.0966)}.\Pi_3^{(-1.022)}.\Pi_4^{(0.2654)}.\Pi_5^{(0.0084)}.\Pi_6^{(0.138)}; \quad (7)$$

Table 4. Indices of model.

Pi Terms	Indices
Π_1	0.0407
Π_2	-0.0966
Π_3	-1.022
Π_4	0.2654
Π_5	0.0084
Π_6	0.138

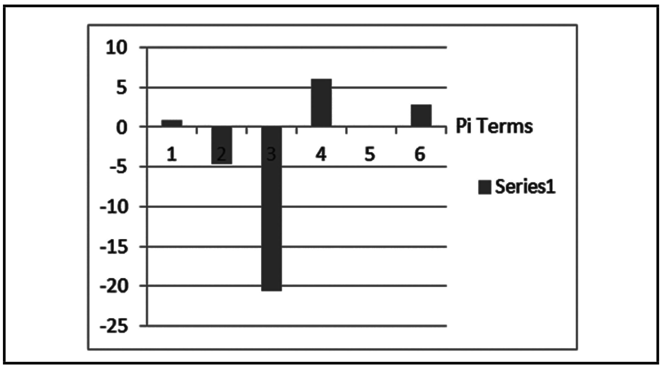

Figure 4. Sensitivity Analysis.

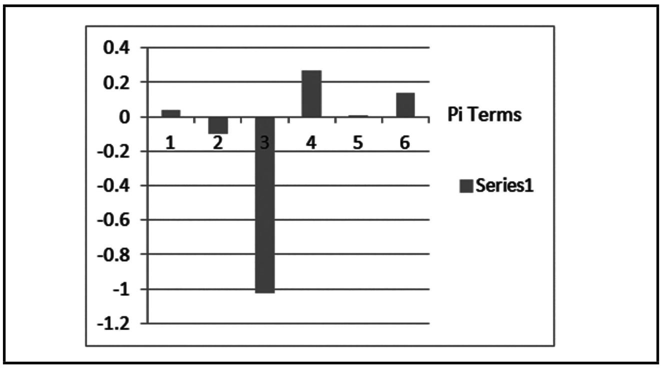

Figure 5. Indices of Model.

7. ESTIMATION OF LIMITING VALUES OF RESPONSE VARIABLES

The final intention of this work was not simply developing the models but to find out the best set of variables, which will result in the maximization or minimization of the response variables. In this section, an attempt was made to find out the limiting values of the response variables. To achieve this, limiting values of the independent π terms, namely Π_1, Π_2, Π_3, Π_4, Π_5, and Π_6 were put in the respective models. In the process of maximization, the maximum value of the independent π term was substituted in the model if the index of the term was positive, and the minimum value was put in if the index of the term was negative. In the process of minimization, the minimum value of the independent π term was put in the model if the index of the term was positive, and the maximum value was put in if the index of the term was negative. The limiting values of these response variables were computed for noise, as shown in Table 5.

Table 5. Limiting values of response variables (noise).

Max. & Min. of Response Pi Terms	Noise
Π_2	1.9737
Π_3	0.4672
Π_6	0.138

8. RELIABILITY OF MODEL

The reliability of the model was established using the relation Reliability = 100 - % mean error, and mean error = $\frac{\sum xi.fi}{\sum xi}$; where xi is percentage of error, and fi is the frequency of occurrence.[8] System Reliability (Rp) is given by the relation = $\Pi_{i=1}^{n}(1 - Ri) = 1 - [(1 - R_1)]$, where Ri is the reliability of the individual model. Therefore, the total reliability of noise is equal to 1-[(1-0.96303105)] = 0.96303105 = 96.303105 %.

9. MODEL OPTIMIZATION

The ultimate objective was the maximization or minimization of the objective functions.[9] The model corresponded to the noise of the ceiling fan. The objective functions for noise needed to be minimized. The model had nonlinear form; therefore, it needed to be converted into a linear form for the purpose of optimization. This was achieved by taking the log of both the sides of the model. The linear programming technique was applied, which is detailed as below for noise.

Taking the log of both the sides of Eq. (7), we get

$$log[\Pi D_1] = log[1.002002] + log[\Pi_1^{(0.0407)}] + log[\Pi_2^{(-0.0966)}] + log[\Pi_3^{(-1.022)}] + log[\Pi_4^{(0.2654)}] + log[\Pi_5^{(0.0084)}] + log[\Pi_6^{(0.138)}]; \quad (8)$$

$$log[\Pi D_1] = log[1.002002] + (0.0407).log[\Pi_1] + (-0.0966).log[\Pi_2] + (-1.022).log[\Pi_3] + (0.32654).log[\Pi_4] + (0.0084).log[\Pi_5] + (0.138).log[\Pi_6]; \quad (9)$$

$$Z(\text{Noise} : \Pi D_1\text{min}) = K + a.X_1 + b.X_2 + c.X_3 + d.X_4 + e.X_5 + f.X_6. \quad (10)$$

Subject to the constraints presented in Eq. (11) (see the top of the next page).

On solving the above problem by using MS solver, we got values of X_1, X_2, X_3, X_4, X_5, X_6, and Z. Thus, ΠD_1 min = Antilog of Z, and corresponding to this value of the ΠD_1 min, the values of the independent π terms were obtained by taking the antilog of X_1, X_2, X_3, X_4, X_5, X_6, and Z. Thus, we optimized the model, and the optimized values of ΠD_1 min, are shown in Table 6.

$$\begin{aligned}
&1 \times X_1 + 0 \times X_2 + 0 \times X_3 + 0 \times X_4 + 0 \times X_5 + 0 \times X_6 \leq \text{-}0.38058\\
&1 \times X_1 + 0 \times X_2 + 0 \times X_3 + 0 \times X_4 + 0 \times X_5 + 0 \times X_6 \geq \text{-}1.18682\\
&0 \times X_1 + 1 \times X_2 + 0 \times X_3 + 0 \times X_4 + 0 \times X_5 + 0 \times X_6 \leq \text{-}0.989601644\\
&0 \times X_1 + 1 \times X_2 + 0 \times X_3 + 0 \times X_4 + 0 \times X_5 + 0 \times X_6 \geq \text{-}0.989601644\\
&0 \times X_1 + 0 \times X_2 + 1 \times X_3 + 0 \times X_4 + 0 \times X_5 + 0 \times X_6 \leq 0.18988\\
&0 \times X_1 + 0 \times X_2 + 1 \times X_3 + 0 \times X_4 + 0 \times X_5 + 0 \times X_6 \geq \text{-}0.30103\\
&0 \times X_1 + 0 \times X_2 + 0 \times X_3 + 1 \times X_4 + 0 \times X_5 + 0 \times X_6 \leq \text{-}0.52288\\
&0 \times X_1 + 0 \times X_2 + 0 \times X_3 + 1 \times X_4 + 0 \times X_5 + 0 \times X_6 \geq \text{-}0.52288\\
&0 \times X_1 + 0 \times X_2 + 0 \times X_3 + 0 \times X_4 + 1 \times X_5 + 0 \times X_6 \leq 0.601653\\
&0 \times X_1 + 0 \times X_2 + 0 \times X_3 + 0 \times X_4 + 1 \times X_5 + 0 \times X_6 \geq \text{-}1.78297\\
&0 \times X_1 + 0 \times X_2 + 0 \times X_3 + 0 \times X_4 + 0 \times X_5 + 1 \times X_6 \leq 0.687115\\
&0 \times X_1 + 0 \times X_2 + 0 \times X_3 + 0 \times X_4 + 0 \times X_5 + 1 \times X_6 \geq \text{-}0.30665
\end{aligned} \tag{11}$$

Table 7. Sequence of influence of independent π terms on dependent π terms.

Dependent Pi terms	Sequence of independent pi terms according to intensity of influence					
Noise: ΠD_1	Π_4	Π_6	Π_1	Π_5	Π_2	Π_3

Table 6. Optimized values of response variables for noise of the ceiling fan.

	Noise: ΠD_1	
Z	0.6591694	1.933186013
X_1	-1.18682	0.305190228
X_2	-0.9896	0.371725351
X_3	0.18988	1.209104496
X_4	-0.52288	0.592810792
X_5	-1.78297	0.168138035
X_6	-0.30665	0.735908124

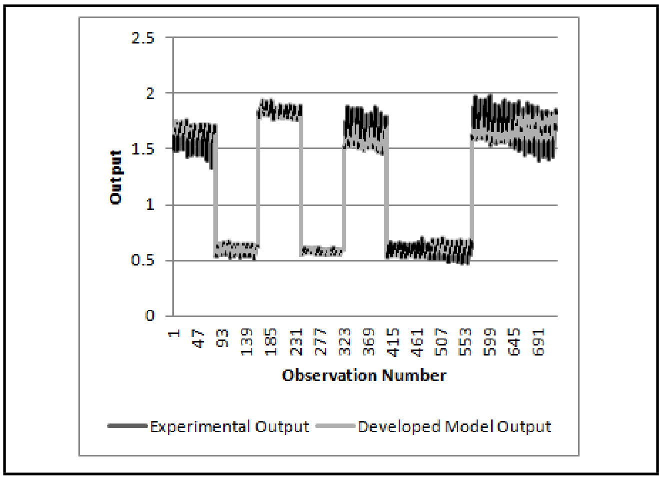

Figure 6. Comparison between Experimental and developed model outputs.

10. RESULTS AND DISCUSSION

The indices of the model are indicates of how the phenomenon is affected because of the interaction of various independent terms in the models. The sequence of influence of the indices of the various independent terms on dependent term is shown in Table 6. The following primary conclusions appear to be justified from the above model:

- The absolute index 0.2654 of Π_4 is the highest index of ΠD_1. The factor Π_4 is related to the number of nuts and bolts, the number of washers, and the number of screws, and it is the most influential term in this model. The value of this index is positive, indicating the involvement of the number of nuts and bolts, the number of washers and the number of screws has a strong impact on ΠD_1.
- The absolute index 0.0084 of Π_5 is the lowest positive index of ΠD_1. The factor Π_5 is related to field parameters, and is the least influential term in this model. The low value of the absolute index indicates that the factor field parameter need improvement.
- The indices of the dependent terms are shown in Table 3. The negative indices indicate the need for improvement. The negative indices of Π_2 (bearing parameters) and Π_3 (clamp parameters) are inversely varying with respect to ΠD_1.
- The constant (K) represents the effect of extraneous (uncontrollable) variables on the phenomenon under investigation, *i.e.* the effect on ceiling fan noise.
- The sensitivity of the input parameters with respective to the noise of the ceiling fan are shown in Table 1.

It is observed that the phenomenon of noise in ceiling fans was very complex because of the variation in the number of variables affecting the phenomenon. The noise responses of the experimental results and DA model results are plotted in the MATLAB, as shown in Fig 6. Both the results overlap each other, which shows that the results obtained by experiment are in close agreement with the results obtained by DA models. The correlation coefficient, root mean square, and reliability are calculated as 0.990176%, 0.07942%, and 95.6978964 %.

Hence, it is clear that the generalized empirical experimental data-based model developed for the noise of a ceiling fan completely represents the phenomenon under investigation. It indicates the validity of the developed model.

11. CONCLUSION

In the present investigation all independent parameters were worked out for the analysis of the noise in ceiling fans. From the analysis, it seems that the developed model can be successfully used for the computation of dependent terms for a given set of independent terms. Indian industries can use the data for the calculation of noise in ceiling fans. From this study, it can be observed that there is a need for modification in the existing experimental setup. The authors proposed the modified ceiling fan setup by using the piezoelectric technique to reduce the noise.

REFERENCES

1. Scharff, Robert. *The Fan Book*, Reston Publishing Co, (1983).
2. Schenck, H. *Theories of Engineering Experimentation*, McGraw Hill Book Co, New York, (1961).
3. Modak, J. P. and Bapat, A. R. Formulation of generalized experimental model for a manually driven flywheel motor and its optimization, *Applied Ergonomics*, U.K., **25** (2), 119–122, (1994).
4. Behzadmehr, *et. al.* Sensitivity analysis of entrance design parameters of a backward-inclined centrifugal fan using DOE method and CFD calculations, *ASME*, **128**, 446–453 (2006).
5. Ho, S. H., *et. al.* Thermal comfort enhancement by using a ceiling fan, *Applied Thermal Engineering,* **29**, 1648–1656, (2009).
6. Neise, W. and Barsikow, B. Acoustic similarity laws for fans, *ASME*, **104**, 162 – 168, (1982).
7. Takushima, A., *et. al.* Fan noise reduction of household refrigerator, *IEEE Transactions on Industry Applications*, **28** (2), 287–292, (1992).
8. Basu, S. K. and Pal, D. K. *Design of Machine Tools*, Oxford and IBH Publishing Co. Pvt. Ltd., Fourth Edition, (1990).
9. Rao, S. S. *Optimization Theory and Applications*, Wiley Eastern Ltd., 2nd Ed., (1984).
10. Benzakein, J. Research on fan noise generation, *Journal of Acoustical Society of America*, **51** (5), 1427–1438, (1972).
11. Beranek, *et. al.* Noise of centrifugal fans, *Journal of Acoustical Society of America*, **27** (2), 217–219, (1955).
12. Tatwawadi, V. H., Modak, J. P., and Chilbule, S. G. Mathematical modelling and simulation of working of an enterprise manufacturing electric motors, *International Journal of Industrial Engineering*, **17** (4), 341–359, (2010).
13. Maling, G. C. Dimensional analysis of blower noise, *The Journal of the Acoustical Society of America*, **35** (10), 1556–1564 (1963).
14. Nashimoto, A., *et. al.* Aerodynamic noise reduction by use of a cooling fan with winglets, *SAE International Journal*, **01-0531**, (2003).
15. Behzadmehr, A., Mercadier, Y., and Galanis, N. Sensitivity analysis of entrance design parameters of a backward-inclined centrifugal fan using DOE method and CFD calculations, *ASME*, **128**, 446–453, (2006).
16. Miragliotta, G. The power of dimensional analysis in production systems design, *Elsevier: International Journal of Production Economics*, **131**, 175–182, (2011).

An Investigation of Initial Shock Cell Formation in Turbulent Coanda Wall Jets

Caroline P. Lubert
James Madison University, Virginia, USA

Christian R. Schwantes
Stanford University, California, USA

Richard J. Shafer
University of Colorado Boulder, Colorado, USA

(Received 1 July 2014; accepted 30 September 2015)

Turbulent Coanda wall jets are present in a multitude of applications.[1] Their obvious advantages for flow deflection are often outweighed by disadvantages related to the increased noise levels associated with such jets. Better predictions of Coanda jet noise would allow the Coanda effect to be more widely applied, and its potential to be fully realized. This paper applies the method of characteristics to a steady two-dimensional axisymmetric supersonic flow in order to determine the location of the first shock cell downstream of the nozzle. This phenomenon has previously been found to be particularly important in determining both the OASPL and peak frequency of the broadband high-frequency Shock-Associated Noise (BBSAN) emitted by a given jet configuration.[10,20] The current work has also illuminated the relationship between cell location and flow characteristics, and thus the effect of jet operating conditions on BBSAN can now be determined.[11] The relationship between cell location and jet breakaway is also under investigation. Predictions are compared with experimental results obtained using flow visualization techniques. This work is in the process of being extended so that the Rankine-Hugoniot conditions can be used to predict the shock cell structure (and thus the BBSAN) along the entire jet.[22]

NOMENCLATURE

C_+	Characteristic moving towards Coanda surface
C_-	Characteristic moving away from Coanda surface
a	Speed of sound (m/s)
(x, y)	Cartesian coordinates of point of interest
(u, v)	Velocity components at point of interest (x, y) along the x and y-axes respectively (m/s)
θ	Angle streamline makes with x-axis
α	Mach angle
λ_+	Slope of characteristic moving towards Coanda surface
λ_-	Slope of characteristic moving away from Coanda surface
δ	Dirac delta function. $\delta = 1$: axisymmetric flow, $\delta = 0$: planar 2D flow
γ	Ratio of specific heat capacities
R_c	Radius of circular part of flare (m)
R_f	Radius of interior stem of flare (m)
h	Exit slot (mm)
y_0	y-value assigned at lip (m)
p_e	Nozzle exit pressure (psig)
p_a	Ambient (atmospheric) pressure (psig)
p_o	Reservoir pressure (psig)
M_e	Exit Mach number
U_{jx}	Jet exit velocity (m/s)

1. INTRODUCTION

1.1. The Coanda Effect

The Coanda effect, discovered early in the twentieth century by Romanian mathematician and scientist Henri Coanda, is the phenomenon whereby '... when a jet is passed over a curved surface it bends to follow the surface, entraining large amounts of air as it does so...'.[1–3] Consider a fluid element exiting a nozzle adjacent to a curved surface. The radial equilibrium of the element leads to the development of a pressure field which forces the fluid against the surface, and this effect is reinforced by the slightly enhanced viscous drag which is experienced by the jet on its wall side as it exits the nozzle, and which also tends to deflect it towards the wall. Subsequently, this pressure field will continue to force the jet towards the surface. An additional viscous effect, namely the entrainment of the ambient fluid between the jet and the surface, may also help to move the jet towards the wall. The effect breaks down under certain operating conditions, at which point jet breakaway occurs. A hysteresis effect is subsequently observed. The Coanda effect is noticed in the natural world (with both positive and negative consequences) and is frequently invoked in aeronautics, maritime technology and industrial engineering.[1] The substantial flow deflection offered by the Coanda principle is generally accompanied by enhanced levels of turbulence and increased entrainment. A direct consequence of these effects is often a significant escalation in the associated noise levels, and it is posited that this disadvantage has prevented its application from becoming more widespread in recent years.[4] Clearly, better understanding of the noise emission characteristics of turbulent Coanda jets will facilitate improvements in prediction and attenuation of such noise.

1.2. Principal Noise Sources Associated with Turbulent Coanda Wall Jets

The jet under consideration here is assumed to issue at high velocity (200–500 m/s) from an annular exit slot. Immediately upon exit it is adjacent to a solid three-dimensional Coanda surface. More detailed information concerning the geometry of interest is shown in Fig. 1. Although this representation is that of a Coanda flare of the type used in the petroleum industry[5,6] (an example of which is shown in operation in Fig. 2), the experimental methods and models developed herein can easily be applied to other types of three-dimensional Coanda jet flows.

Although Coanda jets emit both low- and high-frequency noise, it is the latter that is generally the most destructive, irritating and also the easiest to attenuate. Both broadband noise and discrete tones are emitted, although the appearance of the tones is rather sporadic. Thus, the focus of the current work is on the broadband high-frequency noise. There are two principal sources of such noise in Coanda jets; turbulent mixing noise (TMN) and shock-associated noise (SAN). A comprehensive investigation of TMN associated with these jets has already been undertaken.[7–9] The other principal high frequency acoustic source commonly observed in such flows is SAN, and this paper presents the results of a preliminary investigation into the SAN generated by the mixing layer of a three-dimensional turbulent jet flowing adjacent to a solid Coanda surface.

As mentioned previously, configurations such as that shown in Fig. 1 emit both low- and high-frequency noise. It is the latter that is of greatest interest, since it is both the most annoying to the human ear, and the easiest to attenuate. This paper will focus on SAN.

1.3. Shock Associated Noise (SAN)

It is well known that, in contrast to subsonic jets, conditions at a downstream point in a supersonic jet cannot affect those upstream.[10] In this way, discontinuities in flow properties can arise. Depending upon the relative pressure difference between the nozzle exit pressure (p_e) and the ambient pressure (p_a) a shock cell structure is formed in the jet plume close to the jet exit slot. The interaction between this structure and the large-scale coherent turbulence in the jet shear layer generates the high-frequency sound known as SAN. This phenomenon has been studied in great detail for free jets.[11–15] It has previously been noted that turbulent Coanda wall jets display at least some similar characteristics to their two-dimensional counterparts, and thus in order to facilitate a preliminary investigation into the nature and behavior of SAN in Coanda flows, this simplifying assumption will be made.[7] However, when the flow is three-dimensional, complicating factors such as radial expansion and streamline curvature are present, and should be accounted for in future models.

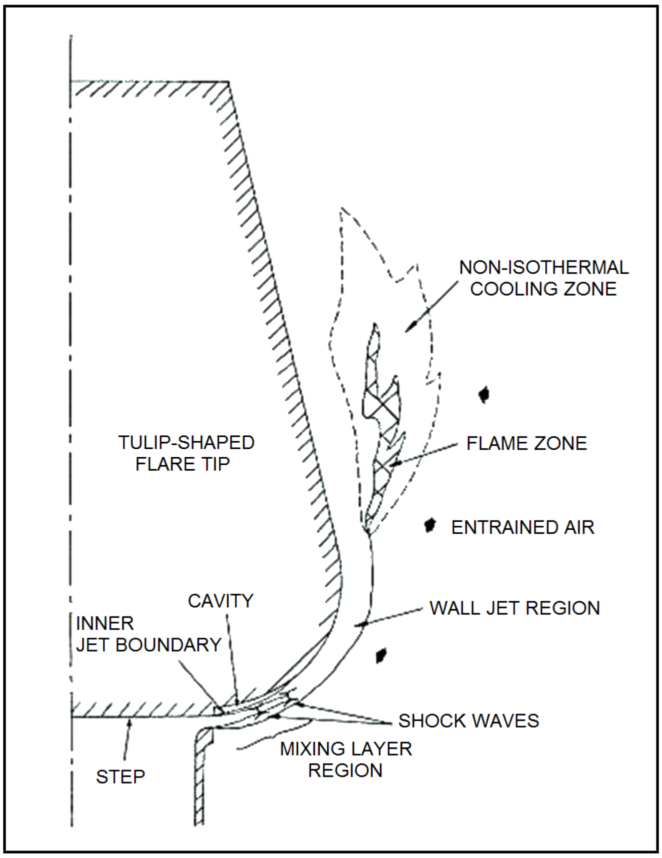

Figure 1. The flow field and combustion zone of a Coanda flare.

2. SHOCK WAVES IN COANDA FLOWS

The flow under consideration in the current work is that associated with a turbulent Coanda flare of the type shown in Fig. 1. Green has shown that one-dimensional flow theory can be used to describe the flow through a convergent-divergent nozzle of the kind present in the Coanda flare.[10] Thus, the jet emerging from the exit slot is supersonic for almost all operating pressures, and shock waves are formed in the vicinity of the nozzle exit. The exact location of these shock waves depends upon the relative magnitudes of the pressure in the reservoir supplying the nozzle, p_0, and the pressure of the medium into which the jet flows, known as the ambient or back pressure, p_a. Assuming that flow in the divergence is isentropic, the jet pressure at exit, p_e, is given by

$$p_e = p_0 \left[1 + \left(\frac{\gamma - 1}{2}\right) M_e^2)\right]^{\frac{-\gamma}{\gamma-1}}; \tag{1}$$

where p_0 is the pressure in the reservoir supplying the nozzle, γ is the ratio of specific heats and M_e is the exit Mach number.[10]

If the pressure at the nozzle exit, p_e, equals the ambient pressure, i.e. $p_e = p_a$, then the jet is said to be correctly expanded. In this case, the jet is parallel-sided with a uniform Mach number throughout, and is free of shock waves. In general, Coanda flare jets are rarely perfectly-expanded in practice, but are typically either under- or over-expanded, and an adjustment of the exit pressure via compression (condensation) or expansion (rarefaction) waves will occur. This leads to the formation of a shock cell structure within the mixing layer region of the jet. See Fig. 1.

Consider, for example, an under-expanded jet. In this case, $p_e > p_a$ and a fan of expansion waves (waves such that the

Figure 2. An operating Coanda flare.

pressure and density of a base flow decrease on crossing them) will be generated at the lip of the nozzle exit slot. On interacting with a free jet boundary, the expansion waves cause the boundary to be displaced outwards, and this effect can be seen in Fig. 3. The expansion waves will reflect as either expansion or compression waves as they interact with a boundary. In order to preserve constant pressure at the jet boundary, the incident and reflected waves will be of opposite kinds and so an expansion wave reflects as a compression wave (pressure and density increase on crossing it) and vice versa. However, when a wave reflects from a solid surface such as the flare-tip, zero normal velocity must be preserved at the wall, and so an expansion wavefront will be reflected as an expansion wavefront, for example.

The coalescence of several compression waves forms a shock wave, which reflects as a shock wave from the solid flare tip surface and then reflects at the jet boundary as an expansion wave. The pattern of expansion waves, compression waves, and shock waves repeats itself periodically and the quasi-periodic constituents of this pattern, known as shock cells, are shown schematically in Fig. 1. Typically a series of 6–10 shock cells will form in the jet exhaust. Figure 3 shows the flow structure typically observed in the mixing layer region of the jet. Shock cells are clearly seen as light and dark lines in the figure. Turbulent eddies convected downstream within the mixing layer region of the jet cause these shocks to be deformed. This distortion of the shock front propagates away as the broadband, but strongly peaked sound waves known as SAN. This acoustic phenomenon has several interesting aspects. Firstly, there is a strong directivity associated with the SAN emitted by moving sound waves. It has been observed

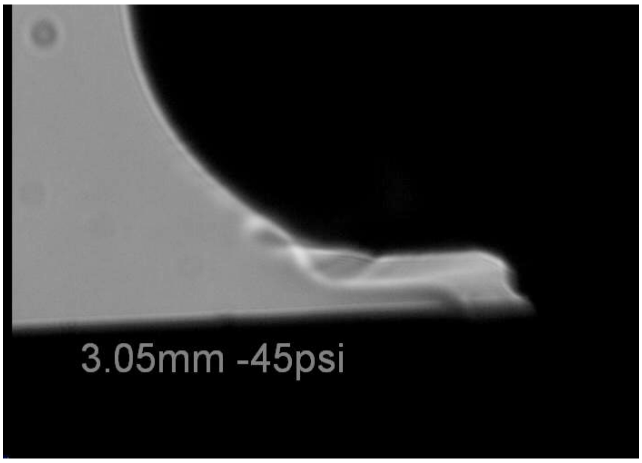

Figure 3. Typical flow structure in Coanda flare mixing layer. Slot width, $h = 3.05$ mm, operating pressure $= 45$ psig.

that a turbulent eddy can successively interact with several shock waves, generating multiple sound sources (one resulting from each interaction).[11] Additionally, a feedback cycle is often present, leading to the generation of discrete, harmonically related tones known as screech tones.

The Coanda flare being studied is convergent-divergent and supersonic under most operating conditions. It is well known that the flow just downstream of the jet exit slot is responsible for most of the flare noise generation and that most of the SAN is produced in this region.[10] Thus in order to fully comprehend this high-frequency acoustic emission, it is very important to understand the behaviour of the flow in the initial region near the nozzle exit. Green has previously shown that one-dimensional flow theory and the method of characteristics can be used to describe flow through this nozzle, at least until the first shock is formed.[7,10,17,18] The method of characteristics has previously been applied[19,20] to the inviscid core of a supersonic jet (following the method of Dash et al.[21] whereby the outer shear layer and surface boundary layer are ignored). In this case, the aim of modelling the jet structure (particularly, first shock cell location) was so that jet breakaway could be better predicted.[19,20] Indeed, comparison of predictions with experimental results for the location of the first shock cell (at low blowing pressures and before any shock waves occur) is good. Specifically, according to Gilchrist and Gregory-Smith, 'The method of characteristics is shown to be adequate for calculating the [shock cell structure in the] inviscid core of the underexpanded [flat] jet'.[20] In the current work, it is the location of the first shock cell that is of interest, since 'for high speed jets, the shock cell structure close to the slot is very important'.[20] Note that in a curved jet, the rapid growth of the outer shear layer (caused by streamline curvature) means that the shock cell structure is shorter than in equivalent plane jets.[20]

3. MATHEMATICAL DETERMINATION OF INITIAL SHOCK CELL LOCATION

3.1. Theory: Method of Characteristics

For a steady two-dimensional irrotational flow, the governing equations are the speed of sound relationship, an equation expressing irrotationality and the Gas Dynamic equation.

These form a system of two coupled quasi-linear nonhomogeneous partial differential equations (PDEs) of the first-order in two independent variables, x and y. (Note that in this context, 'quasi-linear ... of the first-order' means that a PDE is nonlinear in the dependent variables (u and v, the flow velocity components) but linear in the first partial derivatives, (u_x, u_y, v_x, v_y) of these dependent variables). These equations govern both subsonic and supersonic flow. However, the coefficients of the various derivatives are such that the mathematical type of the PDEs changes from elliptic when $M < 1$ (i.e. subsonic flow) to hyperbolic for supersonic flow ($M > 1$). For the two-dimensional supersonic turbulent Coanda flow under consideration, these hyperbolic PDEs can be solved using the Method of Characteristics (MOC). Such equations have the property that they can be reduced to ordinary differential equations (ODEs) known as compatibility equations, which are valid along specific, related curves known as characteristics. Physically, characteristics represent the path of propagation of a physical disturbance.

For a steady two-dimensional irrotational flow, it is well known[16] that the governing equations yield compatibility equations

$$\left(u_{\pm}^2 - a_{\pm}^2\right) du_{\pm} + \left[2u_{\pm}v_{\pm} - \left(u_{\pm}^2 - a_{\pm}^2\right)\lambda_{\pm}\right] dv_{\pm} - \frac{a_{\pm}^2 v_{\pm}}{y_{\pm}} dx_{\pm} = 0; \tag{2}$$

which are valid along the C_+ (where $+$ denotes the direction towards the flare tip surface) and C_- (away from the flare tip) characteristics described by

$$\frac{dy}{dx_{\pm}} = \lambda_{\pm} = \tan\left(\theta_{\pm} \mp \alpha_{\pm}\right); \tag{3}$$

where $\theta_{\pm}$ is the angle that the flow streamline makes with the x-axis, and $\alpha_{\pm}$ is the Mach angle. Note the unusual sign convention used in Eq. (5). This follows that used by Green in which the x-axis is vertical and the y-axis is horizontal.[10] In the case of a supersonic flow, the characteristics are the Mach lines of the flow. Since Eqs. (2) and (3) are non-linear, they must be discretized and solved by numerical means. In the present work, following Green, the Euler predictor-corrector method is used.[10]

3.2. Numerical Solution: Euler Predictor-Corrector Method

Numerical determination of the location of the shock cells in a Coanda flare jet is based on a modified Euler predictor-corrector finite difference method. This is an iterative algorithm that proceeds in two steps. The prediction step calculates a rough approximation of the desired quantities and the corrector step then refines this initial approximation. At each point (x, y) along the characteristics, the velocity components (u, v) associated with that location (x, y) must be determined. In order to do so, the region of interest must be divided into three separate areas: interior points (which have both C_+ and C_- characteristics), wall points (which have only C_+ characteristics) and jet boundary points (with only C_- characteristics).

3.2.1. Interior Points

Equation (3) defines two characteristics passing through a typical interior point, (x, y), in the flow field, and Eq. (2) specifies one relationship between the velocity components u and v on each of the characteristics. In order to be able to find u and v at a given point, (x, y), it is necessary to obtain two independent relationships between u and v at that point. This can be achieved by construction of a network such that two characteristics intersect at a common point. For example, consider the case shown in Fig. 4, where the velocity components (u, v) are known at every point (x, y) along the curve, Γ. The locations of points 1 and 2 are known, as are the velocity components there. The solution at a new point, 4, is found by extending the C_+ characteristic from point 1 and the C_- characteristic from point 2. The location of point 4, (x_4, y_4) and the solution there, (u_4, v_4), are found by simultaneously solving the characteristic and compatibility equations, respectively.

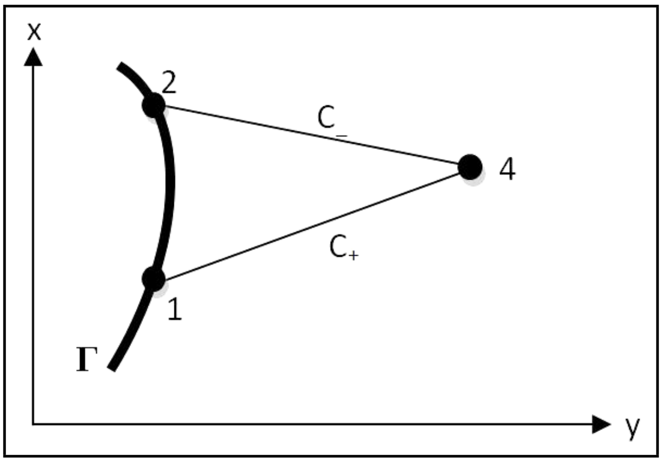

Figure 4. Solution at an interior point by the Method of Characteristics.

From Eq. (3), the characteristic equations can be rewritten in terms of first-order finite difference equations as

$$y_4 - y_1 = \lambda_+(x_4 - x_1); \tag{4}$$

and

$$y_4 - y_2 = \lambda_-(x_4 - x_2). \tag{5}$$

λ_+ and λ_- are given by Eq. (3). Equations (4) and (5) can thus be solved for the two unknowns to yield the new location (x_4, y_4). Recall that the compatibility equation, Eq. (2), is actually two equations. One is

$$\left(u_{+}^2 - a_{+}^2\right) du_{+} + \left[2u_{+}v_{+} - \left(u_{+}^2 - a_{+}^2\right)\lambda_{+}\right] dv_{+} - \frac{a_{+}^2 v_{+}}{y_{+}} dx_{+} = 0; \tag{6}$$

which is valid along the C_+ characteristic, (moving towards the flare surface) and the other comes from Fig. 4, which has 2
known initial values

$$u_+ = u_1, \quad v_+ = v_1, \quad y_+ = y_1. \tag{7}$$

Substituting Eq. (7) into Eq. (6), together with the first order finite difference approximation

$$dx_+ = x_4 - x_1, \quad du_+ = u_4 - u_1, \quad dv_+ = v_4 - v_1; \tag{8}$$

then Eq. (6) becomes a function of only two unknowns, u_4 and v_4. Similarly for the C_- characteristic (moving away from the flare surface). Solving these two equations yields predicted approximations to the location and velocity at a new point, 4,

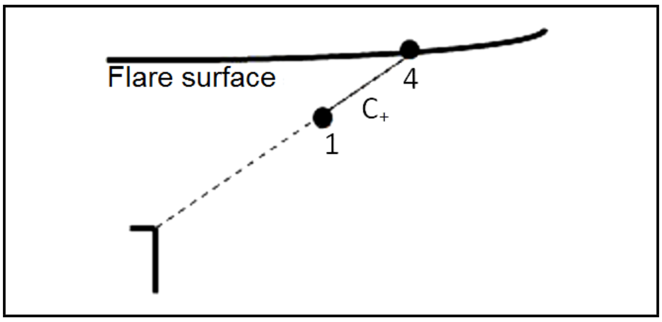

Figure 5. Notation used in MOC for wall points.

namely x_4, y_4, u_4 and v_4. These predictor values are then combined with the initial values to obtain average values of the flow properties using

$$y_+ = \frac{y_1 + y_4}{2}, \quad u_+ = \frac{u_1 + u_4}{2}, \quad v_+ = \frac{v_1 + v_4}{2}; \quad (9)$$

and

$$y_- = \frac{y_2 + y_4}{2}, \quad u_- = \frac{u_2 + u_4}{2}, \quad v_- = \frac{v_2 + v_4}{2}. \quad (10)$$

Note that x is not needed, since it is absent in the compatibility equations. Average values of $\theta_\pm$, $V_\pm$, $a_\pm$, $M_\pm$, $\alpha_\pm$ and $\lambda_\pm$ are then determined by substituting $u_\pm$ and $v_\pm$ from Eqs. (9) and (10) into the previous equations. Substitution of the values thus obtained into the characteristic Eqs. (4) and (5) yields the corrected values, x_4 and y_4. Insertion of these average values, together with the newly obtained corrected values (x_4, y_4) and the first order finite difference approximations into the compatibility equations yields corrected values u_4 and v_4.

These correctors are then used with the initial values to recalculate the average values. Insertion of the new averages yields new corrector values. For a given point (e.g. point 4) the predictor-corrector method should be iterated in this way until the required degree of convergence is reached. This is typically when the difference between two successive sets of corrector values is below a pre-specified tolerance level. Once the flow characteristics for a given interior point are calculated, the entire process is repeated for the next point along the same characteristic in the direction from the nozzle lip to the flare surface (C_+ characteristics).

Once this entire characteristic is formed, the method returns to the nozzle lip and the next C_+ characteristic (fanning away from the lip) and repeats the process. On completion of this fan of characteristics, the method locates the points where each of these characteristics meets the flare surface and, beginning with the left-most point, moves away from that point down a characteristic until it meets the jet boundary. The process is repeated for all these C_- characteristics until that fan is completed. The method then works from the ends of these C_- characteristics (located at the jet boundary) back towards the flare surface, and continues in this way until the first shock wave forms.

3.2.2. Wall Points

In the case of the flare boundary, there are no C_- characteristics since they would lie inside the flare surface (see Fig. 5), and thus the characteristic equations are replaced by a single equation

$$\lambda_+ = \tan(\theta_+ - \alpha_+). \quad (11)$$

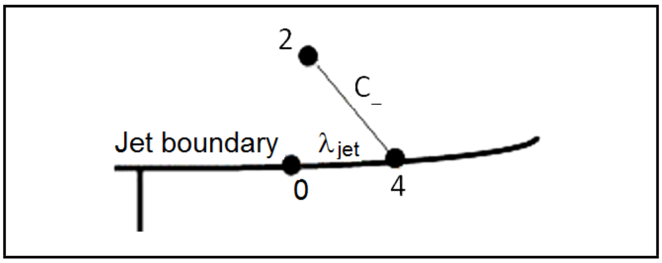

Figure 6. Notation used in MOC for jet boundary points.

Since θ_+ and $\alpha_+$are known, λ_+ can be determined from Eq. (11).

The first order finite difference approximation given by Eq. (4) can be combined with the equation of the Coanda surface, for a given R, d and y_0, namely

$$y_4 = \sqrt{R^2 - (x_4 - R - d)^2} + y_0; \quad (12)$$

and solved to obtain x_4 and y_4. Along the wall, interest is in u_+ and v_+ at the (now) known point (x_4, y_4). Since $\frac{dy}{dx}\big|_{\text{wall}}$ represents the slope of the Coanda surface at the known point (x_4, y_4), then it is a known constant, k. Assuming that the flow has to remain attached to the wall—that is, the velocity follows the tangent to the wall—then

$$\frac{v_4}{u_4} = \frac{dy}{dx}\bigg|_{\text{wall}} = k; \quad (13)$$

or

$$v_4 = k\, u_4. \quad (14)$$

Substitution into the relevant compatibility equation yields the first approximation to the predictors (x_4, y_4) and (u_4, v_4). The predictor-corrector method is then iterated as described previously until the desired stopping criteria is reached.

3.2.3. Jet Boundary Points

For the jet boundary, there are no C_+ characteristics (see Fig. 6), so we have only

$$\lambda_- = \tan(\theta_- + \alpha_-). \quad (15)$$

Again, since θ_- and α_- are known, λ_- can be determined from Eq. (15). Now along the jet boundary

$$\frac{dy}{dx}\bigg|_{\text{jet}} = \lambda_{\text{jet}} = \frac{v_0}{u_0}; \quad (16)$$

where λ_{jet} is approximated numerically by the (constant) slope of the secant line from the previous (known) point on the jet boundary, 0, to the new point, 4, namely

$$\lambda_{\text{jet}} = \frac{y_4 - y_0}{x_4 - x_0}. \quad (17)$$

Thus Eq. (17) relates the two unknowns x_4 and y_4. Also recall from before that the first order finite difference approximation at the jet boundary is given by Eq. (5), which can be rewritten as

$$\lambda_- = \frac{y_4 - y_2}{x_4 - x_2}. \quad (18)$$

Equations (17) and (18) are two equations with two unknowns (x_4 and y_4) and can be solved to find x_4 and y_4. Work is currently underway to determine the jet boundary empirically as a function of slot width, h, and operating pressure, p_0. Once this is known, instead of using Eq. (17) to approximate λ_{jet} numerically using the slope of the secant line between points 0 and 4, the slope can be found analytically (as for the wall point).

Along a free pressure boundary, the total velocity is a function of the pressure, and since the pressure is atmospheric, the total velocity, V_{total} is known.[16] Thus

$$u_4 = (V_{\text{total}}^2 - v_4^2)^{1/2} \tag{19}$$

can be used together with the compatibility equation to determine u_4 and v_4. As previously, the predictor-corrector method is repeated until the desired stopping criteria is reached.

The method is initialized at the nozzle exit with the number of waves in the expansion fan, N_e, and the number of characteristics in the exit plane, N_c. Wherever they intersect, the location (x, y) of these N_c points and the velocity (u, v) at each point is found. The method proceeds along the expansion line towards the flare surface (or jet boundary, depending on whether we are on a C_+ or C_- characteristic) to find the next point. Once the flare surface is reached, the process is repeated for the next expansion line. As soon as the pre-specified number of lines in the expansion fan (N_e) is reached, the method proceeds along their reflections from the flare to the jet boundary and repeats the process. Shock waves are formed where these lines coalesce. The method is based on the assumption that the flow in the expansion region is a simple wave. Figure 7 shows the shock cell structure predicted by the method described above under the operating conditions $p = 60$ psig, $U_{jx} = 418$ m/s, and $h = 3.05$ mm.

Note the free-jet boundary displacement in Fig. 7. This agrees with the observed behaviour shown in Fig. 3 and described in Section 2. Work is currently underway to use experimental data to determine the equation of the flow boundary as a function of jet operating conditions. Input of this more accurate free-jet boundary (rather than the current assumption of a constant jet width, which is clearly highly unrealistic) will lead to an improved MOC model. Other methods of solving the MOC numerically are currently being investigated, and the associated results compared with those of the Euler predictor-corrector method.

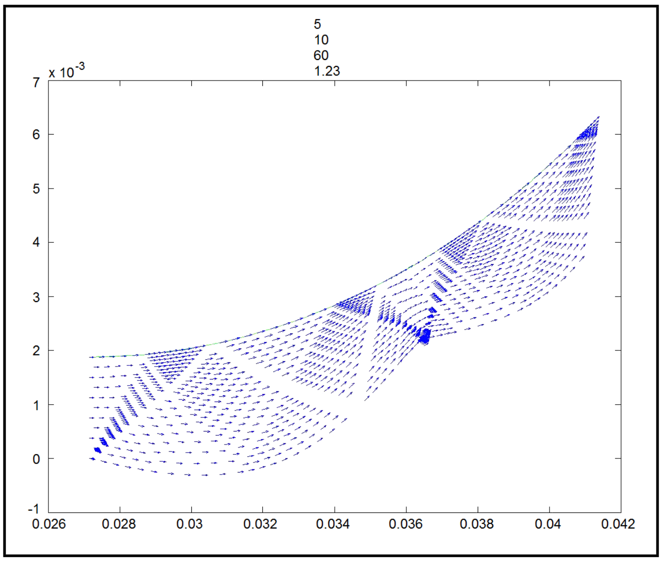

Figure 7. Predicted shock cell structure, $p = 60$ psig, $U_{jx} = 418$ m/s, $h = 3.05$ mm.

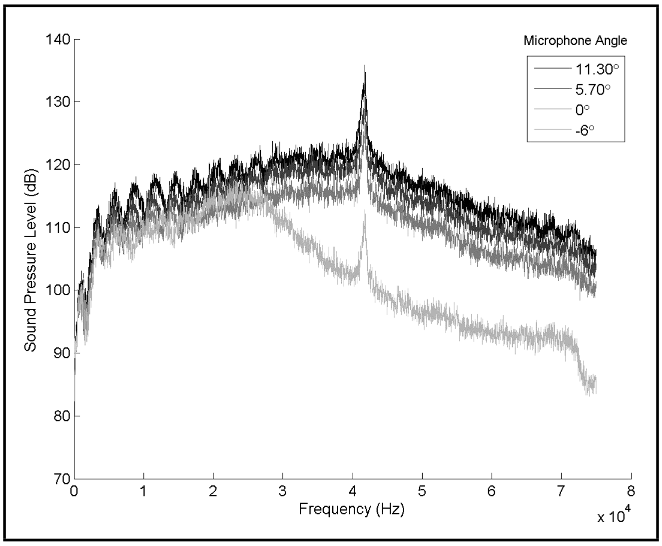

Figure 8. Flare Spectrum (54 mm diameter, 2.39 mm slot width, operating pressure 35 psig).

4. COMPARISON WITH EXPERIMENTAL RESULTS

Experiments were conducted in a 5 m × 2.5 m × 2.5 m anechoic chamber. The Coanda surface had the following dimensions: $R_c = 18.056$ mm, $R_f = 9$ mm. The jet exit velocities (U_{jx}) were between 200 m/s and 500 m/s, and the exit slot (h) varied from 1.14 mm to 3.23 mm. All experiments were carried out at ambient (room) temperature and pressure. Figure 3 shows the flow structure typically observed in the mixing layer region of the jet. Shock cells are clearly seen in the figure, and the interaction of large-scale coherent structures with these shock cells produces both broadband (BBSAN) and discrete-tone SAN, as shown in Fig. 8.

Figure 9 shows the predicted shock cell pattern superimposed on the previously described experimental results, for $U_{jx} = 467$ m/s, and $h = 3.05$ mm. Other predictions exhibit similar features. The arrows represent the (u, v) vectors at each point predicted by the intersections of characteristics, starting with the flow in the exit plane as well as the initial expansion fan. Shock waves are formed at the coalescence of these vectors, and both the dark regions on the flow visualization figures, and the higher concentration of vectors (shown in white) correspond to regions of higher pressure.

Comparison indicates that the preliminary model of SAN is relatively accurate at predicting the location of the first shock cell formation.[24] Cells further from the exit slot are less well predicted, and future work will focus on modifying this preliminary model to include radial expansion and streamline curvature, which is anticipated to improve these predictions.

For reasons described previously, a key characteristic of interest is the location of the first shock cell and its dependence on flow characteristics.[10,20,24] BBSAN has previously been shown to be independent of jet temperature.[11] Figure 10 shows how the location of the first shock appears relatively unaffected by jet exit velocity, U_{jx}. Note that one of the reasons that it is extremely difficult to discern a clear relationship between shock cell behaviour and jet operating characteristics is the presence of occasional, but highly disruptive, discrete tones in

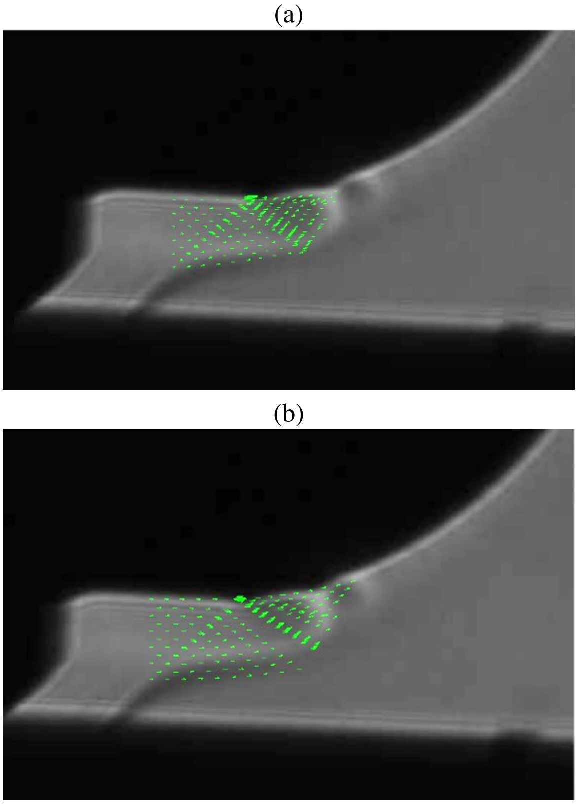

Figure 9. Comparison of experimental and theoretical results. (a) $h = 2.82$ mm; 30 psig (b) $h = 3.23$ mm; 35 psig.

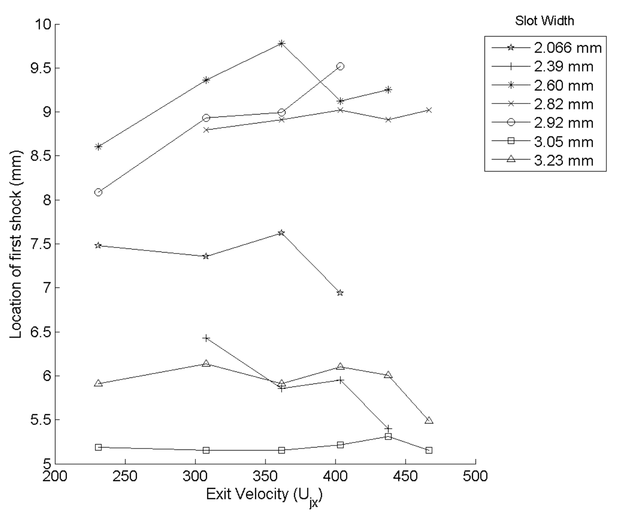

Figure 10. Variation in location of first shock cell with U_{jx}.

some of the experimental data.[11,23–25] From Fig. 11 it appears that the location of the first shock cell is invariant with slot width. However, since the data are sparse, more experiments are needed to confirm this assertion, especially since Powell[24] asserts that the location of the first shock cell is proportional to h.

As mentioned previously, typically 6–10 shock cells are formed in the exhaust of the turbulent Coanda flare jet, with shock cell spacing decreasing as we move away from the exit nozzle. Since the spacings do not vary too much, typically an average shock cell spacing, L, is used. Preliminary data on the variation of shock cell length from cell-to-cell (for the first

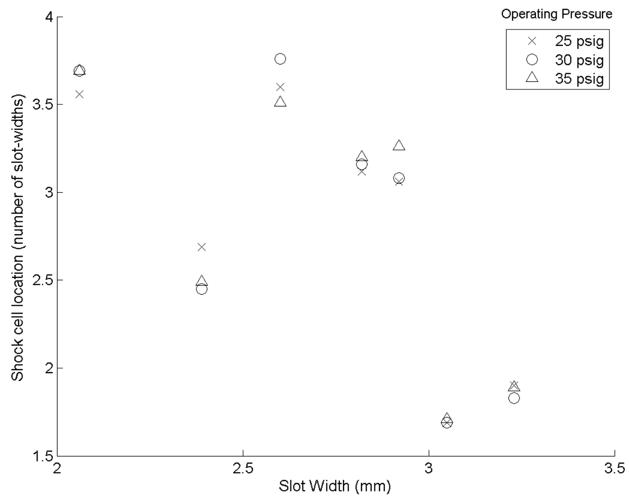

Figure 11. Variation in location of first shock cell with h.

five shocks) indicates that there is no clear pattern with respect to U_{jx} or p from shock to shock. Initial results indicate that the shock cell length is approximately equal to the slot width h,[23] whereas Powell[24] observed in the 2D case that L is proportional to both p and h. Harper-Bourne and Fisher[11] suggest a possible relationship of the form

$$L = 1.1\beta h; \qquad (20)$$

where β is the shock strength, which is a function of the local jet Mach number.

Breakaway is the phenomenon that is often observed in Coanda flows when a lip shock is formed at the lower edge of the exit slot. This lip shock generates a separation bubble on the Coanda surface that grows in size with operating pressure and ultimately causes the flow to separate from the Coanda surface to which it was formerly attached.[7] When parameters such as operating pressure, nozzle exit slot width, and curvature are increased, the location of this separation bubble retreats around the Coanda surface back towards the nozzle exit, and, at some critical point, the flow breaks completely away from the surface.[19] See Fig. 12 for details.

At high speeds, the separation process is usually further complicated by shock wave/boundary layer interaction.[7] The breakaway process is shown in more detail by the set of Schlieren photos in Figs. 13(a)–13(d). In the present experimental work, for a given slot width, the operating pressure was continuously increased until breakaway was observed via the Schlieren flow visualisation system. The observed breakaway slot width-operating pressure (or exit velocity) combinations, are shown in Fig. 14. It should be noted that, for high speed Coanda flows, when the stagnation pressure is increased until breakaway occurs, and then decreased to make the flow reattach, it is found that the pressure has to be reduced to a considerably lower level than the breakaway pressure before reattachment occurs. This hysteresis effect occurs over a substantial range of operating pressures.[7] Figure 15 shows how the SPL is affected by breakaway. As soon as breakaway occurs, a steep drop in SPL is observed, as the flow is redirected away from the horizontal. One of the motivations for the current interest in shock cell location (especially the location of the first shock cell, before the shock waves occur) is the potential for better

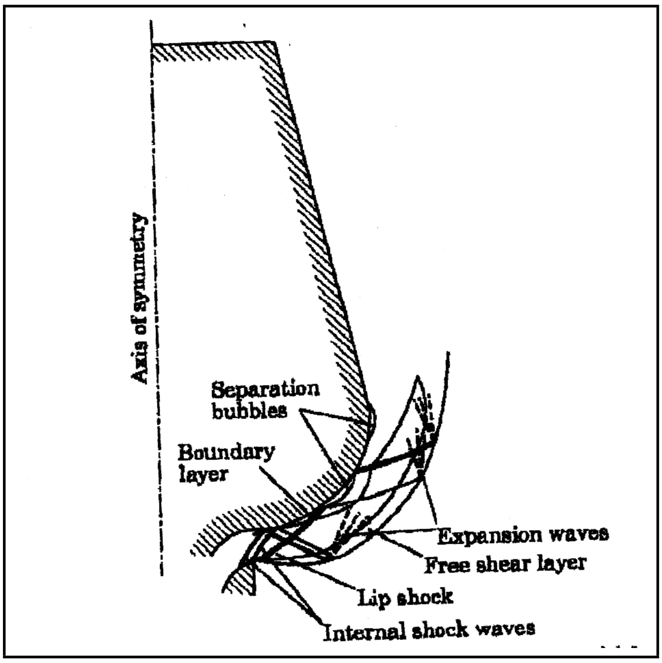

Figure 12. Schematic of key features of the flow field for a Coanda flow.[7] (Reproduced with permission of reference [7]).

prediction of jet breakaway.[20]

Figure 16 shows the frequency spectra for $h = 1.9$ mm and a horizontal observer. For this slot width, breakaway occurs at 23 psig, and this is exhibited in Fig. 15 by the reduced SPL spectrum for 25 psig, compared to 20 psig. This is also exhibited in Fig. 16 by the lower SPL levels observed at 30 psig and 40 psig compared to 20 psig. The relationship between breakaway and location of the first shock cell is currently being investigated. As discussed previously, because of its complex nature, the flare jet is almost always imperfectly expanded.[8] Indeed, the flow near the nozzle exit (especially for a stepped flare) is found to be supersonic and underexpanded at most operating pressures,[10] leading to the formation of a series of shock cells.[8] The interaction of the jet turbulence with these shock waves produces two noise components; screech (discrete) tones and BBSAN.[11] Although BBSAN is generally present, the screech tones (which are thought to be produced by a feedback loop mechanism[24]) require sound waves of sufficient intensity to reach the jet nozzle exit region, or the loop cannot be sustained. Since such waves are not always present;[8] the focus here is on BBSAN. Harper-Bourne and Fisher developed the first prediction method for BBSAN.[11] In their model, the noise generation depends on a nearly coherent interaction between the turbulence in the jet shear layer and the jet shock cell structure. This interaction is modelled by a series of correlated point sources that radiate either constructively or destructively. It is well known that most of the SAN is produced in the region just downstream of the nozzle exit.[10] Thus the location of the shock cells is of primary importance in determining both the BB shock cell noise spectrum and the peak frequency of the BBSAN emitted by a given jet configuration.[11,22] For example, Harper-Bourne and Fisher[11] have shown that the SAN peak frequency, f_p, is related to the (average) shock cell spacing, L, by

$$f_p = \frac{U_c}{L(1 - M_c \cos(\theta))}; \tag{21}$$

where U_c is the eddy convection velocity and $(1 - M_c \cos(\theta))$

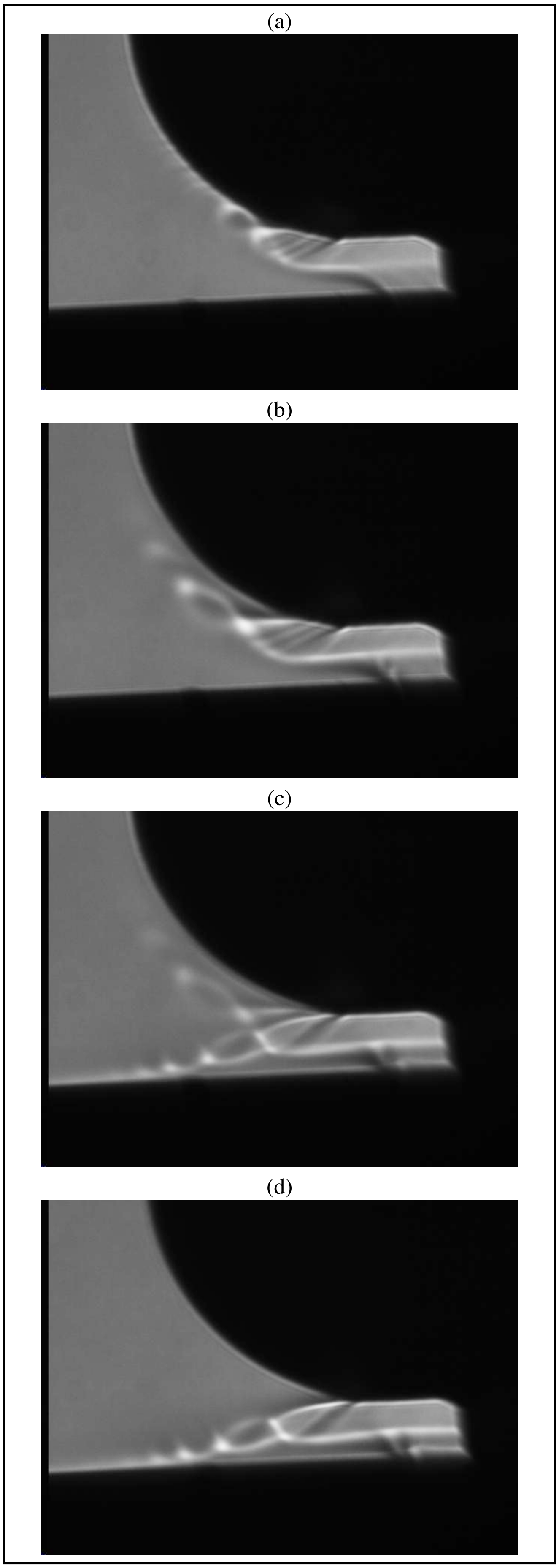

Figure 13. Schlieren photographs showing breakaway, 2.82 mm slot width (a) 45 psig (b) Before breakaway (c) During breakaway (d) After breakaway.

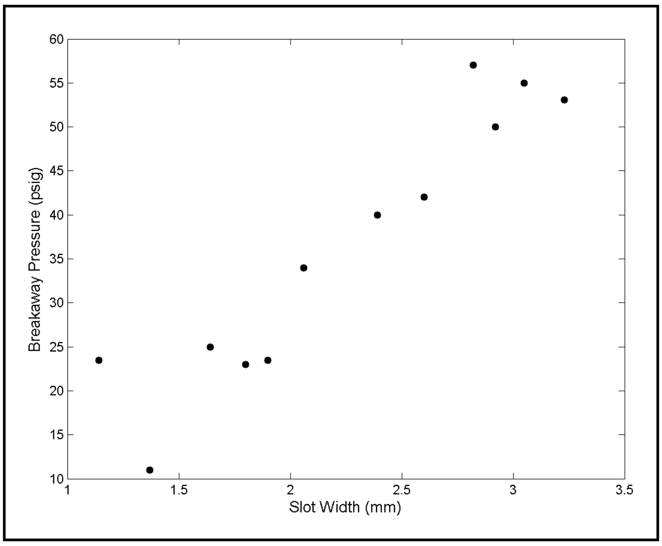

Figure 14. Variation in breakaway pressure with slot width.

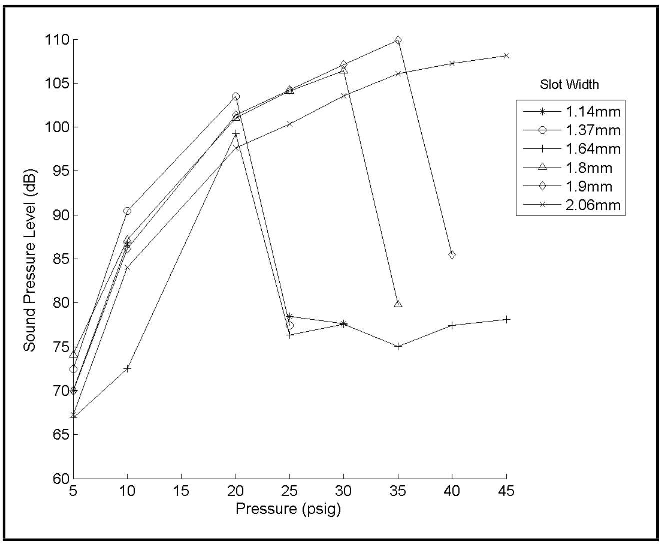

Figure 15. Effect of breakaway on SPL.

is a Doppler factor incorporating the variation in retarded time and source phasing. This agrees with the assertion of Powell[24] for both a 2D nozzle and a round nozzle that the acoustic wavelength is inversely proportional to L.[24]

The current work is part of an effort to illuminate the relationship between cell location and flow characteristics such as operating pressure and slot width. Following the work of Tam et al.,[22] once a computational model has been developed to predict the shock cell structure in the jet, the Fourier modes of the shock cell structure can be calculated. Thus the interaction of the large scale turbulent structures with the shock cells (the source of BBSAN) can be thought of as the interaction of these structures with the different Fourier modes. Interaction with a particular mode generates a unique 'peak' in the shock cell noise spectrum, with the dominant peak usually generated by the first (fundamental) mode.[22] The sound intensity and directionality can also be determined from the geometry of the sound field.[24] Tam et al.[22] obtained good agreement with experimental data by applying these methods to dual stream jets, although they note (as do the current authors) that clearly '…the computation of the shock cell structure is but the first step in the development of a shock cell

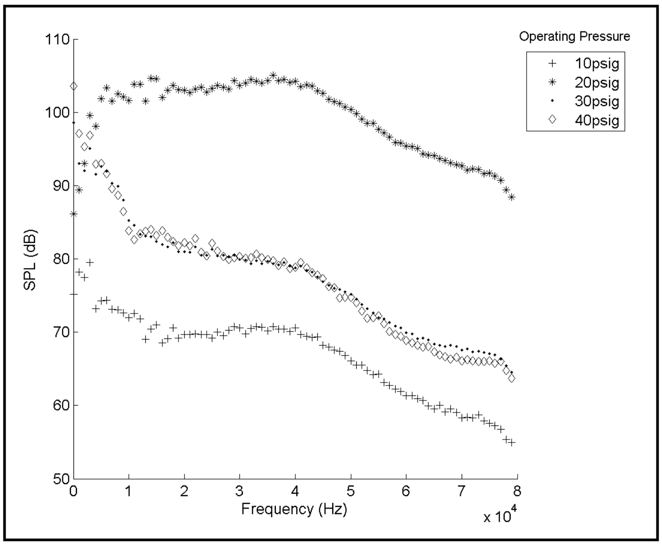

Figure 16. Effect of breakaway on frequency spectra, 1.9 mm slot width.

noise prediction methodology/theory'. Thus the current work is part of an ongoing research programme to combine the previous approaches[11,20,24] to Coanda jets, and in this way (via the determination of the effect of jet operating conditions on shock cell structure), determine the effect of jet operating conditions on BBSAN. It should be noted that alternative models of BBSAN show reasonable agreement with the proposed approach.[12,13,22]

5. SUMMARY AND CONCLUSIONS

A theoretical method of predicting the shock cell structure associated with a three-dimensional turbulent Coanda wall jet is presented, and compared with experimental data. The governing coupled quasi-linear partial differential equations are solved numerically using the MOC with the Euler predictor-corrector method. In addition to being a useful model in its own right, it has been noted[10] that the MOC is useful in helping to interpret Schlieren photos. In this way, the location of the shock cells is determined. The qualitative displacement of the free-jet boundary is accurately modeled by the current method (Fig. 7), as are general features such as the relative invariance of shock cell location with p and h (Figs. 10 and 11). The relatively constant shock cell spacing is also observed in Fig. 7. The presence of discrete tones in the data disrupt observed trends, and means that the data are relatively sparse. Separation of the flow or breakaway is achieved across the entire range of operating conditions ($p = 10 - 60$ psig, $h = 1.14 - 3.23$ mm) at certain pressure/slot width combinations. It occurs at higher pressures for larger slot widths. The relationship between breakaway and the observed shock waves is currently being investigated in more detail by using the Schlieren images (see Fig. 13) in conjunction with the acoustical measurements. Sudden drops in SPL (see Fig. 15) denote that breakaway has occurred, and this is being correlated with the associated operating conditions in an attempt to determine whether such a relationship exists.

Clearly, the above work needs to be extended to better model three-dimensional turbulent Coanda wall jet flows. For example, three-dimensional jets require the inclusion of radial flow and longitudinal vortices. Indeed, such vortices have previously been utilised in Coanda flows to disrupt the coherent structures in a flow, thereby weakening the shock cell structure and reducing the OASPL.[25] Curved 3D jets differ from plane 3D jets because they exhibit radial expansion and streamline curvature. Indeed, in a curved jet, the rapid growth of the outer shear layer (caused by streamline curvature) means that the shock cell structure is shorter than in equivalent plane jets.[20] These features also tend to promote enhanced turbulence levels, and thus Coanda wall jet flows are even more complex than curved free jets, since they contain solid surface/shock wave and shock wave/boundary layer interactions. It is intended that future modelling work will incorporate many of these features.

REFERENCES

1. Lubert, C. P. On some recent applications of the Coanda effect, *International Journal of Acoustics and Vibration*, **16** (3), 144–153, (2011). http://dx.doi.org/10.20855/ijav.2011.16.3286

2. Coanda, H. Procédé de propulsion dans un fluide, *Brevet d'Invention*, Gr. 6 Cl. 2, no. 762688, République Française, (1932).

3. Reba, I. Applications of the Coanda effect, *Scientific American*, **214**, 84–92, (1966). http://dx.doi.org/10.1038/scientificamerican0666-84

4. Lubert, C. P. Application of turbulent mixing noise theory to flows over Coanda surfaces, *International Journal of Acoustics and Vibration*, **13** (1), 17–30, (2008). http://dx.doi.org/10.20855/ijav.2008.13.1221

5. Desty, D. H. No smoke with fire, *Proc. of the Institution of Mechanical Engineers*, **197A**, 159–170, (1983). http://dx.doi.org/10.1243/pime_proc_1983_197_018_02

6. Desty, D. H., Boden, J. C., and Witheridge, R. E. The origination, development and application of novel premixed flare burners employing the Coanda effect, *85th National AIChE Meeting*, Philadelphia, (1978).

7. Carpenter, P. W. and Green, P. N. The aeroacoustics and aerodynamics of high-speed Coanda devices, Part 1: Conventional arrangement of nozzle and surface, *Journal of Sound and Vibration*, **208** (5), 777–801, (1997). http://dx.doi.org/10.1006/jsvi.1997.1202

8. Parsons, C. An experimental and theoretical study of the aeroacoustics of external-Coanda gas flares, PhD Diss., University of Exeter, UK, (1988).

9. Smith, C. and Carpenter, P. W. The effect of solid surfaces on turbulent jet noise, *Journal of Sound and Vibration*, **185** (3), 397–413, (1995). http://dx.doi.org/10.1006/jsvi.1995.0388

10. Green, P. N. The fluid dynamics and aeroacoustics of external Coanda flares, PhD Diss., University of Exeter, UK, (1987).

11. Harper-Bourne, M. and Fisher, M. J. The noise from shock-waves in supersonic jets, *AGARD Conference Proceedings*, **131**, Paper 11-1, (1973).

12. Tam, C. W. K. Stochastic model theory of broadband shock-associated noise from supersonic jets, *Journal of Sound and Vibration*, **116**, 265–302, (1987). http://dx.doi.org/10.1016/s0022-460x(87)81303-2

13. Tam C. W. K. and Tanna, H. K. Shock-associated noise of supersonic jets from convergent-divergent nozzles, *Journal of Sound and Vibration*, **81** (3), 337–358, (1982). http://dx.doi.org/10.1016/0022-460x(82)90244-9

14. Morris, P. J. and Miller, S. A. E. The prediction of broadband shock-associated noise using RANS CFD, *Proc. of the 15th AIAA/CEAS Aeroacoustics Conference*, Paper 2009-3315, (2009). http://dx.doi.org/10.2514/6.2009-3315

15. Miller, S. A. E. and Morris, P. J. The prediction of broadband shock-associated noise including propagation effects, *International Journal of Aeroacoustics*, **11** (7), (2011). http://dx.doi.org/10.2514/6.2011-2923

16. Zucrow, M. J. and Hoffman, J. D. *Gas Dynamics; Volume II*, Krieger, Florida, (1977).

17. Carpenter, P. W. and Green, P. N. The generation of noise in external Coanda-type waste-gas flares, *Proc. of the Institute of Acoustics*, **6** (1), (1984).

18. Bull, D. The shock associated noise of the Indair flare, Undergraduate Project Report, University of Exeter, UK, (1980).

19. Gilchrist, A. R. The development and breakaway of a compressible air jet with streamline curvature and its application to the Coanda flare, PhD Diss., Durham University, UK, (1985).

20. Gilchrist, A. R. and Gregory-Smith, D. G. Compressible Coanda wall jet: Predictions of jet structure and comparison with experiment, *International Journal of Heat and Fluid Flow*, **9** (3), 286–295, (1988). http://dx.doi.org/10.1016/0142-727x(88)90039-2

21. Dash, S. M., Beddini, R. A., Wolf, D. E., and Sinha, N. Viscous/inviscid analysis of curved sub- or supersonic wall jets, *AIAA Journal*, **23** (1), 12–13, (1985). http://dx.doi.org/10.2514/3.8865

22. Tam, C. K. W., Pastouchenko, N. N., and Viswanathan, K. Computation of shock cell structure of dual-stream jets for noise prediction, *AIAA Journal*, **46** (11), (2008). http://dx.doi.org/10.2514/1.37045

23. Lubert, C. On some recent experimental results concerning turbulent Coanda wall jets, *Proc. of Meetings on Acoustics*, **22**, (2015). http://dx.doi.org/10.1121/2.0000040

24. Powell, A. On the mechanism of choked jet noise, *Proceedings of the Physical Society. Section B*, **66**, 1039-1056, (1953). http://dx.doi.org/10.1088/0370-1301/66/12/306

25. Carpenter, P. W. and Smith, C. The aeroacoustics and aerodynamics of high-speed Coanda devices, Part 2: Effects of modification for flow control and noise reduction, *Journal of Sound and Vibration*, **208** (5), 803–822, (1997). http://dx.doi.org/10.1006/jsvi.1997.1203

Geometrically Nonlinear Free Axisymmetric Vibrations Analysis of Thin Circular Functionally Graded Plates Using Iterative and Explicit Analytical Solution

Rachid El Kaak and Khalid El Bikri

Mohammed V University in Rabat, Ecole Normale Supérieure de l'Enseignement Technique de Rabat, Département de génie mécanique, LaMIPI, B.P. 6207, Rabat Instituts, 10100 Rabat, Morocco

Rhali Benamar

Mohammed V University in Rabat, Ecole Mohammadia d'Ingénieurs, LERSIM, Av. Ibn Sina, Rabat, Morocco.

(Received 14 December 2014; accepted 15 June 2015)

This paper deals with nonlinear free axisymmetric vibrations of functionally graded (FG) thin circular plates whose properties vary in thickness. The inhomogeneity of the plate is characterized by a power law variation of the Young's modulus and mass density of the material along the thickness direction, whereas Poisson's ratio is assumed to be constant. The theoretical model is based on Hamilton's principle and spectral analysis using a basis of admissible Bessel's functions to yield the frequencies of the circular plates under clamped boundary conditions on the basis of the classical plate theory. The large vibration amplitudes problem, reduced to a set of nonlinear algebraic equations, is solved numerically. The nonlinear to linear frequency ratios are presented for various values of the volume fraction index n showing a hardening type nonlinearity. The distribution of the radial bending stresses associated to the nonlinear mode shape is also given for various vibration amplitudes and compared with those predicted by the linear theory. Then, explicit analytical solutions are presented, based on the semi-analytical model previously developed by El Kadiri et al. for beams and rectangular plates. This model allows direct and easy calculation for the first nonlinear axisymmetric mode shape with its associated nonlinear frequencies and nonlinear bending stresses of FG circular plates, which are expected to be very useful in engineering applications and in further analytical developments. An excellent agreement is found with the results obtained by the iterative method.

1. INTRODUCTION

The concept of functionally graded materials (FGMs) was first introduced in 1984 as ultrahigh-temperature resistant materials for aircraft, space vehicles, and other engineering applications.[1] FGMs are nonconventional composite materials that are microscopically inhomogeneous, and their mechanical properties vary continuously in one or more directions. This is achieved by gradually varying the volume fraction of the constituent materials. The continuity of the material properties reduces the influence of the presence of abrupt interfaces and avoids high interfacial stresses. Furthermore, FGMs can be tailored to achieve particular desired properties, and the gradation in properties of materials can optimize the stress distribution.

Many studies have been devoted to FG plate vibrations in the literature. Allahverdizadeh et al.[2] investigated the nonlinear free and forced vibration of thin circular FG plates. Praveen and Reddy[3] conducted the nonlinear transient thermoelastic analysis of FG ceramic-metal plates using the finite element method. Yang and Shen[4] examined the dynamic response of initially stressed FGM rectangular thin plates subjected to impulsive loads. The effects of the volume fraction index, the foundation stiffness, the plate aspect ratio, the shape and duration of the applied impulsive load on the dynamic response of FGM plates have been studied in this work. Also, the vibration characteristics and the transient response of shear-deformable FGM plates made of temperature-dependent materials in thermal environments have been examined by Yang and Shen.[5] The differential quadrature technique, the Galerkin approach, and the modal superposition method have been used to determine the transient response of the plate subjected to lateral dynamic loads. Huang and Shen[6] discussed the nonlinear vibration and dynamic response of FG plates in a thermal environment by using an improved perturbation technique. The results reveal that the temperature field and the volume fraction distribution have significant effects on the nonlinear vibration and the dynamic response of simply supported rectangular plates with no in-plane displacements. Reddy and Cheng[7] studied the harmonic vibration problem of FG plates by means of a three-dimensional asymptotic theory formulated in terms of the transfer matrix. Prakash and Ganapathi[8] analyzed the asymmetric flexural vibration and thermoelastic stability of FG circular plates. They used a finite element method to solve the problem. Efraim and Eisenberger[9] studied the exact vibration analysis of thick annular isotropic and FGM plates of variable thicknesses. The motion equations that they obtained by the first order shear deformation theory have been solved by the exact element method. Dong[10] presented an analysis of three-dimensional free vibration of FG annular plates via Chebyshev-Ritz method. Malekzadeh et al.[11] discussed the in-plane free vibration of FG circular arches with temperature-dependent properties under a thermal environment. They assumed that the material properties and temperatures vary along the thickness direction, the governing equation and boundary conditions were obtained by the Hamilton principle. Viswanathan et al.[12] studied free vibration of a symmetric angle-ply laminated annular circular plate of variable thickness using the first order shear deformation theory using spline function approximation. The equations of motion for the plates are derived using the first order shear deformation theory. The solutions of displacement functions are assumed in a separable form to obtain a system of coupled differential equations in terms displacement and rotational functions, and these functions are approximated by Bickley-type splines of order three. The vibration of 3- and 5-layered plates, made up of two types of materials and two types of boundary conditions, are considered. A generalized eigenvalue problem is obtained and solved numerically for an eigenfrequency parameter and for an associated eigenvector of spline coefficients. Ebrahimi[13] studied geometrically nonlinear vibration of a piezoelectrically actuated FGM plate with an initial large deformation, based on Kirchhoff's-Love hypothesis with Von-Karman-type geometrical large nonlinear deformation. Recently, Kermani, Ghayour, and Mirdamad[14] reported a free vibration analysis of multi-directional FG circular and annular plates using a semi analytical/numerical method called state space-based differential quadrature method. Viswanathan, Javed, and Aziz[15] discussed the free vibration of laminated antisymmetric angle-ply annular circular plates with inclusion of the first order shear deformation theory using a spline function approximation by applying a point collocation method. The equations of motion of the plates are derived using first order shear deformation theory.

In the present work, the large axisymmetric free vibration amplitudes of clamped immovable thin FG circular plates is analyzed by using and adapting the model previously presented by Haterbouch and Benamar[16,17] for large vibration amplitudes of isotropic circular plates. By assuming harmonic motion and expanding the transverse displacement in the form of the finite series of basic functions—namely the linear free vibration mode shape of the clamped circular plate—obtained in terms of Bessel's functions, the discretized expressions for the total strain energy and kinetic energy have been derived. In addition to the classical mass and rigidity tensors, a fourth order tensor appears due to the nonlinearity in these expressions. The application of Hamilton's principle reduced the large amplitude free vibration problem to a set of nonlinear algebraic equations, which have been solved numerically in each case, leading to the first nonlinear axisymmetric mode shape of clamped circular plates. The relationships between the nonlinear to linear frequency ratio have been obtained, as well as the mode shape and the non-dimensional maximum vibration amplitude for the first nonlinear mode shape of circular plates, showing hardening type nonlinearity and the dependence of the first mode shape on the amplitude of vibration.

2. GENERAL FORMULATION

2.1. Problem Definition

As mentioned above, FGMs are nonconventional composite materials whose mechanical properties vary continuously due to gradual change in the volume fraction of the constituent material. In this study, a fully clamped thin circular plate of a uniform thickness h and a radius a is considered. The coordinate system is chosen so that the middle plane of the plate coincides with the polar coordinates (r, θ), the origin of the coordinate system being at the centre of the plate with the z-axis downward, the top surface of the plate is ceramic-rich, whereas the bottom surface is metal-rich, as depicted in Fig. 1.

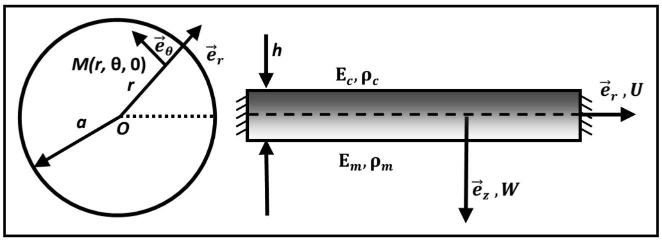

Figure 1. Geometry of FG clamped circular plate.

Table 1. Material properties used in the FG circular plate

Material	Property	
	E (GPa)	ρ (kg/m^3)
Silicon nitride (Si3N4)	355.2715e9	2370
Stainless steel (SUS304)	207.7877e9	8166

2.2. Mechanical Properties of FGCP

FGMs are usually modelled as an inhomogeneous isotropic linear elastic material. However, here it is assumed that the material properties of FGM plates vary continuously through the plate thickness as a function of the volume fraction and the properties of constituent materials, from full ceramic at the top surface to full metal at the bottom. A power law distribution is used for the volume fraction of the constituents (metal and ceramic) as follows:[18]

$$V_m(z) = \left(\frac{z}{h} + \frac{1}{2}\right)^n; \tag{1}$$

$$V_c(z) + V_m(z) = 1; \tag{2}$$

where subscripts m and c refer to the metal and ceramic constituents, respectively; V_m and V_c denote the volume fraction of metal and ceramic, respectively; n is called the volume fraction index or material constant; and z is the thickness coordinate $(-h/2 \leq z \leq h/2)$. Fully metal and fully ceramic are represented in Fig. 2, respectively, by zero and infinity values of the material constant n. Based on the linear role of the mixture, the effective mechanical properties of FGMs can be expressed as[18]

$$P = P_c V_c + P_m V_m; \tag{3}$$

where P_m and P_c denote the specific properties of metallic and ceramic constituents, respectively. Therefore, all the mechanical and thermal properties of the FGM plate, such as Young's modulus, E, can be written as

$$E(z) = E_c + (E_m - E_c)V_m. \tag{4}$$

Poisson's ratio, ν, is assumed to be constant for simplicity and convenience.

In what follows, a metal, stainless steel (SUS304) and ceramics, silicon nitride (Si3N4) system of FGMs is considered. These material properties are given in Table 1.

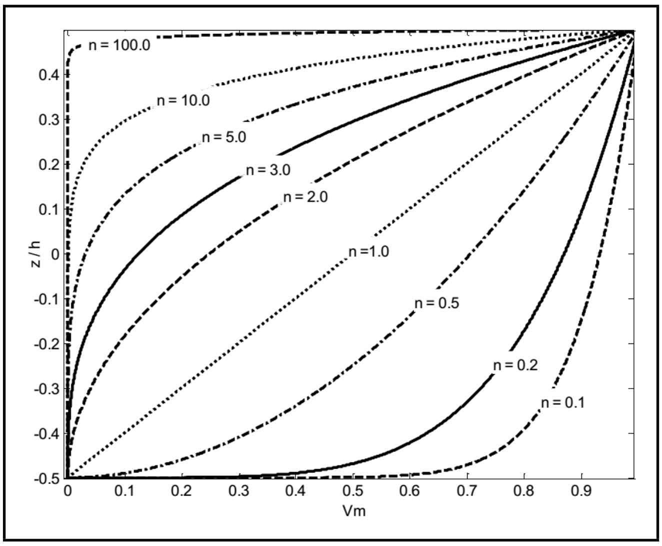

Figure 2. Volume fraction of metal along the thickness.

2.3. Vibration Analysis

Considering axisymmetric vibrations of the FG circular plate, the displacements are given in accordance with the classical plate theory:

$$u_r(r,z,t) = U(r,t) - z\frac{\partial W_{(r,t)}}{\partial r},$$
$$u_\theta(r,t) = 0, \quad u_z(r,t) = W(r,t); \tag{5}$$

where U and W are the in-plane and out-of-plane displacements of the middle plane point $(r,\theta,0)$ respectively, and u_r, u_θ and u_z are the displacements along $\vec{e}_r$, $\vec{e}_\theta$ and $\vec{e}_z$ directions, respectively.

The non-vanishing components of the strain tensor in the case of large displacements are given by Von-Karman relationships:

$$\{\varepsilon\} = \{\varepsilon^0\} + z\{K\} + \{\lambda^0\}; \tag{6}$$

in which $\{\varepsilon^0\}$, $\{K\}$ and $\{\lambda^0\}$ are given by

$$\{\varepsilon^0\} = \begin{bmatrix}\varepsilon_r^0\\ \varepsilon_\theta^0\end{bmatrix} = \begin{bmatrix}\frac{\partial U}{\partial r}\\ \frac{U}{r}\end{bmatrix}; \tag{7}$$

$$\{K\} = \begin{bmatrix}K_r\\ K_\theta\end{bmatrix} = \begin{bmatrix}-\frac{\partial^2 W}{\partial r^2}\\ -\frac{1}{r}\frac{\partial W}{\partial r}\end{bmatrix}; \tag{8}$$

$$\{\lambda^0\} = \begin{bmatrix}\lambda_r\\ \lambda_\theta\end{bmatrix} = \begin{bmatrix}\frac{1}{2}\left(\frac{\partial W}{\partial r}\right)^2\\ 0\end{bmatrix}; \tag{9}$$

For the FGM circular plate shown in Fig. 1, the stress can be expressed as:

$$\{\sigma\} = [Q]\{\varepsilon\} \tag{10}$$

in which $\{\sigma\} = [\sigma_r\ \sigma_\theta]^T$ and the terms of the matrix $[Q]$ can be obtained by the relationships given, for example, in Timoshenko, Weinsowsky-Krieger, and Jones.[19] The force and moment resultants are defined by

$$(N_r, N_\theta) = \int_{-h/2}^{h/2} (\sigma_r, \sigma_\theta)\, dz; \tag{11}$$

$$(M_r, M_\theta) = \int_{-h/2}^{h/2} (\sigma_r, \sigma_\theta)\, z\, dz. \tag{12}$$

The in-plane forces and bending moments in the plate are given by

$$\begin{bmatrix}N\\ M\end{bmatrix} = \begin{bmatrix}A & B\\ B & D\end{bmatrix}\begin{bmatrix}\{\varepsilon^0\} + \{\lambda^0\}\\ \{K\}\end{bmatrix}. \tag{13}$$

A, B, and D are the symmetric matrices given by the following equation:

$$(A_{ij}, B_{ij}, D_{ij}) = \int_{-h/2}^{h/2} Q_{ij}\left(1, z, z^2\right) dz. \tag{14}$$

Here, the Q_{ij}'s are the reduced stiffness coefficients of the plate. The expression for the bending strain energy V_b, the membrane strain energy V_m, the coupling strain energy V_c and the kinetic energy T are given by

$$V_b = \pi \int_0^a D_{11}\left[\left(\frac{\partial^2 W}{\partial r^2}\right)^2 + \frac{1}{r^2}\left(\frac{\partial W}{\partial r}\right)^2 + 2\frac{\nu}{r}\frac{\partial W}{\partial r}\frac{\partial^2 W}{\partial r^2}\right] r\, dr; \tag{15}$$

$$V_m = \pi \int_0^a A_{11}\left[\left(\frac{\partial U}{\partial r}\right)^2 + \frac{\partial U}{\partial r}\left(\frac{\partial W}{\partial r}\right)^2 + \frac{1}{4}\left(\frac{\partial W}{\partial r}\right)^4 + \frac{U^2}{r^2} + \frac{2\nu U}{r}\frac{\partial U}{\partial r} + \nu\frac{U}{r}\left(\frac{\partial W}{\partial r}\right)^2\right] r\, dr; \tag{16}$$

$$V_c = \pi \int_0^a -B_{11}\left[\frac{\partial^2 W}{\partial r^2}\left(\frac{\partial W}{\partial r}\right)^2 + \frac{\nu}{r}\frac{\partial W}{\partial r}\left(\frac{\partial W}{\partial r}\right)^2\right] r\, dr; \tag{17}$$

and

$$T = \pi I_0 \int_0^a \left(\frac{\partial W}{\partial r}\right)^2 r\, dr; \tag{18}$$

where I_0 is the inertial term given by

$$I_0 = \int_{-h/2}^{h/2} \rho(z)\, dz. \tag{19}$$

An approximation has been adopted in the present work consisting of neglecting the contribution of the in-plane displacement U in the membrane strain energy expression. Such an assumption has been made when calculating the first two nonlinear mode shapes of circular plates and fully clamped rectangular plates.[16,20,21,23] For the first nonlinear mode shape, the range of validity of this assumption has been discussed in the light of the experimental and numerical results obtained for the nonlinear frequency-amplitude dependence and the nonlinear bending stress estimates obtained at large vibration amplitude.[20,22] In order to examine the effects of large vibration amplitudes on the membrane stress patterns for clamped circular plates, the contribution of the in-plane displacement U should be taken into account in the membrane strain expression. The assumption introduced above leads to

$$V_m = \frac{\pi A_{11}}{4}\int_0^a \left(\frac{\partial W}{\partial r}\right)^4 r\, dr. \tag{20}$$

The total strain energy, V, is then given by

$$V = \pi \int_0^a \frac{A_{11}}{4}\left(\frac{\partial W}{\partial r}\right)^4 - B_{11}\left[\frac{\partial^2 W}{\partial r^2}\left(\frac{\partial W}{\partial r}\right)^2 + \frac{\nu}{r}\frac{\partial W}{\partial r}\left(\frac{\partial W}{\partial r}\right)^2\right] + D_{11}\left[\left(\frac{\partial^2 W}{\partial r^2}\right)^2 + \frac{1}{r^2}\left(\frac{\partial W}{\partial r}\right)^2 + 2\frac{\nu}{r}\frac{\partial W}{\partial r}\frac{\partial^2 W}{\partial r^2}\right] r\,dr. \tag{21}$$

2.3.1. Discretization of the Total Strain and Kinetic Energy Expressions

If the space and time functions are supposed to be separable and harmonic motion is assumed, the transverse displacement W can be written as

$$W(r,t) = w(r)\sin(\omega t). \tag{22}$$

The spatial function $w(r)$ is expanded in the form of a finite series of n basic functions $w_i(r)$ as follows:

$$w(r) = a_i w_i(r); \tag{23}$$

in which the usual summation convention for the repeated index i is used over the range $[1, n]$. The transverse displacement $W(r,t)$ is then given by:

$$W(r,t) = a_i w_i(r)\sin(\omega t). \tag{24}$$

The discretization of the total strain and kinetic energy expressions is made by substituting the expression for $W(r,t)$ given in Eq. (24) into Eqs. (18)–(21) and rearranging. This leads to the following expressions:

$$V = \frac{1}{2}a_i a_j k_{ij}\sin^2(\omega t) + \frac{1}{2}a_i a_j a_k c_{ijk}\sin^3(\omega t) + \frac{1}{2}a_i a_j a_k a_l b_{ijkl}\sin^4(\omega t); \tag{25}$$

$$T = \frac{1}{2}\omega^2 a_i a_j m_{ij}\cos^2(\omega t); \tag{26}$$

in which m_{ij}, k_{ij}, b_{ijkl} and c_{ijk} are the mass tensor, the linear rigidity tensor, the fourth order nonlinear rigidity tensor and the third order nonlinear coupling tensor, respectively. The expressions for these tensors are

$$m_{ij} = 2\pi I_0 \int_0^a w_i w_j r\,dr; \tag{27a}$$

$$k_{ij} = 2\pi D_{11}\int_0^a \left(\frac{d^2 w_i}{dr^2}\frac{d^2 w_j}{dr^2} + \frac{1}{r^2}\frac{dw_i}{dr}\frac{dw_j}{dr} + 2\frac{\nu}{r}\frac{dw_i}{dr}\frac{d^2 w_j}{dr^2}\right) r\,dr; \tag{27b}$$

$$c_{ijk} = -2\pi B_{11}\int_0^a \left(\frac{d^2 w_i}{dr^2}\frac{dw_j}{dr}\frac{dw_k}{dr} + \frac{\nu}{r}\frac{dw_i}{dr}\frac{dw_j}{dr}\frac{dw_k}{dr}\right) r\,dr; \tag{27c}$$

$$b_{ijkl} = \frac{\pi A_{11}}{2}\int_0^a \left(\frac{dw_i}{dr}\frac{dw_j}{dr}\frac{dw_k}{dr}\frac{dw_l}{dr}\right) r\,dr. \tag{27d}$$

2.3.2. Formulations of the Governing Equations

The dynamic behavior of the structure is governed by Hamilton's principle, which is symbolically written as

$$\delta \int_0^{\pi/2\omega} (V - T)dt = \delta\emptyset = 0. \tag{28}$$

Replacing T and V by their discretized expressions given by Eqs. (25) and (26) in the energy condition Eq. (28), integrating the time functions in the range $\left[0, \frac{\pi}{2\omega}\right]$ and calculating the derivatives with respect to the a_i's leads to the following equation:

$$\frac{3\pi}{32\omega}a_j a_k a_l b_{rjkl} + \frac{3\pi}{32\omega}a_i a_k a_l b_{irkl} + \frac{3\pi}{32\omega}a_i a_j a_l b_{ijrl} + \frac{3\pi}{32\omega}a_i a_j a_k b_{ijkr} - \left(\frac{\pi}{8\omega}a_j m_{rj}\omega^2 + \frac{\pi}{8\omega}a_i m_{ir}\omega^2\right) + \left(\frac{\pi}{8}a_j k_{rj} + \frac{\pi}{8}a_i k_{ir}\right) + \left(\frac{2}{6\omega}a_j a_k c_{rjk} + \frac{2}{6\omega}a_i a_k c_{irk} + \frac{2}{6\omega}a_i a_j c_{ijr}\right) = 0. \tag{29}$$

The precedent equation can be rewritten as:

$$\left(\frac{\pi}{4\omega}a_i k_{ir}\right) + \left(\frac{3\pi}{8\omega}a_i a_j a_k b_{ijkr}\right) + \left(\frac{1}{\omega}a_i a_j c^s_{ijr}\right) - \left(\frac{\pi}{4\omega}a_i m_{ir}\omega^2\right) = 0. \tag{30}$$

It appears from Eqs. (27a)–(27b) and (27d) that the tensors m_{ij} and k_{ij} are symmetric, and that the fourth order tensor b_{ijkl} is such that

$$b_{ijkl} = b_{klij} = b_{jilk} = b_{ikjl}. \tag{31}$$

On the other hand, a third order tensor c^s_{ijk} is defined by Eq. (29) such that

$$c^s_{ijk} = \frac{1}{3}\left(c_{kij} + c_{ikj} + c_{jik}\right). \tag{32}$$

Consequently, Eq. (28) reduces to the following set of nonlinear algebraic equations:

$$a_i k_{ir} + \frac{3}{2}a_i a_j a_k b_{ijkr} + \frac{4}{\pi}a_i a_j c^s_{ijr} - \omega^2 a_i m_{ir} = 0; \tag{33}$$

for $r = 1, \ldots, n$. This can be written in a matrix form as

$$\{A\}^T[K]\{A\} + \frac{3}{2}\{A\}^T[B(A)]\{A\} + \frac{4}{\pi}\{A\}^T[C(A)]\{A\} - \omega^2\{A\}^T[M]\{A\} = 0. \tag{34}$$

Pre-multiplying Eq. (30) by the vector $(A)^T = [a_1\ a_2 \ldots a_n]$ leads to the following expression for ω^2:

$$\omega^2 = \frac{a_i a_j k_{ij} + \frac{3}{2}a_i a_j a_k a_l b_{ijkl} + \frac{4}{\pi}a_i a_j a_k c^s_{ijk}}{a_i a_j m_{ij}}. \tag{35}$$

To simplify the analysis and the numerical treatment of the set of nonlinear algebraic equations, a non-dimensional formulation has been considered by putting the spatial displacement function as

$$w_i(r) = h w_i^*(r^*); \tag{36}$$

where $r^* = r/a$, the non-dimensional radial coordinate, and Eq. (30) may be rewritten in non-dimensional form as

$$2a_i k_{ir}^* + 3a_i a_j a_k b_{ijkr}^* + \frac{8}{\pi} a_i a_j c_{ijr}^{s*} - 2\omega^{*2} a_i m_{ir}^* = 0. \quad (37)$$

The m_{ij}^*, k_{ij}^*, c_{ijk}^* and b_{ijkl}^* terms are non-dimensional tensors related to the dimensional ones by the following relationships:

$$m_{ij} = 2\pi I_0 h^2 a^2 m_{ij}^*; \quad (38a)$$

$$k_{ij} = \frac{2\pi D_{11} h^2}{a^2} k_{ij}^*; \quad (38b)$$

$$c_{ijk} = \frac{-2\pi B_{11} h^3}{a^2} c_{ijk}^*; \quad (38c)$$

$$b_{ijkl} = \frac{\pi A_{11} h^4}{2a^2} b_{ijkl}^*. \quad (38d)$$

These non-dimensional tensors are defined by

$$m_{ij}^* = \int_0^a w_i^* w_j^* r^* dr^*; \quad (39a)$$

$$k_{ij}^* = \int_0^a \left(\frac{d^2 w_i^*}{dr^{*2}} \frac{d^2 w_j^*}{dr^{*2}} + \frac{1}{r^{*2}} \frac{dw_i^*}{dr^*} \frac{dw_j^*}{dr^*} + 2\frac{\nu}{r^*} \frac{dw_i^*}{dr^*} \frac{d^2 w_j^*}{dr^{*2}} \right) r^* dr^*; \quad (39b)$$

$$c_{ijk}^* = \beta \int_0^a \left(\frac{d^2 w_i^*}{dr^{*2}} \frac{dw_j^*}{dr^*} \frac{dw_k^*}{dr^*} + \frac{\nu}{r^*} \frac{dw_i^*}{dr^*} \frac{dw_j^*}{dr^*} \frac{dw_k^*}{dr^*} \right) r^* dr^*; \quad (39c)$$

$$b_{ijkl}^* = \alpha \int_0^a \left(\frac{dw_i^*}{dr^*} \frac{dw_j^*}{dr^*} \frac{dw_k^*}{dr^*} \frac{dw_l^*}{dr^*} \right) r^* dr^*; \quad (39d)$$

where ω^* is the non-dimensional nonlinear frequency parameter defined by

$$\omega^{*2} = \gamma \omega^2; \quad (40)$$

in which ω^{*2} is given by the following expression:

$$\omega^{*2} = \frac{a_i a_j k_{ir}^* + \frac{3}{2} a_i a_j a_k a_l b_{ijkr}^* + \frac{4}{\pi} a_i a_j a_k c_{ijk}^{s*}}{\omega^{*2} a_i a_j m_{ir}^*}. \quad (41)$$

The parameters α, β, and γ are given by

$$\alpha = \frac{A_{11} h^2}{4D_{11}}; \quad (42a)$$

$$\beta = \frac{-B_{11} h}{D_{11}}; \quad (42b)$$

$$\gamma = \frac{I_0 a^4}{D_{11}}. \quad (42c)$$

2.4. Bending Stress Expressions

The bending strains ε_{br} and $\varepsilon_{b\theta}$ are given by

$$\varepsilon_{br}(z) = -z \left(\frac{d^2 w}{dr^2} \right); \quad (43a)$$

$$\varepsilon_{b\theta}(z) = -z \left(\frac{1}{r} \frac{dw}{dr} \right). \quad (43b)$$

By using the classical thin plate assumption of plane stress and Hooke's law, the radial and circumferential bending stresses are given by

$$\sigma_{br} = -\frac{zE(z)}{(1-\nu^2)} \left[\left(\frac{d^2 w}{dr^2} \right) + \nu \left(\frac{1}{r} \frac{dw}{dr} \right) \right]; \quad (44)$$

$$\sigma_{b\theta} = -\frac{zE(z)}{(1-\nu^2)} \left[\left(\frac{1}{r} \frac{dw}{dr} \right) + \nu \left(\frac{d^2 w}{dr^2} \right) \right]. \quad (45)$$

In terms of the non-dimensional parameters defined in the previous section, the radial and circumferential bending stresses σ_{br} and $\sigma_{b\theta}$ can be defined by

$$\sigma_{br} = -\frac{z^* E(z^*) h^2}{(1-\nu^2) a^2} \left[\left(\frac{d^2 w^*}{dr^{*2}} \right) + \nu \left(\frac{1}{r^*} \frac{dw^*}{dr^*} \right) \right]; \quad (46)$$

$$\sigma_{b\theta} = -\frac{z^* E(z^*) h^2}{(1-\nu^2) a^2} \left[\left(\frac{1}{r^*} \frac{dw^*}{dr^*} \right) + \nu \left(\frac{d^2 w^*}{dr^{*2}} \right) \right]. \quad (47)$$

Table 2. Non-dimensional linear frequencies, associated with the axisymmetric modes of a clamped FG circular plate for $i = 1, \ldots, 6$.

i	1	2	3	4	5	6
$(\omega_l^*)_i$	10.21	39.77	89.10	158.18	247.00	355.56

3. NUMERICAL RESULTS AND DISCUSSION

3.1. Numerical Details

The basic functions w_i^* to be used in the expansion series of w in Eq. (23) must satisfy the theoretical clamped boundary conditions (i.e., zero displacement and zero slopes along the circular edge). Since the linear problem of free axisymmetric flexural vibration of a clamped circular plate has an exact analytical solution, the chosen basic functions w_i^* were taken as the linear free oscillation mode shapes of fully clamped circular plates given by[24]

$$w_i^*(r^*) = A_i \left[J_0(\beta_i r^*) - \frac{J_0(\beta_i)}{I_0(\beta_i)} I_0(\beta_i r^*) \right]. \quad (48)$$

where β_i is the i^{th} real positive root of the transcendental equation

$$J_1(\beta) I_0(\beta) + J_0(\beta) I_1(\beta) = 0; \quad (49)$$

in which J_n and I_n are, respectively, the Bessel and the modified Bessel functions of the first kind and of order n. The parameter β_i is related to the i^{th} non-dimensional linear frequency parameter $(\omega_l^*)_i$ of the plate by

$$\beta_i^2 = (\omega_l^*)_i. \quad (50)$$

Leissa's study[25] features examples of numerical values of $(\omega_l^*)_i$, and the first six values are given here in Table 2. A_i is chosen such that

$$\int_0^1 w_i^{*2} r^* dr^* = 1. \quad (51)$$

Therefore, a set of orthonormal functions, and the mass tensor associated with the chosen transverse displacement is given by

$$m_{ij}^* = \int_0^1 w_i^* w_j^* r^* dr^* = \delta_{ij}; \quad (52)$$

where δ_{ij} is the Kronecker delta symbol. The first six basic functions w_i^*, $i = 1, \ldots, 6$ are plotted in Fig. 3.

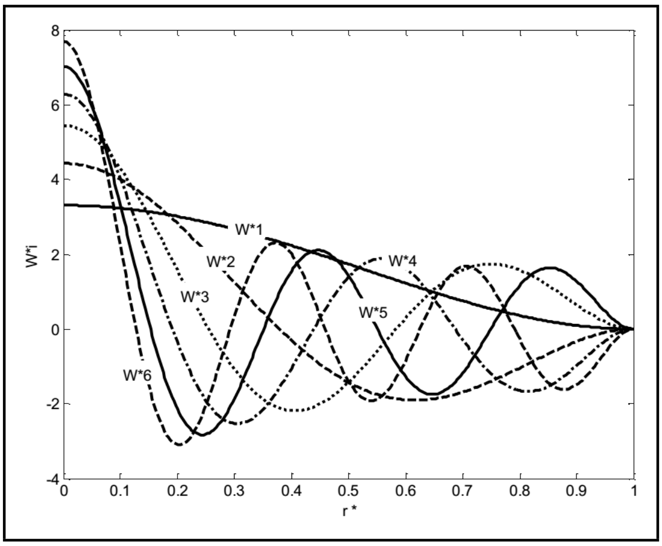

Figure 3. Axisymmetric out-of plane natural modes of vibration for a clamped circular plate W_i^* for $i = 1, \ldots, 6$.

3.2. Iterative Method of Solutions and Analysis of Numerical Results

3.2.1. Iterative Method of Solutions

The set of nonlinear algebraic Eqs. (37) has been solved numerically by using the Harwell library routine NS01A, based on a hybrid iterative method combining the steepest descent and Newton's methods to obtain the numerical results presented for the first nonlinear mode shape of a thin FG circular plate. This method does not require a very good initial estimate of the solution or a step procedure, similar to other methods described for beams and rectangular plates.[20–23] It was adopted here to ensure rapid convergence when varying the amplitude, which allowed solutions to be obtained with a quite reasonable number of iterations. The fundamental nonlinear mode shape was calculated in the neighborhood of the linear solution corresponding to a small numerical value of the coefficient $a_{r0}(r_0 = 1)$ of the basic function w_{r0}^*. The resulting solution was then used as an initial estimate for the following step corresponding to higher values of $a_{r0}(r_0 = 1)$.

3.2.2. Numerical Results and Discussion

The first six linear axisymmetric eigenfunctions of the model presented above were used, respectively, to obtain the first nonlinear axisymmetric mode shape. The results obtained numerically from iterative solutions of the nonlinear algebraic system Eq. (37) are summarized in Table 3. The computed values of $a_2, a_3, \ldots, a_6$ obtained for assigned values of a_1 varying from 0.005 to 0.75 correspond to maximum dimensionless vibration amplitudes varying from 0.0165 to 2.386 and are given in Table 3. In each table, a_i represents the contribution of the i^{th} basic function w_i^*. The variable $w_{\max}^*$ is the maximum non-dimensional amplitude, and $(\omega_{nl}^*/\omega_l^*)$ is the ratio of the non-dimensional nonlinear frequency parameter defined in Eq. (41) to the corresponding non-dimensional linear frequency parameter given in Table 3. It can be seen from this table that the non-dimensional nonlinear frequencies calculated here from the nonlinear analysis for low amplitudes of up to 0.04 (very small values of a_1 and a_2) coincide exactly with the corresponding linear ones. Also, near to the linear frequency of a given mode, only the corresponding basic function has a significant contribution. At large vibration amplitudes, the mode contributions and the resonance frequency increase with the amplitude of vibration. The corresponding rate of increase decreases with the order of the mode considered and becomes negligible for the higher modes.

Table 4. Effect of large vibration amplitudes on the frequencies of the first non-linear axisymmetric mode shape of a clamped FG circular plate ($n = 0.5$).

Non-linear frequency ratio			
$W_{\max}^*$	n	Present work	From graph[2]
0.2	0.5	1.0076	1.0074
0.4		1.0300	1.0259
1.0		1.1752	1.1629
1.5		1.3626	1.3370

Table 5. Frequency ratio $(\omega_{nl}^*/\omega_l^*)$ of a clamped isotropic circular plate ($n = 0.0$).

$W_{\max}^*$	2008[2]	2003[16]	1961[26]	1962[27]	Present analysis
0.2	1.0075	1.0072	1.0070	1.0079	1.0108
0.4	1.0296	1.0284	1.0278	1.0313	1.0421
0.8	1.1135	1.1073	1.1065	1.1194	1.1560
1.0	1.1724	1.1615	1.1617	1.1808	1.2318
1.5	1.3567	1.3255	1.3343	1.3711	1.4542

3.2.3. Amplitude Frequency Dependence

The dependence of the nonlinear frequency on the non-dimensional vibration amplitude is listed in Table 4 for the first nonlinear axisymmetric mode shape of the FG circular plate for $n = 0.5$. From this table, it is observed that the nonlinear frequency increases with increasing vibration amplitudes. It can be also observed that the results calculated via the present model exhibit a higher increase of the frequency compared with those obtained by Haterbouch and Benamar[2] with a discrepancy of 6.22% for a value of the non-dimensional amplitude $w_{\max}^* = 1.0$ and 0.41% for a non-dimensional vibration amplitude $w_{\max}^* = 0.2$. This may be attributed to the negligence of in-plane displacements in the present theory. Table 5 shows the comparison of the nonlinear frequency ratio of the first mode shape of the isotropic circular plates (case of $n = 0$) with those obtained for some isotropic circular plates in the literature.

Figure 4 shows the dependence of the frequency ratio of the clamped FG circular plate on the amplitude of vibration for various values of the power law index n. As may be seen in this figure, by increasing the values of the power law index in the range $[0, 2]$, the frequency increases. For values higher than $n = 2.0$, the frequency decreases when n increases. This may be expected, since when the power law index $n = 0.0$ or $n = 1000.0$, the material is pure metallic or pure ceramic, respectively, and the non-dimensional frequency corresponds to the isotropic material case.

3.2.4. Amplitude Dependence of the First Nonlinear Axisymmetric Mode Shape of FG Circular Plates

Previous studies[20–23] have shown that the nonlinear mode shapes of beam- and plate-like structures are amplitude dependent. This effect is illustrated in the present case in Fig. 5 in which the normalized nonlinear mode shapes of the first axisymmetric mode of the clamped FG circular plate are plotted for various values of the maximum non-dimensional amplitudes. All curves show the amplitude dependence of the first

Table 3. Contribution coefficients to the first non-linear axisymmetric mode shape of the clamped FG circular plate, obtained numerically from iterative solution of the non-linear system in Eq. (37).

$w^*_{\max}$	ω^*_{nl}/ω^*_l	a_1	a_2	a_3	a_4	a_5	a_6
0.0165	1.0000	0.005	-5.0666 E-008	9.3961 E-009	-2.5725 E-009	8.0453 E-011	-3.8763 E-013
0.0330	1.0003	0.01	-3.2327 E-007	1.0681 E-007	-3.7776 E-009	8.9118 E-010	-3.1623 E-010
0.0661	1.0012	0.02	-2.6017 E-006	8.6160 E-007	-2.5008 E-008	3.1887 E-009	-5.8694 E-010
0.1322	1.0048	0.04	-1.0800 E-008	7.3254 E-009	-5.5800 E-009	5.9800 E-009	-1.0800 E-010
0.2641	1.0190	0.08	-1.6245 E-004	5.4556 E-005	-1.8763 E-006	2.8340 E-007	-4.5036 E-008
0.3299	1.0294	0.10	-3.1274 E-004	1.0588 E-004	-3.9480 E-006	6.4564 E-007	-9.7508 E-008
0.4934	1.0643	0.15	-1.0059 E-003	3.4978 E-004	-1.6334 E-005	3.2094 E-006	-4.5234 E-007
0.8165	1.1646	0.25	-4.0663 E-003	1.5171 E-003	-1.0883 E-004	2.7996 E-005	-4.2409 E-006
1.1347	1.2924	0.35	-9.4441 E-003	3.8097 E-003	-3.8014 E-004	1.1767 E-004	-2.1055 E-005
1.4495	1.4366	0.45	-1.6788 E-002	7.2922 E-003	-9.2628 E-004	3.2968 E-004	-6.9137 E-005
1.7625	1.5906	0.55	-2.5619 E-002	1.1875 E-002	-1.8036 E-003	7.1673 E-004	-1.7152 E-004
2.0746	1.7507	0.65	-3.5523 E-002	1.7397 E-002	-3.0261 E-003	1.3140 E-003	-3.5021 E-004
2.3862	1.9151	0.75	-4.6185 E-002	2.3678 E-002	-4.5770 E-003	2.1363 E-003	-6.2198 E-004

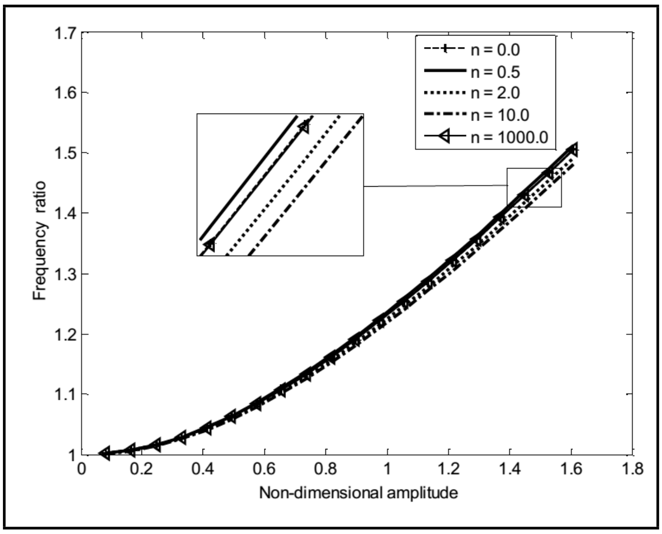

Figure 4. Effect of the power law index n on the variation of the non-linear frequency ratios $(\omega^*_{nl}/\omega^*_l)$ of the clamped FG circular plate with the amplitude of vibration.

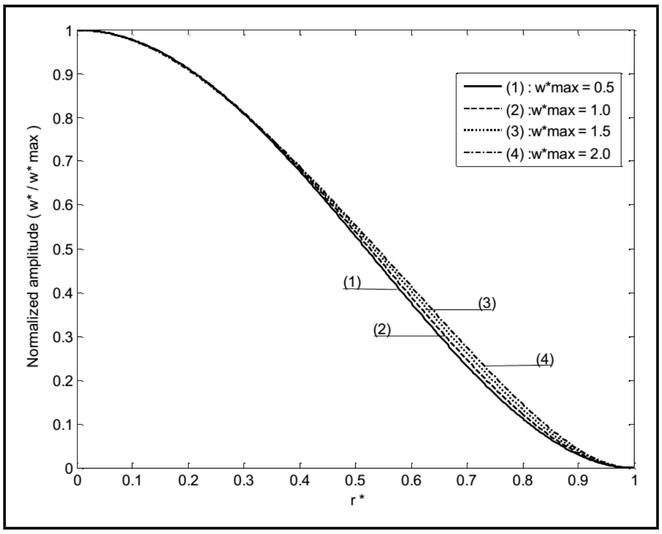

Figure 5. Normalized first non-linear axisymmetric mode shape of FG circular plate at various non-dimensional amplitudes and the power index $n = 0.5$.

axisymmetric nonlinear mode shape with an increase of curvatures near to the clamped edges, which may lead one to expect that the bending stress near to the edges of the plate increases nonlinearly with the increase of the vibration amplitude. This is examined in the next subsection.

3.2.5. Analysis of the Bending Stress Distribution Associated with the First Nonlinear Axisymmetric Mode Shape of FG Circular Plates

As mentioned above, the present multimodal model allows not only determination of the amplitude-frequency dependence, but also the deformation of the mode shape due to the geometrical nonlinearity. From this last result, it was expected that the effect of the amplitude of vibration on the distribution of the associated bending stress would be of a great significance since the bending stress is related to the derivatives of the amplitude dependent transverse mode shape.

The radial bending stress distributions associated with the first axisymmetric nonlinear mode shape with non-dimensional radius are plotted in Fig. 6. It can also be seen in Fig. 7 that the nonlinear radial bending stresses exhibit a higher increase near to the clamped edge compared with that expected in linear theory. The rate of increase in the radial bending stress is about 1.52, the rate of increase expected in linear theory for the first mode.

Figures 8–9 present the effect of the volume fraction index on the bending stress at the clamped edge and the plate center

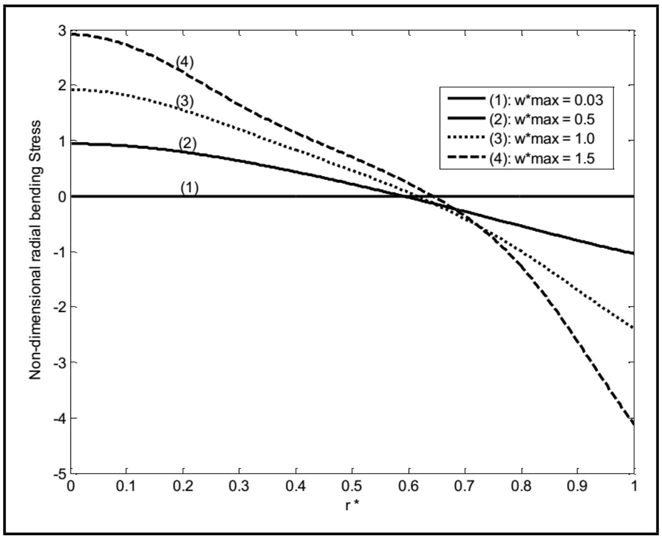

Figure 6. Non-dimensional radial bending stress associated to the first non-linear axisymmetric mode shape of a clamped FG circular plate for $n = 0.5$ and various non-dimensional vibration amplitudes.

through the plate thickness. It is obvious that by increasing the gradient index (n), the variation of Young's modulus becomes increasingly abrupt through the thickness and, consequently, the stress varies accordingly. It is observed that the stress variation through the plate thickness is linear for the completely ceramic-rich and metal-rich plates corresponding, respectively, to $n = 0.0$ and $n = \infty$, while the behavior is nonlinear and

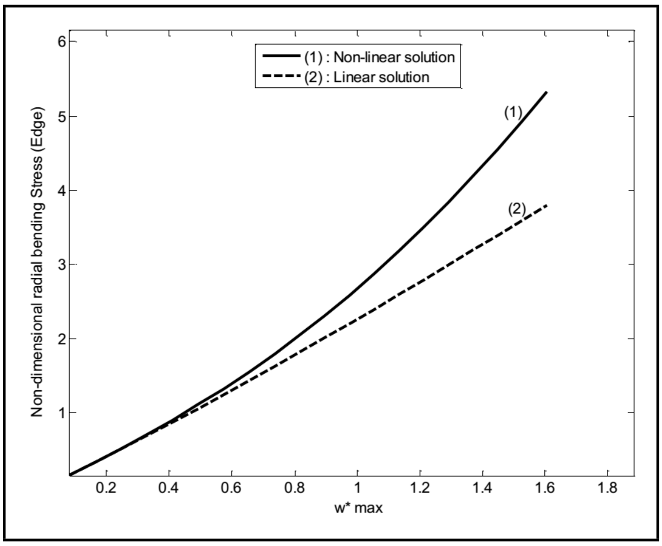

Figure 7. Effects of large vibration amplitudes on the non-dimensional radial bending stress at the edge of the FG circular plate.

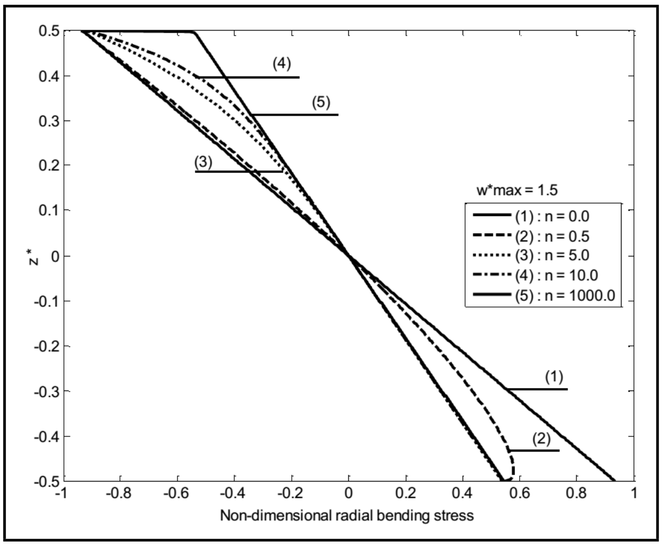

Figure 9. Effect of the volume fraction index n on the radial bending stress through the thickness at the clamped Edge of the FG circular plate.

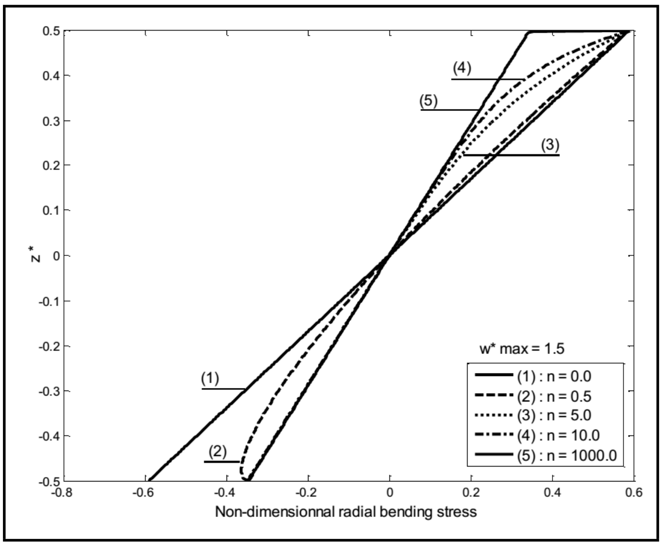

Figure 8. Effect of the volume fraction index n on the radial bending stress through the thickness at the clamped center of the FG circular plate.

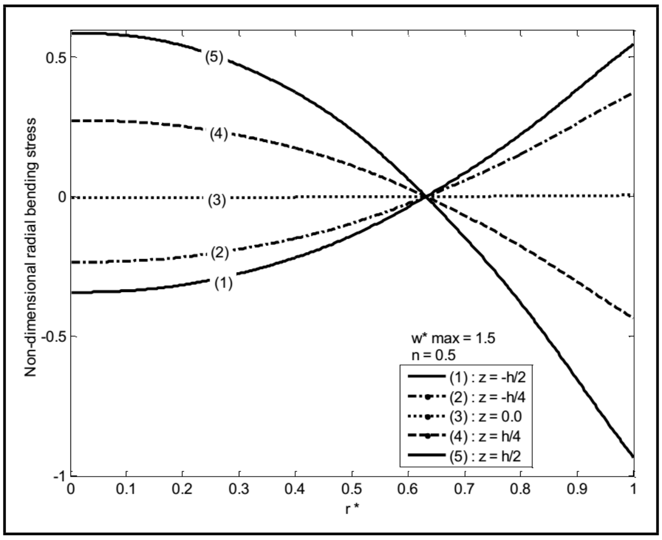

Figure 10. Variation of the radial bending stress at different levels of FG circular plate for $n = 0.5$.

is governed by the variation of the properties in the thickness direction for the FGCP. Figure 10 depicts the variation related to the bending stress of a clamped FG circular plate at different levels of the plate cross-section for the power law index $n = 0.5$ and the vibration amplitude $W^*_{\text{max}} = 1.5$.

3.2.6. Explicit Analytical Solution

The purpose here is to replace the iterative method of the solution of the set of the nonlinear algebraic equation, Eq. (37), necessary to obtain the clamped FG circular plate nonlinear axisymmetric mode shape and associated nonlinear resonant frequencies at large vibration amplitudes by an explicit solution, which may be appropriate for engineering purposes or for further analytical investigations. This explicit solution is obtained by applying and adapting the so-called first formulation developed for many beams and plates cases studied by El Kadiri, Benamar, and White[28] and El Kadiri and Benamar.[29] A comparison is then made between the two solutions—numerical iterative and analytical—in order to determine exactly the range of validity of the last approximate approach. To illustrate the method, the fundamental nonlinear mode shape is considered

Table 6. Numerical values of the modal parameters k^*_{ii} and b^*_{111i}.

i	k^*_{ii}	b^*_{111i}
1	104.363105549862	421.176182024113
2	1581.74423079117	320.895319824783
3	7939.54845205673	-562.906703667013
4	25022.2457661498	51.9601847057999
5	61012.1806626721	-15.6321082304476
6	126429.530992020	6.09018059687781

here by taking $r_0 = 1$. The analysis for the higher nonlinear modes would proceed similarly. A less constraining assumption, compared to the single mode approach, is made by neglecting in the expression $a_i a_j a_k b^*_{ijkr}$, appearing in Eq. (37), which leads to a simple formulation, leading to explicit expression for the amplitude dependence first nonlinear mode of the FG circular plates.

3.2.7. Explicit Expression for the Amplitude Dependence First Nonlinear Mode of FG Circular Plate

The first formulation is based on an approximation, which consists in neglecting in the expression $a_i a_j a_k b^*_{ijkr}$ of Eq. (37) when the first FG circular plate nonlinear mode is examined,

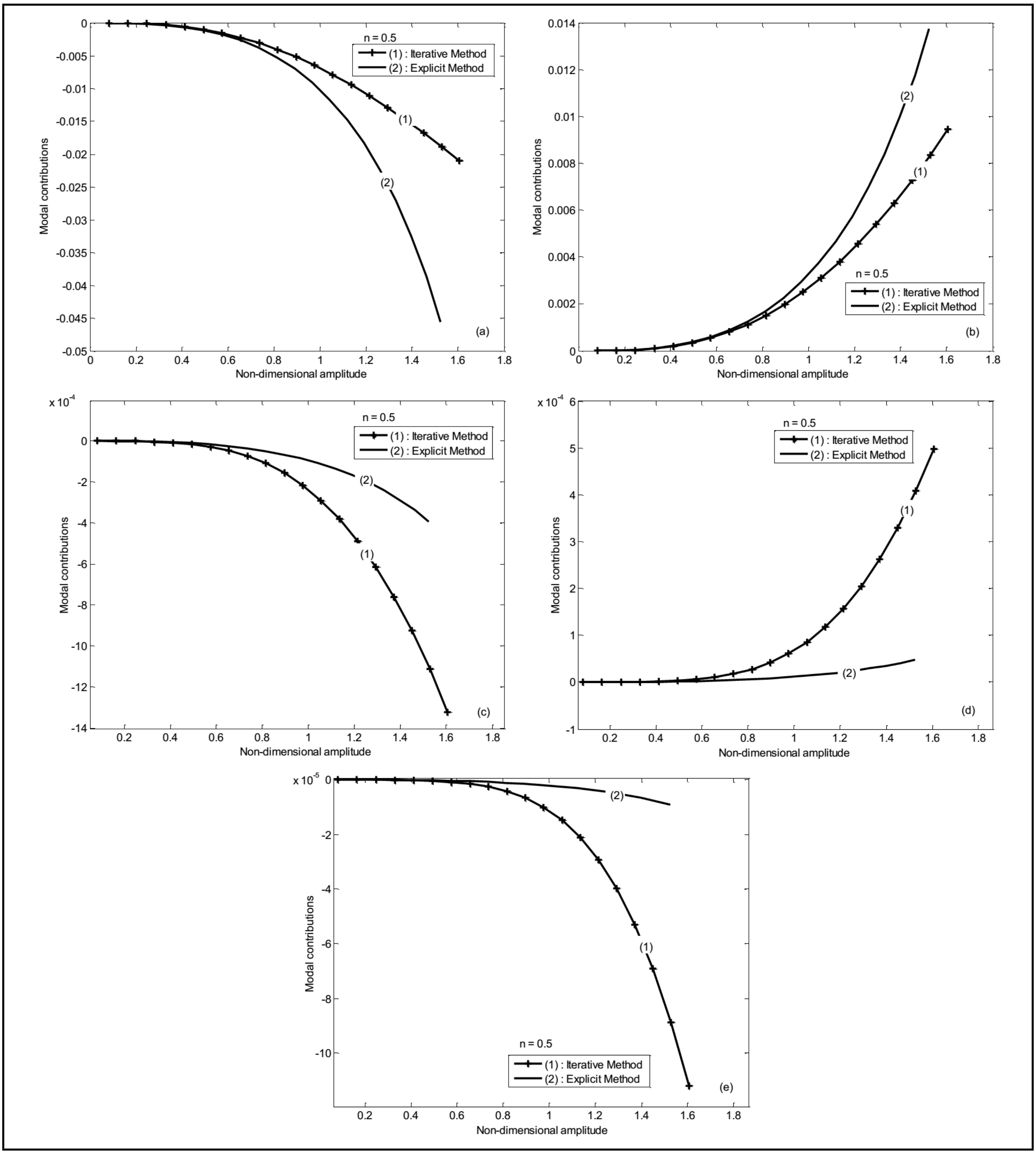

Figure 11. Comparison between the values of the modal contributions of the first non-linear mode shape of the FG circular plate.

the first, second and third order terms with respect to ε_i, i.e. the terms of the type $a_1^2\varepsilon_k b^*_{11kr}$, $a_1\varepsilon_j\varepsilon_k b^*_{1jkr}$, or $\varepsilon_i\varepsilon_j\varepsilon_k b^*_{ijkr}$, so that the only remaining term is $a_1^3 b^*_{111r}$. Thus, Eq. (37) becomes

$$\left(k^*_{ir} - \omega^{*2}_{nl1} m^*_{ir}\right)\varepsilon_i + \frac{3}{2}a_1^3 b^*_{111r} = 0; \tag{53}$$

for $r = 2, \ldots, 6$, in which the repeated index i is summed over the range $[1, 6]$. Since the use of linear FG circular plate mode shapes as basic functions leads to diagonal mass and rigidity matrices, the above system permits one to obtain explicitly the basic function contributions $\varepsilon_2, \ldots, \varepsilon_6$ of the second and higher functions corresponding to a given value of the assigned first basic function contribution a_1, as follows:

$$\varepsilon_r = -\frac{3}{2}\frac{a_1^3 b^*_{111r}}{\left(k^*_{rr} - \omega^{*2}_{nl1} m^*_{rr}\right)}; \tag{54}$$

where $r = 2, \ldots, 6$.

The ε_r's, $(r \neq 1)$, depend on the known parameter m^*_{rr}, k^*_{rr}, b^*_{111r}; the assigned value a_1, and the nonlinear frequency parameter ω^*_{nl1}. To express simply ω^{*2}_{nl1} with an acceptable accuracy, the single-function formula obtained from Eq. (41),

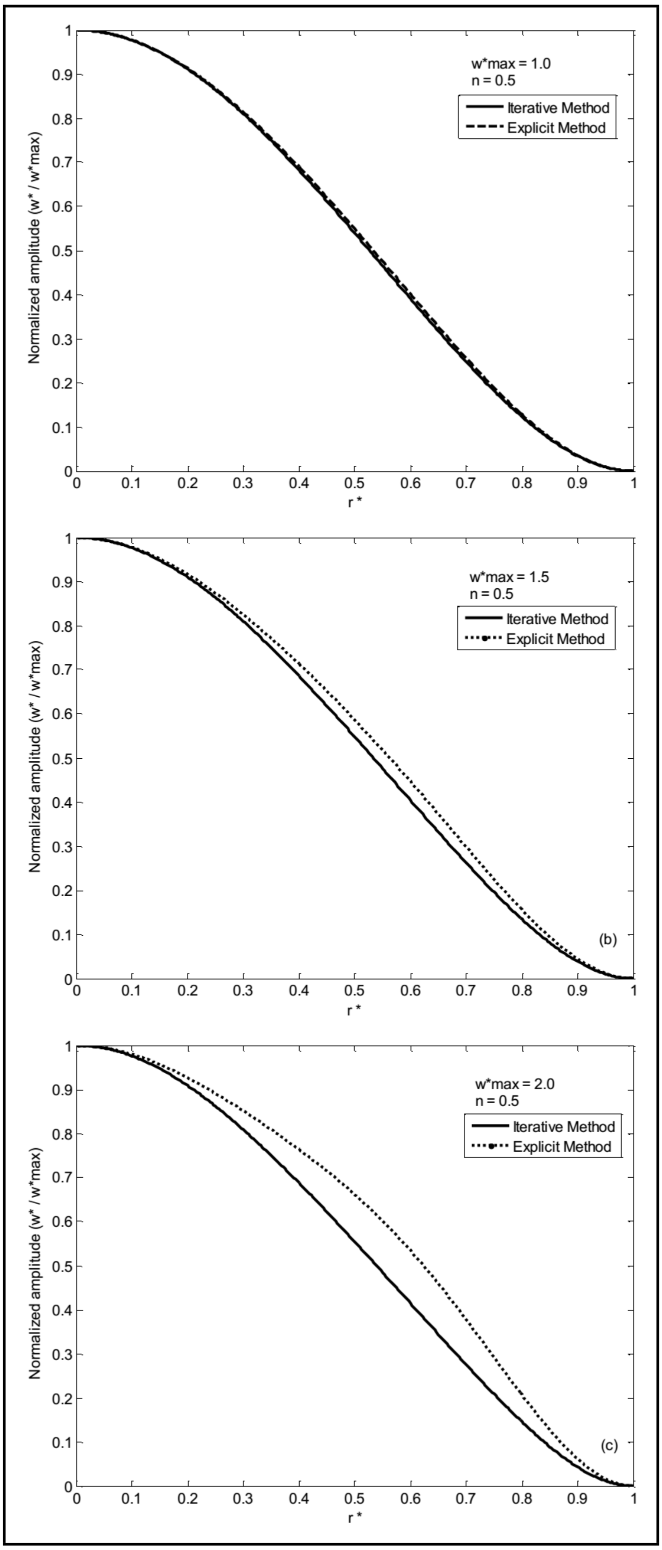

Figure 12. Comparison between the normalized radial section of the first non-linear axisymmetric mode shape of a clamped FG circular plate for the power law index $n = 0.5$ and various non-dimensional amplitudes. (—): Iterative method of solution. (- - -): Explicit analytical solution.

in which all of the a_i's, except a_1, are taken equal to zero, and is used as follows:

$$\omega_{nl1}^{*2} = \frac{k_{11}^*}{m_{11}^*} + \frac{3b_{1111}^*}{2m_{11}^*}a_1^2. \tag{55}$$

In the case considered here, the mass matrix is identical to the identity matrix $m_{11}^* = m_{rr}^* = 1$, and by substituting

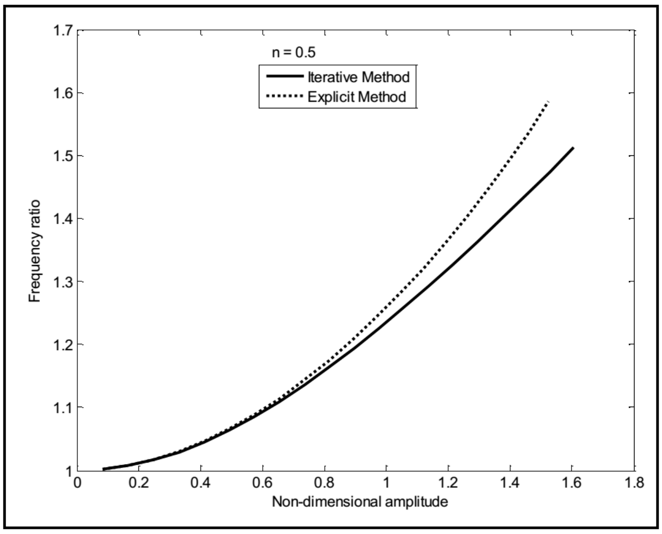

Figure 13. Comparison of frequencies parameter $(\omega_{nl}^*/\omega_l^*)$ for the first non-linear clamped FG circular plate. (—): Iterative method of solution. (- - -): Explicit analytical solution.

Table 7. Comparison between values of frequency parameter $(\omega_{nl}^*/\omega_l^*)$ associated with the first non-linear axisymmetric mode shape of a clamped FG circular plate, obtained by iterative and explicit analytical solution at various values of the maximum non-dimensional amplitude $w_{\max}^*$.

	Non-linear frequency ratio $(\omega_{nl}^*/\omega_l^*)$		
$w_{\max}^*$	Iterative solution	Explicit solution	Deviation (%)
0.5	1.0662	1.0678	0.1500
0.6	1.0939	1.0971	0.2925
0.7	1.1252	1.1308	0.4976
0.8	1.1603	1.1692	0.7670
0.9	1.1984	1.2118	1.1181
1.0	1.2393	1.2583	1.5331
1.1	1.2831	1.3088	2.0029
1.2	1.3291	1.3628	2.5355
1.5	1.4610	1.5217	4.1546

Eq. (55) into Eq. (54) leads to

$$\varepsilon_r = \frac{3a_1^3 b_{111r}^*}{2\left(k_{11}^* + \frac{3}{2}a_1^2 b_{1111}^* - k_{rr}^*\right)}; \tag{56}$$

where $r = 2, \ldots, 6$.

Equation (56) is an explicit simple formula, allowing direct calculation of the higher mode contributions to the first nonlinear mode shape of the FG circular plate as functions of the assigned first mode contribution a_1 and the known parameters k_{rr}^* and b_{111r}^* (given in Table 6). Then, defines the first nonlinear amplitude-dependent FG circular plate mode shape $w_{nl1}^*(r^*, a_1)$ is given as a series involving the circular plate modal parameters depending on the first six axisymmetric functions $w_1^*(r^*), w_2^*(r^*), \ldots, w_6^*(r^*)$:

$$w_{nl1}^*(r^*, a_1) = a_1 w_1^*(r^*) + \sum_{r=2}^{6} \frac{3a_1^3 b_{111r}^*}{2\left(k_{11}^* + \frac{3}{2}a_1^2 b_{1111}^* - k_{rr}^*\right)} w_r^*(r^*); \tag{57}$$

in which the predominant term, proportional to the first linear mode shape, is $a_1 w_1^*(r^*)$, and the other terms, proportional to the higher linear mode shapes $\varepsilon_2 w_2^*(r^*), \ldots, \varepsilon_6 w_6^*(r^*)$, are the corrections due to the nonlinearity.

It may be seen in Figs. 11(a)–11(e) in which the higher mode contributions obtained by the explicit approximate solution are plotted against the maximum non-dimensional vibration am-

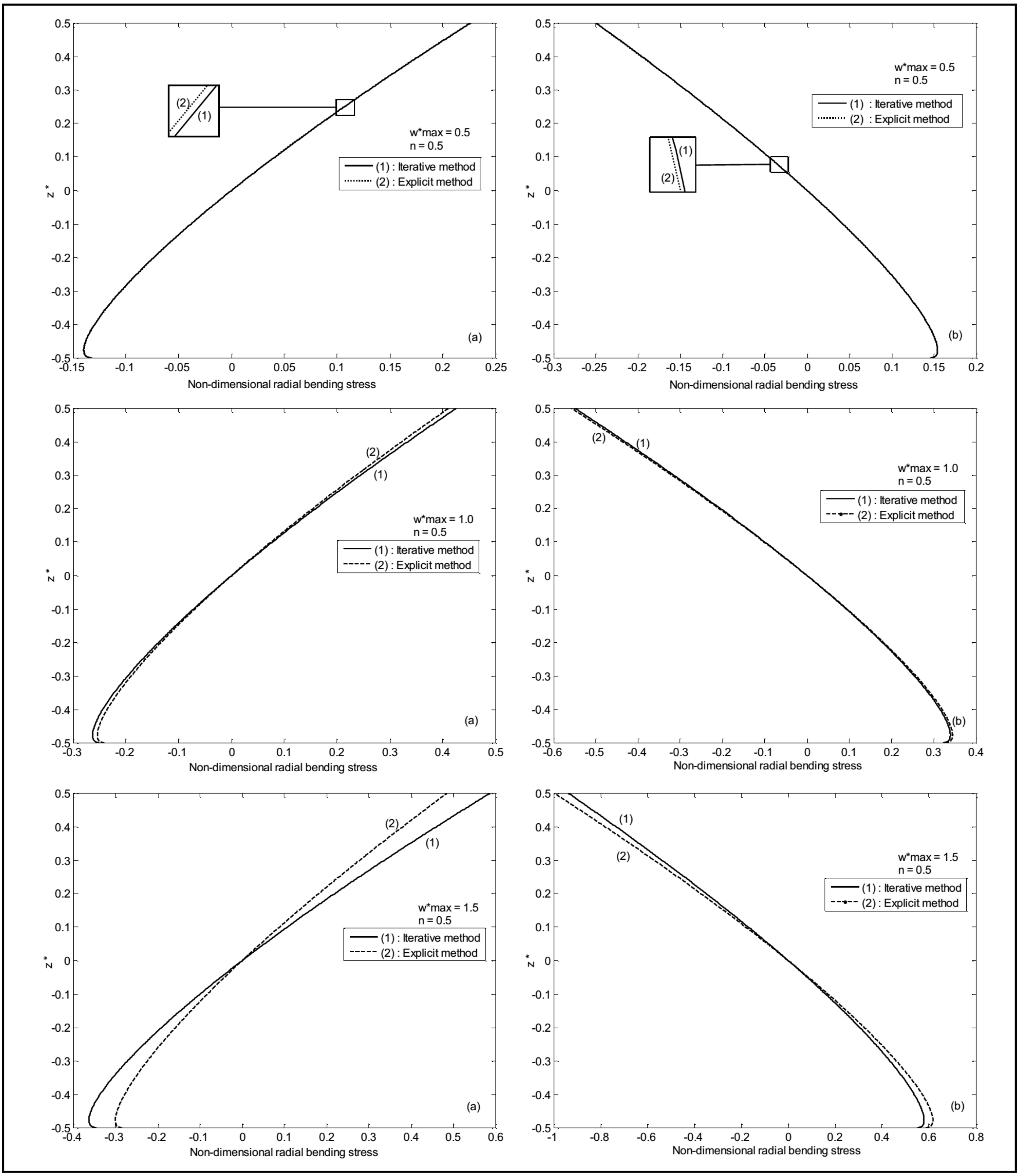

Figure 14. Comparison between dimensionless radial bending stresses distribution along the thickness, at the clamped Center (a) and the clamped Edge (b) of the FG circular plate for various non-dimensional vibration amplitudes. (—): Iterative method of solution. (- - -): Explicit analytical solution.

plitude and compared with that obtained by the iterative solution.

3.2.8. Validity Domain of the Analytical Solutions

The explicit analytical method of solution applied here to the first nonlinear mode shape of a clamped FG circular plate appears to be very appropriate for the analysis of geometrically nonlinear free vibration problems. Since it is based on an assumption concerning the order of magnitude of the basic function contribution coefficients, its domain of validity has to be delimited.

To have an accurate conclusion concerning this domain of validity, especially in engineering applications, a criterion was adopted based on the effect of the assumptions made on the mode shape, the nonlinear frequencies, and the radial bending stress obtained at the clamped edge and center of the FG circular plate are examined.

The normalized first nonlinear axisymmetric mode shape, obtained by numerical iterative solution and explicit analytical solution, is plotted in Figs. 12(a)–12(c) for various values of the maximum dimensionless vibration amplitude. It can be observed that the nonlinear effect increases with increasing the amplitude of vibration, and it may be seen from these figures that the first normalized nonlinear mode shape obtained by explicit approximate solution is in excellent agreement with that obtained by the iterative method of solution for maximum dimensionless vibration amplitude up to 1 and 0.5, respectively.

In Fig. 13, the nonlinear frequency estimates, calculated using the single-function formula in Eq. (55) and the complete formula in Eq. (41), are plotted against the maximum dimensionless vibration amplitude, for the axisymmetric mode shape and the numerical results thus obtained for various values of the maximum non-dimensional amplitude are listed in Table 7. Table 7 and Fig. 13 show that the single-mode approach gives a good estimate of nonlinear frequency parameter $(\omega_{nl}^*/\omega_l^*)$ with a percentage error induced by the explicit approach solution that does not exceed 4.20% for the first axisymmetric mode shape at $w_{\max}^* = 1.5$ compared with the one given by Eq. (41).

The dimensionless radial bending stress distribution along the thickness is associated with the first nonlinear axisymmetric mode shape obtained by the iterative method and that obtained by the analytical method and are plotted in Figs. 14(a) and 14(b) for various maximum dimensionless vibration amplitude. It may be seen from these figures that the radial bending stress obtained by the two approaches are in excellent agreement for maximum dimensionless vibration amplitude up to 1 and 0.5 for the first nonlinear axisymmetric FG circular plate mode shape. As may be seen in the corresponding figures, the error increases with increasing the vibration amplitude. For example, the error induced by the first formulation in the bending stress, corresponding to the first nonlinear mode, at the clamped edge of the FG circular plate, is 0.10 for a dimensionless amplitude of vibration equal to 0.5 times the plate thickness and does not exceed 6.0% for a dimensionless amplitude of vibration equal to 1.5. It can then be concluded that the explicit analytical method gives acceptable results with respect to the nonlinear bending stress estimates for vibration amplitudes up to once the plate thickness for the first nonlinear mode shape.

4. CONCLUSIONS

The nonlinear free vibrations of FG circular plates have been examined using a theoretical model for geometrically nonlinear free vibrations. The model based on Hamilton's principle reduces the nonlinear free vibration problem to solution of a set of nonlinear algebraic equations. The amplitude dependence of the first nonlinear mode shape of clamped FG circular plates and the associated nonlinear parameters has been obtained via iterative solution of a set of nonlinear algebraic equations, involving a fourth order tensor due to the geometrical nonlinearity.

Considering the results obtained, numerical data corresponding to various values of the volume fraction index n are plotted and discussed. Also, the results show that the nonlinear frequency increases with increasing vibration amplitudes, and all curves show the amplitude dependence of the stress distribution and a higher increase of the bending stress near to the clamps compared with the rate of increase obtained in the linear theory.

In order to obtain explicit analytical solutions for the first nonlinear axisymmetric mode shape of the FG circular plates, which are expected to be very useful in engineering applications and in further analytical developments, the improved version of the semi-analytical model developed by El Kadiri, Benamar, and White[28] and El Kadiri and Benamar[29] for beams and rectangular plates has been developed and adapted for the FG circular plate, which are shown to be in a good agreement with the iterative method.

Further investigations are needed to determine the membrane stress distribution at large vibration amplitudes by taking into account in the theory the effects of the in-plane displacements. It is also necessary to carry out a parametric study concerning the effect of the graded material properties such as Young's modulus E and the mass density ρ on the nonlinear vibration behavior of the plate.

REFERENCES

1 Koizumi, M. Functionally gradient materials the concept of FGM, *Ceramic Transactions*, **34**, 3–10, (1993).

2 Allahverdizadeh, A., Naei, M. H., and Bahrami, M. N. Nonlinear free and forced vibration analysis of thin circular functionally graded plates, *Journal of Sound and Vibration*, **310** (4–5), 966–984, (2008). http://dx.doi.org/10.1016/j.jsv.2007.08.011

3 Praveen, G. N. and Reddy, J. N. Nonlinear transient thermo elastic analysis of functionally graded ceramic-metal plates, *International Journal of Solids and Structures*, **35** (33), 4457–4476, (1998). http://dx.doi.org/10.1016/s0020-7683(97)00253-9

4 Yang, J. and Shen, H.-S. Dynamic response of initially stressed functionally graded rectangular thin plates, *Composite Structures*, **54** (4), 497–508, (2001). http://dx.doi.org/10.1016/s0263-8223(01)00122-2

5 Yang, J. and Shen, H.-S. Vibration characteristics and transient response of shear-deformable functionally graded plates in thermal environments, *Journal of Sound and Vibration*, **255** (3), 579–602, (2001). http://dx.doi.org/10.1006/jsvi.2001.4161

6 Huang, X.-L. and Shen, H.-S. Nonlinear vibration and dynamic response of functionally graded plates in thermal environment, *International Journal of Solids and Structures*, **41** (9–10), 2403–2427, (2004). http://dx.doi.org/10.1016/j.ijsolstr.2003.11.012

7 Reddy, J. N. and Cheng, Z. Q. Frequency of functionally graded plates with three-dimensional asymptotic approach, *Journal of Engineering Mechanics*, **129** (8), 896–900,(2003). http://dx.doi.org/10.1061/(asce)0733-9399(2003)129:8(896)

8 Prakash, T. and Ganapathi, M. Asymmetric flexural vibration and thermoelastic stability of FGM circular plates using finite element method, *Composites Part B: Engineering*, **37** (7-8), 642-649, (2006). http://dx.doi.org/10.1016/j.compositesb.2006.03.005

[9] Efraim, E. and Eisenberger, M. Exact vibration analysis of variable thickness thick annular isotropic and FGM plates, *Journal of Sound and Vibration*, **299** (4–5), 720–738, (2007). http://dx.doi.org/10.1016/j.jsv.2006.06.068

[10] Dong, C. Y. Three-dimensional free vibration analysis of functionally graded annular plates using the Chebyshev-Ritz method, *Materials and Design*, **29** (8), 1518–1525, (2008). http://dx.doi.org/10.1016/j.matdes.2008.03.001

[11] Malekzadeh, P., Atashi, M. M., and Karami, G. In-plane free vibration of functionally graded circular arches with temperature-dependent properties under thermal environment, *Journal of Sound and Vibration*, **326** (3–5), 837–851, (2009). http://dx.doi.org/10.1016/j.jsv.2009.05.016

[12] Viswanathan, K. K., Javed, S., Aziz, Z. A., and Prabakar, K. Free vibration of symmetric angle-ply laminated annular circular plate of variable thickness under shear deformation theory, Meccanica, **50** (12), 3013–3027, (2015). http://dx.doi.org/10.1007/s11012-015-0175-3

[13] Ebrahimi, F., Naei, M. H., and Rastgoo, A. Geometrically nonlinear vibration analysis of piezoelectrically actuated FGM plate with an initial large deformation, *Journal of Mechanical Science and Technology*, **23** (8), 2107–2117, (2009). http://dx.doi.org/10.1007/s12206-009-0358-8

[14] Kermani, I. D., Ghayour, M., and Mirdamadi, H. R. Free vibration analysis of multi-directional functionally graded circular and annular plates, *Journal of Mechanical Science and Technology*, **26** (11), 3399–3410, (2012). http://dx.doi.org/10.1007/s12206-012-0860-2

[15] Viswanathan, K. K., Javed, S., and Aziz, Z. A. Free vibration of antisymmetric angle-ply laminated annular circular plate, *Lecture Notes in Engineering and Computer Science*, **3 LNECS**, 2136–2141, (2013).

[16] Haterbouch, M. and Benamar, R. The effects of large vibration amplitudes on the axisymmetric mode shapes and natural frequencies of clamped thin isotropic circular plates, Part I: Iterative and explicit analytical solution for nonlinear transverse vibrations, *Journal of Sound and Vibration*, **265** (1), 123–154, (2003). http://dx.doi.org/10.1016/s0022-460x(02)01443-8

[17] Haterbouch, M. and Benamar, R. The effects of large vibration amplitudes on the axisymmetric mode shapes and natural frequencies of clamped thin isotropic circular plates, Part II: Iterative and explicit analytical solution for nonlinear coupled transverse and in-plane vibrations, *Journal of Sound and Vibration*, **277** (1–2), 1–30, (2004). http://dx.doi.org/10.1016/j.jsv.2003.08.039

[18] Shen, H.-S. *Functionally Graded Materials*, CRC Press, (2009). http://dx.doi.org/10.1201/9781420092578

[19] Timoshenko, S., Weinsowsky-Krieger, S., and Jones, R. M. *Mechanics of Composite Materials*, McGraw-Hill Kogakusha, Ltd. Tokyo, (1975), International Student Edition, Vol. 51.

[20] Benamar, R., Bennouna, M. M. K., and White, R. G. The effects of large vibration amplitudes on the mode shapes and natural frequencies of thin elastic structures, Part II: Fully clamped rectangular isotropic plates, *Journal of Sound and Vibration*, **164** (2), 295–316, (1993). http://dx.doi.org/10.1006/jsvi.1993.1215

[21] El Kadiri, M., Benamar, R., and White, R. G. The nonlinear free vibration of fully clamped rectangular plates: Second nonlinear mode for various plate aspect ratios, *Journal of Sound and Vibration*, **228** (2), 333–358, (1999). http://dx.doi.org/10.1006/jsvi.1999.2410

[22] Benamar, R., Bennouna, M. M. K., and White, R. G. The effects of large vibration amplitudes on the mode shapes and natural frequencies of thin elastic structures, Part III: Fully clamped rectangular isotropic plates-measurements of the mode shape amplitude dependence and the spatial distribution of harmonic distortion, *Journal of Sound and Vibration*, **175** (3), 377–395, (1994). http://dx.doi.org/10.1006/jsvi.1994.1335

[23] El Bikri, K., Benamar, R., and Bennouna, M. Geometrically nonlinear free vibrations of clamped simply supported rectangular plates. Part I: The effects of large vibration amplitudes on the fundamental mode shape, *Computers and Structures*, **81** (20), 2029–2043, (2003). http://dx.doi.org/10.1016/s0045-7949(03)00152-4

[24] Sridhar, S., Mook, D. T., and Nayfeh, A. H. Nonlinear resonances in the forced responses of plates, Part I: Symmetric responses of circular plates, *Journal of Sound and Vibration*, **41** (3), 359–373, (1975). http://dx.doi.org/10.1016/s0022-460x(75)80182-9

[25] Leissa, A. W. *Vibrations of Plates*, NASA SP-160, U.S. Government Printing Office, Washington, DC, (1969).

[26] Yamaki, N. Influence of large amplitudes on flexural vibrations of elastic plates, *ZAMM — Journal of Applied Mathematics and Mechanics*, **41** (12), 501–510, (1961). http://dx.doi.org/10.1002/zamm.19610411204

[27] Nowinski, J. L. Nonlinear transverse vibrations of circular elastic plates built-in at the boundary, *Proc. of the Fourth US National Congress on Applied Mechanics*, **1**, 325–334, (1962).

[28] El Kadiri, M., Benamar, R., and White, R. G. Improvement of the semi-analytical method, for determining the geometrically nonlinear response of thin straight structures. Part I: application to clamped-clamped and simply supported-clamped beams, *Journal of Sound and Vibration*, **249** (2), 263–305, (2002). http://dx.doi.org/10.1006/jsvi.2001.3808

[29] El Kadiri, M. and Benamar, R. Improvement of the semi-analytical method, for determining the geometrically nonlinear response of thin straight structures. Part II: first and second nonlinear mode shapes of fully clamped rectangular plates, *Journal of Sound and Vibration*, **257** (1), 19–62, (2002). http://dx.doi.org/10.1006/jsvi.2002.5026

Two-Temperature Generalized Thermoelastic Infinite Medium with Cylindrical Cavity Subjected To Time Exponentially Decaying Laser Pulse

Eman A. N. Al-Lehaibi

Department Mathematic, College of Science and Arts Sharoura, Najran University, KSA

(Received 14 March 2015; accepted 17 September 2015)

The present work is devoted to a study of the induced temperature and stress fields in an elastic infinite medium with cylindrical cavity under the purview of two-temperature thermoelasticity. The medium is considered to be an isotropic homogeneous thermoelastic material. The bounding plane surface of the cavity is loaded thermally by time exponentially decaying laser pulse. An exact solution of the problem is obtained in Laplace transform space, and the inversion of Laplace transforms have been carried numerically. The derived expressions are computed numerically for copper, and the results are presented in graphical form.

1. INTRODUCTION

In-depth research has been conducted on generalized thermoelasticity theories in solving thermoelastic problems in place of the classical uncoupled/coupled theory of thermoelasticity. The absence of any elasticity term in the heat conduction equation for uncoupled thermoelasticity appears to be unrealistic, since the produced strain causes variation in the temperature field due to the mechanical loading of an elastic body. The parabolic type of heat conduction equation results in an infinite velocity of thermal wave propagation, which also contradicts the actual physical phenomena. By introducing the strain-rate term in the uncoupled heat conduction equation, the analysis to incorporate coupled thermoelasticity has been extended by Biot.[1] Although the first paradox was over, the parabolic type partial differential equation of heat conduction remains, which leads to the paradox of infinite velocity of the thermal wave. To eliminate this paradox, generalized thermoelasticity theory was developed subsequently. Due to the advancement of pulsed lasers, fast burst nuclear reactors, and particle accelerators, which can supply heat pulses with a very fast time-rise, Bargmann.[2] and Boley[3] generalized thermoelasticity theory is receiving serious attention. Chandrasekharaiah reviewed the development of the second sound effect.[4] Recently, mainly two different models of generalized thermoelasticity are being extensively used: one proposed by Lord and Shulman and the other proposed by Green and Lindsay.[5,6] Lord and Shulman theory (L-S) suggests one relaxation time, and according to this theory, only Fourier's heat conduction equation is modified; however, Green and Lindsay theory (G-L) suggests two relaxation times, and both the energy equation and the equation of motion are modified.

The so-called ultra-short lasers are those with pulse duration ranging from nanoseconds to femtoseconds in general. In the case of ultra-short-pulsed laser heating, the high-intensity energy flux and ultra-short duration laser beam, have introduced situations where very large thermal gradients or an ultra-high heating speed may exist on the boundaries, according to Sun et al.[7] In such cases, as pointed out by many investigators, the classical Fourier model, which leads to an infinite propagation speed of the thermal energy, is no longer valid for Tzou.[8,9] The non-Fourier effect of heat conduction takes into account the effect of mean free time (thermal relaxation time) in the energy carrier's collision process, which can eliminate this contradiction. Wang and Xu have studied the stress wave induced by nanoseconds, picoseconds, and femtoseconds laser pulses in a semi-infinite solid.[10] The solution takes into account the non-Fourier effect in heat conduction and the coupling effect between temperature and strain rate. It is known that characteristic elastic waveforms are generated when a pulsed laser irradiates a metal surface.

The two-temperatures theory of thermoelasticity was introduced by Gurtin and Williams,[11] Chen and Gurtin,[12] and Chen et al.,[13,14] in which the classical Clausius-Duhem inequality was replaced by another one depending on two temperatures; the conductive temperature φ and the thermodynamic temperature T, the first is due to the thermal processes, and the second is due to the mechanical processes inherent between the particles and the layers of elastic material, this theory was also investigated by Iean.[15] Abbas solved many problems that discussed the two-temperature theory of thermoelasticity and also the thermoelastic medium with cylindrical cavity.[16–20]

Only in the last decade has the theory of two-temperature thermoelasticity been noticed, developed in many works, and found its applications mainly in the problems in which the discontinuities of stresses have no physical interpretations. Among the authors who contribute to this theory, Quintanilla studied existence, structural stability, convergence, and spatial behavior for this theory.[21] Youssef introduced the generalized Fourier law to the field equations of the two-temperature theory of thermoelasticity and proved the uniqueness of solution for homogeneous isotropic material.[22,23] Puri and Jordan recently studied the propagation of harmonic plane waves,[23] and Magaa and Quintanilla[24] have studied the uniqueness and growth solutions for the model proposed by Youssef.[25]

The present work is devoted to a study of the induced temperature and stress fields in an elastic infinite medium with cylindrical cavity under the purview of two-temperature thermoelasticity. The medium is considered to be an isotropic homogeneous thermoelastic material. The bounding plane surface of the cavity is loaded thermally by non-Gaussian laser beam with pulse duration of 2 ps. An exact solution of the problem is obtained in Laplace transform space, and the inversion of Laplace transforms have been carried numerically. The derived expressions are computed numerically for copper, and the results are presented in graphical form.

2. THE GOVERNING EQUATIONS

Consider a perfectly conducting elastic infinite body with cylindrical cavity occupies the region $R \leq r < \infty$ of an isotropic homogeneous medium whose state can be expressed in terms of the space variable r and the time variable t such that all of the field functions vanish at infinity.

We can use the cylindrical system of coordinates (r, ψ, z) with the z-axis lying along the axis of the cylinder. Due to symmetry, the problem is one-dimensional with all the functions considered depending on the radial distance r and the time t. It is assumed that there is no external forces act on the medium.

Thus the field equations in cylindrical one dimensional case can be put as in:[25]

$$(\lambda + 2\mu)\, \frac{\partial e}{\partial r} - \gamma \frac{\partial T}{\partial r} \; = \rho \frac{\partial^2 u}{\partial t^2}; \tag{1}$$

$$\nabla^2 \varphi = \frac{\rho C_E}{K} \left(\frac{\partial}{\partial t} + \tau_o \frac{\partial^2}{\partial t^2} \right) \theta + \frac{T_o \gamma}{K} \left(\frac{\partial}{\partial t} + \tau_o \frac{\partial^2}{\partial t^2} \right) e - \frac{\rho}{K} \left(1 + \tau_o \frac{\partial}{\partial t} \right) Q; \tag{2}$$

$$\varphi - T = a \nabla^2 \varphi; \tag{3}$$

$$\sigma_{rr} = 2\,\mu \frac{\partial u}{\partial r} + \lambda e - \gamma\, (T - T_o)\,; \tag{4}$$

$$\sigma_{\psi\,\psi} = 2\,\mu \frac{u}{r} + \lambda\, e - \gamma\, (T - T_o)\,; \tag{5}$$

$$\sigma_{zz} = \lambda e - \gamma \,(T - T_o)\,; \tag{6}$$

$$\sigma_{z\,r} = \sigma_{\psi\,r} = \sigma_{z\,\psi} = 0; \tag{7}$$

$$e = \frac{1}{r} \frac{\partial\, \;(r\, u)}{\partial\, r}; \tag{8}$$

where $\nabla^2 = \frac{\partial^2}{\partial r^2} + \frac{1}{r} \frac{\partial}{\partial r}, \lambda, \mu$, Lames constants, ρ density, C_E specific heat at constant strain, α_T coefficient of linear thermal expansion, $\lambda = (3\lambda + 2\mu)\alpha_T$, t is the time, T is the temperature, T_0 is the reference temperature, $\theta = (T - T_o)$ is the thermo-dynamical temperature increment such that $\frac{|\theta|}{T_o} << 1$, φ is the heat conductive temperature, $\sigma_{ij}, i, j = r, \psi, z$ are the components of stress tensor, e is the cubic dilatation, u is the displacement, K is the thermal conductivity, τ_o is the relaxation time, a is non-negative parameter (two-temperature parameter), and Q is the heat source per unit mass.

2.1. The Mathematical Modeling

The Fourier heat transfer equation due to time exponentially decaying laser pulse for a one dimensional body can be written as:[7]

$$\nabla^2 \varphi = \frac{\rho C_E}{K} \left(\frac{\partial}{\partial t} + \tau_o \frac{\partial^2}{\partial t^2} \right) \theta + \frac{\gamma T_o}{K} \left(\frac{\partial}{\partial t} + \tau_o \frac{\partial^2}{\partial t^2} \right) e - \frac{\rho I_1 \delta}{K} \left(1 + \tau_o \frac{\partial}{\partial t} \right) \left[e^{-\upsilon t - \delta r} \right]; \tag{9}$$

where $I_1 = (1 - r_f) I_0$ is the power intensity after surface reflection; I_0 is laser peak power intensity; r_f is reflection coefficient; υ is laser pulse parameter; and δ is absorption coefficient.

2.2. Dimensionless of the Governing Equations

For convenience, we shall use the following non-dimensional variables:[25]

$$\begin{aligned} (r', u', R', R_0) &= c_o \eta \,(r, u, R', R'_0)\,, \\ (t', \tau'_o) &= c_o^2 \eta \;(t, \tau_o)\,, \\ \theta' &= \frac{T - T_o}{T_o}, \\ \varphi' &= \frac{\varphi - T_o}{T_o}, \\ \sigma' &= \frac{\sigma}{\mu}; \end{aligned} \tag{10}$$

where $c_0^2 = \frac{\lambda + 2\mu}{\rho}$ and $\eta = \frac{\rho C_E}{K}$.
Hence, we obtain (where the primes are suppressed for simplicity)

$$\nabla^2 e - b \nabla^2 \theta \; = \frac{\partial^2 e}{\partial t^2}; \tag{11}$$

$$\nabla^2 \varphi = \left(\frac{\partial}{\partial t} + \tau_o \frac{\partial^2}{\partial t^2} \right) \theta + \varepsilon_1 \left(\frac{\partial}{\partial t} + \tau_o \frac{\partial^2}{\partial t^2} \right) \, e - \varepsilon_2 \left(1 + \, \tau_o \frac{\partial}{\partial t} \right) \left[e^{-\upsilon t - \delta r} \right]; \tag{12}$$

$$\varphi - \theta = \omega \nabla^2 \varphi; \tag{13}$$

$$\sigma_{rr} = \; \beta^2 \frac{\partial u}{\partial r} + \left(\beta^2 - 2 \right) \frac{u}{r} - \alpha\, \theta; \tag{14}$$

$$\sigma_{\psi\psi} = \left(\beta^2 - 2 \right) \frac{\partial u}{\partial r} + \, \beta^2 \frac{u}{r} - \alpha\, \theta; \tag{15}$$

$$\sigma_{zz} = \left(\beta^2 - 2 \right) \, e - \alpha \; \theta; \tag{16}$$

where, $c_o = \sqrt{\frac{\lambda + 2\,\mu}{\rho}}$ is longitudinal wave speed; $\eta = \frac{\rho\, C_E}{K}$ is the thermal viscosity; $\varepsilon_1 = \frac{\gamma}{\rho\, C_E}$ is the dimensionless mechanical coupling constant; $\alpha = \frac{\gamma T_o}{\mu}$ is the dimensionless thermoelastic coupling constant; and $\omega = a\, c_o^2 \eta^2$ is the dimensionless two-temperature parameter, $\beta = (\frac{\lambda + 2\mu}{\mu})^{1/2}$, $b = \frac{\alpha}{\beta^2}$ and $\varepsilon_2 = \frac{I_1 \delta}{C_E T_o c_o^2 \eta}$.

2.3. The Solution in the Laplace Transform Domain

We use the Laplace transform of both sides of the last equations defined as:

$$\bar{f}(s) = \int_0^\infty f(t)\, e^{-sr} dt. \tag{17}$$

Hence, we obtain

$$\nabla^2 \bar{e} = s^2 \bar{e} + b\nabla^2 \bar{\theta}; \tag{18}$$

$$\nabla^2 \bar{\varphi} = h\,\bar{\theta} + \varepsilon_1\, h\,\bar{e} - F(s,r); \tag{19}$$

$$\bar{\theta} = \bar{\varphi} - \omega \nabla^2 \bar{\varphi}; \tag{20}$$

$$\bar{\sigma}_{rr} = \beta^2 \bar{e} + 2\frac{\bar{u}}{r} - \alpha\,\bar{\theta}; \tag{21}$$

$$\bar{\sigma}_{\psi\psi} = \left(\beta^2 - 2\right)\bar{e} + 2\frac{\bar{u}}{r} - \alpha\,\bar{\theta}; \tag{22}$$

$$\bar{\sigma}_{zz} = \left(\beta^2 - 2\right)\bar{e} - \alpha\,\bar{\theta}; \tag{23}$$

$$\bar{e} = \frac{1}{r}\frac{\partial\ (r\,\bar{u})}{\partial\, r} = \frac{\bar{u}}{r} + \frac{\partial\ \bar{u}}{\partial\, r}; \tag{24}$$

where $F(s,r) = \varepsilon_3 e^{-\delta r}$, $\varepsilon_3 = \frac{\varepsilon_2(1+\tau_o s)}{(s+v)}$ and $h = \left(s + \tau_o s^2\right)$. All the state functions in Eqs. (18)–(24) have zero initial value. An over bar symbol denotes its Laplace transform, and s denotes the Laplace transform parameter.

To simplify the solution of the above differential equations, we will consider the special case of $R = r$.

Thus, we have

$$F(s,R) = \varepsilon_3 e^{-\delta R}, \nabla^2 F(s,R) = \nabla^4 F(s,R) = 0; \tag{25}$$

By using Eqs. (19) and (20), we get

$$\bar{\theta} = (1 - \omega\,\alpha_1)\,\bar{\varphi} - \omega\,\alpha_2\,\bar{e} + \frac{\omega\alpha_1}{h} F(s,R); \tag{26}$$

where $\alpha_1 = \frac{h}{1+\omega h}$ and $\alpha_2 = \varepsilon_1 \alpha_1$.
By substituting Eq. (26) into Eqs. (18) and (19), we obtain

$$\left(\nabla^2 - \alpha_1\right)\bar{\varphi} = \alpha_2 \bar{e} - \frac{\alpha_1}{h} F(s,R); \tag{27}$$

and

$$\left(\nabla^2 - \alpha_3\right)\bar{e} = \alpha_4\,\bar{\varphi} - \frac{\alpha_4}{h} F(s,R); \tag{28}$$

where $\alpha_3 = \frac{s^2+\alpha_2 b(1-\omega\alpha_1)}{1+\omega\alpha_2 b}$, $\alpha_4 = \frac{\alpha_1 b(1-\omega\alpha_1)}{1+\omega\alpha_2 b}$.
Eliminating $\bar{e}$ from Eqs. (27) and (28), we get

$$\left[\nabla^4 - (\alpha_1 + \alpha_3)\nabla^2 + (\alpha_1\alpha_3 - \alpha_2\alpha_4)\right]\bar{\varphi} = \alpha_5 F(s,R); \tag{29}$$

where $\alpha_5 = \frac{(\alpha_1\alpha_3 - \alpha_2\alpha_4)}{h}$.
In a similar manner, we can show that $\bar{e}$ satisfies the equation

$$\left[\nabla^4 - (\alpha_1 + \alpha_3)\ \nabla^2 + (\alpha_1\alpha_3 - \alpha_2\alpha_4)\right]\bar{e} = 0. \tag{30}$$

For finite solutions, the solutions of Eqs. (28) and (29) take the form

$$\bar{\varphi} = \frac{F(s,R_0)}{h} + \sum_{i=1}^{2} A_i\ K_0(p_i r); \tag{31}$$

and

$$\bar{e} = \sum_{i=1}^{2} B_i K_0(p_i r) \tag{32}$$

where $K_0()$ is the modified Bessel function of the second kind of order zero. A_1, A_2, B_1, and B_2 are all parameters depending on the parameter s of the Laplace transform.
p_1^2 and p_2^2 are the roots of the characteristic equation

$$p^4 - (\alpha_1 + \alpha_3)\ p^2 + (\alpha_1\alpha_3 - \alpha_2\alpha_4) = 0 \tag{33}$$

Using Eq. (29), we obtain

$$B_i = \alpha_4 A_i, \quad i = 1, 2. \tag{34}$$

Substituting Eq. (34) into Eq. (32), we get

$$\bar{e} = \alpha_4 \sum_{i=1}^{2} A_i\ K_0(p_i r). \tag{35}$$

Substituting Eq. (35) into Eq. (24), we obtain

$$\bar{u} = -\alpha_4 \sum_{i=1}^{2} \frac{A_i}{p_i} K_1(p_i r) \tag{36}$$

where $K_1()$ is the modified Bessel function of the second kind of order one.
In deriving Eq. (36), we have used the following well-known relation of the Bessel function:

$$\int z\,K_0(z)\ d\,z = -z\,K_1(z);$$

Using Eqs. (31) and (35) in Eq. (26), we obtain

$$\bar{\theta} = \frac{F(s,R_0)}{h} + \sum_{i=1}^{2} \theta_i\,A_i\,K_0(p_i r); \tag{37}$$

where

$$\theta_i = (1 - \omega\alpha_1)\left(p_i^2 - \alpha_3\right) - \omega\alpha_2\alpha_4 \qquad i = 1, 2.$$

Finally, substituting Eqs. (35), (36), and (37) into Eqs. (21)–(23), we obtain the stress components in the form

$$\bar{\sigma}_{rr} = -\frac{\alpha F(s,R)}{h} + \sum_{i=1}^{2} A_i \left[\left(\beta^2\,\alpha_4 - \alpha\theta_i\right) K_0(p_i r) + \frac{2\alpha_4}{r\,p_i} K_1(p_i r)\right]; \tag{38}$$

$$\bar{\sigma}_{\psi\psi} = -\frac{\alpha F(s,R)}{h} + \sum_{i=1}^{2} A_i \left[\left(\left(\beta^2 - 2\right)\ \alpha_4 - \alpha\theta_i\right) K_0(p_i r) - \frac{2\alpha_2}{r\,p_i} K_1(p_i r)\right]; \tag{39}$$

$$\sigma_{zz} = -\frac{\alpha F(s,R)}{h} + \sum_{i=1}^{2} \left[\left(\beta^2 - 2\right)\alpha_4 - \alpha\theta_i\right] A_i\,K_0(p_i r). \tag{40}$$

To complete the solution in the Laplace transform space, we will consider the medium described above as quiescent and the bounding plane of the cavity ($r = R$) traction free, with no thermal loading accept the laser beam:

$$\varphi(R,t) = 0. \tag{41}$$

After using Laplace transform, we have

$$\bar{\varphi}(R,s) = 0. \tag{42}$$

Also, we have

$$\sigma_{rr}(R,t) = 0. \tag{43}$$

After using Laplace transform, we get

$$\bar{\sigma}_{rr}(R,s) = 0. \tag{44}$$

Applying the last two conditions gives

$$\sum_{i=1}^{2} A_i \left(p_i^2 - \alpha_3\right) K_0(p_i R) = -\frac{F(s,R)}{h}; \tag{45}$$

and

$$\sum_{i=1}^{2} A_i \left[\left(\beta^2 \alpha_4 - \alpha\theta_i\right) K_0(p_i R) + \frac{2\alpha_4}{R p_i} K_1(p_i R)\right] = \frac{\alpha F(s,R)}{h}. \tag{46}$$

Solving the last system of equations gives

$$\begin{bmatrix} A_1 \\ A_2 \end{bmatrix} = \begin{bmatrix} l_{11} & l_{12} \\ l_{21} & l_{22} \end{bmatrix}^{-1} \begin{bmatrix} -1 \\ \alpha \end{bmatrix} \frac{F(s,R)}{h} \tag{47}$$

hence $A_1 = \frac{F(s,R)(\alpha l_{12} - l_{22})}{h(l_{11}l_{22} - l_{12}l_{21})}$ and $A_2 = \frac{F(s,R)(l_{21} - \alpha l_{11})}{h(l_{11}l_{22} - l_{12}l_{21})}$, where

$$l_{11} = \left(p_1^2 - \alpha_3\right) K_0(p_1 r);$$

$$l_{12} = \left(p_2^2 - \alpha_3\right) K_0(p_2 r);$$

$$l_{21} = \left(\beta^2 \alpha_4 - \alpha\theta_1\right) K_0(p_1 R) + \frac{2\alpha_4}{R p_1} K_1(p_1 R);$$

and

$$l_{22} = \left(\beta^2 \alpha_4 - \alpha\theta_2\right) K_0(p_2 R) + \frac{2\alpha_4}{R p_2} K_1(p_2 R).$$

Finally, we obtain the solutions in the Laplace transform domain as in Eqs. (48)–(52) (top of the next page).

3. NUMERICAL INVERSION OF LAPLACE TRANSFORM

In order to determine the conductive and thermal temperature, displacement, and stress distributions in the time domain, the Riemann-sum approximation method is used to obtain the numerical results. In this method, any function in Laplace domain can be inverted to the time domain as

$$f(t) = \frac{e^{\kappa t}}{t}\left[\frac{1}{2}\bar{f}(\kappa) + Re\sum_{n=1}^{N}(-1)^n \bar{f}\left(\kappa + \frac{i n\pi}{t}\right)\right]; \tag{53}$$

where Re is the real part and i is imaginary number unit. For faster convergence, multiple numerical experiments have shown that the value of κ satisfies the relation $\kappa t \approx 4.7$.[8]

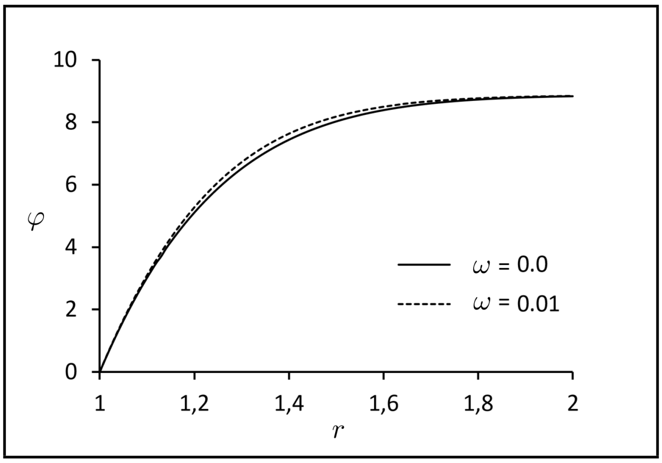

Figure 1. The conductive temperature with different value two-temperature parameter.

3.1. Numerical Results and Discussion

With a view to illustrating the analytical procedure presented earlier, we now consider a numerical example for which computational results are given. For this purpose, copper is taken as the thermoelastic material for which we take the following values of the different physical constants:[25]

$K = 386\,\mathrm{kg\,m\,K^{-1}s^{-3}}$; $\alpha_T = 1.78\,(10)^{-5}\,\mathrm{K^{-1}}$;
$\rho = 8954\,\mathrm{kg\,m^{-3}}$; $C_E = 383.1\,\mathrm{m^2\,K^{-1}\,s^{-2}}$;
$T_o = 293\,\mathrm{K}$; $\mu = 3.86\,(10)^{10}\,\mathrm{kg\,m^{-1}\,s^{-2}}$;
$\lambda = 7.76\,(10)^{10}\mathrm{kg\,m^{-1}\,s^{-2}}$; $\beta^2 = 4$;
$R = 1.0$; $\tau_o = 0.02$;
$t = 0.1$.

From the above values, we get the non-dimensional values of the problem as:

$$b = 0.01041, \quad \alpha = 0.0417232, \quad \varepsilon_1 = 1.618, \quad \varepsilon_2 = 10^2.$$

Figures 1–5 represent the distributions of the conductive temperature, the dynamic-temperature, the stress, the displacement and the strain respectively when $\upsilon = 0.1, \delta = 0.1$ and with different value of two-temperature parameter $\omega = 0.0, 0.01$ to stand on the effect of this parameter on all the studied filed. This group of figures shows that, the two-temperature parameter has significant effects on all the state of functions of the thermoelastic materials. The two-temperature parameter makes the sharp points in the stress, the strain and the displacement distribution disappeared.

Figures 6–10 represent the distributions of the conductive temperature, the thermo-dynamic temperature, the stress, the displacement and the strain respectively when $\omega = 0.01, \upsilon = 0.1$ and with different value of absorption coefficient parameter $\delta = 0.1, 0.05$ to stand on the effect of this parameter on all the studied filed. This group of figures shows that, the absorption coefficient parameter has significant effects on all the states of functions of the thermoelastic materials. When the value of the absorption coefficient parameter increases, all the state functions of the material decrease.

Figures 11–15 represent the distributions of the conductive temperature, thermo-dynamic temperature, stress, displacement, and strain, respectively, when $\omega = 0.01, \delta = 0.1$ and

$$\bar{\varphi} = \frac{F(s,R)}{h}\left[1 + \frac{1}{(l_{11}l_{22} - l_{12}l_{21})}\left[\ (\alpha l_{12} - l_{22})\left(p_1^2 - \alpha_3\right)K_0(p_1 r) + (l_{21} - \alpha l_{11})\ \left(p_2^2 - \alpha_3\right)K_0(p_2 r)\ \right]\right]; \tag{48}$$

$$\bar{\theta} = \frac{F(s,R)}{h(l_{11}l_{22} - l_{12}l_{21})}$$
$$\left[\ 1 + \left((1-\omega\alpha_1)\left(p_1^2 - \alpha_3\right) - \omega\alpha_2\alpha_4\right)\ (\alpha l_{12} - l_{22})\ K_0(p_1 r) + \left((1-\omega\alpha_1)\left(p_2^2 - \alpha_3\right) - \omega\alpha_2\alpha_4\right)(l_{21} - \alpha l_{11})\,K_0(p_2 r)\ \right]; \tag{49}$$

$$\bar{\sigma}_{rr} = \frac{F(s,R)}{h}\left[-\alpha + \frac{(\alpha l_{12} - l_{22})}{(l_{11}l_{22} - l_{12}l_{21})}\left[\left(\beta^2\alpha_4 - \alpha\theta_1\right)K_0(p_1 r) + \frac{2\alpha_4}{rp_1}K_1(p_1 r)\right]\right.$$
$$\left. + \frac{(l_{21} - \alpha l_{11})}{(l_{11}l_{22} - l_{12}l_{21})}\left[\left(\beta^2\alpha_4 - \alpha\theta_2\right)K_0(p_2 r) + \frac{2\alpha_4}{rp_2}K_1(p_2 r)\right]\right]; \tag{50}$$

$$\bar{e} = \frac{\alpha_4 F(s,R)}{h(l_{11}l_{22} - l_{12}l_{21})}\left[(\alpha l_{12} - l_{22})K_0(p_1 r) + (l_{21} - \alpha l_{11})K_0(p_2 r)\right]; \tag{51}$$

$$\bar{u} = -\frac{\alpha_4 F(s,R)}{h\,p_1 p_2(l_{11}l_{22} - l_{12}l_{21})}\left[p_2(\alpha l_{12} - l_{22})K_1(p_1 r) + p_1(l_{21} - \alpha l_{11})K_1(p_2 r)\right] \tag{52}$$

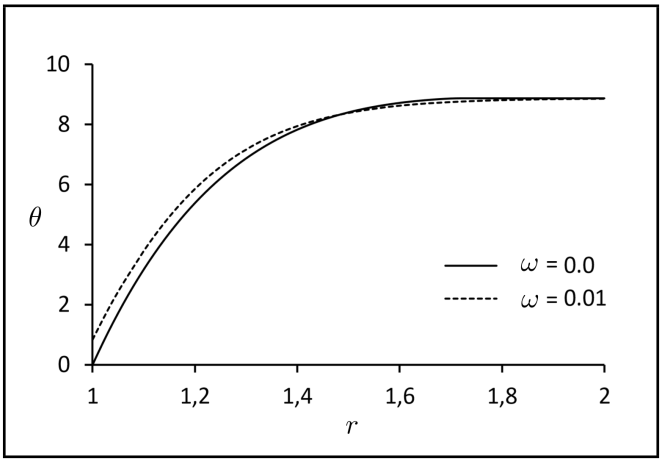

Figure 2. The thermo-dynamic temperature with different value two-temperature parameter.

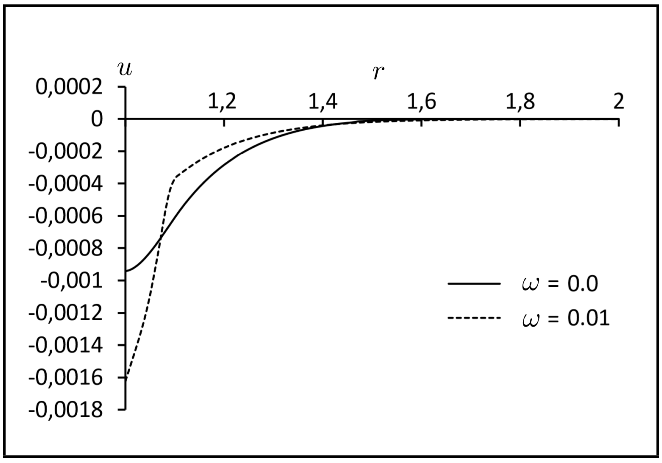

Figure 4. The displacement with different value two-temperature parameter.

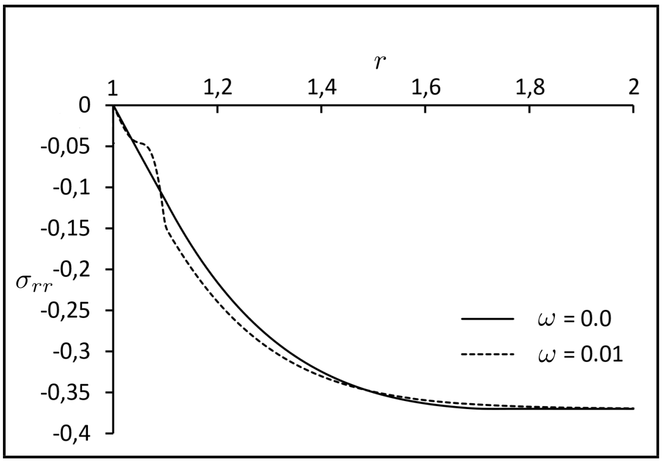

Figure 3. The stress with different value two-temperature parameter.

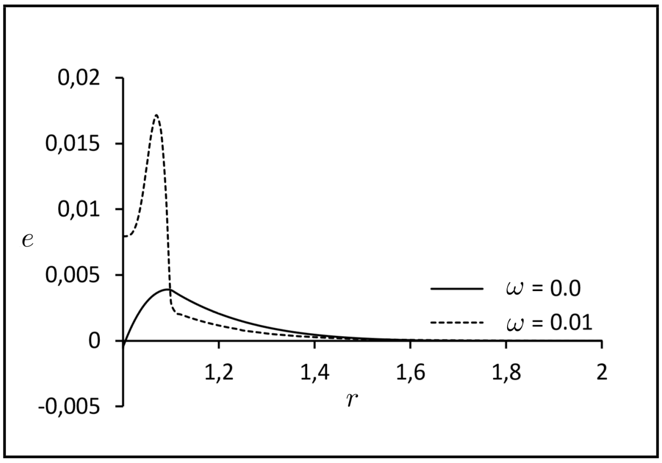

Figure 5. The strain with different value two-temperature parameter.

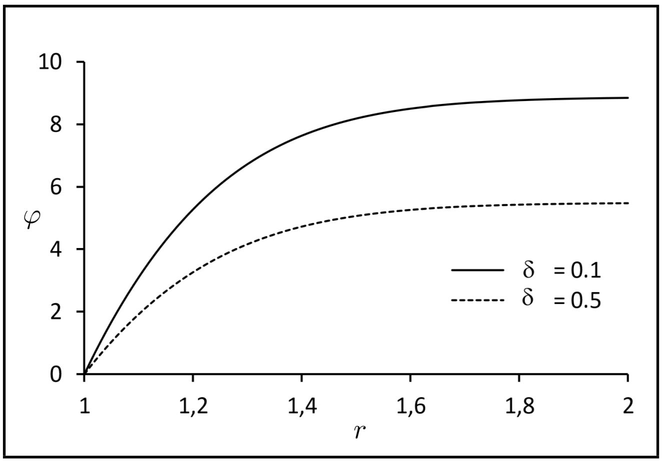

Figure 6. The conductive temperature with different value of absorption coefficient.

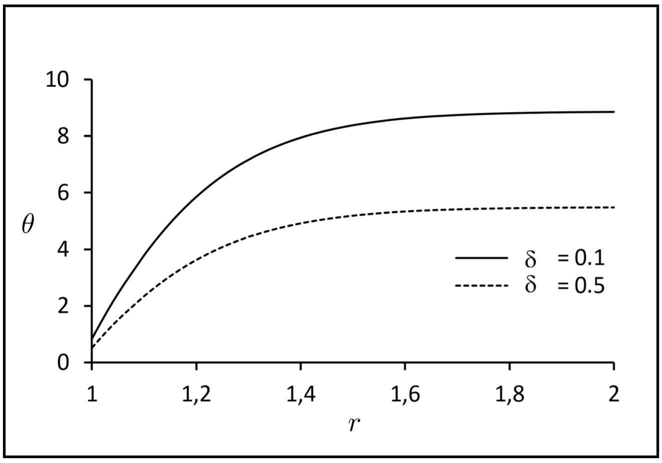

Figure 7. The thermo-dynamic temperature with different value of absorption coefficient.

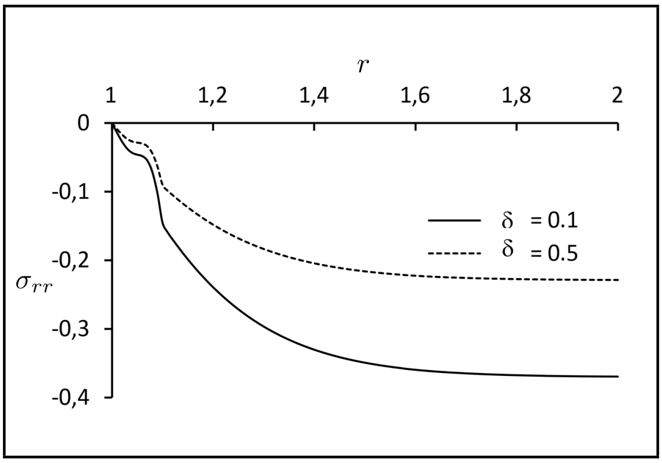

Figure 8. The stress with different value of absorption coefficient parameter.

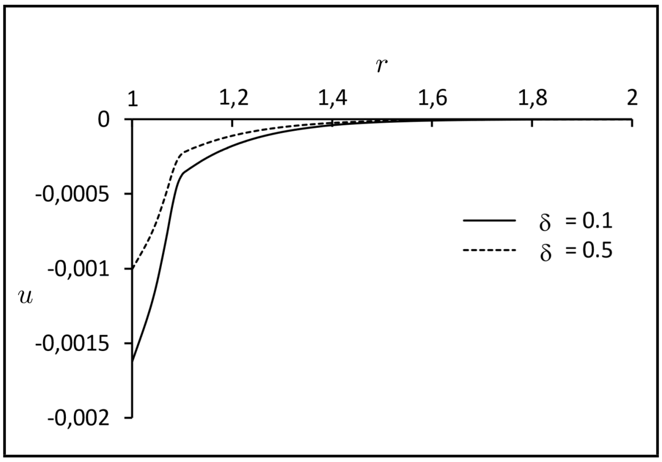

Figure 9. The displacement with different value of absorption coefficient.

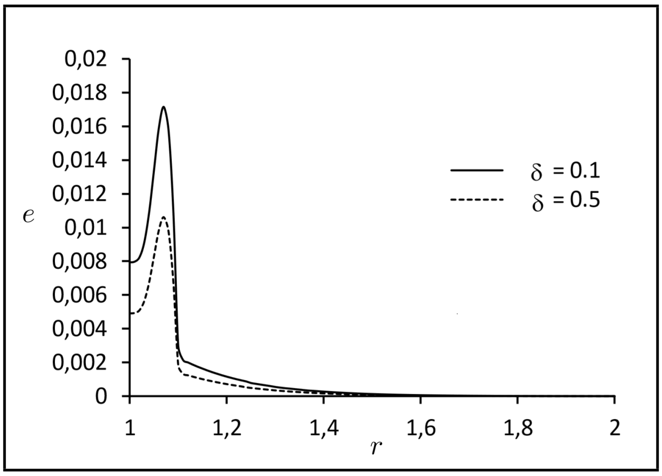

Figure 10. The strain with different value of absorption coefficient.

with different value of laser pulse parameter $\upsilon = 0.1, 0.05$ to stand on the effect of this parameter on all the studied filed. This group of figures shows that the laser pulse parameter has significant effects on the distributions of the conductive temperature, the thermo-dynamic temperature and the stress, while it has weak effects on the distribution of the displacement and the strain. When the value of laser pulse parameter increases, all the state functions of the material decrease.

4. CONCLUSION

In this work, a studying of the induced temperature and stress fields in an elastic infinite medium with cylindrical cavity under the purview of two-temperature thermoelasticity has been done. The medium has been considered to be an isotropic homogeneous thermoelastic material. The bounding plane surface of the cavity is loaded thermally by time exponentially decaying laser pulse and we found the following:

1. The two-temperature parameter has a significant effect on all the studied fields.

2. The absorption coefficient parameter has a significant effect on all the studied fields.

3. When the value of the absorption coefficient parameter increases, all the state functions of the material decrease.

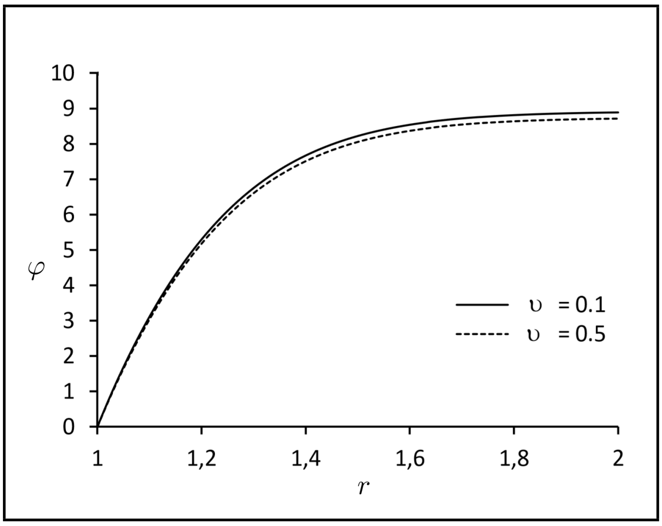

Figure 11. The conductive temperature with different value of laser pulse parameter.

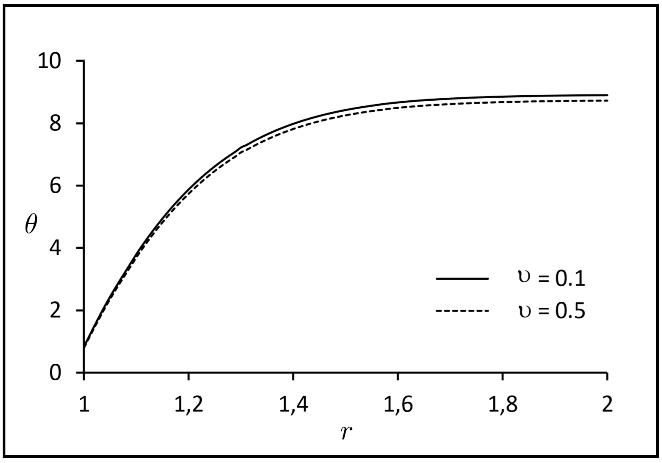

Figure 12. The thermo-dynamic temperature with different value of laser pulse parameter.

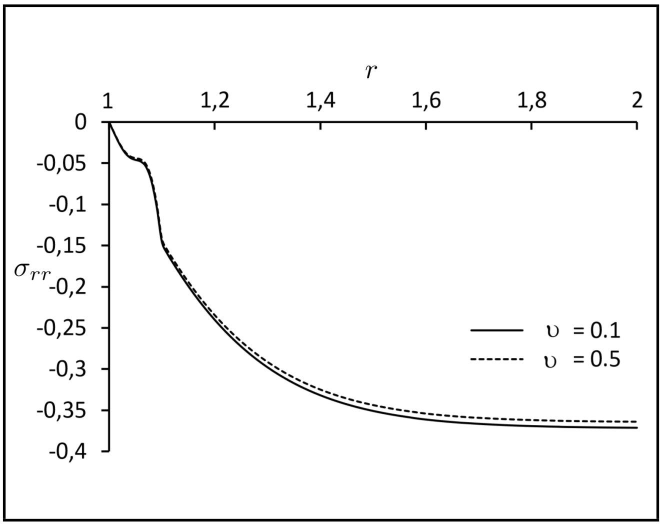

Figure 13. The stress with different value of laser pulse parameter.

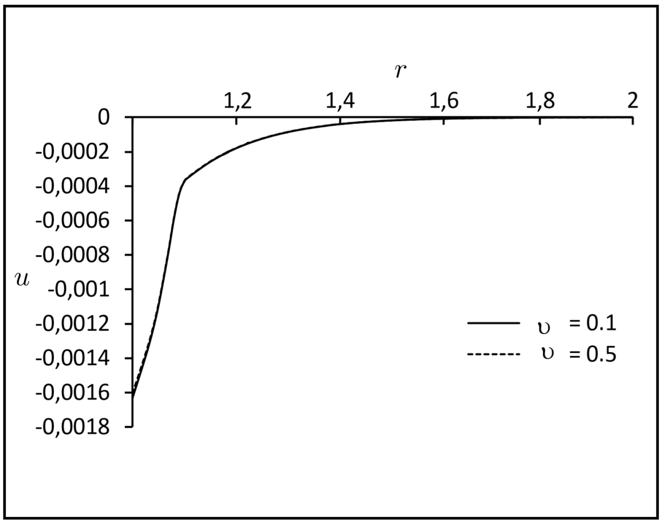

Figure 14. The displacement with different value of laser pulse parameter.

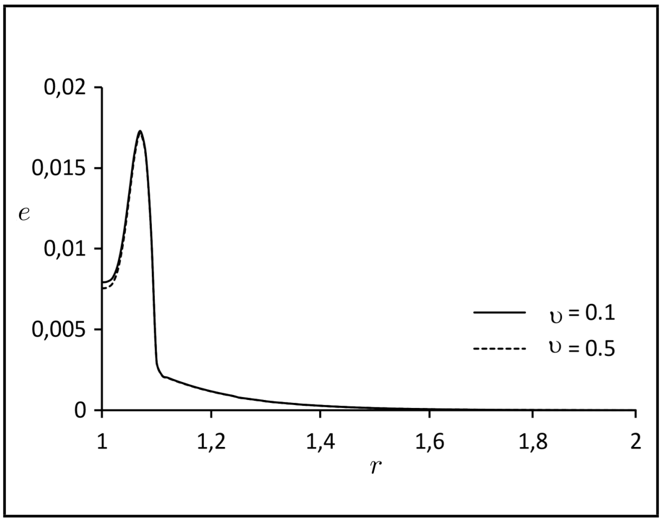

Figure 15. The strain with different value of laser pulse parameter.

4. The laser pulse parameter has significant effects on the distributions of the conductive temperature, the thermo-dynamic temperature, and the stress, while it has weak effects on the distribution of the displacement and the strain.

5. When the value of laser pulse parameter increases, all the state functions of the material decrease.

REFERENCES

[1] Biot, M. A. Thermoelasticity and irreversible thermodynamics, *Journal of Applied Physics* **27**(3), 240–253 (1956). http://dx.doi.org/10.1063/1.1722351

[2] Bargmann, H. Recent developments in the field of thermally induced waves and vibrations, *Nuclear Engineering and Design* **27**(3), 372–385 (1974). http://dx.doi.org/10.1016/0029-5493(74)90181-2

[3] Boley, B. A. *Thermal stresses: a survey*, Springer, (1980). http://dx.doi.org/10.1007/978-1-4613-3156-8_1

[4] Chandrasekharaiah, D. S. Thermoelasticity with second sound: a review, *Applied Mechanics Reviews* **39**(3), 355–376 (1986). http://dx.doi.org/10.1115/1.3143705

[5] Lord, H. W., Shulman, Y. A generalized dynamical theory of thermoelasticity, *Journal of the Mechanics and Physics of Solids* **15**(5), 299–309 (1967). http://dx.doi.org/10.1016/0022-5096(67)90024-5

[6] Green, A. E., Lindsay, K. A. Thermoelasticity, *Journal of Elasticity* **2**(1), 1–7 (1972). http://dx.doi.org/10.1007/BF00045689

[7] Sun, Y., Fang, D., Saka, M., Soh, A. K. Laser-induced vibrations of micro-beams under different boundary conditions, *International Journal of Solids and Structures* **45**(7), 1993–2013 (2008). http://dx.doi.org/10.1016/j.ijsolstr.2007.11.006

[8] Tzou, D. Y. *Macro-to micro-scale heat transfer: the lagging behavior*, CRC Press, (1996). ISBN-10: 156032435X

[9] Tzou, D. Y. *Macro-to microscale heat transfer: The lagging behavior*, In. Taylor & Francis (Washington, DC), (1997).

[10] Wang, X., Xu, X. Thermoelastic wave induced by pulsed laser heating, *Applied Physics A* **73**(1), 107–114 (2001). http://dx.doi.org/10.1007/s003390000593

[11] Gurtin, M. E., Williams, W. O. An axiomatic foundation for continuum thermodynamics, *Archive for Rational Mechanics and Analysis* **26**(2), 83–117 (1967). http://dx.doi.org/10.1007/BF00285676

[12] Chen, P. J., Gurtin, M. E. On a theory of heat conduction involving two temperatures, *Zeitschrift fr Angewandte Mathematik und Physik ZAMP* **19**(4), 614–627 (1968). http://dx.doi.org/10.1007/BF01594969

[13] Chen, P. J., Gurtin, M. E., Williams, W. O. On the thermodynamics of non-simple elastic materials with two temperatures, *Zeitschrift fr angewandte Mathematik und Physik ZAMP* **20**(1), 107–112 (1969). http://dx.doi.org/10.1007/BF01591120

[14] Chen, P. J., Williams, W. O. A note on non-simple heat conduction, *Zeitschrift fr angewandte Mathematik und Physik ZAMP* **19**(6), 969–970 (1968). http://dx.doi.org/10.1007/BF01602278

[15] Ieşan, D. On the linear coupled thermoelasticity with two temperatures, *Zeitschrift fr Angewandte Mathematik und Physik ZAMP* **21**(4), 583–591 (1970). http://dx.doi.org/10.1007/BF01587687

[16] Abbas, I. A. Eigenvalue approach for an unbounded medium with a spherical cavity based upon two-temperature generalized thermoelastic theory, *Journal of Mechanical Science and Technology*, **28**(10), 4193-4198 (2014). http://dx.doi.org/10.1007/s12206-014-0932-6

[17] Abbas, I. A. A problem on functional graded material under fractional order theory of thermoelasticity, *Theoretical and Applied Fracture Mechanics*, **74**, 18–22 (2014). http://dx.doi.org/10.1016/j.tafmec.2014.05.005

[18] Abbas, I. A. A GN model based upon two-temperature generalized thermoelastic theory in an unbounded medium with a spherical cavity, *Applied Mathematics and Computation*, **245**, 108–115 (2014). http://dx.doi.org/10.1016/j.amc.2014.07.059

[19] Abbas, I. A. Fractional order GN model on thermoelastic interaction in an infinite fibre-reinforced anisotropic plate containing a circular hole, *Journal of Computational and Theoretical Nanoscience*, **11**(2), 380–384 (2014). http://dx.doi.org/10.1166/jctn.2014.3363

[20] Abbas, I. A. Three phase lag model on thermoelastic interaction in an unbounded fiber-reinforced anisotropic medium with a cylindrical cavity, *Journal of Computational and Theoretical Nanoscience*, **11**(4), 987–992 (2014). http://dx.doi.org/10.1166/jctn.2014.3454

[21] Quintanilla, R. On existence, structural stability, convergence and spatial behavior in thermoelasticity with two temperatures, *Acta Mechanica* **168**(1–2), 61–73 (2004). http://dx.doi.org/10.1007/s00707-004-0073-6

[22] Youssef, H. M. Theory of two-temperature-generalized thermoelasticity, *IMA journal of applied mathematics* **71**(3), 383–390 (2006). http://dx.doi.org/10.1093/imamat/hxh101

[23] Puri, P., Jordan, P. M. On the propagation of harmonic plane waves under the two-temperature theory, *International journal of engineering science* **44**(17), 1113–1126 (2006). http://dx.doi.org/10.1016/j.ijengsci.2006.07.002

[24] Magaña, A., Quintanilla, R. Uniqueness and growth of solutions in two-temperature generalized thermoelastic theories, *Mathematics and Mechanics of Solids* **14**(7), 622–634 (2009). http://dx.doi.org/10.1177/1081286507087653

[25] Youssef, H. M. Generalized thermoelastic infinite medium with cylindrical cavity subjected to moving heat source, *Mechanics Research Communications* **36**(4), 487–496 (2009). http://dx.doi.org/10.1016/j.mechrescom.2008.12.004

About the Authors

Rashmita Parida received her bachelors degree in mechanical engineering from OSME (presently Government College of Engineering), Keonjhar under BPUT, Rourkela, India in 2009. She received her masters degree in mechanical engineering with a specialization in machine design and analysis from VSSUT, Burla, India in 2013. She received the University Gold Medal and Silver Medal for the Best Engineering Post Graduate and Best Mechanical Engineering Post Graduate, respectively. Since 2014, she has worked as an assistant professor in the Department of Mechanical Engineering at College of Engineering and Technology, Bhubaneswar, India. She was a lecturer at GHITM, Puri, India from 2009 to 2011 and an assistant professor at AITM, Bhubaneswar, India from 2013 to 2014. She taught classes at the undergraduate level including engineering mechanics, mechanics of solids, machine dynamics, and machine design, as well as fatigue, creep, and fracture at the graduate level. Her research interests include linear and non-linear structural vibrations and control and rotor dynamics.

Pusparaj Dash was born in 1965. He completed HSC and ISc in 1982 and 1984 respectively. He obtained his bachelors degree in mechanical engineering in 1988 from UCE (now VSSUT), Burla, India and masters degree in machine design and analysis from REC (now NIT), Rourkela, India in 1990. He received his doctorate degree in mechanical engineering from IIT, Kharagpur, India with a thesis on Study of parametric vibration of sandwich beam in 2001. He worked as a lecturer from 1990 to 2002 at IGIT, Sarang, a reader from 2002 to 2010 at VSSUT, Burla and from 2010 onwards working as a professor in the Department of Mechanical Engineering at VSSUT, Burla, India. He has published nearly thirty research articles related to structural vibration and rotor dynamics in various reputable international and national journals and conference proceedings.

Hisako Orimoto received her BS degree from Hiroshima Prefectural Womens University in 2003, her MS degree from Prefectural University of Hiroshima in 2008, and her D.Eng. degree from Hiroshima University in 2009. After her work as a system engineer in the System Development Division at NTT DATA Chugoku Co. and a Research Associate of Hiroshima National College of Maritime Technology, she is now an assistant professor in the Department of Management Information Systems at Prefectural University of Hiroshima. Her research interests include the digital signal information processing and data processing. Dr. Orimoto received an Excellent Paper Presentation Award from the Institute of Electrical Engineers of Japan and an Incentive Award at the Society of Instrument and Control Engineers in 2010 and 2014, respectively. She is a member of IEICE, SICE, ASJ, and IIAV.

Akira Ikuta received his BE and ME degrees from Kyushu Institute of Technology in 1976 and 1978, respectively, and his D.Eng. degree from Hiroshima University in 1981. After his work as a research associate of electrical engineering at Hiroshima University and an assistant professor of mechanical systems engineering of Kinki University, he is currently a professor in the Department of Management Information Systems, Prefectural University of Hiroshima. His research interests include the digital signal information processing and wave motion environment (sound, vibration and electromagnetic wave). He a member of the Editorial Board of Advances in Acoustics and Vibration. Dr. Ikuta received a Best Paper Award at the 2014 FCTA, 6th in the International Conference on Fuzzy Computation Theory and Applications in 2014. He is a member of IEICE, SICE, ASJ, and IIAV.

Yegui Xiao received his BS degree in electrical engineering from Northeastern University Shenyang, China, in 1984 and his MS and PhD degrees in electrical engineering from Hiroshima University, Higashi-Hiroshima, Japan, in 1988 and 1991, respectively. He is now a professor at the Prefectural University of Hiroshima. He was a visiting professor with the Institute for Computing, Information, and Cognitive Systems (ICICS), University of British Columbia, Vancouver, BC, Canada, in 2002. His main research interests include statistical signal processing, adaptive filters, and machine learning. Dr. Xiao received a Best Thesis Work Award for his BS degree, an Excellent Paper Presentation Award from the Institute of Electrical Engineers of Japan, and a Best Paper Award at the 23rd International Technical Conference on Circuits/Systems, Computers, and Communications, in 1984, 1991, and 2008, respectively. He is a member of IEICE, SICE, and IEEE.

Shuguang, Zuo was born in Hunan, China in 1968. He received his PhD degree from Jilin Industrial University in 1996. He is a Professor of vehicle engineering, Clean Energy Automotive Engineering Center, School of Automotive Studies, Tongji Unversity. He is the co-author of the textbooks, "Road Vehicle Dynamics" and "Road Vehicle Dynamics: Problems and Solutions Workbook". Both books have been published by SAE. He is the author of over 80 journal papers and about 25 of them are indexed by SCI, EI and/or ISTP. His current research interests include vehicle system dynamics and automotive noise, vibration and harshness issues. Prof. Zuo is a member of SAE International and also provides peer review and consultation for several state/enterprise foundation committees. Recent years, he has been in charge of 5 national research projects and 3 province-financed projects. He also leads several research programs in cooperation with various international corporations.

Kaijun, Wei was born in Anhui, China in 1989. She received her Bachelor Degree in Vehicle Engineering from China Agriculture University in 2011 and then became a PhD candidate in Clean Energy Automotive Engineering Center, School of Automotive Studies, Tongji University under supervision of Prof. Shuguang Zuo in Shanghai, China. Her current research interests include the aerodynamic noise and its control of the air supply system in fuel-cell vehicles. She is the co-author of over 10 published papers, and recently gave a speech titled Study on the aerodynamic noise of centrifugal compressors with rotor static eccentricity in the 167th ASA Meeting.

Xudong, Wu was born in Jiangsu, China in 1983. He received his PhD degree in Vehicle Engineering from Tongji University under supervision of Prof. Shuguang Zuo in 2011 and then continued his research in the post-doctorate station in Institute of Acoustics, Tongji University. He is the author of over 30 journal/international conference papers and most of them are indexed by EI, SCI and/or ISTP. Since 2013, he has been an Assistant Professor in Vehicle Engineering, Clean Energy Automotive Engineering Center, School of Automotive Studies, Tongji University. His current research interests include vehicle system dynamics and the application of phononic crystals in the vibration control of clean energy vehicles.

Mojtaba Mahzoon is a professor of mechanical engineering at Shiraz University. He received his BS from Petroleum University of Technology in Abadan, Iran, and both his MS and PhD from the University of California, Berkeley, US. He has studied and researched in many areas of engineering, including applied mathematics, continuum mechanics, dynamical systems, and vibration control. So far, he has supervised about 53 postgraduate students, and his has published over 60 peer-reviewed journal articles. Since 2014, he has been the head of the Mechanical Engineering Department at Shiraz University.

Mohammad Hassan Kadivar is a professor of mechanical engineering at Shiraz University. He received his BS from Shiraz University, his MS and PhD in mechanical engineering from the University of Illinois, US, as well as a PhD in aerospace engineering from Kyushu University, Japan. His area of specialization covers a wide range of engineering applications but mainly focused on composites, structural mechanics, plates and shells, and optimisation methods. He has supervised 45 postgraduate students and published over 35 articles in peer-reviewed journals.

About the Authors

Amirali Kamal Sadeqi has been a researcher of mechanical engineering at the Chamran University of Ahvaz since 2013. He has completed his bachelors and masters programs in mechanical engineering at the Bahonar University of Kerman (2009) and Shiraz University (2012), respectively. His interests and research fields include structural vibration and dynamics, nonlinear modal analysis, viscoelastic and composite materials, FEM, and numerical solutions. He has recently been involved in teaching some undergraduate courses in engineering.

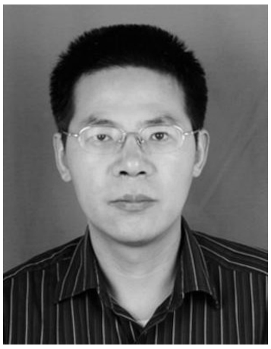

Mao Qibo was born in Zhejiang, P. R. China in 1975. He received the Ph.D degree for research on radiation modes sensor by using shaped piezoelectric materials for structural-acoustic control in Mechanical Engineering from the Jiangsu University, China in 2001. From 2001 to 2003, he joined in Institute of Acoustics, Nanjing University, China as a postdoctoral research fellow continuing his research on active control of sound and vibration by using smart materials. From October 2003 to 2010, he was a research fellow in Laboratory for Acoustics, Empa-Swiss Federal Laboratories for Materials Science and Technology, Switzerland. Since 2010, he has belonged to the staff of Nanchang HangKong University, School of Aircraft Engineering, China. In 2013, he was promoted to the position of a full professor for sound and vibration control, design of adaptive acoustic/vibration absorbers and vibration-based damage detection.

Pooja Singhal has been working as an assistant professor in the Mathematics Department of PCET, Lalru (Punjab), India since 2011. Prior to this, she worked for M.M. University, Mullana (Haryana), India and HIT, Nukur (U.P.), India. She received her PhD degree from CCS University, Meerut in 2013.

Arun Kumar Gupta has been teaching undergraduate and graduate courses of mathematics since 1983. His main duties are teaching, evaluating, and demonstrating. Other than teaching, his research interests are in vibrations of plates. He has participated in many national and international seminars and conferences. He has more than 75 research papers published in international journals of foreign repute. He has reviewed a few international research papers. He is also on editorial boards of different international journals. He guided more than 15 PhD students. Furthermore, he worked as a professor in mathematics at the University of Tikreet, Tikreet, Iraq.

Samer Gowid studied mechanical engineering at Cairo University (Egypt, 2001) and received his MS in mechanical design engineering in 2008. Currently, he is a PhD candidate at the School of Electronic, Electrical and Systems Engineering, Loughborough University (UK) and a teaching assistant of mechanical engineering at Qatar University (Qatar). Samer is a member of the Control Systems research group members at Loughborough University, working on the profitability, reliability, and maintenance optimization of LNG liquefaction section on Floating LNG terminal (FLNG). His work includes the development of a robust CBM system for FLNG centrifugal equipment.

Roger Dixon is a professor of Control Systems, Associate Dean of Research, Head of the-Control Systems research group,and the director of the Systems Engineering Doctorate Centre at Loughborough University (UK). His research focuses on various aspects of control systems engineering, including the application of model-based control systems design, model-based fault detection and isolation, system condition/health monitoring and fault tolerant design (of controllers and actuators). Prof. Roger is a Fellow of the Higher Education Academy, Fellow of the Institution of Mechanical Engineers, and group representative to the United Kingdom Automatic Control Council (UKACC).

Saud Ghani is the Associate Dean of Development and Industrial Relations at the College of Engineering, Qatar University (Qatar). From 2011 to 2014, he was the Head of Mechanical and Industrial Engineering Department. Dr. Saud received his PhD from the Department of Mechanical,Materials and Manufacturing Engineering, University of Nottingham (UK, 2002). His research focuses on various aspects of thermofluids engineering including: CFD, experimental fluid mechanics and flow visualization, biomedical engineering, airflow through human airways, and CSF flow.

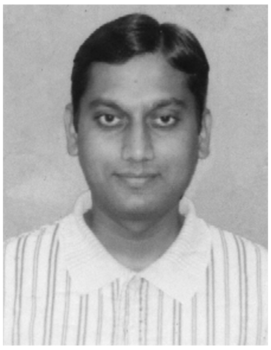

Rupesh V. Bhortake received the Master of from University of Pune, Maharashtra, India, and he is doing his Ph.D. in Mechanical Engineering at North Maharashtra University, Maharashtra, India. At present he is working as an Associate Professor in TSSMs, Padmabhooshan-Vasantdata Patil Institute of Technology, Bavdhan, Pune -411021, Maharashtra. Mr. Rupesh Bhortake is a also lifetime member of Indian Society for Technical Education. (ISTE), Institute of Engineers and ASME. His interesting area of research is Noise and Vibration.

Bimlesh Kumar received Ph.D. degree in Mechanical Engineering from National Institute of Technology, Jamshedpur India, with a specialization in Noise and Vibration. At present he is working as Principal, J.T.M.C.O.E. Faizpur-425524, Jalgaon Maharashtra, India. He is Ph.D. recognized guide at North Maharashtra University, Solapur University, Bharti Vidyapeeth University, Pune, Singhania University, Tiberalla University, Rajasthan, and Satyabhama University, Chennai also Chairman and member on various committees at University level like Selection Committee for Principals and Faculty, LIC and Research Centre Recognition. Life member of ITI, ISTE, ISTD, ISRMTT, SAEI and IIAV.

Caroline Parsons Lubert graduated from the University of Exeter, UK, with a BS in mathematics in 1984 and a PhD in engineering in 1988. Her PhD study, titled An experimental and theoretical study of the aeroacoustics of external-Coanda gas flares, was awarded for work jointly conducted with British Petroleum, plc. She subsequently worked as a postdoctoral research fellow in the University of Exeters School of Engineering, where she developed mathematical models of crossflow microfiltration systems. From 1992 to 1999 she was a lecturer in the School of Mathematics and Statistics at the University of Plymouth, UK. In August 1997, she was awarded Young Logistician of the Year by the International Society of Logistics. In 1999, she joined the Mathematics and Statistics Department at James Madison University (USA), where she is a professor of mathematics. Caroline is the technical editor of a number of international conferences and journals and a co-recipient of a US Patent (#US 6,763,337 B1: Weighted Wedge Defuzzification for Conceptual Design Evaluation). She is also the recipient of several awards for both teaching and research. For the last fifteen years, her research has focused on developing and validating models for predicting the high-frequency noise (Turbulent Mixing Noise and Shock-Associated Noise) emitted by Turbulent Coanda Wall Jets.

About the Authors

Christian Schwantes received his BS in 2010 at James Madison University, studying chemistry and mathematics. In 2015, he completed his PhD in chemistry in the lab of Dr. Vijay Pande at Stanford University in Stanford, California, where he studied protein folding using computer simulation. His main interests are in analysis: specifically developing novel machine learning algorithms and building statistical models for turning complicated datasets into human-comprehensible insight.

Ricky Shafer received his BS in mathematics from James Madison University and his MS in applied mathematics from the University of Colorado Boulder. He is currently working at The Cincinnati Insurance Company in Cincinnati, USA. His work uses generalized linear models to develop pricing plans for homeowner insurance products. His current research centers on utilizing machine learning algorithms on insurance data. These include random forests, gradient boosting, and association analysis.

Rachid El Kaak received his associate degree in mechanical engineering from University of Mohammed V, Rabat, Morocco, in 2003 and his MS degree in physics from the University of Hassan II, Casablanca, Morocco, in 2011. Now, he is a PhD student in the Departement of Mechanical Dngineering, ENSET-Cedoc: ST2I-LaMIPI University of Mohammed V, Rabat, Morocco. His main research interests include functionally graded structures, dynamics, and vibrations.

Khalid El Birki is a professor in mechanical engineering, specifically in vibration and composite studies at the High School of Technology, Mohammed V University of Rabat, Morocco. He graduated with a degree in mechanics of materials in 1992 from the Mohammed V University of Rabat, Morocco. He received his MS in mechanical engineering in 1995 from the Faculty of Applied Sciences, Sherbrooke University, Canada. He received his PhD in 2004 from the Mohammadia School of Engineering, Mohamed V University of Rabat, Morocco.

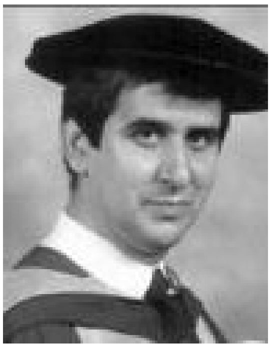

Rhali Benamar is a professor of mechanical engineering and vibration studies at Mohammedia School of Engineering, Mohamed V University, Agdal, Rabat, Morocco. He got a degree in civil engineering in 1982 from the Ecole National des Ponts et des Chausses, Paris, France. He received his PhD degree in 1990 from the Institute of Sound and Vibration, University of Southampton, U.K.

Eman A. N. Al-Lehaibi is an assistant professor at a branch of Najran University in the Department of Mathematics. Al-Lehaibi obtained a BS, MS, and PhD in applied mathematics from Om al-Qura University, graduating with honors. Al-Lehaibi currently serves as the Vide Dean of Mathematic Department in Sharourah and a supervisor of Quality Unit Department in the Faculty of Science and Arts. Additionally, Al-Lehaibi was a trainer of CORT program for faculties in various Saudi universities. Current research interests include thermoelectricity and applications on fractional order thermoelasticity.

IIAV Fellows and Senior Member

The following seven members: Barry Gibbs, UK; Bela Buna, Hungary; Lars Håkansson, Sweden; Eric Herrera, USA; Jian Kang, UK; Marek Pawelczyk, Poland; and Jun Yang, China have been admitted to the grade of Fellow by the International Institute of Acoustics and Vibration (IIAV).

Barry Gibbs

Professor Barry Gibbs is a member of the Acoustics Research Unit in the Liverpool University School of Architecture. His main research is into sources of structure-borne sound, particularly for prediction and control of noise in buildings. Other interests include low frequency sound transmission in buildings and the development of acoustic sources for sonic cleaning of industrial processes. He serves on national and international standards committees on machine noise and vibration and has acted as consultant in room acoustics, environmental noise and for noise control engineering. He holds or has held over twenty major research grants for research ranging from analysis of the vibration of structural elements to the use of impulse response methods in acoustics field measurement. A recently funded project, on vibro-acoustic transmission in buildings, is in collaboration with the Fachhochschule Stuttgart-Hochschule fur Technik and stems from his role as the UK representative on European standards committees concerned with the characterisation of vibrating sound sources. He is the author and co-author of over 80 journal papers and over 150 conference papers and was founding co-editor of the journal Building Acoustics, a quarterly international journal on the acoustics of the built environment. Prof. Gibbs has been principal supervisor for approximately 20 PhD students and has examined about the same number at universities in the UK, the Netherlands, Hong Kong and Australia.

Bela Buna

Since 1994 Bela Buna serves as head and main owner of a company concerned with environmental protection. His main field of activity is in acoustics, noise and vibration control. He is a member of the Acoustical Committee of the Hungarian Academy of Science, a member of the German and French Acoustical Societies and fellow of the UK Institute of Acoustics. Previously, he worked for 27 years at the Institute of Transport Sciences, Budapest. He received a M.Sc. in traffic engineering and later in electrical engineering (instruments and process control). He speaks English, German, and some French. His Ph.D. thesis was concerned with the prediction of road transport noise. Dr. Buna has been involved in international studies and study tours, and has represented Hungary in various working groups (ISO, ECE, EU, and the EU WG6 Railway Noise). He has published more than 55 articles (some in various journals, e.g., ATA, Applied Acoustics, Noise Control Engineering, Vehicle Design) and presented papers at international conferences. He has written four books, and book chapters (in Verminderung des Verkerslärms of Springer Verlag, and the Transportation Noise Reference Book of Butterworths. Dr. Buna has recently organised a workshop in Hungary on the application of numerical methods in acoustical planning under the Hungarian Academy of Science. He has also taken part in different European common projects and regularly writes book reviews for the IJAV.

Lars Håkansson

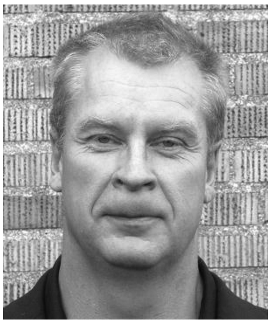

Lars Håkansson received the M.Sc. degree in Electrical Engineering from Lund University of Technology, Lund, Sweden, and the Ph.D. degree, in Mechanical Engineering from Lund University of Technology, Sweden, in 1989 and 1999, respectively. He joined Blekinge Institute of Technology (BTH) 1999 and was appointed senior lecturer in electrical engineering and continued to expand his research within the area of noise and vibration control. In 2005 he was appointed associate professor and received the responsibility, as principal researcher and advisor, for the active control group in the Department of Signal Processing, BTH. Dr. Håkansson is a professor in the Department of Applied Signal Processing (former Department of Signal Processing), at BTH. His current research interests are in signal analysis, condition monitoring, signal processing, active noise and vibration control, remotely controlled laboratories, analytical and experimental modelling of mechanical and acoustical systems. He has a keen interest on developing new technology and his research is generally in collaboration with industry. This has resulted in several patents. Lars Håkansson is a member of the IIAV and the Scandinavian Vibration Association (SVIB). He is a member of the Editorial Board of the Journal of Low Frequency Noise, Vibration and Active Control and of the Editorial Board of the Journal of Advances in Acoustics and Vibration.

Eric Herrera

Eric Herrera's career has spanned over 25 years in NASA, Boeing, Bombardier, Xerox, Freudenberg, Alliant Techsystems (ATK), Boeing Defense and Space. He is currently serves in a multidisciplinary leadership role with the Boeing Company. He has developed methodologies for increasing productivity such as accelerated PD (APD) & Systems Integration Hybrid Engineering (SIHE) now adopted in the industry. In addition, he has headed up two state of the art laboratories, staffing, P&L, technology and project management. He has also participated in the FAA certification of Boeing aircraft, made possible by use of modeling and predictive codes. In addition, he has developed codes to model aerodynamic/structural interactions as well as near and far field fluctuations. He was also involved in developing novel composite material for the Sealaunch launch vehicle, now being used on Boeing Aircraft. He also participated in the inaugural launch of the Sealaunch vehicle from a floating platform at sea. This required developing new predictive tools for unique dynamic loads and environments. Eric received numerous patent awards for new materials and technology, such as optimized fiberglass structures with inherent damping, composite polymers, vibration controlling devices. He participated in the inaugural launch of the NASA/ATK Ares 1-X launch vehicle and designed isolation devices for components that were on this maiden flight.

Jian Kang

Jian Kang is the Professor of Acoustics at the University of Sheffield School of Architecture. Prof Kang obtained his first degree and MSc from Tsinghua University in China, and PhD in acoustics from the University of Cambridge. He worked at the University of Cambridge and the Fraunhofer Institute of Building Physics in Germany. He is a fellow of the UK Institute of Acoustics, a fellow of the Acoustical Society of America, an EPSRC College member, and the Editor in Environmental Noise for Acta Acustica united with Acustica. His publications include three books, over 100 papers in refereed journals, and more than 300 conference papers and technical reports. He has been the principal investigator for over 50 research projects supported by funding bodies including EPSRC, EU, British Academy and Royal Society, and a consultant for more than 50 acoustics and noise control projects internationally. Prof. Kang is the coordinator of the WUN (Worldwide Universities Network) Environmental Acoustics Network; chair of the EU funded COST Network on Soundscape of European Cities and Landscapes, with 40+ international partners in various disciplines and sectors; and co-chair of the EPSRC funded Noise Futures network, with 30 members from various sectors including researchers, policy makers and consultants.

Marek Pawelczyk

Marek Pawelczyk obtained his M.Sc. in 1995, Ph.D. in 1999, D.Sc. (habilitation) in 2005, and attained the scientific title of professor in 2014. He is currently a full titular professor at the Silesian University of Technology, and holds the positions of vice-director of the Institute of Automatic Control, and Head of Measurements and Control Systems Division. He also gained professional experience at a number of universities in Germany, UK, and Denmark. He is an author of three books on active control, about 150 journal and proceedings papers, and five patent applications. He has been a frequent reviewer for several international journals, book publishers, international conferences, and Ph.D. theses in several countries. He has served on many scientific committees and organising committees of international conferences. He cooperates closely with industrial companies. He is a co-author of several projects including: ultrasonic monitoring of petroleum fractions; safety monitoring in mines; active personal hearing protections systems; active noise control in industrial halls; active control of machinery; noise reduction in large-scale HVAC systems; active noise control in headrests; and semi-active control of vehicle suspension. He has received many prizes from domestic and international organizations. He has been involved in the IIAV for many years. Since 2008 he has been the Managing Editor of the International Journal of Acoustics and Vibration. In 2007-2011 he was the Vice-President for Communications, and in 2012-2014 President of the IIAV. He was the General Chair of the 16th ICSV held in Krakow, Poland, in 2009.

Jun Yang

Jun Yang is a Distinguished Professor of Chinese Academy of Sciences and is now the Executive director of the Acoustical Society of China. He chaired the Local Organizing Committee for the 21st International Congress on Sound and Vibration (ICSV21) and contributed significantly to acoustics research and education. Prof. Yang has been engaged in the research and development of acoustics and signal processing for nearly 30 years. His research interests include noise and vibration control, active control system, communication acoustics, 3D audio system, acoustic signal processing, and nonlinear acoustics. He has completed over 30 research projects for industries and the government, and received over 100 million RMB in research and development funds. Prof. Yang has published more than 150 refereed papers in journals and book chapters, over 200 papers in conferences. He has been granted 40 domestic and international patents.

Thomas Lorenzen, USA, has been admitted to the grade of Senior Member by the International Institute of Acoustics and Vibration (IIAV.)

Thomas Lorenzen

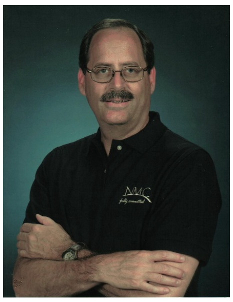

Thomas Lorenzen started work at dBA Inc (an acoustical engineering firm) in 1989 after graduating from Georgia Tech. He has worked in the electronics and/or building industry for all of his adult life. After completing several semesters of college credit in architectural design, he changed his course of study to electronics engineering due to his interest in this rapidly evolving field. After receiving degrees in engineering (ASEET, BSEE), Mr. Lorenzen worked for several manufacturers and contractors in related areas while pursuing post-graduate studies in architectural acoustics (MS – architectural acoustics). Thomas Lorenzen has background and experience in projects dealing with acoustics, communication systems, and noise control. He has the following certifications and professional affiliations: Acoustical Society of America (ASA), Audio Engineering Society (AES), Institute of Noise Control Engineering (INCE), Institute of Electrical and Electronics Engineers (IEEE), National Society of Professional Engineers (NSPE), Music Educators National Conference (MENC), ”Syn-Aud-Con”, International Communications Industries Association (ICIA) Design Council. Mr. Lorenzen has been the principal acoustician for dBA Acoustics inc., for over 26 years.